DISS. ETH NO. 29765

The Thermal Emission and Time-Variability of Earth as an Exoplanet

A thesis submitted to attain the degree of

DOCTOR OF SCIENCES of ETH ZURICH

(Dr. sc. ETH Zurich)

presented by

Jean-Noël Mettler

Master of Science UZH in Theoretical Astrophysics and Cosmology

University of Zürich

born on September 7, 1991

accepted on the recommendation of

Prof. Dr. S. P. Quanz

Prof. Dr. R. Helled

2023

Cover illustration: Artist impression by the author J.-N. Mettler.

Hubble Legacy Field: NASA, ESA, G. Illingworth and D. Magee (University of California, Santa Cruz), K. Whitaker (University of Connecticut), R. Bouwens (Leiden University), P. Oesch (University of Geneva,) and the Hubble Legacy Field team

Earth: JMA Himawari-8/9, https://registry.opendata.aws/noaa-himawari

Aqua satellite: NASA, Published source: "Spacecraft Icons" at NASA Science, Image hosted by smd-prod.s3.amazonaws.com

Thermal emission data: AIRS Science Team/Larrabee Strow (2019), AIRS/Aqua L1C Infrared (IR) resampled and corrected radiances V6.7, Greenbelt, MD, USA, Goddard Earth Sciences Data and Information Services Center (GES DISC)

Abstract

The field of exoplanet research is a young and vibrant area of study, continually evolving and expanding as new discoveries and technologies emerge. More than 5500 exoplanets in over 4000 planetary systems have been found in the last two decades by various detection techniques. While many of these detected worlds are unsuitable for supporting life, there is a growing number of potentially habitable terrestrial planets being discovered. For the first time in human history, advancements in technology and science now place us on the verge of being able to search for signs of life beyond our solar system. This requires the direct detection of their atmospheres, which provide invaluable insights into planetary habitability and the potential discovery of extraterrestrial life. One key challenge, however, is the correct interpretation of their spectra. Measured exoplanet spectra are global averages (due to the large exoplanet-observer separation). Hence, local variations in the atmospheric composition, pressure-temperature ($P-T$) structure, and clouds are unresolved. Additionally, due to the faint nature of their signals, the temporal and spectral resolution is limited. Thus, observations of terrestrial habitable zone exoplanets are spatially and temporally averaged, low-resolution spectra. To prepare for future attempts to characterize these distant habitable worlds, studying Earth and its characteristics from afar offers a unique opportunity to explore a truly habitable and inhabited world. In this thesis, I follow a data driven approach to investigate Earth's thermal emission spectrum and its time-variability in the context of exoplanet research. By leveraging the wealth of Earth observation data, I investigate Earth's time-resolved and spectrally-limited thermal emission spectrum for five specific target locations in Chapter 2. Then I expand the analyses from time-resolved to spatially- and time-unresolved mid-infrared (MIR) spectra for different full-disk observing geometries in Chapter 3. In Chapter 4, I use these disk-integrated MIR spectra

as input for atmospheric retrievals and, for the first time, perform a systematic retrieval analysis of real disk- and time-averaged Earth spectra, where the retrieval results can be compared to ground truths from Earth observation. My research yielded two comprehensive datasets with matching ground truths. Using these datasets, I demonstrated that a representative, disk-integrated thermal emission spectrum of Earth does not exist. Instead, both the thermal emission spectrum and the strength of spectral absorption features show seasonal variability and depend on viewing geometry. In addition, a strong spectral degeneracy with respect to viewing geometry and season was found. This indicates that multi-epoch measurements and time-dependent signals may be required in order to fully characterize planetary environments. Finally, investigating Earth as a directly imaged exoplanet by means of the future MIR space mission concept LIFE, showed that that the mission would correctly identify Earth as a planet where life could thrive, with detectable levels of bioindicators, a temperate climate, and surface conditions that allow for liquid surface water. In conclusion, the analyses and results presented in this thesis, demonstrate the power of thermal emission data for the characterization of habitable terrestrial exoplanets, but they also caution us to be careful in the analysis and interpretation. The interdisciplinary approach of exoplanetary science, planetary science, and remote sensing of Solar System bodies offers a promising framework to pave the way for the detection of life beyond our solar system.

Zusammenfassung

Die Exoplanetenforschung ist ein junges und dynamisches Forschungsgebiet, das sich im Zuge neuer Entdeckungen und Technologien ständig weiterentwickelt und ausweitet. In den letzten zwei Jahrzehnten wurden mehr als 5500 Exoplaneten in über 4000 Planetensystemen mit Hilfe verschiedener Nachweismethoden entdeckt. Während viele dieser entdeckten Welten für Leben ungeeignet sind, werden immer mehr potenziell bewohnbare terrestrische Planeten entdeckt. Zum ersten Mal in der Geschichte der Menschheit sind wir dank des technologischen und wissenschaftlichen Fortschritts in der Lage, nach Anzeichen für Leben jenseits unseres Sonnensystems zu suchen. Dies erfordert die direkte Beobachtung ihrer Atmosphären, die uns essenzielle Informationen über die Bewohnbarkeit von Planeten und die mögliche Entdeckung außerirdischen Lebens liefern. Eine grosse Herausforderung besteht jedoch darin, ihre Spektren richtig zu interpretieren. Gemessene Exoplanetenspektren sind globale Mittelwerte (aufgrund der grossen Entfernung zwischen Exoplanet und Beobachter). Das bedeutet, dass lokale Variationen in der Zusammensetzung der Atmosphäre, im Druck-Temperatur-Profil (P–T) und in Wolken nicht aufgelöst werden können. Ausserdem ist die zeitliche und spektrale Auflösung aufgrund der schwachen Signale begrenzt. Beobachtungen von terrestrischen Exoplaneten sind daher räumlich und zeitlich gemittelte Spektren mit geringer Auflösung. Zur Vorbereitung zukünftiger Versuche, diese fernen bewohnbaren Welten zu charakterisieren, bietet die Untersuchung der Erde und ihrer Eigenschaften aus der Ferne eine einzigartige Gelegenheit, eine tatsächlich bewohnte und bewohnbare Welt zu erforschen. In dieser Arbeit verfolge ich einen datengetriebenen Ansatz, um das thermische Emissionsspektrum der Erde und seine zeitliche Veränderung im Kontext der Exoplanetenforschung zu untersuchen. Unter Verwendung von Erdbeobachtungsdaten untersuche ich das zeitlich aufgelöste und spektral begrenzte

thermische Emissionsspektrum der Erde für fünf spezifische Ziele in Kapitel 2. Anschließend erweitere ich die Analysen auf räumlich und zeitlich nicht aufgelöste Infrarotspektren für verschiedene Beobachtungsgeometrien der gesamten Erdscheibe in Kapitel 3. In Kapitel 4 verwende ich diese scheibenintegrierten Infrarotspektren als Input für unser hochmodernes atmosphärisches Retrieval-Framework und führe zum ersten Mal eine systematische Retrieval-Analyse von echten scheibenintegrierten Erdspektren durch, wobei die Retrieval-Ergebnisse mit Erdbeobachtungsdaten verglichen werden können. Meine Forschung hat zu zwei umfassenden Datensätzen mit entsprechenden Erdbeobachtungsdaten (ground truths) geführt. Mit diesen Datensätzen konnte ich zeigen, dass es kein repräsentatives, scheibenintegriertes thermisches Emissionsspektrum der Erde gibt. Sowohl das thermische Emissionsspektrum als auch die Stärke der spektralen Absorptionsmerkmale zeigen jahreszeitliche Variabilität und hängen von der Beobachtungsgeometrie ab. Ausserdem habe ich eine starke spektrale Entartung in Abhängigkeit von der Beobachtungsgeometrie und der Jahreszeit festgestellt. Dies deutet darauf hin, dass mehrere Messungen und zeitabhängige Signale erforderlich sind, um die planetare Umgebung vollständig zu charakterisieren. Schliesslich zeigte die Untersuchung der Erde als direkt abgebildeter Exoplanet im Rahmen des zukünftigen MIR-Weltraumteleskopkonzepts LIFE, dass die Mission die Erde korrekt als einen Planeten identifizieren würde, auf dem Leben gedeihen könnte. Mit nachweisbaren Biosignaturen, einem warmen Klima und Oberflächenbedingungen, die flüssiges Oberflächenwasser ermöglichen. Zusammenfassend zeigen die in dieser Arbeit vorgestellten Analysen und Ergebnisse die Stärken thermischer Emissionsdaten für die Charakterisierung bewohnbarer terrestrischer Exoplaneten, mahnen aber auch zur Vorsicht bei der Analyse und Interpretation. Der interdisziplinäre Ansatz der Exoplanetenforschung, der Planetenforschung und der Fernerkundung von Objekten des Sonnensystems bietet einen vielversprechenden Rahmen, um den Weg für die Entdeckung von Leben jenseits unseres Sonnensystems zu ebnen.

Contents

List of Figures

List of Tables

But why, some say, the Moon? Why choose this as our goal? And they may well ask, why climb the highest mountain?(...). We choose to go to the Moon and do the other things, not because they are easy, because they are hard; because that goal will serve to organize and measure the best of our energies and skills, because that challenge is one that we are willing to accept, one we are unwilling to postpone, and one we intend to win (...).

— JFK, 1962

1 Introduction

1.1 Context and Motivation

When Voyager 1 took one last glimpse at our home planet in 1990 before leaving its planetary neighbourhood, it captured a portrait of our world: A pale blue dot suspended in a sunbeam surrounded by the cosmic dark. From this unique vantage point, this seemingly insignificant planet holds a profound significance. It is the only world we know of today that harbors life, a delicate biosphere teeming with diversity and wonder. For countless generations, humans have pondered the questions, "Are we alone in the universe?" and "How unique is Earth?". For the first time in human history, advancements in technology and science now place us on the verge of being able to address these questions and search for signs of life in and beyond our solar system.

Up until the 1990s, when Voyager captured the iconic *pale blue dot* picture, there was no observational evidence of planets beyond our own solar system. This all changed with the pivotal turning point in the mid-'90s, marked by the publication of Mayor and Queloz (1995)'s landmark discovery of the first extrasolar planet in another planetary system. A revolutionary discovery that forever altered our understanding and sparked a new era of astronomy and exoplanetary discovery. Their groundbreaking achievement was recognized with a share of the 2019 Nobel Prize in Physics.

In the last two decades, the field of exoplanet research grew and the search for

exoplanets continued. Nowadays, more than 5500 confirmed exoplanets[1] have been found by various detection techniques. These planets exhibit a wide range of planetary masses, radii, temperatures, orbital parameters, and host stellar properties (e.g., Batalha, 2014; Burke et al., 2015). This surprising diversity is one of the most remarkable findings in the field of exoplanet discovery. From the observational data, it becomes apparent that the most common type of planet is about two times the size of Earth or smaller (Marcy et al., 2014), a so called *Super-Earth*. Another interesting type is called *Hot Jupiters*, which are Jupiter-sized planets (or slightly larger due to their puffy atmospheres) that have very short orbital periods of below 10 days. The absence of both types of planets in our Solar System suggests that Solar System analogs, both in system architecture and type of planets, must be somewhat rare as none have been found so far. Although they are relatively challenging to detect.

Despite the fact that the majority of these detected planets are too massive or have extreme temperatures that are unsuitable for supporting life on their surfaces, numerous potentially habitable terrestrial planets have already been identified (Kane et al., 2016) orbiting in the so-called habitable zone (HZ; Kasting et al., 1993) of their host stars. Specific examples would be planets e, f, and g in the TRAPPIST-1 system, LHS 1140b, Proxima Centauri b, Kepler-442b, Kepler-186f, or TOI-700d (Montet et al., 2015; Anglada-Escudé et al., 2016; Dittmann et al., 2017; Gillon et al., 2017; Quintana et al., 2014; Gilbert et al., 2020). Due to detection biases, a considerable number of these identified exoplanets are larger than Earth and orbit close to the inner edge of their habitable zones.

Recent advancements in astronomy have yielded compelling statistical evidence indicating that nearly every star in our Milky Way Galaxy is accompanied by at least one planet (Cassan et al., 2012) and that terrestrial exoplanets are extremely common (Fressin et al., 2013; Marcy et al., 2014). Roughly, 1 in 5 Sun-like stars have an Earth-sized planet in the habitable zone (Petigura et al., 2013). In this context, "Sun-like" stars refers to G-type stars and "Earth-sized" encompasses planets with radii ranging from one to two times that of Earth. With our own galaxy hosting ~100 billion stars and the universe containing over 100 billion galaxies, the probability of life existing elsewhere appears inevitable. Measuring the distribution of life in the universe requires both the search for habitable environments where life may thrive and the determination of whether these habitable environments in fact do host life (Schwieterman, 2016). The former

[1] http://exoplanet.eu visited September 2023

can be achieved by the analysis of a planet's distance to its host star, determining its effective temperature and surface pressure, and by inferring the presence of habitability markers such as water vapour and atmospheric carbon dioxide (e.g., Des Marais et al., 2002; Kaltenegger et al., 2007; Schwieterman, 2016; Kaltenegger, 2017). Hence, the habitability of a planet can be confirmed by analyzing planetary characteristics. Yet, the ultimate objective is to determine whether an exoplanet is *inhabited* which requires the remote detection of spectroscopic biosignatures.

A biosignature is a feature whose presence or abundance requires a biological origin (Des Marais et al., 2002). They can be grouped into three categories: gaseous, surface, and temporal biosignatures. In this scheme, gaseous biosignatures are direct or indirect products of metabolism, surface biosignatures are spectral features imparted on radiation reflected or scattered by organisms, and temporal biosignatures are modulations in measurable quantities that can be linked to the actions and time-dependent patterns of a biosphere (Meadows, 2006, 2008; Schwieterman et al., 2018). Thus, the search for life beyond our solar system will focus on spectral signatures of exoplanets. The spectral features of biosignatures can be detected across a range of electromagnetic wavelengths, including visible light, near-infrared, and mid-infrared where the most optimal coverage for detection falls within the range of 0.5 - 25 microns (micrometers [µm]) (e.g., Des Marais et al., 2002).

Despite this seemingly limited wavelength coverage, the detection and characterization of exoplanets, both giants and terrestrial ones, relies on sophisticated instruments designed to overcome various challenges. One of the primary constraints is spectral coverage, which refers to the range of wavelengths the instrument can observe. Different types of exoplanets emit or reflect light at specific wavelengths, making broad spectral coverage crucial for comprehensive observations. Additionally, spectral resolution plays a vital role in distinguishing subtle variations in the light spectrum, allowing to extract valuable information about a planet's composition and atmospheric properties. Another significant challenge is the contrast between the host star and the planet, as exoplanets are typically much dimmer ($\sim 10^{-9}$ in the reflected light and $\sim 10^{-6}$ in thermal emission) than their parent stars.

These challenges underscore the need for advanced observational tools as well as sophisticated detection methods and data post-processing to overcome the limitations. Both ground-based telescopes and space-based telescopes play

pivotal roles in the field of astronomy and astrophysics, each offering unique advantages and facing their own set of limitations. Ground-based telescopes are located on Earth's surface and are often larger in size, allowing for greater light-collecting capabilities. They can be equipped with sophisticated instruments that provide high-resolution (resolution of up to 200'000, e.g., Pepe et al., 2014) observations. However, ground-based telescopes are subject to atmospheric disturbances, exhibiting temperature variations that lead to distinct differences in densities and refractive indices, which can degrade the quality of observations. Additionally, due to Earth's bright thermal background, ground-based mid-infrared observations are less sensitive than those from cooled space-borne telescopes. Space-based telescopes, like the Hubble Space Telescope or the James Webb Space Telescope, operate above Earth's atmosphere and are not affected by atmospheric interference or the thermal background. This enables them to capture sharper and clearer images and offer unparalleled advantages in observing faint and distant objects over long observation periods. They also have the advantage of observing a wider range of wavelengths, including ultraviolet and X-ray regions, which are largely absorbed by the atmosphere. Yet, space-based telescopes are more expensive to build, have smaller mirrors compared to some ground-based telescopes, and are limited in spectral coverage and resolution. The combination of both, ground- and space-based, telescopes is of course most valuable as they are complementary and the synergy maximizes the potential for scientific discovery.

The discovery of potentially habitable exoplanets sparked interest in spectroscopic studies of exoplanet surfaces and atmospheres for signs of life. Thus, over the next decades, the long-run goal of exoplanet science will be the characterization of the atmospheres of temperate terrestrial exoplanets in order to assess their habitability and search for indications of biological activity. This requires the direct detection of their signals over interstellar distances. From the ground, the 30–40 m Extremely Large Telescopes (ELTs) may provide us with the first images and high-resolution spectroscopy data of a few terrestrial exoplanets, once they are online in the late 2020s (e.g., Quanz et al., 2015; Snellen et al., 2015). However, none of the currently planned missions or projects are capable of detecting and characterizing the atmospheres of a statistically meaningful sample of temperate rocky exoplanets. As a result, the exoplanet community has to wait until space-based direct imaging is realized in future missions like the Habitable Exoplanet Observatory (Habex; Gaudi et al., 2020), Large Ultraviolet Optical Infrared Surveyor (LUVOIR; The LUVOIR Team, 2019), or the Large Interferometer For

Exoplanets (LIFE; Quanz et al., 2018).

The first generation of such terrestrial exoplanet detection and characterization missions will not be capable of spatially resolving the planets due to the large distances of at least several parsecs at which the exoplanets typically will be observed. Even with the most powerful telescopes conceived today, including the recently launched James Webb Space Telescope (JWST; Gardner et al., 2006), they will remain spatially unresolved point sources. Moreover, the relatively low plan net-to-star contrast ratio significantly limits the temporal sampling and the provided spectral information will be averaged over the observable disk and integration time. The latter may vary between several days and weeks to build up an adequate signal to noise ratio to detect biosignatures, depending on the target and mission concept. For example, in the specific case of JWST, which pushes the limits from detecting towards characterizing Jovian to super Earth exoplanets, the accumulation of transmission spectra from hundreds of transits is required in order to reach a signal to noise ratio high enough to potentially confirm the presence of biosignature pairs like O_2 & CH_4 or O_3 & N_2O (e.g., Krissansen-Totton et al., 2016; Fauchez et al., 2019; Lustig-Yaeger et al., 2019; Wunderlich et al., 2019; Tremblay et al., 2020). Hence, considering the mission's lifetime and the telescope time necessary for the detection of atmospheric biosignatures, probably only a few attempts will be made on specific targets.

One of the key challenges in atmospheric characterization is the interpretation of remote observations, which are limited in spatial, temporal and spectral resolution due to the vast distances involved and the limitations of current technology. During the integration time of future direct imaging missions, the spectral appearance and characteristics of a (rocky) planet change as it rotates around its spin axis and as spatial differences from clear and cloudy regions, contributions from different surface types as well as from different hemispheres evolve with time. In combination with the observed diversity of exoplanets, which is thought to also extend to their atmospheric mass and composition, makes the characterization of the planetary environment even more difficult. To overcome these challenges, the development and validation of sophisticated models are crucial in order to extract valuable information from these observations. Yet, the interpretation of the observed spectrum is not unique and a plethora of solutions exist to describe a planet's surface and atmospheric characteristics as the temporally and spatially unresolved data show spectral degeneracies. Without thorough exploration and validation of the parameter space, it is unlikely that we will be able to accurately

infer the expected, wide range of potential climates found on habitable exoplanets (e.g., Paradise et al., 2021; Mettler et al., 2023).

For the time being, obtaining the *in situ* data necessary for the validation of exoplanet models is limited to our Solar System. And although our spectral libraries and insights about the formation, composition and atmospheric properties of our neighbouring planets and their moons are continuously growing, Earth remains invaluable as the most extensively studied planet with abundant data and, foremost, as the sole known globally habitable planet harboring life. Therefore, Earth and its unique characteristics remain the key reference point to study the factors required for habitability and (the origin of) life (e.g., Meadows and Barnes, 2018; Robinson and Reinhard, 2018).

1.2 Earth Remote Sensing and the Search for Habitability and Life

To identify Earth analogs around distant stars and uncover potential signs of life, the direct detection of their signal is required. Determining whether a planet is habitable or inhabited comes down to understanding its exoplanetary atmosphere. For exoplanets, we can measure brightness, brightness temperatures, and chemical abundances through spectra by atmospheric photometry or spectroscopy. Analyzing the observed spectra (through atmospheric retrievals (e.g., Madhusudhan, 2018b)) will lead to constraints on the composition, structure, and dynamics of the atmospheres. This will yield valuable insights into planetary habitability and could lead to the detection of life. One key challenge in exoplanet characterization, however, is the correct interpretation of their spectra. Due to the large distances involved (typically spanning several parsecs) features of exoplanets are condensed into a tiny speck of light. Hence, they remain spatially unresolved point sources. To prepare for future attempts to characterize distant habitable worlds, studying Earth and its characteristics from afar offers a unique opportunity to explore a truly habitable and inhabited world by means of remote characterization.

Spatially-resolved flyby data from the *Pioneer 10/11* (Bender et al., 1974; Baker et al., 1975; Gehrels, 1976; Ingersoll et al., 1976; Kliore and Woiceshyn, 1976) and *Voyager 1/2* (Kohlhase and Penzo, 1977; Hanel et al., 1977) missions in the 1970s initiated the exploration of key concepts for the characterization of planetary

bodies other than Earth in our solar system. The photometric and spectroscopic observations, ranging from the ultraviolet to infrared, allowed planetary scientists to infer unprecedented details for these worlds such as planetary energy balance, surface and atmospheric chemical, thermal and composition properties including cloud and aerosol formation and distribution (for an extensive review see, Robinson and Reinhard, 2018). In 1993, Sagan et al. (1993) and Drossart et al. (1993) constituted a control experiment by applying remote sensing tools and techniques to search for life on Earth by analysing *Galileo* spacecraft (Johnson et al., 1992) Earth-flyby data. Their data indicated a habitable world with water, carbon, chemical energy, and signs of biological activity that modulates surface and atmospheric properties.

In the endeavour of getting a more distant point of view and high-resolution spectral data of Earth, instruments on several space probes like the Mars Global Surveyor (MGS) / Thermal Emission Spectrometer (TES), EPOXI, Lunar Crater Observation and Sensing Satellite (LCROSS), and Deep Space Climate Observatory (DSCOVR) (e.g., Christensen and Pearl, 1997; Livengood et al., 2011; Robinson et al., 2014; Yang et al., 2018) were pointed towards our home planet. Another method involves Earth-shine observations, where the reflected light from Earth is re-reflected from the unlit part of the Moon (e.g., Turnbull et al., 2006; Pallé et al., 2009). However, such data taken from a remote vantage point are limited in terms of viewing geometry and/or temporal coverage.

On the other hand, the regular monitoring of Earth, in particular from Earth-orbiting satellites and to some extent also from other spacecraft, yielded a rich collection of Earth observation data, which has been used to investigate Earth's appearance in both reflected light and thermal emission (for a recent review see, e.g., Robinson and Reinhard, 2018, and references therein). Such data offer an extensive temporal, spatial, and spectral coverage which can be tailored to represent exoplanet observation data (Tinetti et al., 2006a; Hearty et al., 2009; Gómez-Leal et al., 2012) or at least be interpreted in such a context. In the beginning of this thesis, I have analysed spatially resolved, single-surface measurements by the Moderate Imaging Spectroradiometer (MODIS), then I adopted the same approach as in Hearty et al. (2009) by using Atmospheric Infrared Sounder (AIRS) data and applied a similar limb darkening weighting function to the observations. Yet, the investigated time span, the disk-integrated full-disk viewing geometries, and the goal differ from their approach.

1.3 Earth Observation Instruments

Throughout this thesis, I have utilized data from three Earth observing instruments: the Atmospheric Infrared Sounder (AIRS; Aumann et al., 2003), the Moderate Imaging Spectroradiometer (MODIS; Remer et al., 2005), and the Infrared Atmospheric Sounding Interferometer (IASI; Blumstein et al., 2004). In the following subsections 1.3.1 - 1.3.3, the instruments will be discussed briefly in the order of their appearance.

AIRS and MODIS are installed on a scientific research satellite called *Aqua*, which is a fundamental component of NASA's international Earth Observing System (EOS). Being part of the "A-Train", Aqua and other satellites like OCO-2 and CloudSat fly in formation and provide complementary observations of aerosols, clouds, and atmospheric properties. The coordinated measurements from these satellites contribute to a better understanding of Earth's climate system and the effects of aerosols and clouds on the Earth radiation budget (Winker et al., 2003).

Aqua's primary mission is to provide comprehensive insights into Earth's water cycle and its various components (Parkinson, 2003a). Additionally, it extends its impact by delivering essential measurements of radiative energy fluxes and aerosols. Thus, the mission has significantly contributed to improving our understanding of global dynamics and processes occurring on the land and cryosphere, the oceans, and the atmosphere. Although, having originally been developed for a six-year lifespan, Aqua, that was launched in 2002, has far exceeded that goal and has a strong chance of operating successfully until 2026, when instrument shutdown and spacecraft passivation procedures will take place. Currently, four out of the six instruments, AIRS, AMSU, CERES, and MODIS continue transmitting high-quality data, whereas only reduced data quality from AMSR-E is received. The sixth instrument, HSB, was able to collect approximately nine months of high quality data before it failed in February 2003. In total, Aqua streams 89 Gigabytes of data a day to the ground stations.

The satellite is revolving Earth at an altitude of 705 km in a highly circular orbit with a near-polar, sun-synchronous trajectory. Orbiting the Earth approximately every 98.8 minutes, the satellite crosses the equator during its northward pass at 1:30 p.m. and during its southward pass at 1:30 a.m. daily, ensuring the collection of afternoon data.

Originally named EOS-PM to emphasize the afternoon contrast, Aqua passes within 10 degrees of each pole on every orbit, completing about 16 revolutions around Earth each day, thereby scanning the entire planet every one to two days, depending on the instrument's swath. The spacecraft's orbit track changes daily, resulting in a 16-day repeat cycle, during which it completes a total of 233 revolutions before returning to its initial track (e.g., Parkinson, 2003a).

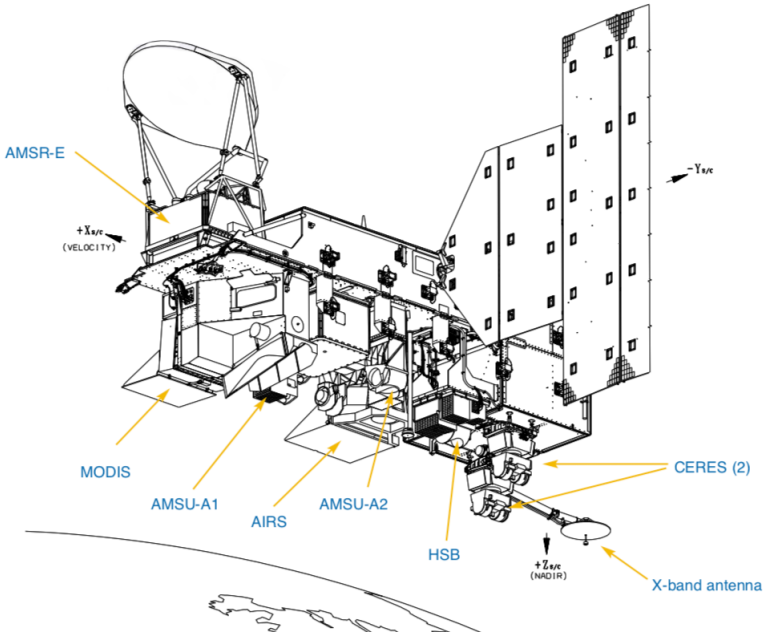

Figure 1.1: Line drawing of the Aqua spacecraft, with the six Earth-observing instruments and the X-band antenna labelled. The AMSU-A1 and AMSU-A2 work together as a single unit. The fully deployed solar array, shown on the top right, stretches 14 m into space (Parkinson, 2003a). Image courtesy: Reto Stöckli, TRW

Table 1.1: Aqua Specifications. Adapted from https://aqua.nasa.gov/content/about-aqua

Orbit:	Type: Sun-synchronous, near-polar, circular
	Altitude: 705 km
	Equatorial Crossings: 1:30 p.m. (south to north) and 1:30 a.m. (north to south)
	Inclination: 98.2°
	Period: 98.8 minutes
	Repeat Cycle: 16 days (233 revolutions)
Dimensions:	2.7 m x 2.5 m x 6.5 m stowed; 4.8 m x 16.7 m x 8.0 m deployed
Mass:	2,934 kg (1,750 kg spacecraft, 1,082 kg instruments, 102 kg propellants)
Power:	4,600 W silicon cell array and a NiH_2 battery
Average Data Rate:	89 Gbytes/day
Design Life:	6 years

1.3.1 Moderate Imaging Spectroradiometer (MODIS)

The Moderate Imaging Spectroradiometer is a cross-track, multi-disciplinary scanning radiometer with 36 spectral channels measuring visible and infrared bands in the wavelength range of 0.4–14.4 μm. The instrument focuses on both biological and physical measurements of the Earth-atmosphere system, generating approximately 40 data products from its observations. With horizontal spatial resolutions at nadir of 250 m, 500 m, and 1000 m, MODIS provides the most detailed spatial information among all the instruments aboard the Aqua satellite (Parkinson, 2003a). The products range from the ocean's photosynthetically active radiation, chlorophyll fluorescence and sea ice albedo to the land's land cover type, fires and land surface temperature and emissivity. For the atmosphere, they include cloud thermodynamic phase, aerosol optical depth and cloud top properties. As for all Aqua data products, the availability of the data is exceptional, as it is distributed not only through the EOS Data and Information Service (EOSDIS) but also via Distributed Active Archive Centers (DAACs) at Goddard Space Flight Center, the EROS Data Center in Sioux Falls, South Dakota, and National Snow and Ice Data Center (NSIDC) in Boulder, Colorado, as well as over 100 Direct

Broadcast (DB) stations distributed world-wide (aqua.nasa.gov, 2006).

Aqua MODIS is the second MODIS instrument in space, as its twin is orbiting Earth on another EOS-PM satellite called *Terra* that has been launched in 1999. According to Parkinson (2003b), Aqua's instrument incorporates some modifications over Terra's design such as a reduction in optical and electronic cross talk among the different bands and an improved radiative response versus scan-angle for the thermal emissive bands. In addition, a gain change has been made in two of the Aqua MODIS bands (bands 31 and 32, measuring at wavelengths of 10.78–11.28 μm and 11.77–12.27 μm, respectively) in order to have these bands saturate at a temperature of about 340K rather than saturating at about 400K as on Terra, allowing greater detail for temperatures below 340K. The change is aimed at improving the MODIS derived sea surface temperatures calculated from the data of these two bands (Parkinson, 2003b).

The instrument employs a conventional imaging spectroradiometer concept, consisting of a cross-track scan mirror and collecting optics, and a set of linear arrays with spectral interference filters located in four focal planes. The optical arrangement provides high radiometric sensitivity (12 bit) imagery throughout the channels. With a temporal resolution of 5 minutes, MODIS achieves a maximum swath of 2330 km by 2030 km at the equator due to a ± 55-degree scanning pattern. This leads to low-latitude data gaps between successive orbits, preventing full global daytime or nighttime coverage within a day. Although these data gaps are filled in on subsequent days, the full global coverage is obtainable every two days. Further in depths information about the design of MODIS can be obtained from Parkinson (2003a) , modis.gsfc.nasa.gov (2023) and aqua.nasa.gov (2006). An overview of its instrument specifications can be seen in Table 1.2.

As the satellite moves in the along-track direction, the rotation mirror of MODIS sweeps in the across-track direction, as illustrated by figure 1.2. The detectors (10 for the 1km band) are aligned in the along-track direction on four focal plane arrays and as they are swept across the Earth view, 203 consecutive scans sampled 1354 times in the cross-track direction are performed for each detector, corresponding to approximately 5 minutes worth of data. A granule of data will be composed of 1354 by 2030 pixels, resulting in a spatial coverage of 2330 km by 2030 km.

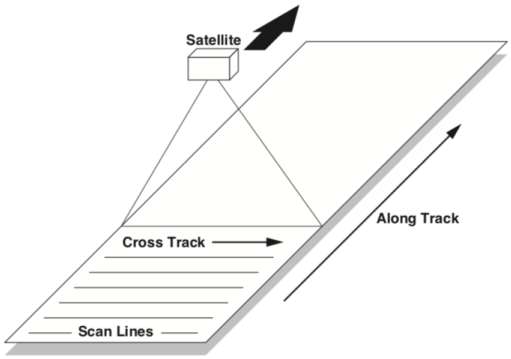

Figure 1.2: A typical satellite swath of a scanning instrument such as MODIS. The scan lines are approximately perpendicular to the direction of motion of the satellite ground track. (Klein et al., 1999)

The right figure displays a thermal image recorded by MODIS capturing a portion of the northwestern coast of Africa, encompassing Mali, Niger, Nigeria, and a segment of the Sahara desert at the lower section. The image also reveals parts of the North Atlantic Ocean at the top and right borders, while the River Niger forms an "L"-shaped structure towards the center-left. The color scheme corresponds to spectral radiance values, denoted in W/(m^2 µm sr), with red indicating high values and blue representing lower values. A reference line on the right-side color bar signifies the mean spectral radiance value for the entire area, which is approximately 8.7 W/(m^2 µsr).

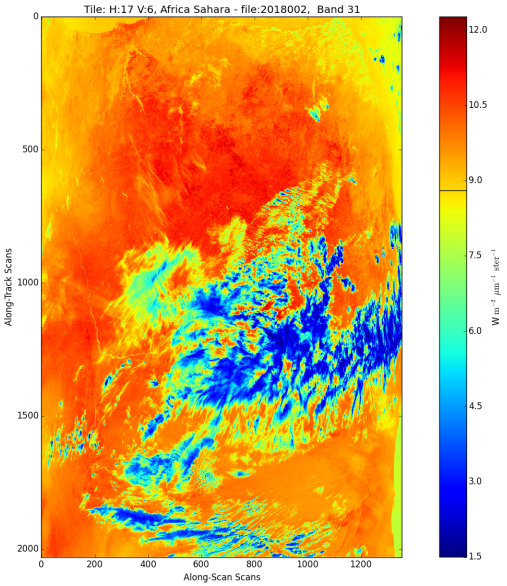

Figure 1.3: Thermal image composed of MODIS data showing parts of west Africa along with cloud formations.

Table 1.2: MODIS instrument specifications. Source: modis.gsfc.nasa.gov (2023)

Channels:	36 spectral bands
Spectral Range:	20 bands within 0.4–3.0 µm; 16 bands within 3–14.5 µm
Spatial Resolution:	250 m (bands 1-2), 500 m (bands 3-7), 1000 m (bands 8-36)
Swath Dimensions:	2330 km (cross track) by 10 km (along track at nadir)
Size:	1.0 x 1.18 x 1.63 m
Weight:	228.7 kg
Power:	162.5 W (single orbit average)
Data Rate:	10.6 Mbps (peak daytime); 6.1 Mbps (orbital average)
Design Life:	6 years

1.3.2 Atmospheric Infrared Sounder (AIRS)

Like MODIS, the Atmospheric Infrared Sounder is orbiting on the Aqua spacecraft. AIRS is a hyperspectral device with 2378 spectral channels, and it is designed to measure detailed, global observations of the vertical structure of the Earth's atmosphere by measuring outgoing longwave radiation in the infrared (IR) range between 3.74 to 15.4 µm (Aumann et al., 2003; Heidar et al., 2021). Hyperspectral imaging in the IR has become a pivotal source of satellite data in order to asses climate change, monitor atmospheric conditions, measure greenhouse gas content, and retrieve geophysical parameters. Currently, AIRS is one of seven operating hyperspectral infrared sounders in space (Table 1 in Heidar et al., 2021). While four are maintained by NASA and NOAA, three are operated by the European Organisation for the Exploitation of Meteorological Satellites (EUMETSAT). Their Infrared Atmospheric Sounding Interferometer (IASI) instruments are installed on three spacecrafts and are valuable complements to AIRS, offering advantages in various atmospheric research and remote sensing applications.

AIRS (shown in Figure 1.4) is a continuously operating cross-track scanning infrared sounder, consisting of a telescope that feeds an echelle spectrometer. The AIRS spectrometer acquires 2378 spectral samples at resolutions, $\lambda \setminus \delta\lambda$ ranging from 1086 to 1570, in three spectral bands: 3.74-4.61 µm, 6.20-8.22 µm, and 8.8-15.4 µm. The measured spectra are calibrated to an accuracy better than 1 ppm using absorption features in the upwelling spectrum. Moreover, they are

corrected for time-varying spectral calibration, which includes compensating for Doppler shifts caused by Earth's rotation (Strow et al., 2006). Newer Level 1C [2] products now offer corrections for spatial nonuniformity and spectral drifts, alongside cleaned and gap-filled radiances achieved through principal component reconstruction. A disk-integrated Level 1C radiance spectrum (v6.7) for an equatorial viewing geometry is shown in Figure 1.5.

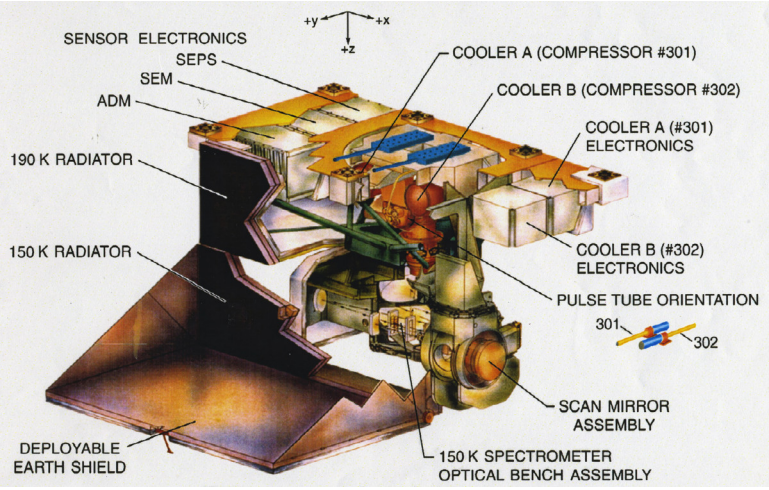

Figure 1.4: Labelled schematic of the AIRS instrument and its components. µm. Source: https://airs.jpl.nasa.gov/mission/airs-project-instrument-suite/airs/

While several spectral gaps were filled, one big gap between 4.6-6.2 µm is still visible, lying in a strong water absorption feature centered at 6.2 µm (e.g., Catling et al., 2018).

1.3.3 Infrared Atmospheric Sounding Interferometer (IASI)

Similar to AIRS, the Infrared Atmospheric Sounding Interferometer is a hyperspectral instrument with the primary mission to provide highly accurate data about the atmosphere, land, and oceans, which is essential for weather forecasting and climate research. It achieves this using a precisely calibrated Fourier Transform

[2] Satellite processing levels progress from raw data at Level 0 to calibrated and geolocated data at Level 1B and 1C, and further processed data products at higher levels, incorporating corrections, enhancements, and geophysical parameters (level 3) as well as model output or results from analyses of lower-level data (e.g., variables derived from multiple measurements) (level 4).

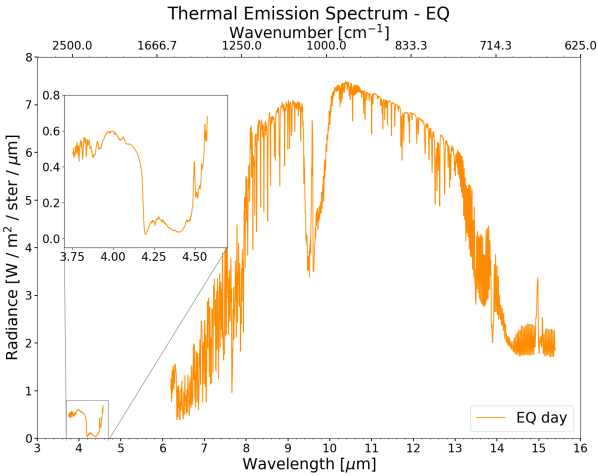

Figure 1.5: A level 1C (v6.7) disk-integrated thermal emission spectrum for the Africa-centered equatorial viewing geometry, EQ. AIRS spectra have a gap between 4.6-6.2 µm due to broken channels.

Spectrometer (FTS) that operates in the spectral range of 3.62 – 15.5 µm and an associated infrared imager in the 10.3 – 12.5 µm range. The FTS employs a Michelson interferometer to generate interferograms, which are then processed onboard to derive atmospheric information. For a detailed instrument description and how it operates, see Blumstein et al. (2004).

Spectral requirements dictate that IASI covers a broad spectral range with high spectral resolution. Unlike AIRS, IASI's spectral range extends continuously between 3.62 – 15.5 µm without gaps, encompassing 8461 spectral channels with a spectral resolution of 0.25 cm^{-1} (apodised: 0.5 cm^{-1}). At a temperature of 280 K, the instrument's noise equivalent differential temperature (NEΔT) is 0.5-2.0 K, 0.2-0.5 K, and 0.2-0.3 K at 3.62 – 5 µm, 5.0 – 8.3 µm, and 8.3 – 15.5 µm, respectively. At Earth's peaking wavelength range 10.3 – 12.5 µm, IASI measures the radiances to an uncertainty of 0.8 K at 280 K. Geometrically, it scans the Earth's surface in a plane perpendicular to the satellite's orbit track, ensuring a swath of approximately 2400 km. Daily global coverage is achieved since the instrument is installed on three satellites.

Table 1.3: AIRS instrument specifications. Source: Chahine et al. (2006)

Channels:	2378 spectral channels
Spectral Range:	3.74 – 15.4 µm
Spatial Resolution:	1350 m (spectrometer), 2300 m (VIS/NIR)
Spectral Resolution:	1200 ($\lambda/\Delta\lambda$)
Swath Dimensions:	1650 km (cross track) by 13.5 km (along track at nadir)
Size:	1.40 x 1.50 x 0.76 m
Weight:	177 kg
Power:	220 W
Data Rate:	1.27 Mbps
Design Life:	6 years

1.4 Earth's Thermal Emission Spectrum

1.4.1 The Thermal Emission Spectrum and Absorption Features

The stellar radiation reaching a planet is partly scattered back into space and partly absorbed and then re-emitted as thermal radiation. This can be observed through two types of spectra: the reflectance spectrum and the thermal emission spectrum. While we observe the reflected starlight off a planet in the UV to NIR in the former spectrum, the latter emerges from the planet's emitted flux in the MIR, dependent on its temperature. Figure 1.6 shows a simple flux comparison between the sun and a selection of solar system planets as seen from a distance comparable to that of a nearby star (10 pc). While the star's blackbody curve is shown in magenta, the planet's wavelength-independent albedo reflectance spectrum (first peak) and their thermal emission spectra (second peak) are drawn in black. For Earth, a pure molecular absorption spectrum is superimposed in blue for reference (Figure source: Des Marais et al., 2002).

From the figure, we note that the reflectance spectra of planets align with the star's peak wavelength. This is due to the fact that the planets reflect and scatter more light at the wavelengths where their host star emits the most energy. Their thermal emission spectra, however, peak at different wavelengths. This difference is attributed to their distinct distances from the star, resulting in varying amounts

of irradiance received, along with differences in planetary characteristics. Bodies at different temperatures will emit thermal radiation at different wavelengths, following the Planck's law of blackbody radiation. Warmer planets will emit more radiation at shorter wavelengths (higher energy) and cooler planets will emit more radiation at longer wavelengths (lower energy). This leads to their thermal emission spectra peaking at different wavelengths, unlike the consistent alignment seen in the reflectance spectra due to scattering and reflection processes. Additionally, the figure illustrates the flux contrast between a planet and the star. For a Jupiter-sized planet, the star is about a billion times brighter (x10^9) in the optical wavelength range, while in the thermal wavelength range this factor reduces to a million (x10^6). For rocky planets the planet-to-star contrast is even smaller. The Earth-Sun contrast ratio, for example, is $\sim 10^{-10}$ in the visible (at 0.5 μm) and $\sim 10^{-7}$ in the MIR (at 10 μm). Hence, the ratio improves in the MIR over the visible by a factor of a thousand.

The reduced flux contrast in the thermal wavelength range is not the only reason why it is favorable to observe the thermal emission of terrestrial exoplanets. The MIR is rich in information required to characterize temperate terrestrial planets and to assess their potential habitability. Observations in the MIR provide valuable information regarding surface temperature and pressure, atmospheric thermal structure, planetary radius, presence (or absence) of an atmosphere, as well as atmospheric composition and structure with meaningful molecular gas abundance constraints (e.g., Des Marais et al., 2002; Line et al., 2019). Many molecules have strong absorption bands in the MIR and even at relatively low spectral resolutions, absorption features of key greenhouse gases and/or bioindicators such as O_3, CH_4, CO_2, N_2O, and H_2O can be detected (e.g., Christensen and Pearl, 1997; Hearty et al., 2009; Line et al., 2019, also, see Figure 1.8).

These spectral features are created when the re-emitted radiation propagates through the atmosphere and is affected by absorption, emission, and scattering processes. Besides chemistry, the dominant mode of interaction between molecules and MIR radiation in the troposphere and stratosphere is absorption. IR-absorbing molecules absorb at a wide range of wavelengths corresponding to transitions between different forms of energy levels. Most of the absorption features found in the MIR spectrum are vibration-rotation bands, for which the band center is determined by a vibrational transition, with simultaneous rotational transitions forming branches of discrete lines on either side of the center (e.g., Goody and Hu, 2003). The abundance of an atmospheric species needed to

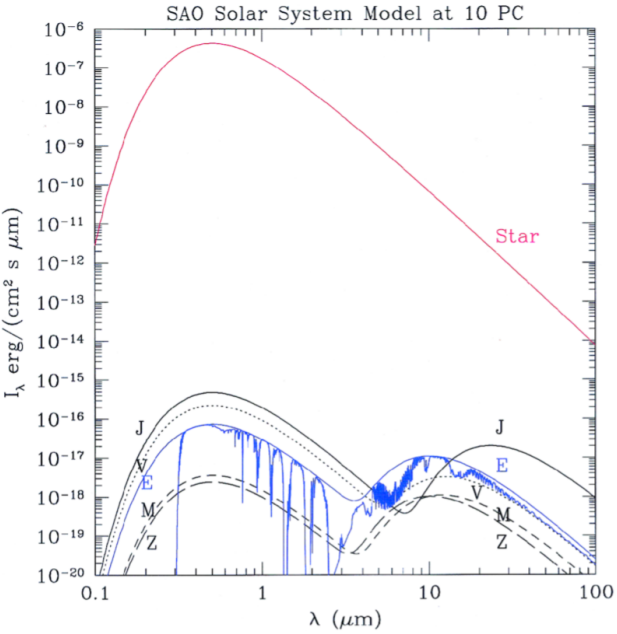

Figure 1.6: A model spectrum of the solar system observed at 10 pc. Simple wavelength-independent albedo reflectance (first peak) and Planck emission (second peak) spectra are shown for various planets and the zodiacal light (Z, 0.1 AU diameter patch centered at 1.0 AU from the central star). For reference, a pure molecular absorption spectrum is superimposed in blue for the Earth. (source: Des Marais et al., 2002)

detect a spectral feature at a certain resolution varies (e.g., Des Marais et al., 2002; Selsis, 2002; Kaltenegger et al., 2007).

While in the reflected light the observable depth of a feature is dependent on the abundance and stellar irradiation at the specific wavelength, in the MIR it is dependent on the abundance and the temperature difference between the emitting/absorbing layer and the continuum (Des Marais et al., 2002; Kaltenegger, 2017). Furthermore, the line shapes of absorption features are affected by three line-broadening processes: natural, Doppler, and pressure broadening [3].

[3] **Natural broadening** results from the Heisenberg uncertainty principle. The energy of excited states between collision and decay spreads out in energy, which translates to a spread in frequency, thus, wavelength. **Doppler broadening** occurs when atoms or molecules in motion cause a spread in observed frequencies due to the Doppler effect. **Pressure broadening** originates from interactions/-collisions between molecules or atoms, which provide or remove energy during radiative transitions

Although wavelength-dependent, in the MIR pressure broadening dominates in tropospheres and Doppler broadening dominates at higher altitudes (above middle stratospheres) (e.g., Catling and Kasting, 2017, Chapter 2.5). As further discussed in subsections 3.3.4, the varying depth of broadened lines can be quantitatively described by Equivalent Width (EW), a fundamental integrated measure of the extent to which a spectral line can reduce radiation. In the case of optically thin gas, doubling the amount or path length will double the absorption. When there is complete absorption in the line center, in the case of optically thick gas, the absorption feature becomes saturated. Increasing the abundance of the absorbing gas then leads to a nonlinear increase in absorption (square root law) in the line's wings only.

Figure 1.7 shows the absorption bands of Earth's atmosphere and their influence on the incoming solar and outgoing thermal radiation. While the middle panel displays the total absorption and scattering of the atmosphere, the lower panel shows individual absorption spectra of major habitability markers and bioindicators and how they contribute at specific wavelengths to the total transmittance of the atmosphere.

In contrast to absorption bands, there are wavelength ranges where an atmosphere can be transparent to specific wavelengths. So called atmospheric windows. These play an important role, especially in the optical and infrared, as they affect the distribution of energy flows and temperatures within a planet's energy balance. Depending on cloud coverage, water vapor, and other trace gases, these windows enable thermal energy to radiate into space, leading to a cooling effect. In modern Earth's atmosphere, one such window exists, for example, between $8-12$ µm. This specific region experiences minimal absorption by molecules, rendering it suitable for observing the warmest and therefore brightest emitting altitudes. For transparent atmospheres, as in the case of Earth and Mars, the surface temperature can be directly measured. This principle can also be applied to exoplanets, if spectral windows probing the surface can be identified. In Earth remote sensing applications, the spectral region between $8-12$ µm is frequently used for measuring surface temperatures. However, this window would close if the atmospheric water abundance or CO_2 pressure were to significantly increase (see spectra of H_2O and CO_2 in lower panel of Figure 1.7). The former scenario could arise due to increased evaporation rates, for instance, in the inner part of

so that emission and absorption occur over a broader wavelength range. See Catling and Kasting (2017) Chapter 2.5 for an in-depth review.

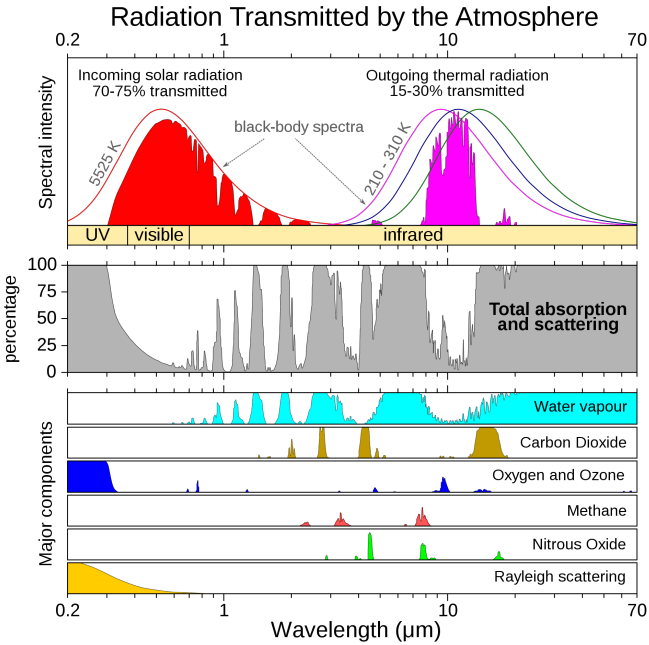

Figure 1.7: Atmospheric absorption. This illustration shows the absorption bands within Earth's atmosphere (middle panel) and their influence on solar and thermal emission radiation (top panel). The lower panel displays individual absorption spectra for major greenhouse gases, along with Rayleigh scattering. Note that the peaks in the blackbody spectra (top panel) were adjusted to have the same height for ease in presentation. (source: Peixoto and Oort, 1992)

the HZ, while the latter might occur at the outer part of the HZ or in the case of a very young Earth (Kasting et al., 1993; Kopparapu et al., 2013). Hence, for terrestrial Earth-like planets that are much warmer than our home planet, the surface temperature cannot be directly inferred from MIR observations. In this case, the observed emission would originate from a region that is located several water scale heights higher in the atmosphere, yielding a lower temperature than the actual surface temperature. Additionally, with the lack of atmospheric windows, a planet could undergo a runaway greenhouse effect, converting conditions from Earth-like to Venus-like (e.g., Ingersoll, 1969; Catling and Kasting, 2017).

Figure 1.8, as shown in Line et al. (2019), shows a simulated, cloud-free Earth thermal emission spectrum at 10 pc (left, black line) as observed with a space-based

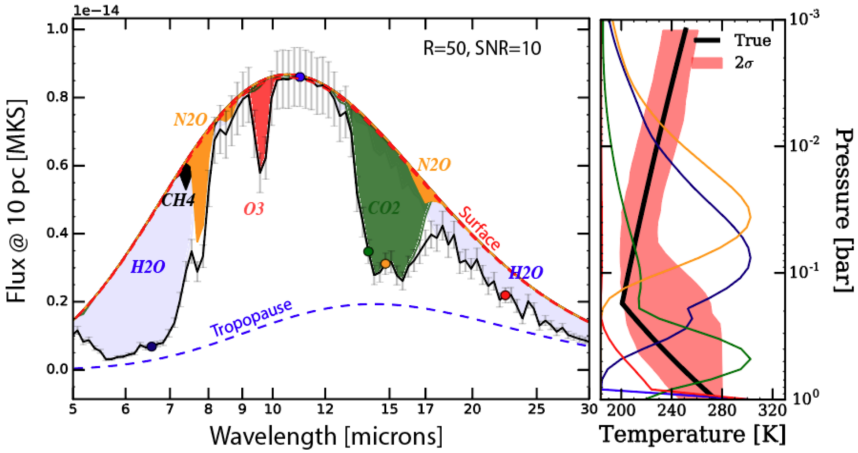

Figure 1.8: Simulated spectra of a cloud-free Earth at 10 pc in the MIR as observed with a space-based interferometer with a $R = 50$, $S/N = 10$ (light grey error bars). Key molecular absorbers are highlighted along with blackbody curves for reference. The right panel shows the $P-T$-profile (black) and the thermal contribution functions at the wavelengths of the colored markers. The red error envelope represents the uncertainty on the constraints for the instrument setup. (source: Line et al., 2019)

interferometer with a $R = 50$, $S/N = 10$ (light grey error bars). In the left panel, the absorption features of key molecular absorbers in the MIR are highlighted. By using a blackbody approximation, the temperature of an emitting layer can be constrained. The red and blue lines represent blackbody curves at Earth's surface and tropopause temperatures, respectively. The accuracy of the constraint is strongly dependend on the quality of the fit along with the sensitivity and resolution of a spectrum. Hence, different wavelengths probe different emitting layers within the atmosphere, which is why MIR observations can be used to infer the atmospheric structure. This is also indicated by the dark blue, blue, green and orange markers, which each probe a different wavelength. While the dark blue and red markers probe atmospheric layers near the tropopause (at ≈10-12 km), the blue marker probes the afore mentioned atmospheric window at 11 µm. Considering the cloud-free nature of the spectrum, it is possible to penetrate deepest into the troposphere and observe the warmest and therefore brightest emitting altitudes. For the wavelength indicated by the blue marker, a direct measurement of the surface temperature is possible. The right panel of the Figure shows the temperature structure ($P-T$-profile) in black, alongside the thermal

contribution functions that indicate the origins of emission corresponding to the wavelengths of the colored markers. A more in-depth illustration of Earth's emission contribution function is shown in Figure 1.9, which shows the emission contribution as a function of altitude and wavelength. Bright regions correspond to a high contribution to the emission spectrum of Earth at the given atmospheric pressure region. The brightest emitting layer is the surface and/or layers near by [4]. Atmospheric windows, through which surface radiation can be directly observed, are clearly visible. Furthermore, while the emission contribution around the O_3 feature centered at 9.6 µm reaches pressure regions ~0.3 bar, emission around the CO_2 features centered at 4.3 µm and 15 µm as well as H_2O centered at 6.2 µm contribute up to 10^{-3} bar. Above that pressure level, MIR emission spectra contain negligible to no signatures from these atmospheric layers. Although clouds affect the thermal emission spectrum, as we will see in subsection 1.4.2, Earth's cloud deck is approximately at an altitude of around ~10-12 km (between 0.2-0.1 bar), which is not high enough to fully mute the signatures.

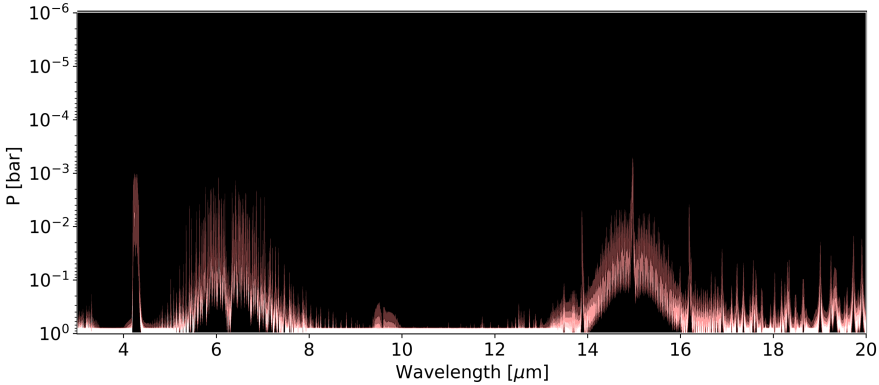

Figure 1.9: Earth's emission contribution function generated with petitRADTRANS. Bright regions correspond to a high contribution to the emission spectrum of Earth at the given atmospheric pressure region. (source: Figure adapted from the original by B.S.Konrad, private communication)

[4]This depends on the underlying surface type and climate conditions. In the case of the Antarctic Plateau, a significant surface-based thermal inversion exists that is not just a major feature of the region's climate, but also a driver of some aspects of its climate, including near-surface winds and atmospheric radiation. The inversion, due to the higher emissivity of the snow-surface compared to the surrounding atmosphere, results in an averaging 10 K inversion between the surface and 30 m above the ground. The strongest temperature gradient is within the lowest 20 cm. Furthermore, the inversion is destroyed during day time but quickly reforms at night (Hudson and Brandt, 2005, and references therein).

1.4.2 The Thermal Emission Spectrum in the Presence of Clouds

Clouds have a significant impact on a planet's energy balance. On Earth, low-altitude clouds reflect incoming solar energy back towards space, reducing the stellar energy available for heating the atmosphere, also known as the albedo effect. High-altitude clouds, on the other hand, reduce radiative losses to space as they trap more heat than low clouds. Due to their wavelength dependent absorption and scattering properties, (multi-layered) clouds affect a planetary emission spectra by generally decreasing the observed flux of a spectrum associated with the dampening of spectral absorption features. The dampening affects not only features that originate below the cloud layers but also features forming above (e.g., Kitzmann et al., 2011).

Figure 1.10 illustrates a modelled Earth MIR spectrum combining effects of spectral absorption features and five different cloud layers (Des Marais et al., 2002). The light green line in the plot represents a cloud-free spectrum. In the absence of clouds, it becomes possible to penetrate deeply into the troposphere and observe emission from the warmest and brightest emitting altitudes, as already discussed in previous subsections. When the planet is covered with high-altitude clouds (pink) near the tropopause, the lowest curve would be observed. The spectrum represents essentially a blackbody spectrum at the tropopause temperature in combination with superimposed emission features from the warmer stratospheric layers situated at higher altitudes. The Figure also illustrates the impact of clouds at varying altitudes on spectral intensity, demonstrating that low clouds (around 1 km) are more transparent to mid-infrared radiation compared to medium (6 km) and high-altitude (12 km) clouds.

Therefore, fitting blackbody curves to the spectral shape of MIR emission spectra for deriving surface temperatures from low-resolution spectra results in progressively underestimated temperatures with increasing amount of high-level clouds. Hence, clouds significantly alter the measured apparent temperature of a planet as well as the detectability of spectral signatures in the MIR (Kitzmann et al., 2011).

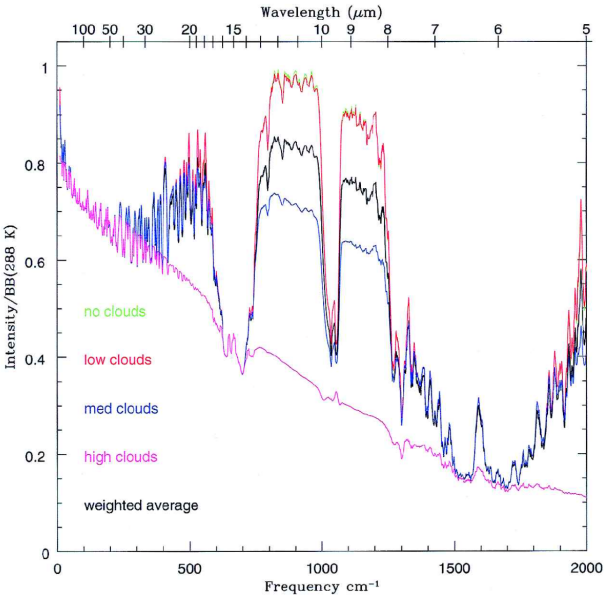

Figure 1.10: Clouds and their effect on the MIR spectrum. In their study, Des Marais et al. (2002) modeled Earth's MIR spectrum by incorporating the influences of spectral absorption features along with five distinct cloud conditions. (source: Des Marais et al., 2002)

1.4.3 The Thermal Emission Spectrum of other Terrestrial Solar System Planets

The atmospheric composition of terrestrial planets is controlled by diverse factors such as geochemical exchanges, tectonics, atmospheric escape, photochemistry, and if present, biology (e.g., Catling and Kasting, 2017). The given stage of its evolution also plays a crucial role, as for example Earth's spectral appearance has changed significantly in the past 4.5 Gyr (e.g., Kasting and Catling, 2003; Kaltenegger et al., 2007; Meadows, 2008; Arney et al., 2016; Reinhard et al., 2017; Rugheimer and Kaltenegger, 2018). Thus, the combination of these factors and time gives rise to a wide range of atmospheric compositions, leading to substantial diversity within a broad parameter space. Examining our four terrestrial planets in the solar system, three have a significant atmosphere. Earth's atmosphere is primarily composed of nitrogen (78%) and oxygen (21%), whereas the atmospheres of Venus and Mars are dominated by carbon dioxide (97% and 95%, respectively).

Also, Earth's patchy cloud coverage is unique among the three terrestrial planets. While Venus is completely covered in sulfuric acid clouds, Mars has negligible cloud coverage.

Figure 1.11 illustrates a comparison between the reflected (a) and thermal emission (b) spectra of Earth, Venus and Mars as observed at a resolution of $R = 100$ (Selsis et al., 2008). Reflection spectra combine both solar and planetary spectral lines. Due to the small size and low albedo of Mars, the reflectance spectrum was multiplied by 10 to enhance visibility on the linear scale. However, no significant features are visible. On the contrary, Earth's reflectance spectrum displays distinct features attributed to O_2 and H_2O, along with a pronounced ozone Chappuis band centered at 0.6 µm. The sharp spectral feature at 0.76 µm indicates a significant presence of oxygen. In the shorter wavelengths, a notable increase in albedo towards the blue is indicative of Rayleigh scattering, an effect arising from the gaseous components in the atmosphere (Selsis et al., 2008). Venus, on the other hand, exhibits the highest spectral intensity in its reflected light spectrum due to its high Bond albedo of 0.77. Additionally, signatures of CO_2 become observable at wavelengths exceeding 1 µm, while the signatures of molecular oxygen at 0.76 µm and water remain absent.

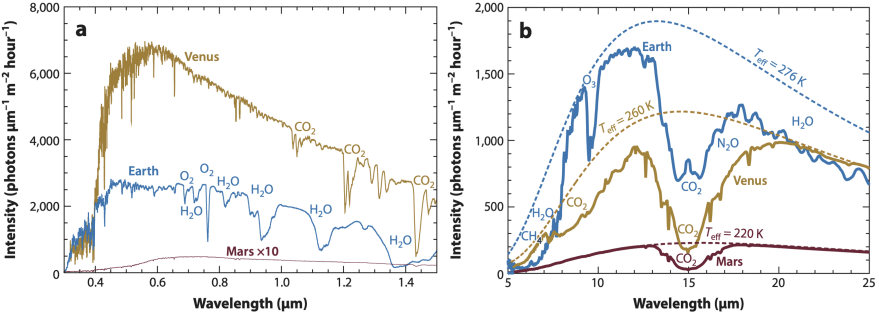

Figure 1.11: Spectra of Earth, Venus and Mars as observed at 10 pc and $R = 100$. a) shows the reflection spectra in the UV–VIS–NIR range. b) shows the MIR thermal emission, along blackbody emission of a planet of the same radius at the maximum brightness temperature of the spectrum. The presented spectra are model results, validated after comparisons with observations. (source: Selsis et al., 2008; Kaltenegger, 2017)

The MIR spectrum of Earth exhibits deep and strong features of O_3 centered at 9.6 µm and CO_2 centered at 15 µm. Furthermore, the spectrum is winged by a water vapour absorption feature (centered at 6.2 µm) and continua (>18 µm).

The width of the bands for the first two molecules and water vapour allow for a detection at resolutions as low as 10 (e.g., Selsis et al., 2008; Konrad et al., 2022). The presence of CH_4 can be detected through its feature centered at 7.7 µm with lower detection limits of $R = 50$, $S/N = 10$. Although present in Earth's atmosphere, CO, N_2, and O_2 are unconstrained in the MIR (e.g., Catling et al., 2018; Konrad et al., 2022). Examining the MIR spectra of Venus and Mars, the only strong features observable at low resolutions are due to CO_2. While CO_2-CO_2 collision-induced absorption shapes the whole spectrum of Venus, only the 15 µm CO_2 band is detectable on Mars (Selsis et al., 2008). Additionally, despite having a surface temperature of ~735 K, the blackbody curve fit reveals an effective temperature estimate of ~260 K for Venus. Hence, Venus appears cooler than Earth (T_{eff}= 276 K). This arises from the thick Venusian cloud cover, which allows only for atmospheric layers above 1 bar to be observed and not from emitting layers near the surface at ~93 bars. Moreover, Earth's MIR spectrum exhibits a distinctive 'emission' peak at the center of the O_3 and CO_2 absorption features. This unique feature indicates a temperature inversion in Earth's atmosphere, resulting from a temperature increase between the tropopause and stratosphere due to the absorption of sunlight by the ozone layer.

Overall, the comparative study of our solar system terrestrial planets' spectra showed that Earth stands out with a unique blend of atmospheric gases, marked by the presence of O_2, O_3, CH_4, and H_2O as evidenced by distinct spectral features in its reflectance and MIR emission spectra. The presence of O_2 and O_3 at high concentrations is the result of oxygenic photosynthesis driven by a thriving biomass. In co-existence with a reducing gas like CH_4, the pair is a particularly strong indication of life (e.g., Lovelock, 1965; Krissansen-Totton et al., 2016, 2018; Schwieterman et al., 2018). Without life constantly replenishing O_2 at high quantities, these species would react in the non-equilibrium conditions of the atmosphere, making the simultaneous detection of both (O_2 and CH_4) impossible in low-resolution spectra (e.g., Selsis, 2002). In addition, CH_4 in combination with CO_2 alongside the absence or low abundance of CO is a particularly compelling biosignature since the combination of the two represents carbon in its most reduced and most oxidized forms, which is hard to explain without life (e.g., Krissansen-Totton et al., 2018). Thus, the detection of these spectral features on an habitable exoplanet would be a significant indicator of the presence of life (e.g., Selsis, 2002; Segura, A. et al., 2007).

1.5 Biosignatures

On Earth, the impact of life on the geochemical environment and the composition of the atmosphere throughout billions of years of coevolution led to the suggestion that alien biospheres should be detectable remotely via spectroscopy (Lovelock, 1965; Lovelock et al., 1975; Olson et al., 2018a). This is based on the premise that life will modify the atmosphere and surface, and that the modification will be detectable on a global scale (Des Marais et al., 2002). This holds true for Earth since changes induced by life in its surface and atmospheric properties can be observed from space, many in disk-averaged observations (e.g., Sagan et al., 1993; Turnbull et al., 2006; Hearty et al., 2009).

Hence, the term *biosignature* is coined as an object, substance, and/or pattern whose origin specifically requires a biological agent (Marais and Walter, 1999; Des Marais et al., 2008). In the context of astronomical observations, a biosignature is commonly understood to be the presence of a gas or other feature that is indicative of a biological agent (Schwieterman et al., 2018). As proposed by Meadows (2006, 2008), these can be grouped into three broad categories: *gaseous*, *surface*, and *temporal* biosignatures.

The former are direct or indirect products of metabolism and constituents in the planetary atmosphere that are significantly out of chemical equilibrium. Good examples are O_2, CH_4, and N_2O in abundant quantities in our atmosphere. A much stronger potential biosignature, however, is the coexistence of CH_4 and/or N_2O in the presence of O_2, which indicates a chemical disequilibrium (e.g., Margulis and Lovelock, 1974; Meadows, 2006; Krissansen-Totton et al., 2016).

Surface biosignatures are spectral characteristics in the surface reflectance resulting from radiation being reflected or scattered by organisms, examples include chlorophyll pigments or the *red edge* reflectivity of leaves [5] (Gates et al., 1965; Seager et al., 2005).

Temporal biosignatures refer to modulations in measurable quantities in either atmospheric or surface properties, primarily driven by seasonal variations in

[5] The vegetation red edge (VRE) describes the high reflection of land vegetation in the near-infrared. On Earth, this sudden increase in reflectivity can be observed near 0.7 µm, which is the result of adaptation of the phototrophs to their spectral environment. Hence, the spectral signature of the red edge will shift for exoplanets, due to different planetary atmospheres and host star spectral types (e.g., Wolstencroft and Raven, 2002; Seager et al., 2005; Lehmer et al., 2021; Barrientos et al., 2023).

biomass (further discussed in 3.3.4). On Earth, seasonal patterns in insolation (due to Earth's axial tilt) shift the balance between photosynthesis and aerobic respiration, resulting in oscillations of atmospheric CO_2 and O_2 (Keeling et al., 1976). The search for seasonality as a biosignature would avoid many assumptions about specific metabolisms and provide an opportunity to directly quantify biological fluxes (Olson et al., 2018b).

However, a prospective exoplanet biosignature will inherently carry the label of a "potential" biosignature, as it could have alternative explanations. The spectroscopic signals that hint at signs of life are measurements with associated uncertainties and the potential for various interpretations. So called *false positives* occur when abiotic (planetary) processes mimic a biosignature. For example, the biogenic source of CH_4 is through methanogenesis, often mediated by degradation of organic matter. Yet, geothermal or primordial methane are abiotic false positives. The biogenic source of O_2 is photosynthesis associated with the splitting of H_2O. Yet, O_2 is produced during the loss of an ocean through evaporation and photodissociation of H_2O (see Catling et al., 2018, for an extensive list of biosignatures and their biogenic or abiogenic sources). Even seasonal changes in planetary reflectivity, composition induced by dust storms, or photochemistry are examples of abiotic false positives (Meadows, 2006). Hence, confirming potential biosignatures for an exoplanet requires evaluating them within the context of the planetary environment. As concluded by Krissansen-Totton et al. (2022), the discovery of life on exoplanets, will probably not be a moment in time but it will involve years or even decades of debate, with multiple observations and instruments to resolve ambiguities. Further, they state that no single molecule, surface or spectral feature is likely to provide definitive evidence, and multiple lines of evidence may be required to rule out false positives.

1.6 Exoplanets and Their Direct Detection in the Mid-Infrared

In order to characterize terrestrial HZ exoplanets and search for traces of life, the direct detection of their signal is required. This is possible with a detection method called (High-Contrast) *Direct Imaging* which involves the direct detection of photons from an exoplanet. However, the challenge lies in disentangling the faint exoplanet emission from the much brighter stellar radiation. The efficiency

of this separation process ultimately sets the detection limits of an instrument. Limiting factors are the planet-to-star flux ratio (contrast), and the angular separation between the planet and star (angular resolution). Typically, the contrast worsens at smaller angular separations. These challenges shape the current observational bias in the exoplanet population that is observable with the direct imaging method, favoring young and massive planets at large separations from their host stars. Young planets are inherently hot due to their formation process, and massive planets are brighter due to their large surface areas.

Terrestrial HZ exoplanets are detectable with current and approved future observatories. However, these instruments will not have the capability to characterize and search for life in a statistically meaningful sample. For instance, in 2019, the NEAR (New Earths in the Alpha Centauri Region) experiment was conducted at the Very Large Telescope (VLT) to observe the habitable zones of Alpha Centauri A and B (nearest neighbouring system at 1.5 pc) in the search for a super Earth companion. Demonstrating the potential for ground-based MIR imaging, the NEAR experiment observed the system for a total of 100 h. The data revealed a faint signal that could be either an 5-7 Earth diameter exoplanet, part of a zodiacal disk, or simply an instrumental artifact of unknown origin (Wagner et al., 2021). For current advancements and limitations in the field of ground-based direct imaging, see e.g., Vigan et al. (2017); Nielsen et al. (2019); Langlois et al. (2021); Tschudi and Schmid (2021); Tschudi et al. (in prep.). Moving from 8-10 m class telescopes at the VLT to the 30-40 m Extremely Large Telescopes (ELT) (operational late 2020s) will significantly reduce the required telescope time and reach the contrast limits necessary for detecting Earth-sized planets. Yet, even in the Era of the ELTs only a handful of stars in the immediate vicinity of the Sun can be probed for true Earth analogs (Lin et al., 2019). For more distant objects, the required time-on-target becomes prohibitively long. Conducting MIR direct imaging from ground-based observatories poses an extremely challenging task due to the presence of Earth's atmosphere (adaptive optics required for removing atmospheric disturbance) and the high thermal background of the atmosphere and the telescope itself. Particularly at wavelengths around ~10 µm, where the thermal radiation from Earth-sized planets peaks. Hence, space-based telescopes are needed for investigating the atmospheric diversity of dozens of terrestrial exoplanets via the thermal emission (Line et al., 2019).

The exoplanet community is working toward more capable observatories. LUVOIR (The LUVOIR Team, 2019) and HabEx (Gaudi et al., 2020) were designed to

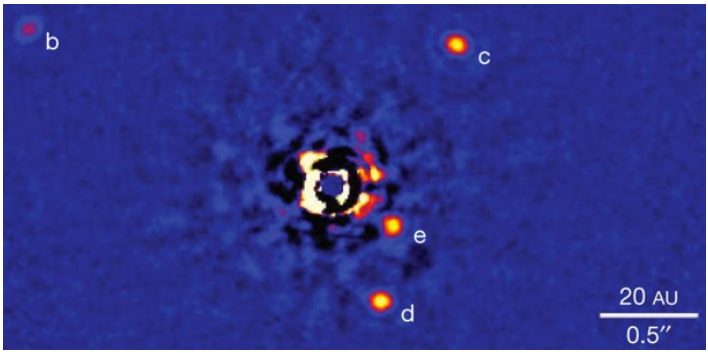

Figure 1.12: High-contrast observations with the Keck and Gemini telescopes performed by Marois et al. (2008, 2010) have revealed four planets orbiting the star HR 8799, with projected separations of 15 (e), 24 (d), 38 (c), and 68 (b) astronomical units (AU). Multi-epoch data show counter clockwise orbital motion for all four imaged planets. Wang et al. (2018) constrained their masses to be $5.8\pm0.5 M_{Jup}$ for planet b and $7.2^{+0.6}_{-0.7} M_{Jup}$ for planets c, d, and e. (source: Marois et al., 2010)

directly measure the stellar light reflected by terrestrial exoplanets at ultraviolet, optical, and near-infrared (UV/O/NIR) wavelengths. Following the evaluation of both concepts in the Astro 2020 Decadal Survey in the United States (National Academies of Sciences, Engineering, and Medicine, 2021), the space-based UV/O/NIR Habitable Worlds Observatory (HWO) was recommended. Regarding the MIR wavelength range, the Large Interferometer For Exoplanets (LIFE; Quanz et al., 2018), is currently the only complementary approach of a large, space-based MIR direct imaging concept mission that aims to directly measure the MIR spectrum of terrestrial HZ exoplanets in a statistically meaningful sample (e.g., Kammerer and Quanz, 2018b; Quanz et al., 2021a, 2022). In space the thermal background noise is less of a challenge and in combination with nulling interferometry, the required spatial resolution, contrast and sensitivity is achieved and allow for the detection of rocky planets orbiting stars within 20-25 pc (e.g., Kammerer and Quanz, 2018b).

The analyses in this thesis are conducted with the future prospect of directly imaged terrestrial HZ exoplanets in mind. In Chapter 4, we will assess the potential for detecting bioindicators on Earth-like exoplanets using LIFE and investigate the impacts of variables such as viewing geometry, seasonality, and patchy clouds on the characterization.

1.7 Thesis Outline

As highlighted earlier, observations of terrestrial HZ exoplanets will typically involve spatially and temporally averaged, low-resolution spectra. To prepare for future attempts to characterize these distant habitable worlds, studying Earth and its characteristics from afar offers a unique opportunity to explore a truly habitable and inhabited world by means of remote characterization. In this thesis, I follow a data driven approach to investigate Earth's thermal emission spectrum in the context of exoplanet research. By leveraging the wealth of Earth observation data, my aim is to enhance our understanding of the impact of data-limited, temporally and spatially unresolved observations on the characterization of potential habitable worlds. In the next paragraphs, the content of each chapter will be briefly summarized.

In **Chapter 2**, I investigate flux levels and variations of five single-surface-type target locations on Earth with different climate zones and surface thermal properties. Aiming at investigating whether differences between these target locations are observable in spectrally-limited observations (16 channels, $3.66 - 14.40$ μm), I constructed an Earth observation dataset over a time baseline of 15 years including separate datasets for daytime and nighttime emission per location. Using the dataset, I derive their spectral energy distributions (SEDs) and use Fourier analysis to look for evidence of planetary obliquity in the measured spectral radiance variations. Despite the coarse spectral resolution, the inferred SEDs show differences in the strength of flux levels and absorption features with a strong viewing geometry dependency. Regions close to the equator and toward the North Pole show more dominant O_3 and CO_2 absorption features than the South Pole. These typically strong absorption bands are significantly less pronounced and partially absent in polar regions. This implies that estimating correct abundance levels for these molecules might not be representative of the bulk abundances in these viewing geometries. Additionally, the time-resolved thermal emission spectrum provided insights into seasons/planetary obliquity, but its significance is depended on viewing geometry, spectral band, and number of on-target observations.

In **Chapter 3**, I expand the analyses from spatially resolved locations to disk-integrated Earth views. In the first part, I present an exclusive data set of 2690 disk-integrated MIR thermal emission spectra ($3.75 - 15.4$ μm, $R = 1200$) which I derived from AIRS Level-1C observations for four full-disk viewing geometries.

Using this dataset, I study how Earth's disk-integrated MIR spectral appearance changes as a function of viewing geometry, seasons, and phase angles. In the second part, I isolate four spectral features of bioindicators and habitability markers (CO_2, O_3, CH_4, N_2O) found imprinted in the MIR spectrum and investigate their seasonality and detectability in the context of atmospheric seasonality being a biosignature. My results show that a representative, disk-integrated thermal emission spectrum of Earth does not exist. Instead, both the thermal emission spectrum and the strength of biosignature absorption features show seasonal variability and depend strongly on viewing geometry. In addition, disentangling these small variations in atmospheric seasonality from the noise in future exoplanet observations will be challenging.

In **Chapter 4**, we treat Earth as a directly imaged exoplanet to evaluate if and how well we could characterize an Earth-twin in the MIR using LIFE. Through atmospheric retrievals conducted on MIR spectra sourced from the dataset presented in Chapter 3 and the comparison of the results to Earth remote sensing ground truths, we investigate the accuracy and robustness of the retrieved estimates. The validation of atmospheric retrieval routines against solar system observations is an inevitable step toward characterizing the unknown environments of terrestrial exoplanets in the future. This study is the first where retrievals are systematically run on disk- and time-averaged MIR Earth observation spectra for different viewing geometries and seasons. Despite some biases due to parameter degeneracies, the collective outcome of our analyses across the considered cases based on preliminary minimal LIFE requirements ($R = 50$, $S/N = 10$) consistently points towards the compelling conclusion that the observed planet exhibits distinct absorption features of relevant gases, including potential biosignatures, a temperate climate, and surface conditions that allow for liquid surface water. Multiple lines of evidence strongly indicate the presence of a habitable planet. However, Earth-like atmospheric seasonality in biosignature gases proved challenging to detect and our work emphasizes the need for caution when interpreting retrieval results, suggesting that reduced posteriors or posterior ratios may yield less biased estimates. Additionally, we highlight that the commonly used assumptions of vertically constant abundance profiles and a cloud-free atmosphere could lead to significant retrieval biases.

The final chapter of this thesis, **Chapter 5**, serves as both a conclusion and an outlook. I recap key findings and highlight potential future directions and areas of research that can build upon the insights gained in this work.

Contribution

Based on my review of the cited literature, I wrote the introductory Chapter 1.

2 Spatially-Resolved Earth: Investigating its Thermal Emission and Variation

Adapted from:
"Earth as an Exoplanet. I. Time Variable Thermal Emission Using Spatially Resolved Moderate Imaging Spectroradiometer Data"

J.- N. Mettler, S. P. Quanz, R. Helled

The Astrophysical Journal, 2020, 160,246

Abstract

Among the more than 5000 exoplanets known today, some terrestrial planets have been detected in the so-called habitable zone of their host stars and their number is expected to increase in the near future, energizing a drive to understand and interpret the eagerly awaited wealth of data to identify signs of life beyond our Solar System. So far, Earth remains the best and only example of a habitable (and inhabited) world. Although, it seems extremely unlikely that any other exoplanets will be true Earth-twins, it is important to explore and understand the full range of spectral signatures and variability of Earth in order to inform the design of future instruments and missions, and understand their diagnostic power as well as potential limitations. In this work we use Earth observation data collected by

the MODIS instrument aboard the Aqua satellite. The complete dataset comprises 15 years of thermal emission observations in the 3.66–14.40 μm range for five different locations on Earth (Amazon Rainforest, Antarctica, Arctic, Indian Ocean and the Sahara Desert). We then determine flux levels and variations as a function of wavelength and surface type (i.e. climate zone and surface thermal properties) and investigate whether periodic signals indicating Earth's tilted rotation axis can be detected. Our findings suggest that (1) viewing geometry plays an important role when thermal emission data is analyzed as Earth's spectrum varies by a factor of three and more depending on the dominant surface type underneath; (2) typically strong absorption bands from CO_2 (15 μm) and O_3 (9.65 μm) are significantly less pronounced and partially absent in data from the polar regions implying that estimating correct abundance levels for these molecules might be challenging in these cases; (3) the time-resolved thermal emission spectrum encodes information about seasons/planetary obliquity, but the significance depends on the viewing geometry and spectral band considered.

2.1 Introduction

Since the first detection of an exoplanet around a Sun-like star in 1995 (Mayor and Queloz, 1995), the research field of exoplanets has grown rapidly. As of today, 25 years after the first discovery, there are over 5000 confirmed exoplanets in more than 4000 planetary systems (Alei et al., 2020). Among these discoveries, some terrestrial planets have already been found orbiting in the so-called habitable zone (HZ) of their host stars such as planets e, f, and g in the TRAPPIST-1 system, LHS 1140 b, Proxima Centauri b, Kepler-442b or TOI-700d (Gillon et al., 2017; Dittmann et al., 2017; Montet et al., 2015; Anglada-Escudé et al., 2016; Gilbert et al., 2020). In the future, their number is expected to increase further, primarily thanks to dedicated missions such as TESS (Ricker et al., 2015) and PLATO (Rauer et al., 2014) and ongoing or upcoming radial velocity surveys such as CARMENES (Quirrenbach et al., 2014) or EXPRES (Jurgenson et al., 2016) and HARPS3 (Young et al., 2018).

The long-run goal is the characterization of temperate terrestrial exoplanets' atmospheres in order to assess their habitability and search for indications of biological activity. With the aim of detecting Earth-analogs around other stars, a particularly interesting class of exoplanets will be terrestrial planets with thin N_2-H_2O-CO_2 atmospheres that orbit within the habitable zone of their host stars.

Characterizing these planets and searching for traces of life requires the direct detection of their signal. The first space telescope capable of detecting potential atmospheres of terrestrial exoplanets is expected to be the James Webb Space Telescope (JWST) (e.g., Morley et al., 2017; Krissansen-Totton et al., 2018; Tremblay et al., 2020), which is scheduled for launch in 2021. From the ground, the 30-40m Extremely Large Telescopes may provide us with first images and high-resolution spectroscopy data of a few terrestrial exoplanets, once they will be online in the mid to late 2020s (e.g., Quanz et al., 2015; Snellen et al., 2015). However, none of the currently planned missions or projects is capable of detecting and characterizing the atmospheres of a statistically meaningful sample of temperate, rocky exoplanets, and the exoplanet community has to wait for future missions like HabEx (Gaudi et al., 2020), LUVOIR (The LUVOIR Team, 2019) or LIFE (Quanz et al., 2018).

For the time being, Earth remains the best – and only – example of a truly habitable and inhabited world, offering a unique opportunity to study the remote characterization of potential habitability. Despite the vast diversity of exoplanets (e.g., Batalha, 2014; Burke et al., 2015) and the significant changes in the spectral appearance of Earth over the past 4.5 Gyr (eg., Arney et al., 2016; Kasting and Catling, 2003; Kaltenegger et al., 2007; Meadows, 2008; Reinhard et al., 2017; Rugheimer and Kaltenegger, 2018), it seems unlikely that any other exoplanet will be a true Earth-twin. Nevertheless, it is still useful to explore and understand the full range of spectral signatures and variability of Earth (e.g., due to the presence of oceans, clouds, surface inhomogeneities or polar caps) in order to fine-tune the design of future instruments and missions and understand their diagnostic power as well as potential limitations.

A key challenge arises from the fact that we will observe exoplanets from distances of – typically – at least several parsecs so that even with the most powerful telescopes conceived today they will remain spatially unresolved point sources. So, ideally, in order to study Earth as an exoplanet 'disk-integrated' data should be used. However, such data taken from a remote vantage point and showing the entire disk are limited as they are only obtained from a handful of spacecraft flybys such as *Galileo*, *MGS/TES*, *EPOXI*, *LCROSS* and *DSCOVR* (e.g., Sagan et al., 1993; Christensen and Pearl, 1997; Livengood et al., 2011; Robinson et al., 2014; Yang et al., 2018), spatially resolved satellite observations stitched together to a disk-integrated view of Earth (e.g., Hearty et al., 2009) or from Earth-shine observations, where the reflected light from Earth is re-reflected from the unlit part

of the Moon (e.g., Turnbull et al., 2006; Pallé et al., 2009). Nevertheless, the regular monitoring of Earth, in particular from Earth-orbiting satellites and to some extent also from other spacecraft, yielded a rich collection of Earth observation data, which has been used to investigate Earth's appearance in both reflected light and thermal emission (for a recent review see, e.g., Robinson and Reinhard, 2018). Such data offer an extensive temporal, spatial, and spectral coverage which can be tailored to represent exoplanet observation data or at least be interpreted in such a context.

In this work, we use data collected by the Moderate Imaging Spectroradiometer (MODIS) aboard the Aqua satellite which has been orbiting Earth for the last 18 years. We focus on Earth's thermal emission of specific and representative surface types at mid-infrared (MIR) wavelength. By constructing datasets with a long time baseline spanning more than a decade and hence several orbital periods, we can investigate flux levels and variations as a function of wavelength range and surface type (i.e. climate zone and surface thermal properties) and look for periodic signals. Rotational and seasonal variations of Earth's spectrum and their influence on the detectability of spectral signatures of habitability and biosignatures have been investigated before (e.g., Ford et al., 2001; Cowan et al., 2009; Fujii et al., 2011; Gómez-Leal et al., 2012; Hearty et al., 2009; Livengood et al., 2011; Robinson, 2011; Robinson et al., 2014; Jiang et al., 2018), both based on observational data and simulations. Some studies also investigated Earth's thermal emission as an exoplanet using global climate models to simulate slowly rotating, ocean covered and snowball Earths or to estimate the eccentricity, obliquity and diurnal forcing of Earth-analogs (e.g., Gómez-Leal et al., 2016; Cowan et al., 2012).

While most studies so far focused on the reflected light spectrum, we here concentrate on the thermal emission of Earth and leverage long time baseline of the available data. Observing in the MIR enables us to characterize the thermal structure of exoplanetary atmospheres and provides additional information on the molecular abundances (cf. Hearty et al., 2009). It also offers advantages over observing the reflected light of a planet with regard to seasonality. In this case, Mid-infrared will not be as negatively impacted by the lack of illumination of the winter hemisphere over the course of the orbit (e.g., see Figure 5 in Olson et al., 2018b). Ideally, for a comprehensive understanding of exoplanetary environments, combining the information from thermal emission and reflected light spectroscopy is needed.

We present spectral energy distributions (SEDs) and power spectral densities (PSDs) that were derived from Earth observation data for five specific locations on Earth. The datasets are constructed from 16 discrete channels located in the MIR (3.66–14.40 μm) wavelength regime. To our knowledge, this is the longest continuously recorded time baseline from one satellite constellation using the same instrument for investigating Earth's thermal emission in the context of exoplanet science.

2.2 Methods

2.2.1 Locations and Surface Types

In order to investigate the thermal emission and time variability of Earth, we have focused on specific surface types with different thermal properties and from different climate zones that represent our planet's appearance from afar. Although Earth shows a wide variety of surface characteristics, on large scales it is dominated by oceans, deserts, ice and vegetation. In addition, clouds are also typically covering ~ 67% (King et al., 2013) of the Earth. A comprehensive review about clouds and their effects on Earth's climate can be found in (Kondratyev, 1999) and references therein. In this paper we examine the following five locations: (1) Amazon Rainforest, (2) Antarctica, (3) Arctic, (4) Indian Ocean and (5) Sahara Desert as shown in Figure 2.1. For every location we also investigate the difference in thermal emission between day and night.

The patch for the Sahara Desert covers the area between 10-30° N latitude and 0-30° E longitude. The time when the satellite was above this region varied over the 15 year period between 12:05 - 12:45 UTC and 01:00 - 02:00 UTC for the day and night measurements, respectively. The patches for the Amazon Rainforest were taken between 17:25 UTC - 18:05 UTC and 05:10 UTC - 05:40 UTC. For the Indian Ocean, we analyzed a patch lying below the equator between -10 and -25° S latitude and 65-90° E longitude. Here the time varied between 08:15 - 08:40 UTC for the day and 20:00 - 20:20 UTC for the night measurement. For the Arctic and Antarctica, the satellite was above the target region between 06:00 - 10:35 UTC and 16:30 - 18:55 UTC, respectively. Due to Earth's axial tilt the two polar datasets naturally include day and night measurements.

To ensure single surface type measurements consistent over the full time baseline,

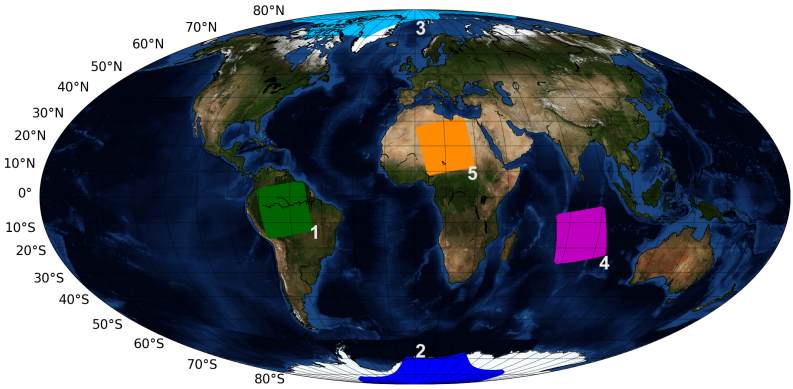

Figure 2.1: World map highlighting the investigated target locations: (1) Amazon Rainforest, (2) Antarctica, (3) Arctic, (4) Indian Ocean and (5) Sahara Desert. At the equator, MODIS achieves a maximum swath size of 2330km by 2030km.

some patches had to be cut as described in section 2.2.2. Since we are interested in how Earth's appearance varies over time, we do not specifically select or deselect any data frames that are dominated by clouds. Instead, the cloud-induced variability in Earth's thermal emission is implicitly included in the analyses.

In order to interpret our analyses in the context of exoplanet science we assume (1) that for an exoplanet the surface types investigated here are dominating the hemisphere that is observed, and (2), related to this, that the integration time in order to collect the exoplanet data is short compared to the rotation period of the planet so that "smearing effects", i.e., the mixing of various surface types, are negligible.

2.2.2 Data Retrieval and Processing

For this study, we used data collected by MODIS, a cross-track, multi-disciplinary scanning radiometer with in total 36 spectral channels measuring visible and infrared bands in the wavelength range of 0.4–14.4 μm. A more detailed introduction to MODIS is provided in Section 1.3. We investigated the calibrated at-aperture radiance for 16 thermal channels (see Table 2.1) with a spatial resolution of 1000 m between January 2003 and December 2017. The data originate from a Level-1B product called *MODIS / Aqua Calibrated Radiances 5-Min L1B Swath*

1km (MYD021KM) collection number 6.1 (LAADS DAAC), which was accessed over NASA's *EARTHDATA Engine*. This product level results from applying sensor calibration to the raw radiance counts (Level-1A) in order to produce calibrated, top-of-atmosphere (TOA) radiances. Due to *Aqua*'s repeating cycle of 16 days, our target locations were monitored twice per month, resulting in 360 data points per location after 15 years of observation.

After downloading the corresponding data from the servers, the files were read and the band specific scaled integers (SI_B) were converted into spectral radiances (L_B) with physical units of W m^{-2}µm^{-1} sr^{-1} according to equation 2.1 (MODIS User Guide, 2017)

$$L_B = \Gamma_B(SI_B - \Theta_B), \tag{2.1}$$

Table 2.1: Summary of all thermal channels of MODIS. Channel 26 covers the 1.360–1.390 µm range and does not probe the Earth's thermal emission. Therefore, it is not listed below. Taken from https://modis.gsfc.nasa.gov/about/design.php.

Primary Use	Channel	Bandwidth (μm)
Surface/Cloud Temperature	20	3.660–3.840
	21	3.929–3.989
	22	3.929–3.989
	23	4.020–4.080
Atmospheric Temperature	24	4.433–4.498
	25	4.482–4.549
Cirrus Clouds/Water Vapor	27	6.535–6.895
	28	7.175–7.475
Cloud Properties	29	8.400–8.700
Ozone	30	9.580–9.880
Surface/Cloud Temperature	31	10.780–11.280
	32	11.770–12.270
Cloud Top Altitude	33	13.185–13.485
	34	13.485–13.785
	35	13.785–14.085
	36	14.085–14.385

where Γ_B and Θ_B refer to radiance scales and radiance offsets for a specific band B, respectively, which are computed inside Level-1B products and are written as attributes to the scientific datasets (SDS). In the MYD021KM Level-1B product, the radiance measured in each channel were generated in 32-bit floating-point format and scaled to a range of [0, 32767]. Any value larger than 32767 represents invalid or unusable data and was removed from the datasets.

The first iteration through this process revealed that in some years the patches of the selected locations were slightly drifting. These drifts are caused by orbital maneuvers which are well known (e.g., Lin et al., 2019). In order to solve this issue we had to custom clip the concerning patches to show the exact same location for each passage. While only a few frames of the Sahara Desert had to be slightly cut, an effort was made to cut the two polar regions patches in a way that the geographical pole lies in the center. As a result, roughly 50% of the Arctic patch had to be clipped to just show the polar cap, thus, instead of having the usual 1354 by 2030 pixels the scene is composed of 600 by 2030 pixels. None of the Amazon Rainforest or Indian Ocean patches had to be cut as they all showed scenes composed of vegetation and water (and clouds), respectively.

2.3 Results

2.3.1 Spectral Energy Distributions (SEDs)

A key diagnostic for investigating the (atmospheric) properties of an exoplanet is its spectral energy distribution (SED). In Figure 2.2 a - d we show the SEDs of all target locations including their day and night comparisons (note the different scales on the y-axes). In Table 2.2 we provide the mean values for all SEDs in tabulated form. The horizontal lines indicate the average radiance measured in every channel over the 15-year observation period. The length of the lines in x-direction corresponds to the channel bandwidth and the error bars in y-direction to the measured standard deviation of the radiance. The latter encodes a mix of intrinsic variability for a given location at a certain time of the year and variations due to seasonal effects (see Figure 2.4). In order to derive the day and night SEDs for the polar regions, their data was split into summer and winter data with each season lasting for 6 months.

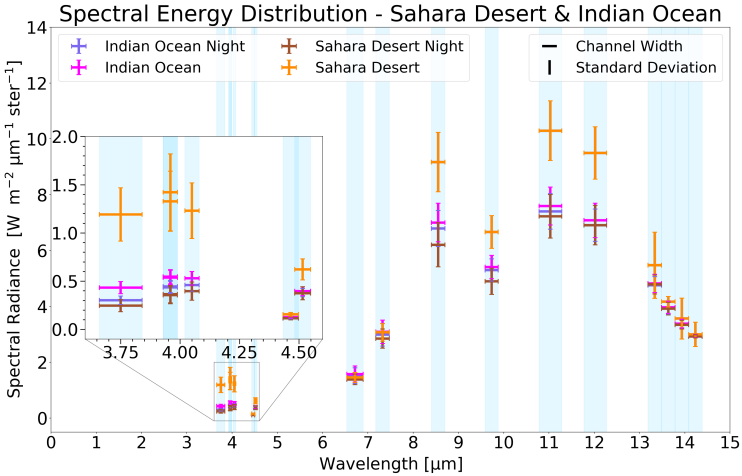

(a) Spectral energy distributions of the Sahara Desert and the Indian Ocean. Their night measurements are shown in sienna and dark green, respectively. The horizontal lines in x-direction correspond to the average radiance measured in every channel over the 15-year observation period and the error bars in y-direction to the standard deviation. The blue shadings indicate the bandwidth of each channel.

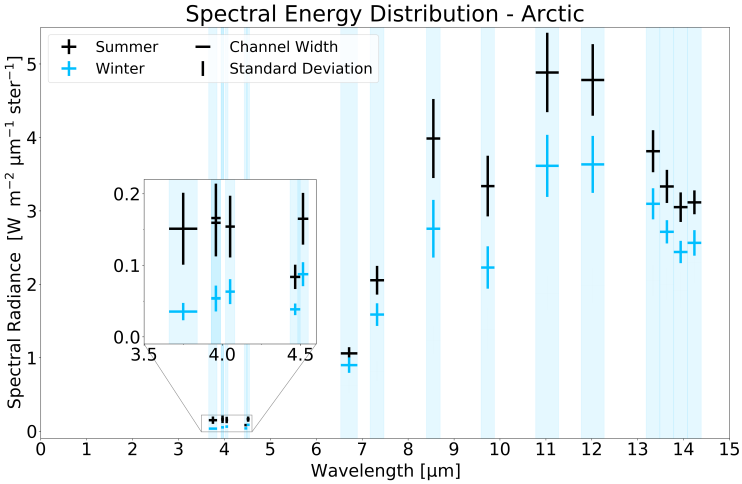

(b) Spectral energy distribution of the Arctic. The summer data is shown in black and includes data from April - September and winter (sky blue) from October - March. The increase towards the end of the spectrum in channel 36 (14.085 - 14.385 µm) is a characteristic feature for this type of location and indicates the emission of CO_2 centered at 15 µm.

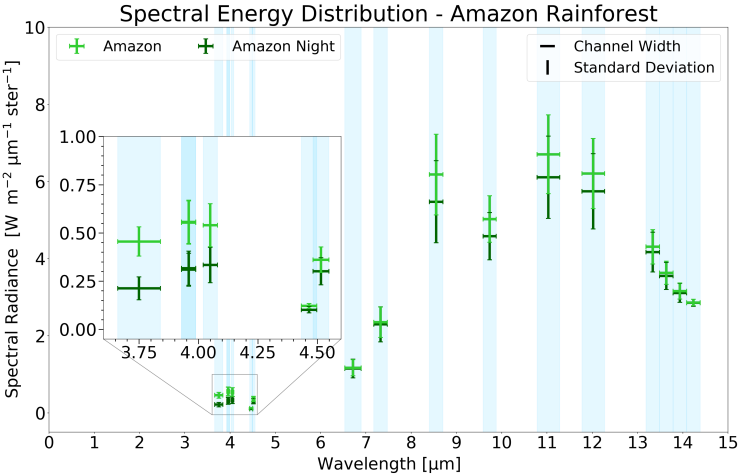

(c) Spectral energy distribution of the Amazon Rainforest displaying the major absorption features of ozone at 9.65 μm and carbon dioxide at 15 μm.

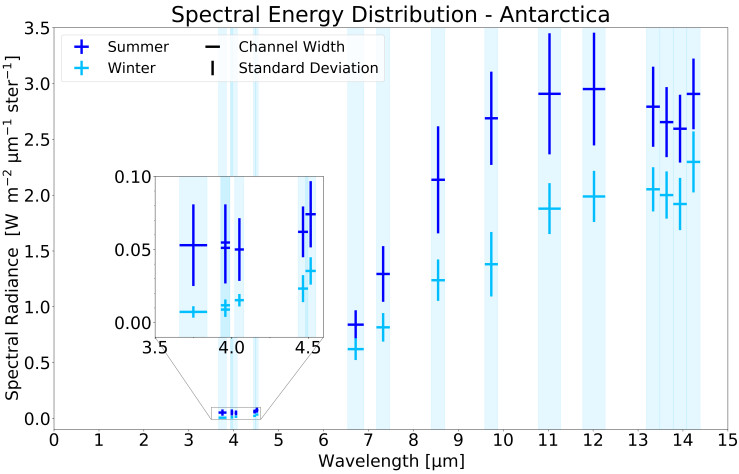

(d) Spectral energy distribution of the Antarctica. Same as Figure b but the definition of summer (blue) and winter (sky blue) is switched. Like the Arctic, the SED shows an upturn in flux in the last channel for both seasons.

Figure 2.2: Spectral energy distributions of all target locations including their day and night comparisons.

For the north pole, summer was defined as from April - September and winter from October - March and vice versa for the south pole. As expected, we find the hottest region, the Sahara Desert, with the highest radiance values followed by the Indian Ocean, Amazon Rainforest, Arctic, and, finally the coldest target location, Antarctica. Throughout the channels and over the entire observation period of 15 years, the Sahara Desert also shows the largest difference between day and night measurements where the flux differs by 30% in channel 31 (10.78 - 11.28 μm). The Indian Ocean data lies in between this range and overall shows a smaller dispersion which could be due to the oceanic large thermal inertia (heat capacity) making them more resistant to temperature changes.

We note the very low level of variations at the shortest wavelength for the two poles and the Indian Ocean which can largely be attributed to the overall low flux levels. In general, comparing the radiance from the equatorial regions to that from the polar regions, the flux differs by up to a factor of about two and three during the day and night, respectively. However, this strongly depends on the channel and location considered.

In order to estimate the effective temperature of each target location, we fitted a black-body curve to every single measurement's SED and calculated the weighted arithmetic mean and the corresponding standard error of the weighted mean from the total set. The results are shown in Table 2.3. Although no comparable

Table 2.2: Resulting mean spectral radiances from the SED analyses in section 2.3.1. All values are stated in physical units of W m^{-2}μm^{-1} sr^{-1}.

		Locations									
		Sahara Desert		Indian Ocean		Amazon Rainforest		Arctic		Antarctica	
		Day	Night	Day	Night	Day	Night	Summer	Winter	Summer	Winter
Channels	20	1.19	0.25	0.43	0.30	0.46	0.21	0.15	0.04	0.05	0.01
	21	1.33	0.36	0.55	0.44	0.55	0.32	0.17	0.05	0.05	0.01
	22	1.42	0.35	0.54	0.43	0.56	0.31	0.16	0.05	0.05	0.01
	23	1.23	0.40	0.53	0.46	0.54	0.33	0.15	0.06	0.05	0.02
	24	0.16	0.11	0.13	0.12	0.12	0.10	0.08	0.04	0.06	0.02
	25	0.62	0.37	0.40	0.38	0.36	0.30	0.17	0.09	0.07	0.04
	27	1.46	1.39	1.58	1.52	1.17	1.15	1.06	0.90	0.84	0.62
	28	3.07	2.85	3.09	2.99	2.35	2.39	2.06	1.59	1.29	0.82
	29	9.17	6.21	7.00	6.79	6.16	5.47	3.99	2.76	2.14	1.24
	30	6.66	4.90	5.41	5.30	5.02	4.58	3.34	2.23	2.69	1.38
	31	10.29	7.23	7.59	7.40	6.70	6.12	4.89	3.61	2.91	1.88
	32	9.49	6.91	7.08	6.91	6.20	5.74	4.78	3.63	2.95	1.99
	33	5.47	4.79	4.83	4.76	4.30	4.16	3.81	3.10	2.79	2.05
	34	4.17	3.92	3.97	3.94	3.63	3.55	3.33	2.72	2.65	2.00
	35	3.56	3.34	3.39	3.37	3.16	3.11	3.05	2.44	2.60	1.92
	36	3.00	2.93	2.95	2.94	2.86	2.85	3.12	2.56	2.91	2.30

Table 2.3: Overview of the resulting effective temperatures after a black-body curve was fitted to every single measurement's SED of a target location and the weighted arithmetic mean and the standard error of the weighted mean were calculated from the set. For the Arctic, summer and winter were defined as from April - September and October - March, respectively, and vice versa for Antarctica.

Target Location	Effective Temperature (K)
Sahara Desert	278.01 ± 0.31
Indian Ocean	267.92 ± 0.21
Amazon Rainforest	260.52 ± 0.20
Arctic Summer	249.18 ± 0.16
Antarctica Summer	233.83 ± 0.06
Sahara Desert Night	264.39 ± 0.20
Indian Ocean Night	266.82 ± 0.20
Amazon Rainforest Night	255.83 ± 0.17
Arctic Winter	236.75 ± 0.12
Antarctica Winter	219.00 ± 0.02

results were found that cover the same observation period, the obtained estimates compare well to daily measurements of the same regions (e.g., Hearty et al., 2009; Hanel et al., 1972; Petitcolin and Vermote, 2002).

Four out of five locations, the Sahara Desert, Indian Ocean, Amazon Rainforest and the Arctic, show similar spectral absorption features in their SEDs. The first feature around ≈ 4.475 µm in channel 24 (4.433 - 4.498 µm) corresponds to the CO_2 band centered at 4.3 µm (Catling et al., 2018). It is followed by a clearly visible ozone absorption band at 9.65 µm, and between channel 33 and 36 (13.2 - 14.4 µm), for the three equatorial regions, the plots show a continues decrease which indicates the next absorption band due to CO_2 centered at 15 µm (e.g., Figure 3 in Schwieterman et al., 2018; Catling et al., 2018).

The two polar regions behave rather different to each other as the south pole displays a seasonal dependence when the drop in variability in channel 30 (centered on the ozone band at 9.65 µm) relative to channels 29 and 31 is compared. During the southern hemisphere summer, the resulting SED for Antarctica (shown in Figure 2.2 d) is missing the dominant ozone absorption feature at 9.65 µm. An existing but less pronounced ozone feature is, however, observable during winter. Due to the missing ozone absorption feature in the summer data, the SED of Antarctica has a shape similar to that of a perfect black-body with a temperature of 233.83 K ± 0.06 K. Also, both polar regions show an upturn in flux towards the

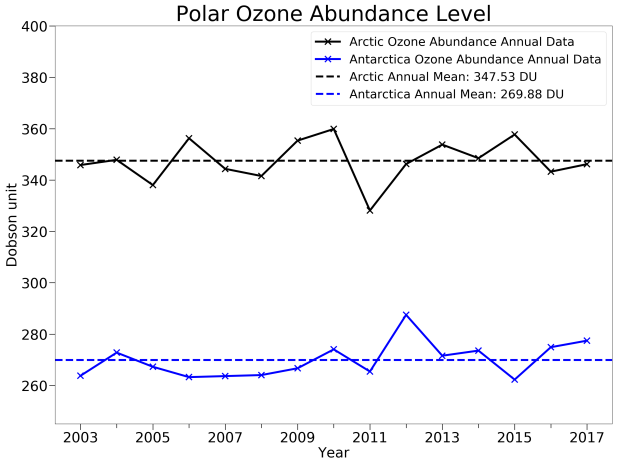

Figure 2.3: A comparison between the Arctic and Antarctic ozone abundance over the same 15-year period that was used to derive the SEDs. Within that time period, the data show that there is 22% less ozone in the south than in the north.

end of the observed wavelength range by MODIS.

A reason for the difference in depth of the ozone absorption feature between the two poles could be the fact that ozone is less abundant in the southern hemisphere. Although, a thinning of the ozone layer has been observed over other regions (e.g., Butchart, 2014, and references therein), such as the Arctic as well as northern and southern midlatitudes, the most severe ozone loss was registered to be recurring in springtime over Antarctica due to chlorofluorocarbons, known as CFCs, that lead to depletion of the ozone layer (Molina and Rowland, 1974). Figure 2.3 shows an ozone abundance dataset for both polar regions over the same 15-year time baseline used in our SED analysis. The dataset was provided by NASA's Ozone Watch. The 15 year Arctic ozone abundance average is calculated to be 347.53 Dobson Units (DU) and 269.88 DU for the Antarctica, indicating that there is on average 22% less ozone around the south pole compared to the north pole within that time period.

Despite the fact that such a shape, and thus temperature, would originate from high altitude clouds, this can be ruled out due to the long observation period. While less ozone is certainly present in the atmosphere above Antarctica, we primarily attribute the lack of a clear absorption feature to the temperature structure

of the atmosphere at this location rather than due to differences in abundance. Balloon soundings showed that 90% of the atmospheric ozone resides in the stratosphere between 10 - 17 km and about 50 km with a peaking abundance around 20 - 25 km. At this altitude the average temperature above the south pole over a 40 year period is roughly ≈ 221 K (NASA Ozone Watch). With the surface temperature being similar to the temperature at the altitude of peak ozone abundance, the absorption feature may not be seen due to the missing contrast in thermal emission.

The observed upturn in channel 36 (14.085 - 14.385 μm) in the SEDs for both polar regions appears to be a characteristic signature of these types of locations. For the poles, it has been known for years that surface-based temperature inversions exist (e.g., Hudson and Brandt, 2005) which are major drivers of some aspects of their climates, including atmospheric radiation. Given that the snow-surface emissivity is greater than the atmospheric emissivity, the inequality in emissivities results in a temperature inversion when the absorbed energy from solar radiation at the surface is small. In this case, some features can appear in emission. Hence, the increase in channel 36 indicates the emission of CO_2 centered at 15 μm.

2.3.2 Power Spectral Densities

In order to investigate whether the planet's obliquity can be inferred from Earth's thermal emission, we decompose the spectral radiance time series into components of different frequencies using Fourier analysis. Specifically, we performed a Discrete Fourier Transform (DFT) on the data to produce a power spectrum, also known as power spectral density (PSD). Since the PSD is the measure of a signal's power content versus frequency, finding trends in the data related to the orbital period would be a strong indication for a tilted spin axis. Figure 2.4 gives an example of the variations in spectral radiance. It shows the time series of the observed spectral radiance in channel 31 (10.78 - 11.28 μm) for the patches over the poles revealing a cyclic behaviour. Due to Earth's obliquity, the poles show higher (lower) spectral radiance readings at the north (south) pole during summer (winter). Fitting a sine function to the data revealed a periodicity of ≈365.25 days, which is very close to the official sidereal year with ≈365.2564 SI days (International Earth rotation and Reference systems Service, 2014). A comparison on the average radiance of the different surface types shows that land masses emit more radiation than ocean or ice covered areas, which is in agreement with previous

studies (e.g., Hearty et al., 2009; Gómez-Leal et al., 2012; Hurley et al., 2014).

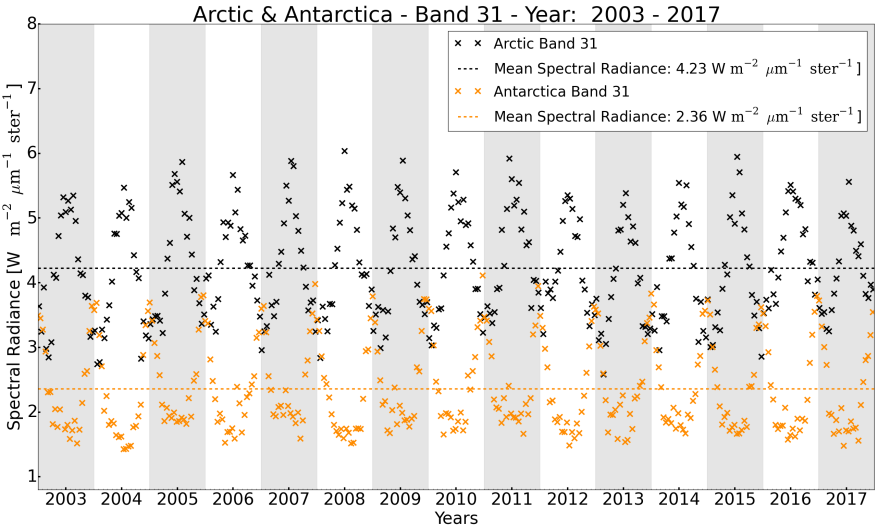

Figure 2.4: Comparison between the two polar regions (Arctic black data points, Antarctica orange data points) for channel 31. Due to Earth's obliquity, the poles do not receive the same insolation at the same time, leading to higher (lower) spectral radiance readings at the north (south) pole during the summer, as seen from the northern hemisphere. The mean radiance level over the 15 years period is indicated by the dashed horizontal lines. The mean spectral radiance difference between the two poles is 1.87 W m^{-2} µm^{-1} sr^{-1}.

A DFT was applied to every channel for each target location by using python's numpy *numpy.fft.fft* module which calculates the one dimensional n-point DFT with the efficient Fast Fourier Transform (FFT) algorithm. As it is a common practice to express the significance of an enhancement by quoting the number of standard deviations it differs from the mean value of the signal, Figure 2.5 shows cycles per year on the x-axis and the significance of a possible signal on the y-axis. It should be noted that the following discussion is based on the results where a DFT is applied to a dataset with a time baseline of 15 years. The results of a one year baseline are discussed further below.

Although the power spectral densities are noisier for the equatorial regions compared to the polar regions throughout all available thermal channels, 92% of all channels and locations including night measurements show a well defined peak (3σ and more) at 1 cycle per year as displayed in Figure 2.6. The polar regions

show overall peaks of 10σ or more as well as whole integer repeats which can be interpreted as harmonics, thus artefacts of the method. For these two locations, all thermal MODIS channels seem to be appropriate for looking for evidence of planetary obliquity in the MIR spectrum. Even though some bands are location and surface type dependent, we find four channels (20-23, 03.66-04.08 μm) that produce strong signals (7σ and above) showing evidence of planetary obliquity independent of target location and surface type. These channels are primarily used for surface and cloud temperature measurements as stated in Table 2.1.

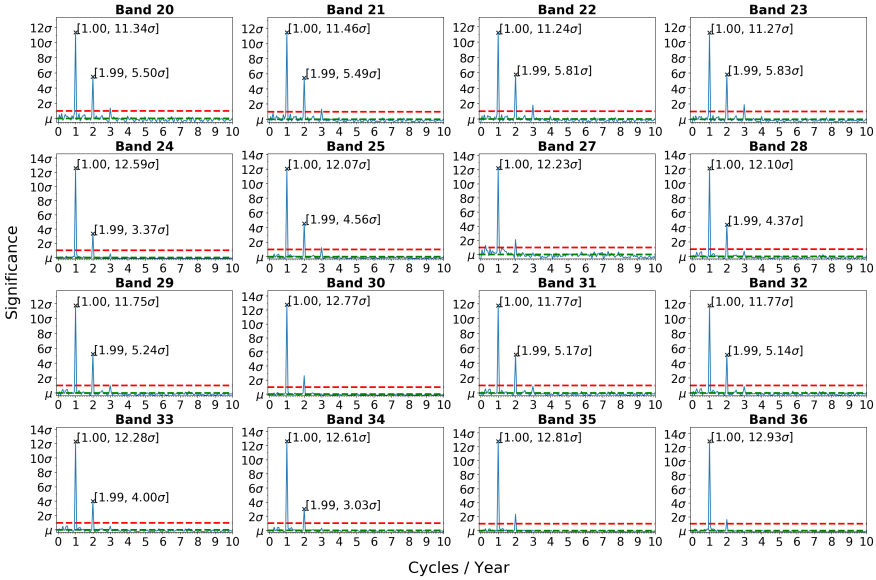

Figure 2.5: Calculated power spectral density for the Antarctica dataset. The figure shows cycles / year on the x- and the significance (σ) of the signal on the y-axis. The green and red dashed lines correspond to the signal's mean and $\pm$ 1σ value, respectively. Due to the clear periodicity in the spectral radiance signal caused by the Earth's obliquity, a relative clean PSD with a noise level well below 1σ can be calculated for the polar regions. All channels show a strong peak (above 11.2σ) at 1 cycle / year and are therefore indicating a tilted rotation axis of Earth. Due to the well defined peaks, all channels are appropriate for looking for evidence of planetary obliquity in the MIR spectrum for the polar regions.

The Sahara Desert (a water-poor region), shows a strong signal (above 11σ) for the first six channels (20-25, 03.66-04.55 μm) that are primarily used for surface, cloud and atmospheric temperature measurements, followed by five channels (29-32 & 34, 08.40-12.27 μm & 13.49-13.79 μm) that deliver an intermediate signal

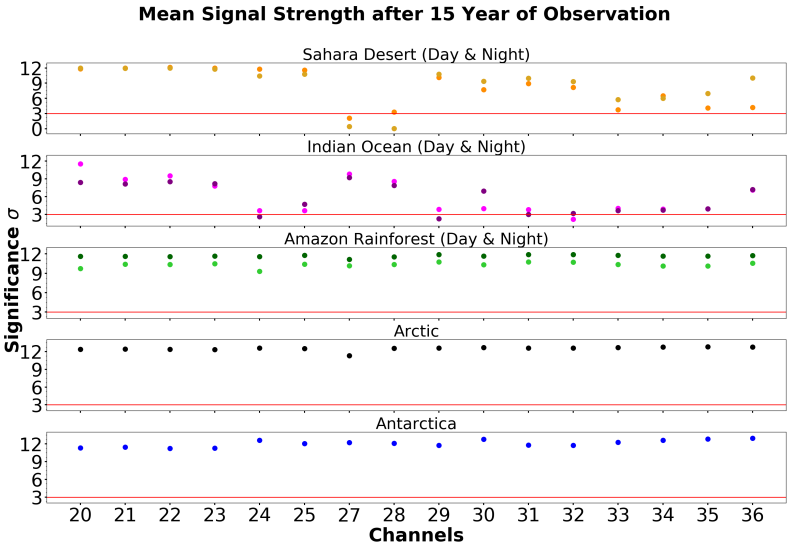

Figure 2.6: PSD analysis for 15 consecutive years of observation to infer the existence of seasons. The figure shows the 16 thermal channels on the x- and the significance σ on the y-axis. The red line indicates the 3σ threshold and the errorbars correspond to the channel specific standard deviation. All channels can be used to infer seasons for the polar regions and the Amazon Rainforest as well as the majority of the channels for the Sahara Desert and Indian Ocean.

strength (above 6.5σ) and five channels (27-28 & 33, 35-36, 06.54-07.48 µm & 13.19-14.39 µm) with less signal strength (below 4.22σ). These bandwidths are primarily used for cirrus clouds, water vapour detection, and cloud top altitude detection.

Besides from the above mentioned channels 20-23 that produce strong signals (11.83-12.15σ), we can deduce from the Indian Ocean (water rich region) power spectral densities that channels 27, 28 and 36 produce also strong signals (above 7σ) as well as that another four channels (30, 33-35) do show a peak at 1 cycle per year but with a low sigma reading (below 4.15σ), implying that in case of observations of a water dominated hemisphere at similar latitude bandwidths covering water absorption bands are less appropriate for detecting evidence of planetary obliquity via thermal emission monitoring.

Since it is very unlikely to observe a rocky, temperate exoplanet around a sun-like

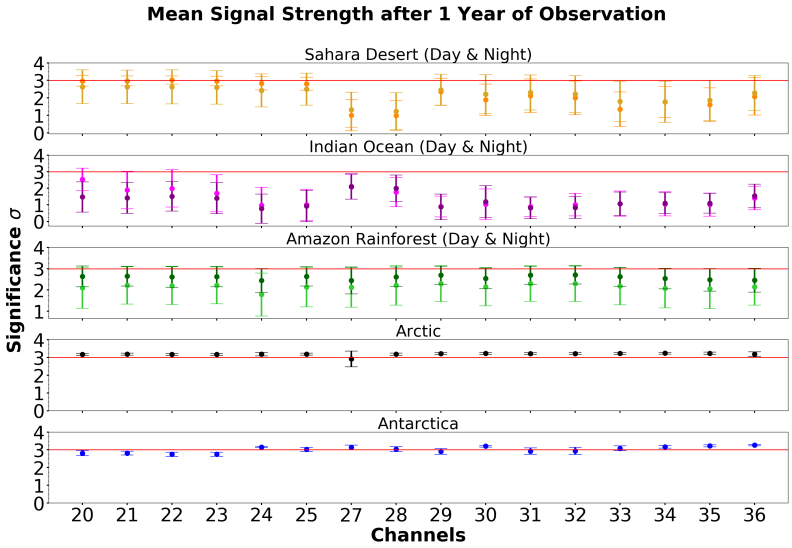

Figure 2.7: Same as Figure 2.6 but now showing the mean significance when 1 year of data are analyzed. Although the trends remain the same independent of observation time, only the Arctic seems to be showing evidence of a tilted rotation axis throughout all thermal channels after one year of observation. For Antarctica, the result is wavelength dependent and suggest nine favourable channels. The difference between day and night measurements for the three equatorial regions are statistically none significant.

star sufficiently frequently along its orbit over a time baseline of 15 years, we investigated the signal strength behaviour for an observation period of only one year. The same DFT analysis was performed separately on each year. For channels that did not show a peak at one cycle per year ±5%, the peak was retrieved from the signal at that orbital period. For each channel, the average of its signal strength throughout the 15 years and the corresponding standard deviation was calculated. The result of the analysis is shown in Figure 2.7.

After one year of observations, the Arctic dataset showed up to 3σ signals for all channels except for channel 27 (06.54 - 06.90 μm) which was the most variable channel in terms of radiance fluctuations. This is likely to be the result of undetectable cirrus clouds. Due to the relative large noise level and a very low reading (1.71σ) in the year 2010, it shows the largest errorbar out of the 16 channels. Only nine channels (24-28, 30, 33-36) lie above the 3σ threshold for the Antarctic target location. Overall the channels show more noise than the matching channels of

the Arctic dataset, resulting in larger standard deviations.

The three equatorial regions display the same behaviour for one year of observation as for 15 years of observation. Especially for channels 27 and 28 in the Sahara Desert and Indian Ocean datasets, as discussed above. None of the channels exceeded the 3σ threshold for the locations in question considering only one year of observation. Their large standard deviations indicate the variability in spectral radiance due to a mixture of cloud coverage and change in seasonal insolation. For these latitudes however, the signal is probably dominated by clouds as they affect the measurements more due to a larger contrast between surface and top of cloud temperature. For the polar regions on the other hand, the signal is not dominated by clouds but by change of seasonal insolation. Indeed studies suggest that cloud coverage varies with distance from the equator where the cloudiest regions are the tropics and temperate zones and the subtropics and the polar regions have between 10-20% less cover (e.g., Rossow and Zhang, 1995; Rossow and Schiffer, 1999; Warren et al., 2007). Furthermore, the results show that the difference between day and night measurements for the three equatorial locations is statistically insignificant in this type of analysis.

While the methodology to infer obliquity in the reflected light is well established (e.g., Kawahara, 2016; Schwartz et al., 2016; Farr et al., 2018), we cannot yet provide quantitative statements on the planet's obliquity based on our results. The underlying idea of our analysis is that by re-observing the planet several times along its orbit (and ideally over more than one orbital period) we can link the observed periodicity in the SED with the orbital period. Therefore we can identify whether a planet has seasons and hence a tilted spin axis. Additional and more quantitative conclusions require disk integrated data and additional modelling. We hope to address this in future research.

2.4 Summary & Conclusions

We investigated the thermal emission and time variability of five single-surface-type target locations on Earth: 1) Amazon Rainforest, (2) Antarctica, (3) Arctic, (4) Indian Ocean and (5) Sahara Desert. We constructed Earth observation datasets containing calibrated spectral radiances from 16 discrete channels between 3.66-14.40 μm over a time baseline of 15 years including separate datasets for day-time and night-time emission of all five locations. The data were collected between

2003 and 2017 by MODIS aboard NASA's Earth observing satellite Aqua which observed every target location twice per month, resulting in 360 measurements per location. From each dataset, we derived spectral energy distributions and used Fourier analysis to look for evidence of planetary obliquity in the measured spectral radiance variations. By fitting black-body curves to the SEDs, we estimated the effective temperature for each target location. Since all our results are based on a time baseline of 15 consecutive years, we compare the time variability results to an observation time of one year in order to investigate whether it is still possible to detect evidence of Earth's tilted rotation axis.

Key results from the inferred SEDs include:

1. As expected, Earth's thermal emission cannot be represented by a single SED. Hence, viewing geometry plays an important role when analyzing exoplanet thermal emission data. At Earth's peaking wavelength, the flux between the equatorial and polar regions varies on average by a factor of about two and three during the day and night, respectively.
2. Despite the coarse spectral resolution, the inferred SEDs showed differences in the strengths of absorption features in the atmosphere. Regions close to the equator and towards the north pole show more dominant O_3 and CO_2 absorption features than the south pole.
3. Given how seasonally variable the atmospheric structure and composition is in the Antarctica, its SED changes over half of an orbit significantly when the ozone feature at 9.65 μm is compared between summer and winter. The lack of a clear ozone absorption feature during summer should be considered as it could lead to a false negative interpretation when searching for biosignatures in exoplanets that are viewed pole-on.
4. The derived effective temperatures averaged over a 15 year observation period are:
    - 278.01 K ± 0.31 K, 267.92 K ± 0.21 K and 260.52 ± 0.20 K for the three equatorial regions Sahara Desert, Indian Ocean and Amazon Rainforest during the day and 264.39 K ± 0.20 K, 266.82 K ± 0.20 K and 255.83 ± 0.17K during the night, respectively.
    - For the two poles we received 249.18 ± 0.16 and 236.75 ± 0.12 for the Arctic and 233.83 ± 0.06 and 219.00 ± 0.02 for Antarctica during summer and winter, respectively.

Key results from the time variability study over the 15-year observation period include:

1. Applying a DFT to the datasets showed that a periodicity of Earth's thermal emission can be observed, providing a strong indication for a tilted spin axis, and therefore seasons.
2. Specifically, 92% of the combined 128 thermal channels show a well defined peak at 1 cycle / year:
   (a) The polar regions displayed a signal strength of at least 10σ for all channels. Therefore, pole-on view measurements are ideal for probing seasonal variations.
   (b) The equatorial regions showed a signal strength of at least 7σ for 72 out of 96 thermal channels, including the night measurements.

Key results from the time variability study over a one year observation period include:

1. For an observation time of one year (~24 data points), the strength of the periodicity signal decreases significantly. For the equatorial regions none of the investigated channels reached a 3σ-signal, and the day and night difference is found to be statistically insignificant. For the polar regions, it is possible to observe signs of obliquity in the thermal emission but the significance depends on the spectral band considered.
2. Compared to the 15-year observation period, the trends of the data distribution are unchanged.
3. Comparing the nature of variability between the equatorial and polar regions, we find that the measurements are dominated by clouds in equatorial regions and by changes of seasonal insolation in polar regions.

Our analyses emphasize the power of thermal emission data for the characterization of habitable terrestrial exoplanets, but they also caution us to be careful in the analysis and interpretation. Depending on viewing geometry and underlying dominant surface type the same planet may appear significantly different. It seems that seasons could be inferred from thermal emission data, but that will

require a significant amount of observing time. Still, combining the information from all channels investigated here may allow to infer the existence of seasons with high confidence in case ~20 data points are available roughly evenly spread over the planet's orbital period. The results obtained in this work should be considered as first steps towards disk-integrated mid-infrared observations of Earth's spectra (e.g., Hearty et al., 2009), in order to explore characteristics that may appear in newly detected exoplanets in the future. The derived datasets could serve as a basis for such further investigations. We plan to perform a disk-integrated analysis in a follow up paper. Furthermore, combining the optical and near-infrared channels of MODIS, that were not considered here, with the thermal emission data would allow us to investigate, for instance, the specific influence of various cloud types on certain channels in order to refine atmospheric models.

Contribution

I was the main contributor of Chapter 2. I sourced and reduced the dataset and wrote the manuscript. Sascha P. Quanz initiated the project and together with Ravit Helled guided the project. Tyler D. Robinson, Edward W. Schwieterman and Michael Schaepman provided valuable comments on the first draft.

3 Spatially-Unresolved Earth: Time-Variable Thermal Emission and Atmospheric Seasonality of Bioindicators

Adapted from:
"Earth as an Exoplanet. II. Earth's Time-variable Thermal Emission and Its Atmospheric Seasonality of Bioindicators"

J.- N. Mettler, S. P. Quanz, R. Helled, S. L. Olson, E. Schwieterman

The Astrophysical Journal, 2023, 946, 82

Abstract

We assess the dependence of Earth's disk-integrated mid-infrared thermal emission spectrum on observation geometries and investigate which and how spectral features are impacted by seasonality on Earth. We compiled an exclusive dataset containing 2690 disk-integrated thermal emission spectra for four different full-disk observing geometries (North & South Pole centered and Africa & Pacific centred equatorial views) over four consecutive years. The spectra were derived from 2378 spectral channels in the wavelength range from 3.75 to 15.4 μm (nominal resolution ≈ 1200) and were recorded by the Atmospheric Infrared Sounder aboard the Aqua satellite. We learned that there is significant seasonal variability in Earth's thermal emission spectrum, and the strength of spectral features of

bio-indicators, such as N_2O, CH_4, O_3 and CO_2 depends strongly on both season and viewing geometry. In addition, we found a strong spectral degeneracy with respect to the latter two indicating that multi-epoch measurements and time-dependent signals may be required in order to fully characterize planetary environments. Even for Earth and especially for equatorial views, the variations in flux and strength of absorption features in the disk-integrated data are small and typically $\leq 10\%$. Disentangling these variations from the noise in future exoplanet observations will be a challenge. However, irrespectively of when the planet will be measured (i.e., day or night or season) the results from mid-infrared observations will remain the same to the zeroth order which is an advantage over reflected light observations.

3.1 Introduction

Spatially-resolved flyby data from the *Pioneer 10/11* (Bender et al., 1974; Baker et al., 1975; Gehrels, 1976; Ingersoll et al., 1976; Kliore and Woiceshyn, 1976) and *Voyager 1/2* (Kohlhase and Penzo, 1977; Hanel et al., 1977) missions in the 1970s initiated the exploration of key concepts for the characterization of planetary bodies other than Earth in our solar system. The photometric and spectroscopic observations, ranging from the ultraviolet to infrared, allowed planetary scientists to infer unprecedented details for these worlds such as planetary energy balance, surface and atmospheric chemical, thermal and composition properties including cloud and aerosol formation and distribution (for an extensive review see Robinson and Reinhard (2018)). In 1993, Sagan et al. (1993) and Drossart et al. (1993) constituted a control experiment by applying remote sensing tools and techniques to search for life on Earth by analysing *Galileo* spacecraft (Johnson et al., 1992) Earth-flyby data. Their data indicated a habitable world with water, carbon, and chemical energy. The data also showed signs of biological activity that modulates surface and atmospheric properties. Among these 'biosignatures', the coexistence of O_2 and CH_4 is a particularly strong indication of life (e.g., Lovelock, 1965; Krissansen-Totton et al., 2016, 2018; Schwieterman et al., 2018).

The impact of life on the geochemical environment and the composition of the atmosphere throughout billions of years of coevolution led to the suggestion that alien biospheres should be detectable remotely via spectroscopy (Lovelock, 1965; Lovelock et al., 1975; Olson et al., 2018a). Today, the advances made in instrumentation and observing techniques allow us to peak and discover planets

beyond our solar system, resulting in a total of 5118 detected exoplanets[1]. Among these discoveries, potentially habitable exoplanets have been found orbiting in the so-called habitable zone (HZ) of their host stars which sparked interest in spectroscopic studies of exoplanet surfaces and atmospheres for signs of life (e.g., Gillon et al., 2017; Dittmann et al., 2017; Montet et al., 2015; Anglada-Escudé et al., 2016; Gilbert et al., 2020). Thus, over the next decades, the long-run goal of exoplanet science will be the characterization of the atmospheres of temperate terrestrial exoplanets in order to assess their habitability and search for indications of biological activity which requires the direct detection of their signals over interstellar distances.

The first generation of such terrestrial exoplanet detection and characterization missions will not be capable of spatially resolving the planets due to the large distances of at least several parsecs at which the exoplanets typically will be observed. Even with the most powerful telescopes conceived today, including the recently launched James Webb Space Telescope (JWST) (Gardner et al., 2006), they will remain spatially unresolved point sources. Moreover, the relatively low planet-to-star contrast ratio significantly limits the temporal sampling and the provided spectral information will be averaged over the observable disk and integration time. The latter may vary between several days and weeks to build up an adequate signal to noise ratio to detect biosignatures, depending on the target and mission concept. For example, in the specific case of JWST, which pushes the limits from detecting towards characterizing Jovian to super Earth exoplanets, the accumulation of transmission spectra from hundreds of transits is required in order to reach a signal to noise ratio high enough to potentially confirm the presence of biosignature pairs like O_2 & CH_4 or O_3 & N_2O (e.g., Krissansen-Totton et al., 2016; Fauchez et al., 2019; Lustig-Yaeger et al., 2019; Wunderlich et al., 2019; Tremblay et al., 2020). Hence, considering the mission's lifetime and the telescope time necessary for the detection of atmospheric biosignatures, probably only a few attempts will be made on specific targets. Therefore, JWST as well as other current technologies are not yet capable of detecting and characterizing the atmospheres of temperate, terrestrial exoplanets in a statistically meaningful sample and the community has to wait until space-based direct imaging is realized in future missions like the Habitable Exoplanet Observatory (HabEx; Gaudi et al., 2020), Large Ultraviolet Optical Infrared Surveyor (LUVOIR; The LUVOIR Team, 2019) or Large Interferometer For Exoplanets (LIFE; Quanz et al., 2018).

[1] http://exoplanet.eu (visited September 27, 2022)

During the integration time of such direct imaging missions, the spectral appearance and characteristics of a planet change as it rotates around its spin axis and as spatial differences from clear and cloudy regions, contributions from different surface types as well as from different hemispheres evolve with time. In addition, twenty years of exoplanet discovery revealed a vast diversity of planets regarding their masses, sizes and orbits (e.g., Batalha, 2014; Burke et al., 2015; Paradise et al., 2021) and it is thought that this diversity also extends to their atmospheric mass and composition, making the characterization of the planetary environment even more difficult. Specifically, the interpretation of the spectrum is not unique and a plethora of solutions exist to describe the planet's surface and atmospheric characteristics.

To achieve the fundamental goal of detecting signs of life on planets beyond our solar system, we will need to be able to interpret this space and time averaged data. Ideally, an exoplanet candidate with the potential of harbouring life would be observed by multiple observing techniques in both the reflected and thermal emission spectrum in order to attempt to fully characterize the planet's nature. Yet, especially for biosignatures, the potential for both false positives and false negatives remains (e.g., Selsis, 2002; Meadows, 2006; Reinhard et al., 2017; Catling et al., 2018; Krissansen-Totton et al., 2022). One way to break this degeneracy and to narrow down the set of possible solutions is by adding information coming from time-dependent signals such as atmospheric seasonality.

The phenomenon of planetary seasonality generally arises for non-zero obliquity or orbital eccentricity planets, and the extent of the atmospheric response is governed by stellar flux incident as well as planetary and atmospheric characteristics (e.g., Kopparapu et al., 2013; Guendelman and Kaspi, 2019). In our solar system, seasonal variations were observed for the gas giant planets such as Uranus, Saturn and Jupiter (e.g., Fletcher et al., 2015; Fletcher, 2021; Shliakhetska and Vidmachenko, 2019; Nixon et al., 2010) as well as for Mars who is prone to the most diverse seasons in the solar system, due to its 25.2° tilt of the spin axis and eccentricity of 0.093 (e.g., Trainer et al., 2019; Leffler et al., 2019).

On Earth, the seasonal variation in atmospheric composition, for example of carbon dioxide (CO_2), is a well-documented and mechanistically understood biologically modulated occurrence (e.g. Keeling, 1960), that is driven by the time-variable insolation and the reacting biosphere. Net fluxes of methane and other trace biological products evolve seasonally, responding to temperature induced

changes in biological rates, gas solubility, precipitation patterns, density stratification, and nutrient recycling (e.g., Khalil and Rasmussen, 1983; Olson et al., 2018b; Schwieterman, 2018).

Since the atmospheric seasonality arises naturally on Earth, it is very likely to occur on other inhabited planets as well. Hence, the search for seasonality as a biosignature on exoplanets is particularly promising and has been proposed by Olson et al. (2018b). Yet, the discussion of time-varying biosignatures has remained qualitative (e.g., Tinetti et al., 2006a,b; Meadows, 2006, 2008; Schwieterman et al., 2018) and the field of exoplanet research lacks a comprehensive understanding of which spectral features are impacted by observable seasonality on inhabited worlds and how these impacts would be modulated by stellar, planetary, and biological circumstances.

Earth offers a unique opportunity to study this aspect, yet it requires investigating our planet from a remote vantage point. Although there are several methods to study Earth from afar such as Earth-shine measurements or spacecraft flybys (for a recent review see, e.g., Robinson and Reinhard, 2018, and references therein), we chose a remote sensing approach which offers the extensive temporal, spatial, and spectral coverage needed to investigate the effect of observing geometries on disk-integrated thermal emission spectra and time-varying signals. However, for Earth orbiting spacecrafts it is impossible to view the full disk of Earth and the spatially resolved satellite observations have to be stitched together to a disk-integrated view (e.g., Tinetti et al., 2006a; Hearty et al., 2009; Gómez-Leal et al., 2012).

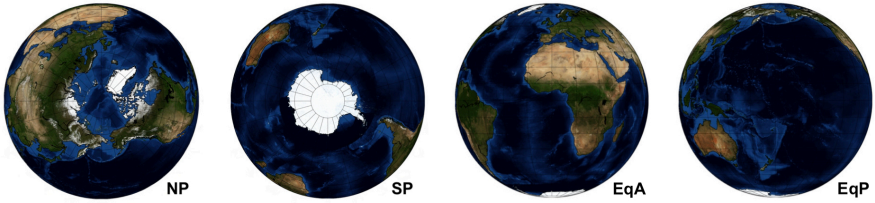

Figure 3.1: The four observing geometries studied in this work. From left to right: North Pole (NP), South Pole (SP), Africa centered (EqA) and Pacific centered equatorial view (EqP). In section 3.3.3, we study integration times longer than the Earth's rotation period. Due to the continuously evolving view of low latitude viewing geometries as the planet rotates, we combine the two equatorial views EqA & EqP to a combined observing geometry, EqC.

In a previous paper (Mettler et al., 2020), we have analysed 15 years of thermal emission Earth observation data for five spatially resolved locations. The data was collected by the Moderate Imaging Spectroradiometer (MODIS) aboard the Aqua satellite in the wavelength range of 3.66 - 14.40 µm in 16 discrete thermal channels. By constructing datasets with a long time baseline spanning more than a decade and hence several orbital periods, we investigated flux levels and variations as a function of wavelength range and surface type (i.e., climate zone and surface thermal properties) and looked for periodic signals. From the spatially resolved single-surface-type measurements, we found that typically strong absorption bands from CO_2 (15 µm) and O_3 (9.65 µm) are significantly less pronounced and partially absent in data from the polar regions. This implies that estimating correct abundance levels for these molecules might not be representative of the bulk abundances in these viewing geometries. Furthermore, it was shown that the time-resolved thermal emission spectrum encodes information about seasons/planetary obliquity, but the significance depends on the viewing geometry and spectral band considered. In this paper we expand our analyses from spatially resolved locations to disk-integrated Earth views and present an exclusive dataset of 2690 disk-integrated mid-infrared thermal emission spectra (3.75 - 15.4 µm: $R \approx 1200$) derived from remote sensing observations for four full-disk observing geometries (North & South Pole, Africa & Pacific centred equatorial view) over four consecutive years at a high temporal resolution (see Figure 3.1 and Table 3.1). Using the dataset, we assess the dependency of Earth's disk-integrated thermal emission spectrum on observing geometries, phase angles and integration times much longer than Earth's rotation period as well as investigate which spectral features of habitability and life are impacted by observable seasonality. In section 3.2, we describe the input data and our method to derive the disk-integrated spectra, in section 3.3 we present and discuss our results. In section 3.4 we put our findings in context with previous works on this matter and close with the conclusions in section 3.5.

3.2 Observations and Data Reduction

We leveraged the extensive temporal, spatial, and spectral coverage of the Atmospheric Infrared Sounder (AIRS) (Chahine et al., 2006) aboard the Earth-monitoring satellite Aqua. Everyday, AIRS obtains 2,916,000 Earth spectra in 2378 spectral channels in the mid-infrared (MIR) wavelength range between 3.75

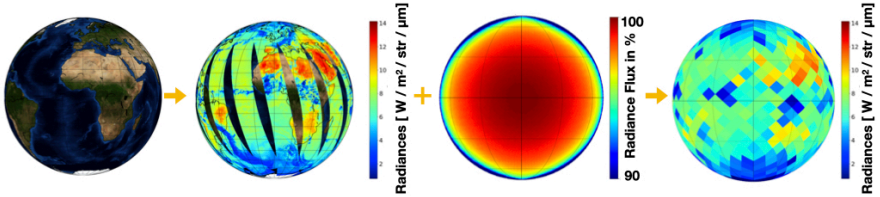

Figure 3.2: An illustration of the method: For every observation geometry the corresponding AIRS radiances were mapped onto the globe and subsampled using the HEALPIX approach. To account for the fact that Earth monitoring instruments are recording their data in the nadir viewing geometry, a limb darkening parametrization adapted from Hodges et al. (2000) was applied to the data before disk-averaging the disk-view. The whole process was repeated for all the 2644 mid-infrared thermal emission spectral channels from the AIRICRAD level 1C satellite product, producing the disk-integrated spectra used in this work.

- 15.4 µm (nominal resolution: λ / $\delta\lambda \approx 1200$). Due to the satellite's operation height of 705 km and due to its Sun-synchronous, near-polar and circular orbit, it revolves Earth in 99 minutes, providing a rich set of spectra consisting of day, night, land and ocean scenes at all latitudes. However, for orbiting spacecrafts like this, it is impossible to view the full disk of Earth which is why the observations have to be tailored to show a spatially resolved, global map of Earth which then can be disk-integrated in order to study Earth's characteristics by means of exoplanet characterization techniques. For our analysis, we have compiled an exclusive dataset of such disk-integrated Earth thermal emission spectra at a high temporal resolution for four different observation geometries over four consecutive years. In total, the dataset comprises 2690 spectra (see table 3.1).

In order to derive the spectra, we have used radiance measurements from an AIRS Infrared (IR) level 1C product (V6.7) called *AIRICRAD*[2], containing calibrated and geolocated radiances given in physical units of $\mathrm{Wm^{-2}}\mu\mathrm{m^{-1}sr^{-1}}$ (Manning et al., 2019). These measured AIRS radiances were then mapped onto the globe at high spatial resolution, and subsampled at spatial grid points with Nside = 128 (196,608 pixels) using the Hierarchical Equal Area and Iso-Latitude Pixelization (HEALPIX) approach (Gorski et al., 2005) which allowed us to easily simulate how Earth would look from different perspectives (see Figure 3.2). The chosen Nside allowed us to sample the data with the best possible resolution. While higher spatial resolution grids would not portrait the data correctly, lower Nside value

[2] https://cmr.earthdata.nasa.gov/search/concepts/C1675477037-GES_DISC.html

grids resulted in differences in the disk-integrated spectra compared to the full resolution average due to the larger pixel sizes.

For our analysis, we defined four specific observing geometries as shown in Figure 3.1: North and South Pole, Africa and Pacific centred equatorial views. Since Earth monitoring instruments observe in the nadir viewing geometry, we applied a simple empirical limb correction function adapted from Hodges et al. (2000) to our disk-views, where the limb-adjusted radiance, $R(\theta)$, with the zenith angle θ, is calculated from the radiance at nadir, $R(0)$, as follows:

$$R(\theta) = \lambda(\theta) \times R(0) \tag{3.1}$$

where $\lambda(\theta)$ is the MIR limb correction function as a function of the satellite zenith angle given as:

$$\lambda(\theta) = 1 + 0.09 \times ln(cos(\theta)) \tag{3.2}$$

This weighting function progressively downweights off-nadir pixels with their cosine of satellite zenith angle in favor of near-nadir pixels, fully taking account of the geometric effects. Furthermore, due to the swath geometry of satellites, daily remote sensing data contain gores, which are regions with no data points, between orbit passes near the equator. These regions are filled within 48 hours as the satellite continues scanning Earth while orbiting it. However, in order to create snapshots of Earth's full disk on a daily basis, one has to consider the missing data.

For the purpose of investigating the impact of missing thermal emission data on the disk-integrated mean, we analyzed 2000 randomly selected AIRS observation frames from which up to 12% data was cut out and compared the results of five different interpolation methods (linear, nearest and cubic python scipy griddata, nearestND and python numpy linear interpolator) to the not interpolated frames. The results showed that the deviation from the original frames to the not interpolated frames with 12% missing data was $\approx 0.2\%$ and less for the interpolated frames. Thus, the effect of missing thermal emission data on the disk-integrated mean is negligible, if the Earth-view disk contains gores of 12% or less missing data. Hence, due to these results and the fact that AIRS daily coverage is more

than 95% of Earth's surface, we have not applied any interpolation methods and refrained from adding artificial data to the scenes. The entire dataset can be shared upon request.

Table 3.1: Dataset overview

Year	Temporal Resolution	Total Days	Day	Night
2016	Every 3rd day	121	X	X
2017	Every 3rd day	121	X	X
2018	Daily	365	X	···
2019	Every 3rd day	121	X	X
Effective number of spectra		#		
NP		405	X	X
SP		408	X	X
EqA_day		765	X	
EqA_night		311		X
EqP_day		391	X	
EqP_night		410		X

3.3 Results

In the following sections we analyse the data for the four viewing geometries presented in Figure 3.1. These viewing geometries evolve throughout the year due to Earth's non-zero obliquity. Figure 3.3 illustrates how the phases change for the equatorial and pole-on viewing geometries. Whereas the former view blends seasons and has a diurnal cycle, the polar view shows one season but blends day and night. Furthermore, some of the observing geometries discussed in section 3.3.3 represent idealized scenarios as they cannot be readily observed for exoplanets by future observatories.

3.3.1 The Seasonal Variability of Earth's Thermal Emission Spectrum for Different Viewing Angles

Here, we investigate the annual variability of Earth's MIR thermal emission spectrum due to obliquity as a function of viewing geometry. For the analysis, the measured spectra are considered to be snapshots, i.e., the integration time is a lot less than Earth's rotation period. The results are shown in Figure 3.4 which displays the time variable change of flux over one full year for both polar and equatorial viewing geometries. For each specific viewing geometry, the annual

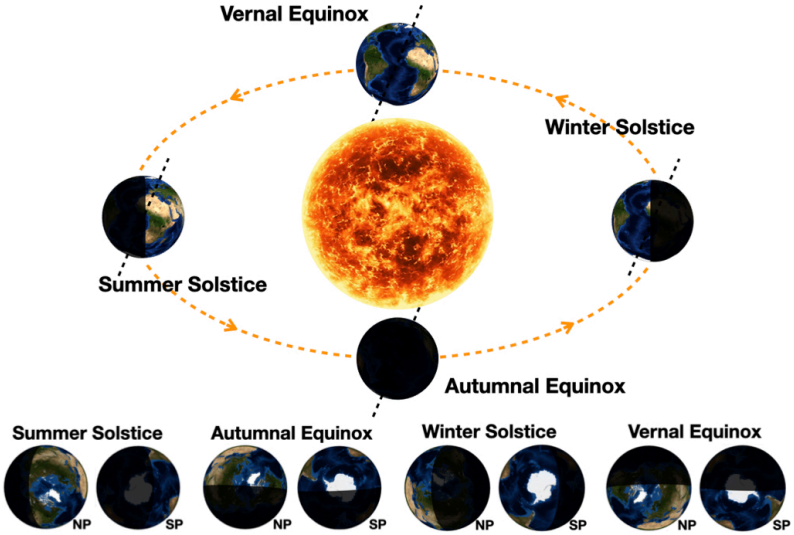

Figure 3.3: Annual change in the position of the Earth on its orbit around the Sun. The graphic in the top panel illustrates a view on Earth from a position in space that is at an increased angle with respect to the ecliptic plane in order to show the different phases of illumination during the solstices and equinoxes. The bottom panel shows the phases for the two polar observing geometries at the same time.

average spectrum was calculated from all disk-integrated measurements taken over four years. The plots also show the minimum and maximum measured spectrum within that time period as well as an average summer and winter spectrum. To determine the latter, the months with the highest / lowest flux measurement per year at Earth's peaking wavelength of 10.4 microns were averaged over four years to get an accurate average spectrum for that season. For the northern hemisphere this turned out to be January and July for the winter and summer season, respectively, and vice versa for the southern hemisphere. To facilitate the quantitative analysis of Figure 3.4, we define the following three atmospheric windows: window 1: 10.2 - 11 μm, window 2: 8 - 9 μm and window 3: 3.9 - 4.1 μm which either lie in the infrared window (8 - 14 μm) or show a maximum absorption of up to ~10%. The results are summarized in table 3.2.

The **north pole centered view (NP)**, shown in Figure 3.1, contains a large landmass fraction and latitudes spanning from the arctic circle down to ~20°N. Hence, it comprises three out of the four main climate zones found on Earth including

the arctic, temperate and tropical zone as well as the sub-polar and sub-tropical transition zones in between them. While the former three climate zones are dominated throughout the year by the same air masses, the sub-polar and sub-tropical transition zones change with seasons as the air masses from neighbouring zones enter at various times of the year. This leads, in combination with the surface characteristics of the continental mass, to a larger expected variability. In the NP view, the arctic zone is dominating the scene and contributes therefore the most to the disk-integrated measured flux, followed by the temperate climate zone. The hottest visible climate zone, tropical, is located close to the edge of the scene and its contribution to the overall disk-integrated average is therefore affected by

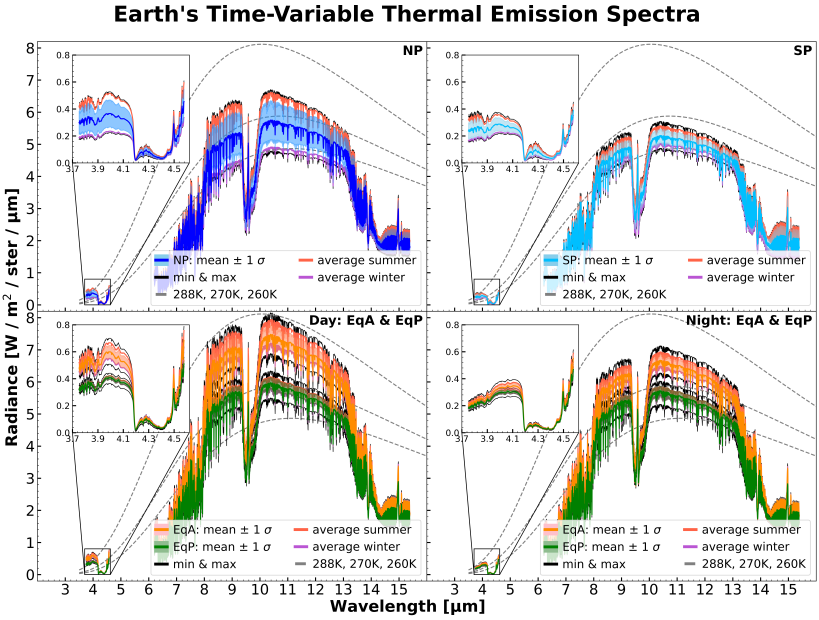

Figure 3.4: A comparison of the disk-integrated thermal emission spectrum for the four different observing geometries (NP, SP, EqA and EqP). The mean represents the annual spectrum averaged over 4 years of data. The shaded area corresponds to the standard deviation of all measurements for that particular observing geometry. The average summer and winter were defined as the months with the highest and lowest flux levels at 10.4 microns, respectively. For the northern hemisphere this turned out to be July and January and vice versa for the southern hemisphere. The dashed lines represent black body curves at three different temperatures: 288K, 270K and 260K.

the limb darkening effect of 5 - 10%. The equatorial and sub-equatorial climate zone is not visible for that viewing geometry.

As expected, NP shows the largest seasonal variability out of the four viewing geometries. At longer wavelengths the flux increases between an average winter and summer by 33% and 42% in the atmospheric window 1 and 2, respectively. At shorter wavelengths in the MIR (window 3), the relative change in flux increases by more than a factor of 2.

Like NP, the **south pole centered view (SP)** is dominated by the arctic climate zone and the tropical zone lies close to the edge, meaning that the flux coming from this region is affected by the limb darkening effect. However, due to the inhomogeneous land distribution of our home planet, the pole-on view of the southern hemisphere can be considered as an ocean dominated view and due to the high thermal inertia of oceans in combination with the dominating arctic climate, the seasonal variability is expected to be less than for the northern hemisphere pole-on view. Comparing the seasonal flux variation of NP to SP shows that the variability is in the order of a third less for longer wavelengths in windows 1 and 2 and a factor of 2 less for shorter wavelengths in window 3. This results in an annual effective temperature change at Earth's peaking wavelength of only 9K for SP whereas for NP it turns out to be 16K. In terms of seasonal variability, SP shows a similar variability in the two longer wavelength band atmospheric windows 1 and 2 (11% and 13%, respectively) than the Pacific-centered, ocean-dominated, equatorial view EqP. However, at shorter wavelengths, e.g. window 3, SP shows a 15% larger variability than EqP. The increased variability at the shorter wavelengths in window 3 could be assigned to a reflected light component and difference of landmass fraction and its surface characteristics contained in these two observing geometries. The pole-on view of the southern hemisphere is centered on the antarctic continent Antarctica and its ice shelves.

The dominating climate zones for the **Africa-centered equatorial viewing geometry (EqA**) are the equatorial and tropical zones as well as the sub-equatorial and sub-tropical transition zones linking them. EqA includes an extended equatorial zone as both the northern part of South America as well as central Africa lie in the view, yet, radiances from the latter contribute more to the disk-integrated mean. Fluxes coming from the temperate and, especially, the arctic climate zones are progressively down weighted by the limb-darkening parametrization. As expected, the Africa-centered equatorial view shows the highest flux readings of

all the viewing geometries during both day and night time in the summer season, reaching an effective temperature of 288K at Earth's peaking wavelength. Its seasonal variability in thermal emission is with 22% - 26% in windows 1 and 2, respectively, the second highest after NP although at shorter wavelengths. The relative change in flux of the range of measured spectra is reaching a similar value (130%). The additional variability and spread in data could be due to the influence of clouds, lowering the overall average of the scene as the contrast between hot and cold regions within the same view is higher than for viewing geometries with a dominating cold region like the arctic climate zone in the case of NP. The relative change in flux between summer and winter at day times (night) is 10% and 12 % (7% and 8 %) in windows 1 and 2, respectively. At shorter wavelengths, the

Table 3.2: Seasonal flux variability - the figures represent the relative change in flux of an average summer versus winter for a specific viewing geometry and have been rounded to the nearest integer. The percentages given in the brackets indicate the relative change in flux of the range between the maximum and minimum measured spectrum. Since the datasets of NP and SP naturally include day (summer) and night (winter) data, the variability for EqA and EqP (day + night) was determined using an average summer and winter from the day and night dataset, respectively. In the lower third of the table, we compare day versus night spectra for the denoted season. To facilitate the quantitative analysis of Figure 3.4, three spectral windows were defined that lie in atmospheric windows.

Observing Geometries	**Window 1 (10.2 - 11µm)**	**Window 2 (8 - 9µm)**	**Window 3 (3.9 - 4.1µm)**
Summer vs. Winter			
NP	33% (39%)	42% (49%)	118% (135%)
EqA (day + night)	22% (29%)	26% (35%)	105% (130%)
EqP (day + night)	11% (19%)	12% (22%)	45% (65%)
SP	11% (17%)	13% (20%)	60% (70%)
EqA (day)	10% (18%)	12% (20%)	20% (39%)
EqA (night)	7% (13%)	8% (15%)	12% (30%)
EqP (day)	6% (15%)	7% (17%)	7% (20%)
EqP (night)	5% (13%)	5% (15%)	9% (25%)
Day vs. Night			
EqA summer	14% (14%)	17% (16%)	77% (75%)
EqA winter	11% (11%)	13% (9%)	65% (65%)
EqP summer	5% (5%)	6% (6%)	35% (35%)
EqP winter	3% (3%)	4% (4%)	35% (35%)

difference is a factor of 2 larger for the day data, while for the night it is only 5% larger. However, when the whole range of measured spectra is considered, the night data also shows a thermal emission variability of a factor of two larger at shorter than at longer wavelengths. The flux variability due to day and night at longer wavelengths is very similar for the summer and winter seasons, deviating only by 3% - 4% in windows 1 and 2, resulting in a change of effective temperature of 7K - 8K. Yet, the diurnal cycle has a larger impact on fluxes measured at shorter wavelengths where the flux readings vary by a factor of 4.5 and 5.5 for summer and winter, respectively, compared to the longer wavelength regime. A contributing cause to the increased variability in the day is the reflected light component of the radiation in window 3 which is larger for the continental areas vs. the ocean-dominated areas.

The second equatorial viewing geometry studied in this work is a **Pacific-centered, ocean-dominated, equatorial view (EqP)** and comprises the same climate zones as EqA. However, due to the lack of landmass near the equator, the equatorial climate zone is not as prominent and extended as in the Africa-centered view, making the tropical and sub-tropical climate zones the dominating climates for that particular Earth view. Furthermore, EqP shows the largest ocean-mass fraction from all the observing geometries, hence, it is expected to show the least variability in thermal emission because of the large thermal inertia of oceans. The sub-arctic and arctic climate zones as well as the majority of the visible landmass are located close to the edge, where the fluxes are affected by the limb-darkening effect. The largest contribution from a landmass is coming from the Australian continent. EqP's seasonal thermal emission variability between an average summer day and an average winter night is around 11% for the longer wavelengths and 45% in window 3. Comparing these values to EqA, which includes the same climate zones but has a different landmass fraction, the variability is a factor of 2 and more less in all three windows and even a factor of 3 less when it is compared to the NP viewing geometry. In terms of seasonal variability EqP is similar to the SP viewing geometry, showing that the dominant factor in keeping the thermal emission variability low is the high thermal inertia of the oceans. Moreover, if Earth was observed in the EqP perspective there is no benefit whether the planet is observed during day or night time or in which season since the thermal emission flux increase is negligibly small (between 3% - 7%) at longer wavelengths. At shorter wavelengths, there is 35% more flux in window 3, independent of the summer or winter seasons.

3.3.2 Earth's Degeneracy in Thermal Emission Spectra

When we observe exoplanets, we will not have prior knowledge of when or from which direction we are attempting to characterize it. We simulated this uncertainty by viewing Earth randomly and found strong spectral degeneracy with respect to viewing geometry. This degeneracy arises due to variable blending of time-variable thermal emission from hemispheres with opposing seasonal signals in disk-integrated views. This complexity complicates remote characterization of planetary environments. Specifically the interpretation of the spectrum is not unique and a plethora of solutions exist to describe the planet's surface and atmospheric characteristics which, in the context of exoplanets, imposes another challenge especially for planets whose orbital elements and obliquity are not well constraint.

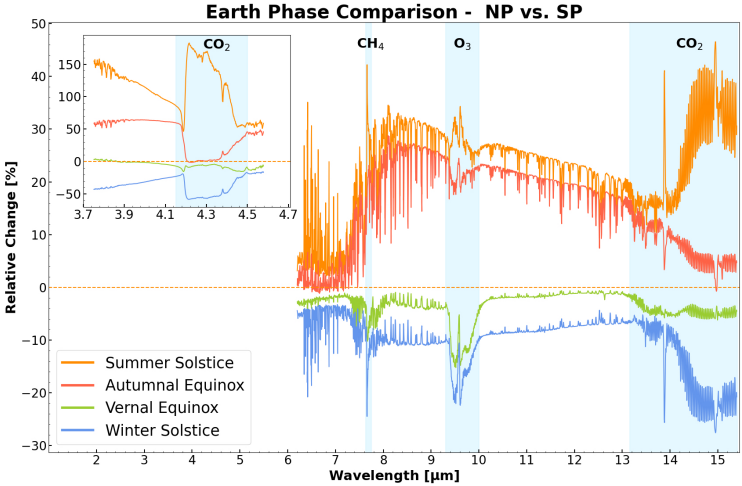

Figure 3.5: Comparing the spectra of the northern to the southern hemisphere at the solstices and equinoxes that occur in June and December and March and September, respectively. The figure shows the relative change of flux, on the y-axis, as a function of wavelength. For this analysis, monthly averaged spectra for these months were calculated.

Three out of the four observing geometries that we have studied for Earth in this work cannot be distinguished from each other with single-epoch observations. The large annual variability of the northern hemisphere NP viewing geometry covers the flux range of EqP and SP and is exceeding lower flux readings than the southern hemisphere view SP for an average winter. Differentiating between

the two hemispheres is especially challenging during March (vernal equinox) where the spectra of NP and SP overlap in all three spectral windows. The same is the case in November with overlapping spectra in the longer wavelength range windows 1 and 2. However, at shorter wavelengths, especially between 3.75 - 4.1 OH, there is a gap of ~ 40% flux difference between SP to NP indicating the different seasons the hemispheres are in at that moment of the orbit as well as including the flux difference of day versus night side. In general the northern hemisphere pole-on view emits 20-30% more flux at longer wavelengths (windows 1 and 2) and between 50-150% at shorter wavelengths (window 1) during summer solstice and autumnal equinox than the southern pole-on view SP (see Figure 3.5). During winter solstice, summer on the southern hemisphere, SP emits ~ 10% more flux at the longer wavelengths and 20 - 40% at shorter wavelengths than the northern hemisphere NP view. The increased variability in flux at shorter wavelengths in the day is due to a contributing factor of a reflected light component.

Moreover, over the course of a year, NP reaches similar flux readings at longer wavelength ranges as the Pacific-centered view EqP in May and September (autumnal equinox). Although, there is a gap at shorter wavelengths between the two May spectra, during autumnal equinox, it is hard to differentiate between a pole-on northern view to an ocean dominated equatorial view. The southern hemisphere SP and EqP show a similar annual variability at longer wavelengths. Differentiating between these two observing geometries is particularly difficult for a quarter of the year as their spectra overlap between December through February where the southern hemisphere's summer is entering the lower flux range of the equatorial winter. At shorter wavelengths, the spectra of SP only overlaps with EqP at the peak of its summer in December.

Although the Africa-centered observing geometry EqA shows the second largest annual variability, the flux level range in atmospheric windows 1 and 2 remains well separated from other viewing geometries and is therefore the only viewing geometry whose range is not intersecting with others. At shorter wavelengths, however, spectra from July for the NP viewing geometry reach flux levels equivalent to EqA's spectra during winter time.

Hence without sufficient knowledge about a planet's orbital parameters and obliquity, interpreting the space and time averaged data based on single-epoch measurements is quite challenging – even for Earth. Therefore multi-epoch

measurements and the resulting time-dependent signals may be required to help breaking the degeneracy in the thermal emission spectra. As previous work has shown, different surface types have different photometric and thermal properties and by adding the time factor, i.e. variability, additional information can be gained for assessing a planet's characteristics and habitability (e.g. Tinetti et al., 2006b; Gómez-Leal et al., 2012; Madden and Kaltenegger, 2020; Mettler et al., 2020; Lehmer et al., 2021).

3.3.3 Observing Earth from an Equatorial Viewing Perspective

In this section, we are focusing on the equatorial viewing geometry and study Earth's thermal emission spectrum as a function of seasons and phase angles, i.e. different contributions of the day- and nightside from the planet, at four specific points in time of Earth's orbit: summer and winter solstice and vernal and autumnal equinox, as shown in the top panel of Figure 3.3. The solstices and equinoxes occur in June and December and March and September, respectively.

For the analysis, we calculate the monthly mean spectra averaged over four years of the afore mentioned months. Hence, we are considering integration times much longer than Earth's rotation period and combine therefore the two equatorial views, EqA and EqP, and denote the resulting dataset EqC. The day and night spectra of the new dataset and how it compares to the polar views is shown in Figure 3.11 in the appendix.

In order to compose the full- and new-Earth phases, day and night equatorial datasets have been used, respectively, while for the half-Earth waxing and waning phase, 50% day and 50% night data of the corresponding months was used. Figure 3.6 shows the comparison of the relative change of flux between the day- versus nightside spectrum at given location on Earth's orbit.

In the wavelength region between 8 - 9 μm and 10 - 11 μm the flux levels from the dayside is between 9 - 12% and 8 - 10% larger, respectively. The day- versus nightside difference varies by ~2.5% for the seasons and these band regions, where the largest relative change is shown during summer followed by autumn, spring and winter in descending order. The order, however, rearranges in wavelength regions with absorption features. At the band centers of CO_2 and O_3 for example, the difference between day- and nightside at winter solstice shows the second largest relative change. At the center of the 15 μm CO_2 feature, Earth emits ~2.5%

and ~4.5% more flux from the fully illuminated disk for winter and summer solstice, respectively, which is 5 to 11 times more than at the autumnal and vernal equinoxes. Similarly to the 15 micron feature, the CO_2 feature centered at 4.3 μm shows the same behaviour except that the difference in emission due to day- and nightside is as large as ~70 - 85%. In general, at shorter wavelengths, 3.7 - 4.6 μm, the difference between fully illuminated and dark disk is the strongest, reaching levels of above 100%, indicating a significant contribution from reflected light.

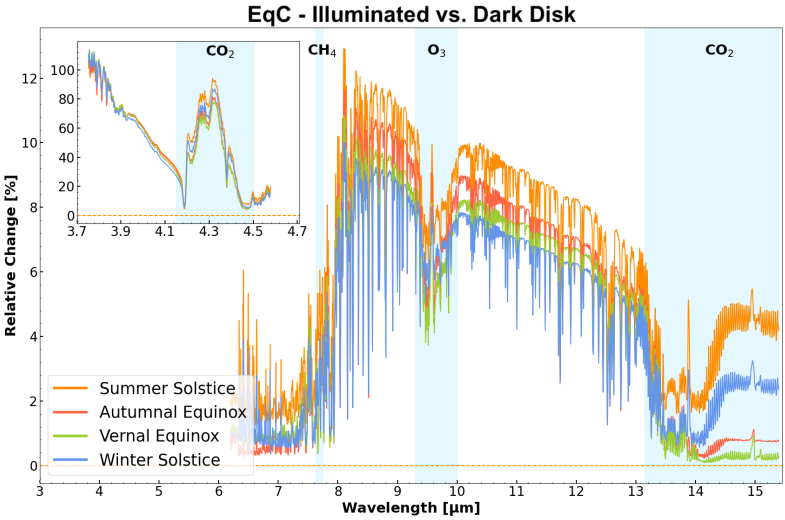

Figure 3.6: Comparing the day versus night side (illuminated vs. dark disk) at different times on Earth's orbit for the combined equatorial view EqC.

The results of the analysis of Earth's thermal emission spectrum as a function of seasons and phase angles are shown in Figure 3.7. Each panel corresponds to a constant equatorial viewing geometry as seen by a remote observer. An example is illustrated in Figure 3.3. The observation direction is indicated by Earth's position during the secondary eclipse in the top right corner of the panels. Keeping the observation direction constant, the panel compares how Earth's spectral appearance changes along one full orbit. Specifically, the relative change in flux is calculated between the target position and winter solstice in order to compare the thermal emission spectra of the different positions on Earth's orbit to each other at increments of a quarter orbit.

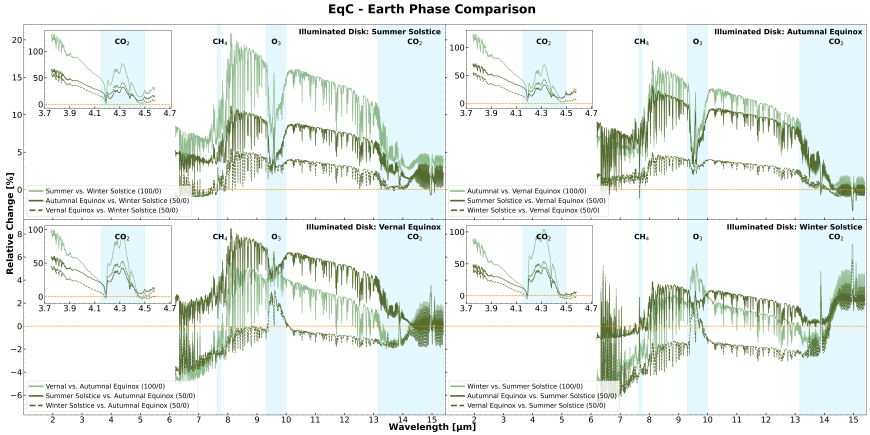

Figure 3.7: Comparing how Earth's spectral appearance changes along one full orbit, given a constant equatorial viewing geometry. Each panel corresponds to a viewing geometry for a remote observer as shown in Figure 3.3 with the relative change in flux on the y- and the wavelength range on the x-axis. The colours as well as the percentages given in the brackets indicate the current phase type of the target position, where 100, 50 and 0 corresponds to illuminated-, partially illuminated-, and dark-disk, respectively. Earth's position during the secondary eclipse for that specific viewing geometry is given in the top right.

Note that our analysis correspond to ideal conditions in comparison to what actual observations would be. Scenarios where the planet is behind or in front of its star are not readily observable.

Depending on the observation direction, Earth's phase at winter solstice changes. Thus, for example, the top left panel in Figure 3.7 corresponds to what a remote observer looking at the Earth-Sun system as shown in Figure 3.3 from the right-hand side would measure. During summer solstice Earth's disk is fully illuminated and partially illuminated at the vernal and autumnal equinox. At winter solstice, Earth is in its new-Earth phase. In this perspective, for a remote observer the largest contrast in relative change in flux would be when the Earth was observed during winter- and half an orbit later during summer solstice, where Earth emits 11 - 19% more flux between 8 - 13 µm. The window region between 8 - 12 µm is especially important since it offers the best chance to estimate a planet's surface temperature (e.g., Des Marais et al., 2002). For the same window region, the difference in flux between spring time (vernal equinox) and winter solstice lies between ~2.5 - 5% and between 6 - 10% during autumnal equinox. Hence, from

the four panels in Figure 3.7 it is apparent that remote observers detecting Earth in an equatorial viewing geometry, where the primary eclipse occurs at winter solstice and secondary eclipse around summer solstice (from the right hand side in Figure 3.3) have the most favourable viewing angle and phase configurations for characterizing seasonal differences in the flux of Earth.

The second best equatorial viewing geometry for detecting our planet's seasonal changes in flux is for observers looking from a direction where Earth's secondary eclipse would occur around autumnal equinox. In the window region between 8 - 12 μm, the fully illuminated disk around autumnal equinox emits still between 10 - 16% more flux than at vernal equinox where Earth's nightside is facing the observer. Furthermore, although being in the half-Earth waxing phase, around summer solstice Earth emits ~2% less flux than the fully illuminated disk due to the hotter temperature and the rather large landmass of the African continent. The relative change in flux of the winter solstice versus vernal equinox is up to ≈ 5%, which is similar as to the top left panel of Figure 3.7 described above. This is mainly due to similar temperatures and the large ocean fraction in the equatorial viewing geometry for Earth which is rather resistant to temperature changes.

For an observing geometry where the Earth's disk is fully illuminated around winter solstice (from the left hand side in Figure 3.3), Earth's nightside is facing the observer during summer solstice. Compared to the vernal equinox waning phase, Earth's nightside emits ~2% more flux between 8 - 12 μm except in the ozone absorption feature. Comparing Earth's emission from the autumnal equinox and winter solstice to the summer solstice nightside, they emit between ~1 - 3.5% more flux. Hence, for such a viewing geometry, determining whether the planet has a non-zero obliquity and, thus, seasons would be very challenging.

3.3.4 Observable Seasonality on Earth

The change in insolation, due to Earth's axial tilt, causes the photometric and spectroscopic appearance of our planet to change on hourly, seasonally and annually time scales. The inhomogeneous distribution of net radiation imbalances drive the global circulations of the atmosphere as well as oceans, and although Earth's eccentricity is nearly circular, there is evidence of greater irradiance in the southern summer than the northern latitudes in the northern summer. Winds and weather patterns adjust to transport heat from higher irradiated regions

to lower ones, introducing climatic variability. While the change in insolation impacts photochemical processes at higher altitudes, affecting the atmospheric composition as well as its vertical temperature structure, the biosphere modulates the seasonal atmospheric composition. Net fluxes of methane and other trace biological products evolve seasonally, responding to temperature induced changes in biological rates, gas solubility, precipitation patterns, density stratification, and nutrient recycling (e.g.: Khalil and Rasmussen, 1983; Olson et al., 2018b). Thus, these temporal modulations can take the form of oscillations in gas concentrations or surface spectral albedo.

Since atmospheric seasonality arises naturally on Earth, it is very likely to occur on other non-zero obliquity and eccentricity planets, and if they are inhabited, life may modulate the seasonal variations in atmospheric composition as well (e.g., Olson et al., 2018b). However, these time-dependent modulations, of physical or biogenic origin, must be present and observable in the disk averaged spectra of those planets if we hope to leverage these signals to recognize exoplanet life. As discussed in the literature (e.g., Ford et al., 2001; Hearty et al., 2009; Gómez-Leal et al., 2012; Schwieterman et al., 2018) as well as in sections 3.3.1 - 3.3.3 in this work, there is a strong seasonal and viewing geometry dependency, posing observational challenges to detect seasonal signals that are driven by obliquity in addition to the current technical limitations of detecting and characterizing terrestrial habitable zone planets. Seasonal contrast increases with obliquity and the effect of obliquity is the strongest near the poles. Yet, observing in a near pole-on view will probe only one hemisphere, while an equatorial view includes variabilities of both visible hemispheres if hemispherical asymmetries, for example in landmass distribution, exist that generate the obliquity driven seasonality. Depending on the landmass fraction and distribution as well as orbital and viewing geometry configurations, the observed magnitude of seasonality will be muted. This relationship arises due to latitude averaging, including contributions from opposing seasons in each hemisphere, in disk-integrated spectra.

In this section, we leverage the temporal and spectral coverage of our dataset in order to quantify the time-varying signal of Earth's observable biosignatures like methane, ozone and nitrous oxide in the MIR and address the question whether the variability is detectable to a remote observer. In addition, we investigate the seasonality of carbon dioxide due to its role in climate regulation and biological activity such as photosynthesis for example.

Calculating Equivalent Widths

For the quantitative analysis we calculate the equivalent width (EW), a measure of strength of an absorption feature, which is defined by

$$W_\lambda = \int (1 - \frac{I_{CRS}}{I_c})\, d\lambda \tag{3.3}$$

where W_λ is the equivalent width and I_{CRS} and I_c the radiance from the continuum removed spectrum and continuum, respectively. In order to calculate the equivalent widths, for each disk-integrated spectrum, we calculated a continuum removed spectrum (CRS) by applying a convex hull technique where we have subtracted the difference between the hull and the original spectrum from a constant. Thus, absorption features within a CRS are always between zero and one and can be easily identified by the points where the spectrum is touched by its convex hull, giving the full depth of the feature. In order to isolate the molecular absorption features of O_3, CH_4, CO_2 and N_2O, we have adopted the spectral band centers and intervals from Catling et al. (2018) and evaluated the normalized radiances at these fixed bandwidth ranges. While the full feature depth of O_3 centered at 9,6 µm and CO_2 centered at 4.3 µm can be inferred directly, the molecular absorption features of N_2O and CH_4 in the MIR at 4.5 µm and 7.7 µm, respectively, lie within an H_2O feature with the center at 6.3 µm. To exclude additional variation induced by the H_2O feature in the isolated features of N_2O and CH_4, we have defined the shoulder points to be at the limits of their bandwidths. Figure 3.8 displays an example of the four isolated absorption features with the normalized radiances on the y-axis and wavelength range on the x-axis. The convex hull or the baseline is shown in red.

Physical Conditions that Affect Equivalent Widths

Besides chemistry, the dominant mode of interaction between molecules and mid-infrared radiation in the troposphere and stratosphere is absorption. Infrared absorbing molecules absorb at a wide range of wavelengths corresponding to transitions between different forms of energy levels (rotational and vibrational). The corresponding cross-sections vary by many orders of magnitude, depending on the nature of the molecule and the transition. Most of the absorption features

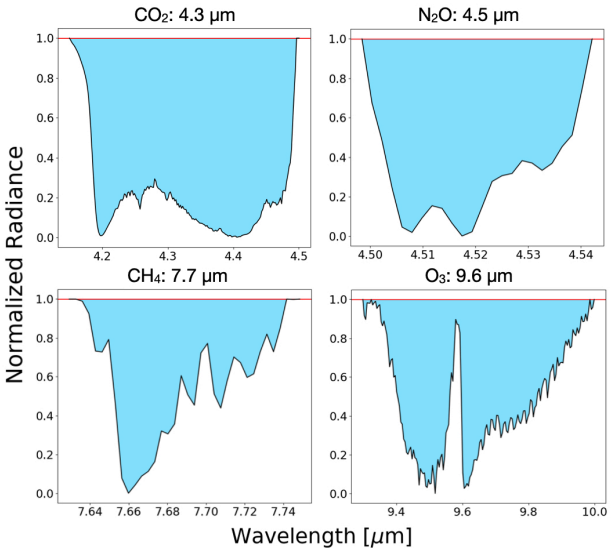

Figure 3.8: The four isolated absorption features of CO_2 (4.3 µm), N_2O (4.5 µm), CH_4 (7.7 µm), and O_3 (9.6 µm) with the normalized radiance and the wavelength on the y- and x-axis, respectively. In order to isolate these spectral features, we have applied a hull difference continuum removal technique, where a convex hull was fitted over the spectrum to define the continuum. The hull difference is obtained by subtracting the difference between the hull and the original input spectrum from a constant. The equivalent widths were then calculated according to equation 3.3. The band widths of the molecular absorption features are 350 nm, 40 nm, 120 nm and 700 nm for CO_2, N_2O, CH_4 and O_3, respectively.

found in the MIR spectrum are vibration–rotation bands, for which the band center is determined by a vibrational transition, with simultaneous rotational transitions forming branches of discrete lines on either side of the center (e.g., Goody and Hu, 2003). Line and band strengths, and thus the equivalent width, are proportional to molecular number density, absorption coefficient per molecule, optical path, and lower state population which is governed by Boltzmann's law and can be highly temperature dependent. While line absorptions saturate with increasing path length, continua, e.g. the water vapor continuum, behave differently and do not saturate. Their relative importance increases at long absorption paths.

Physical conditions in planetary atmospheres can lead to different types and degree of line broadening that can affect equivalent widths. For Earth and the observational data presented in this work, relevant line broadening mechanisms

are pressure (collisional) broadening and thermal (Doppler) broadening. The former is the dominant broadening mechanism in the lower atmosphere (troposphere) and is due to collisions between chemical species with the collision frequency being a strong function of pressure. The thermal broadening is caused by the line-of-sight thermal velocity distribution of molecules at a given temperature in the planetary atmosphere (e.g., Hedges and Madhusudhan, 2016). This type of broadening becomes the dominant mechanism above the Tropopause at ≈ 10 mbar / 30 Km (e.g., Goody and Hu, 2003). Furthermore, water vapor is a very efficient agent to broaden spectral lines of CO_2, N_2O, CH_4 and other gases. The broadening by water vapor is much larger than that of nitrogen and oxygen which are the two main contributors to dry air broadening (e.g., Tan et al., 2019). The amount of water vapor in the terrestrial atmosphere is highly variable both spatially and temporally and can account for up to 5% of the atmosphere in the tropics. Thus, the broadening due to the presence of water vapor as well as the temporal variability in its abundance affects the equivalent width measurement and induce additional variability to the atmospheric seasonality of the molecular absorption features studied in section 3.3.4.

The equivalent width measurements are also affected by non-local thermodynamic equilibrium effects (nLTE) that have a large emission contribution at the core of a spectral band. nLTE emission occurs generally above the stratopause, where solar pumping populates the vibration-rotation energy levels more quickly than collisions can thermally redistribute the energy (e.g., DeSouza-Machado et al., 2007). While nLTE emission is negligible at 15 micron, all stratospheric as well as many of upper atmosphere bands like the 4.3 micron spectral region are impacted.

In addition, changes in the atmospheric temperature structure also affect the equivalent width measurements. The observed emission peaks (e.g., shown in Figures 3.4 and 3.8) at 9.6 μm and 15 μm are caused by layers that are warmer than the top of the troposphere. Because of the high emissivities corresponding to these wavelengths, the radiation escapes into the stratosphere and is emitted only when the partial pressure of CO_2 at 15 microns or O_3 at 9.6 microns is sufficiently low to no longer absorb at these wavelengths. Since the stratosphere gets warmer with increasing altitude, the emission originates from a warmer layer than the top of the troposphere. Thus, changes in the atmospheric temperature structure alters the emission peaks and therefore affects the equivalent width of the absorption feature.

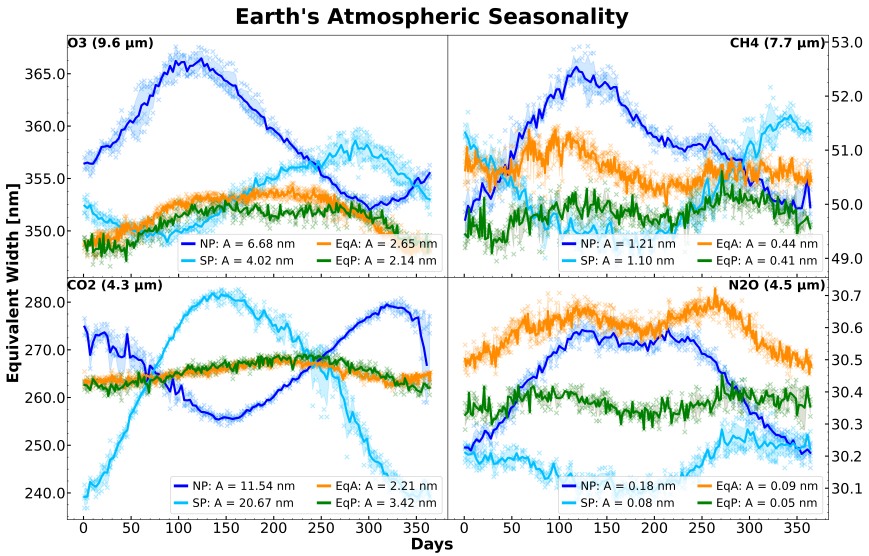

Figure 3.9: Atmospheric seasonality: Four year average of the time-varying equivalent width signal for the different viewing geometries and bio-indicators. The equivalent widths in nanometers and the days are given on the y- and x-axis, respectively. Day zero represents January 1st. The solid lines and shaded areas represent the four year average and one standard deviation of all equivalent width measurements which are shown as a scatter plot. The two polar views show the largest amplitudes and the variation of the northern hemisphere is opposite to the southern one. The signal from the equatorial views are also detectable in the disk-integrated data. However, the amplitude is one to two orders of magnitudes smaller depending on the molecular absorption feature. The full, non averaged seasonality plots for the individual viewing geometries are attached in the appendix 3.12a - 3.12d.

Analysing the Time Series of Equivalent Widths

Figure 3.9 displays the four year average of the annual change in equivalent widths for each viewing geometry and bio-indicator. Day zero represents January 1st. The four molecular absorption features investigated in this work show an annual variation in strength. As expected, the largest amplitudes are shown by the two polar views, NP and SP. Furthermore, the variation time series of the northern hemisphere is opposite to the southern one due to the seasonal cycle of solar insolation. The results are summarized in Table 3.3 and the seasonality plots for the individual viewing geometries are attached in the appendix 3.12a - 3.12d.

Ozone (O_3) reaches peak concentrations of up to 10 ppm in the stratosphere between 15 - 30 km in altitude on Earth and is the result of photochemical reactions that split oxygen (e.g., Grenfell et al., 2007, Figure 1). Yet, the abundance as well as the altitude of the peak vary spatially throughout the year and hemispheres. Since the feature at 9.6 µm is highly saturated, its strength is expected to essentially remain unchanged. From Table 3.3, we deduce the global annual mean EW for O_3 which deviates by 1.03% for the different observing geometries. While the equatorial regions deviate by 0.15% (σ= 0.72 nm) from their mean, the largest difference contribution to the global mean can be assigned to the polar regions whose mean equivalent widths differ by 1.05% (σ = 3.76 nm). The latter also show oscillations with amplitudes of 6.68 nm and 4.02 nm for NP and SP, respectively, which are a factor of ~ 2 - 3 larger than for the equatorial views (EqA: 2.65 nm and EqP: 2.14 nm). The amplitudinal difference for the atmospheric seasonality of ozone results in a 40% difference between the two hemispheres in favour of NP, while the Africa-centered equatorial view shows a 19% larger seasonality in the strength of the O_3 feature than the ocean dominated view EqP. Comparing their seasonal range to the annual mean equivalent widths of the ozone absorption feature results in an annual change in strength, or seasonal variation, of 3.72% and 2.27% for NP and SP and 1.51% and 1.22% for EqA and EqP, respectively.

Although, the band strength in the IR is rather sensitive to the temperature differences between the lower and middle atmosphere, the ozone spectral feature can be weakened by clouds (e.g., Kitzmann et al., 2011). Cross checking with level 3 satellite data (*AIRS3STD* (AIRS Science Team/Joao Teixeira , 2013)), Figure 3.10 panel e) shows that the O_3 abundance trend follows the oscillations shown in the first panel of Figure 3.9 for all the viewing geometries. Even though this might suggest that the EW oscillation is mainly due to variations in O_3 abundance, we cannot exclude contributions from changes in the stratospheric temperature and variability in patchy cloud coverage that decrease the emitted continuum flux and reduce the relative depths of spectral features (e.g., Des Marais et al., 2002).

Methane (CH_4) is the 7th most abundant atmospheric constituent in modern Earth's atmosphere with a surface concentration of 1.87 ppm (Canadell et al., 2021). Roughly 90% of the net surface source is associated to the respiration of methanogenic microbes. Its presence in the atmosphere in combination with CO_2 alongside the absence or low abundance of carbon monoxide (CO) is a particularly compelling biosignature since the combination of the two represents carbon in its most reduced and most oxidized forms which is hard to explain with-

out life (Krissansen-Totton et al., 2018). Also methane's co-existence with ozone is possibly the strongest biosignature. Several sinks exist for methane, yet the most dominant one involves the oxidation of CH_4 with the hydroxyl (OH) or chlorine (Cl) radicals (e.g., Grenfell et al., 2007, Figure 4). Secondary sinks include, for example, photolysis and dry deposition (Grenfell, 2018; Schwieterman et al., 2018). Although, in terrestrial exoplanet atmospheres, CH_4 has a short photochemical lifetime and requires substantial replenishment fluxes in order to accumulate detectable abundances, atmospheric CH_4 on Earth is rather unreactive in the troposphere, residing there for 9.1 ± 0.9 years. Due to its relatively long lifetime compared to the length of the seasonal cycle, its sources being predominantly located near the surface, and the vertical atmospheric transport evening out regional methane differences, CH_4 is considered a well-mixed gas in the troposphere. Yet, satellite measurements also detected methane at stratospheric levels, indicating that winds transport plumes of gas considerable distances from their sources.

Table 3.3: Atmospheric seasonality for the different viewing geometries and molecular absorption features. Besides the annual mean equivalent width and the range of the oscillation, the table states the seasonal variation in the last column where the relative change of the range is compared to the annual mean equivalent width.

Viewing Geometry	Mol. Absorption Feature	Annual mean EW [nm]	Seasonal Range [nm]	Seasonal Variation [%]
NP	O_3	358.88	13.36	3.72
	CH_4	51.10	2.42	4.74
	CO_2	266.90	23.08	8.64
	N_2O	30.44	0.36	1.18
SP	O_3	353.59	8.04	2.27
	CH_4	50.21	2.20	4.38
	CO_2	262.36	41.34	15.76
	N_2O	30.17	0.16	0.53
EqA	O_3	351.59	5.30	1.51
	CH_4	50.65	0.88	1.74
	CO_2	265.22	4.42	1.67
	N_2O	30.59	0.18	0.58
EqP	O_3	350.84	4.28	1.22
	CH_4	49.84	0.82	1.64
	CO_2	265.36	6.84	2.58
	N_2O	30.37	0.10	0.32

The annual strength of the CH_4 absorption feature deviates by 1.08% for the different viewing geometries. The amplitudes of the atmospheric seasonality of methane for the two polar regions are three times larger than for the equatorial viewing geometries and their relative annual "growth" in EW is 4.74% and 4.38% for NP and SP, respectively. Comparing the two hemispheres to each other, the northern hemisphere pole-on view shows a 9% larger seasonality in CH_4 than SP. Between the two equatorial views, the Africa-centered view EqA, shows a 7% larger amplitude than the ocean dominated view EqP, leading to a relative annual growth in EW of 1.74% and 1.65% for EqA and EqP, respectively.

Inspecting the EW time series of NP and SP (see Figures 3.12a and 3.12b for a more detailed view), we can identify atmospheric processes that were outlined in section 2.2 Olson et al. (2018b). The seasonal CH_4 cycle observed for the southern hemisphere is primarily photochemical. Due to the enhanced evaporation during summer time, the increased concentration of tropospheric H_2O leads to a greater photochemical production of OH radicals that oxidize methane at an accelerated rate (see panels a) - d) in Figure 3.10). The opposite effect occurs during winter months, where the cold temperatures mute the destruction of CH_4. The seasonality of methane in the northern hemisphere, on the other hand, shows a biological cycle that is out of phase with the photochemical cycle, leading to a second peak in its time series (Khalil and Rasmussen, 1983). Hence, the observed temporal oscillation for methane in the top right panel of Figure 3.9 is dominantly controlled by the photochemical cycle. For the northern hemisphere the highest abundance of atmospheric methane occurs in late autumn and early spring and the minimum in summer and winter, where for the latter the annual minimum concentration is reached. Thus, the abundance of CH_4 in Earth's atmosphere is more strongly correlated with the surface temperature and the resulting evaporation of water as well as the solar zenith angle that controls the production of hydroxyl radicals than the instantaneous release from biogenic sources (Khalil and Rasmussen, 1983). The abiotic response of methane to the seasonality of tropospheric H_2O is particularly interesting as its oscillation indicates the presence of a large surface water reservoir in liquid state and in combination with its long lifetime against loss methane is a tracer of dynamical motions in the lower atmosphere.

Carbon Dioxide (CO_2) and its seasonal variation in atmospheric composition due to photosynthetic activity is possibly the most well-documented and mechanistically understood biologically modulated occurrence of all the key spectrally

active gases (e.g., Keeling, 1960). With the growth of vegetation mass in spring through summer, the rate of photosynthesis increases and the atmospheric abundance of CO_2 decreases as the carbon is fixed into organic matter. During autumn and winter the rate of photosynthesis, thus the consumption of CO_2, slows as plant matter decays, leading to a rise in its atmospheric concentration. Since the photosynthetic activity is the cause of seasonal fluctuation in CO_2, regions with a higher landmass fraction experience a larger magnitude due to the vegetative cover that drives the seasonal cycle. Both the northern hemisphere continents and the tropics include the majority of land plants. Yet, near the equator the seasonal variations in temperature are less pronounced than at higher latitudes

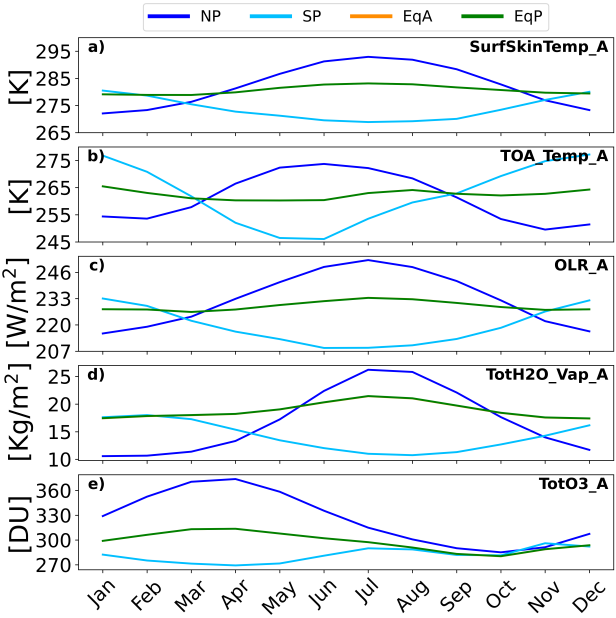

Figure 3.10: The panels a) - e) show four year monthly averages of the surface skin temperature, top of atmosphere (TOA) temperature, outgoing longwave radiation (OLR), total integrated column water vapor burden, and the total integrated column ozone burden, respectively. The data originate from level 3 Earth observation data (*AIRS3STD*) and was disk-averaged for the four viewing geometries for dayside only. *AIRS3STD* provides thermodynamic and trace gases parameters such as the skin temperature for land and sea surface which result from retrievals on the standard pressure levels roughly matching instrument vertical resolution. Due to small differences between the two equatorial views EqA and EqP, the data points (orange) of the former are not visible.

where the seasonal changes in temperature results in large seasonal CO_2 variations. Furthermore, photosynthesis also occurs in the oceans by plankton, algae and some cyanobacteria, however, the sea-air gas exchange flux of CO_2 is ~ 0.1% of the total natural contribution to the carbon dioxide budget (Canadell et al., 2021). Hence, for Earth, there is a latitudinal and hemispherical difference in the magnitude of the CO_2 fluctuation, where the northern hemisphere, due to its larger continental mass and larger seasonal temperature fluctuations, shows a greater amplitude, overall. The oscillation ranges from ~ 3 ppm near the equator to ~10-20 ppm at higher latitudes in the northern hemisphere (Keeling et al., 1996).

In order to analyse carbon dioxide's seasonal change in absorption strength, we have investigated the CO_2 absorption feature centered at 4.3 μm whose emission is originating from altitudes of up to ~ 10 Km. The global mean equivalent width for this CO_2 feature deviates by 0.71% for the four viewing geometries. In terms of amplitudes, however, they differ by 90% where the largest difference is due to the two hemispheres which show a seasonal range of 23.08 nm and 41.34 nm for NP and SP, respectively. Although the northern hemisphere shows a 1.7% larger annual mean EW than the southern hemisphere, unexpectedly, SP shows a 79% larger amplitude than the northern hemisphere view NP, resulting in a seasonal variation of 15.76%. SP's seasonal variation is therefore the largest one across the observing geometries and target molecules, followed by NP's variation of 8.65% for CO_2.

The annual mean EW of the two equatorial views differ by 0.14 nm, yet the pacific dominated observing geometry, EqP, shows a 1.5 times larger seasonal variation than the Africa-centered view EqA. A possible explanation could be due to the fact that the tropical oceans and the high latitude oceans, particularly the southern ocean, contribute the most to the global mean interannual variability. Observation based pCO_2 flux measurements show that emissions of natural CO_2 occur mostly in the tropics and high latitude southern oceans, whereas strong ocean CO_2 sink regions are found in the mid-latitudes associated with the cooling of poleward flowing subtropical surface waters as well as equatorward flowing sub-polar surface waters (e.g., DeVries et al., 2019; Canadell et al., 2021; Long et al., 2021). Comparing the two equatorial views, EqP contains a very prominent CO_2 outgassing region (also a global maxima) which extends from the north of South America along the equator to Indonesia (e.g., Figure 5.9 in Canadell et al., 2021) with a net air-sea flux of 3 times and higher the value of the corresponding

region at similar latitudes in EqA.

Furthermore, non-local thermodynamic equilibrium (nLTE) effects have a large contribution on the flux of the core of the 4.3 μm CO_2 band which might be impacting the seasonal measurements as well (e.g., DeSouza-Machado et al., 2007; López-Valverde et al., 2011).

Nitrous Oxide (N_2O) is a strong greenhouse gas primarily produced by Earth's biosphere as a by-product during the remineralization of organic matter via processes of nitrification and denitrification on land and ocean (e.g., Tian et al., 2020b). Its troposhperic abundance in modern Earth's atmosphere is 332.1 ± 0.4 ppb with a mean atmospheric lifetime of 116 ± 9 years on Earth. The dominant sinks of N_2O involve photolysis and oxidation by electronically excited oxygen atoms, $O(^1D)$, in the stratosphere (e.g., Grenfell et al., 2007, Figure 4), resulting in an annual loss of ~ 13.1 TgN yr^{-1} (Canadell et al., 2021, and references therein). It also contributes to the destruction of stratospheric ozone and its emission has currently the largest ozone depletion potential of all ozone depleting substances (Lessin et al., 2020).Variability in its atmospheric abundance is affected by the net N_2O sources on the ground and the photochemical destruction in the stratosphere. Yet, the production is highly sensitive to environmental conditions such as temperature, ph, oxygen concentrations, among many others, causing strong variability of N_2O emissions in time and space. Due to the fact that abiotic sources of N_2O are two orders of magnitude lower than the biological sources and its potential spectral detectability with several absorption lines across the MIR with significant bands centered at 3.7, 4.5, 7.8, 8.6, and 17 μm, nitrous oxide has been proposed as a strong biosignature (Sagan et al., 1993; Segura et al., 2005; Catling et al., 2018; Schwieterman et al., 2018; Canadell et al., 2021). For Earth's abundances of N_2O, however, most of these bands are weak and/or overlap with CO_2, H_2O and CH_4, requiring a high spectral resolution power to identify individual lines in order to differentiate from overlapping gas absorption features. Yet, in terms of exoplanets, studies show that these features can become more significant for planets in weak-UV environments where N_2O builds up (e.g., Segura et al., 2005; Grenfell et al., 2014; Rugheimer et al., 2015).

From the fourth panel of Figure 3.9, we deduce that the Africa-centered view, EqA, shows the highest mean equivalent width (30.59 nm) followed by NP (30.44 nm), EqP (30.37 nm) and SP (30.17 nm), in descending order. With a global equivalent width average of 30.39 nm, N_2O shows the least variation of all the

target molecules between the different observing geometries which is essentially due to its long photochemical lifetime and solubility. Its deviation is 0.57% (σ = 0.17 nm). Yet, the largest seasonal range is measured for NP (0.36 nm) which is a factor of 2 larger than the amplitudes of SP (0.16 nm) and EqA (0.18 nm) and a factor of 3 larger than the ocean dominated view EqP (0.10 nm). The resulting annual change in strength, compared to the annual mean EW, is 1.18%, 0.53%, 0.59%, 0.33% for NP, SP, EqA and EqP, respectively. Thus, the northern hemisphere pole-on view, NP, shows a seasonal variation of N_2O that is twice as large as the southern hemisphere pole-on view, SP, and the Africa-centered view, EqA, and a factor of 3.7 times larger than the ocean dominated view EqP. In terms of range, the two hemispheres differ by 56% and the two equatorial views by 44%.

The oscillations from observation geometries that include emission from the northern hemisphere (NP, EqA and EqP) show a complex structure containing two to three peaks in their seasonality (see Figures 3.12a and 3.12d in the appendix). It is particularly visible for the EqA observation geometry. Whether this is the effect of a biological cycle that is out of phase with the photochemical cycle in combination with the increased biological rate due to the warmer climate and higher temperatures during summer requires further research. Yet, according to the Intergovernmental Panel on Climate Change, IPCC, oceans contribute 21.2% to the N_2O emission to the atmosphere. For the northern hemisphere, the air-sea fluxes are the highest between late spring to summer, where there is a difference between the emission peak of near coastal and offshore water regions. The latter's emission peaks in late autumn. Hence, physical constraints regulate seasonal patterns of N_2O fluxes. The duration and intensity of water column stratification as well as biological productivity defines the timing, abundance, rate and vertical position of N_2O released to the atmosphere (Canadell et al., 2021; Lessin et al., 2020, and references therein).

3.4 Discussion

Rotational and seasonal variations of Earth's spectrum and their influence on the detectability of spectral signatures of habitability and biosignatures have been investigated before, both based on observational data and simulations as well as in the reflected light and thermal emission (e.g., Ford et al., 2001; Cowan et al., 2009; Hearty et al., 2009; Fujii et al., 2011; Livengood et al., 2011; Robinson, 2011; Gómez-Leal et al., 2012; Robinson et al., 2014; Jiang et al., 2018; Olson et al., 2018b;

Mettler et al., 2020).

We have adopted some aspects of the method for disk-integrating the data from previous studies that investigated Earth's emission in the MIR, e.g., Tinetti et al. (2006a) or Hearty et al. (2009). Yet, our dataset differs especially in terms of time baseline, temporal resolution and effective number of disk-integrated spectra based on satellite observation data. Both previously mentioned studies took advantage of Earth observation data collected by the AIRS instrument which they either used as input data for designing their model, like the former, or studied one day per month for one year / full orbit, as in the latter. Furthermore, the work by Gómez-Leal et al. (2012) presents a dataset of photometric time series with a resolution of 3 hours and a baseline of 22 years. Hence, providing a dataset with a greater baseline and better time resolution. However, for their study they derived the disk-integrated photometric signal of the Earth using top of atmosphere all-sky upward long-wave fluxes that are integrated over a 4-50 µm wavelength interval, thus, not providing spectral information. Therefore, our exclusive dataset comprising 2690 disk-integrated mid-infrared thermal emission spectra with a spectral resolution of 3.75 - 15.4 µm (R ~ 1200) derived from remote sensing observations for four full-disk observing geometries over four consecutive years (2016-2019) at high temporal resolution presented in this work is unique and allows us to study the time variable thermal emission and the atmospheric seasonality of Earth from afar in great detail.

Despite differences in the nature of datasets, results and trends associated to planetary obliquity as well as radiance levels for comparable regions are in agreement with these studies. In further agreement, at the investigated resolution of R≈1200, molecular lines for example of methane, carbon dioxide, ozone, water and nitrous oxide are detectable in the disk-integrated spectra, independent of viewing geometry, time of observation or cloud fraction. Furthermore, our results of disk-integrated spectra reflect the following two statements in Hearty et al. (2009): (1) the O_3 and CO_2 features can appear either in emission or absorption due to temperature inversions in Earth's atmosphere and (2) the 15 µm CO_2 feature is less sensitive to day-night difference than the 4.3 µm CO_2 absorption feature.

3.4.1 Complementarity of UV-O-NIR and MIR Observations

A detailed characterization of the planet's surface, atmosphere, and potential habitability would require the combination of reflected light and thermal emission observations. The MIR thermal emission spectrum of Earth from afar and its time variability contains a wealth of information about the atmospheric and surface environment. Observing in the MIR enables us to characterize the thermal structure of exoplanetary atmospheres and provides additional information on the molecular composition. In general, more molecules have strong absorption bands in the MIR and even at relatively low spectral resolutions, absorption features of key greenhouse gases and/or bio-indicators such as O_3, CH_4,CO_2, N_2O and H_2O can be detected (e.g., Christensen and Pearl, 1997; Hearty et al., 2009). Furthermore, compared to visible wavelengths, the infrared is less affected by the presence of hazes and clouds which is a major challenge for the former (e.g., Kitzmann et al., 2011; Fauchez et al., 2019). Moreover, pressure induced absorption features can indicate bulk atmospheric composition and pressure (e.g., Schwieterman et al., 2015). The observed flux in the MIR can be used for constraining the radius of a terrestrial exoplanet, which is much more difficult in the reflected light. With the planetary radius determined from infrared observations, broadband photometric observations can also constrain the planetary albedo which is necessary to comprehend the planetary energy balance (Pallé et al., 2003). Furthermore, broadband photometric and spectroscopic observations can reveal habitable environments as well as provide information about atmospheric and surface environments. For example, from reflected light observations a planetary colour could be used to identify exo-Earth candidates (Traub, 2003; Fujii et al., 2010), the effect of specular reflectance on a planetary phase curve could reveal surface oceans (Robinson et al., 2010), the vegetation "red edge" in the reflectance spectra would be a strong surface biosignature of land vegetation (e.g., Des Marais et al., 2002; Schwieterman et al., 2018), and the absorption features in the reflected light are suitable for abundance determination as they are not affected by the thermal structure of the atmosphere (e.g., Drossart et al., 1993; Livengood et al., 2011).

With regard to seasonality, however, observing in the MIR offers advantages over observing the reflected light of a planet. In this case, the MIR will not be as negatively impacted by the lack of illumination of the winter hemisphere over the course of the orbit (e.g., see Figure 5 in Olson et al., 2018b). Thus, combining the information from both, the reflected and thermal emission, observations could break some day-night degeneracies. In addition, more information could

be gained about tropospheric water transport and cloud variability from seasonal changes in depths of H_2O bands which could be helpful for retrievals in the MIR. Especially since it remains unclear how patchy clouds would influence our ability to retrieve and understand the atmosphere and surface of an Earth-twin from thermal emission observations.

3.4.2 Clouds and Their Influence on the Thermal Emission Spectra

Although we did not investigate and include additional information on cloud fraction and their thermodynamical phase properties in our study, roughly 67% of Earth is covered by clouds at all times (King et al., 2013). Hence, cloud seasonality and their effect on the MIR thermal emission and the detectability of spectral features, as for example shown in Des Marais et al. (2002); Tinetti et al. (2006a,b); Hearty et al. (2009), is imprinted in our derived spectra and, thus, part of our results.

Gas oscillations by Earth's modern biosphere vary in the order of 1-3% for O_2 and CH_4 (e.g., Schwieterman et al., 2018), indicating that our values of seasonal variations in equivalent widths for NP and SP of 2.37% and 2.19% for CH_4 and 4.32% and 7.88% for O_2 (at 4.3 µm) are affected most probably by varying cloud covers. This is supported by the fact that the origin layer of emission for the CH_4, O_2 and N_2O features studied in this work lie near the middle to upper troposphere, i.e., about 200-300 hPa in the tropics and 400-500 hPa in the polar regions for methane, 300-900 hPa for N_2O and 300-1000 hPa for CO_2 at the afore mentioned wavelengths (e.g., Goody and Hu, 2003, Figure 4). However, differences in the H_2O continuum are also impacting CH_4 and non-LTE effects are impacting CO_2.

Only the ozone feature centered at 9.6 µm lies well above the cloud covers as these wavelengths probe layers from the upper troposphere and lower to mid stratosphere at 10 to 30 - 50 Km in altitude. Although the trend of the annual seasonality in equivalent widths followed the trend of the abundance for O_3, we calculated a seasonal variation between 0.61-1.86% depending on the viewing geometry which differs to the seasonal variability in abundance whose amplitude varies by 10-15% (at 25-35 Km) in the total column value of ~10 ppm (e.g., Schneider et al., 2005). The ozone absorption feature is saturated (like the CO_2 feature at 15 µm), thus, it will not vary linearly with abundance and its measured

spectral variability may be smaller which could explain the difference. We plan to investigate in future studies how cloud fraction, cloud seasonality and their thermodynamical phase properties affect Earth's thermal emission spectra as well as the detection and the result of atmospheric seasonality.

3.4.3 Drivers of Seasonal Variability for Terrestrial Planets

The last 25 years of detection and characterization of exoplanets revealed a vast diversity of planets regarding their masses, sizes and orbits (e.g., Batalha, 2014; Burke et al., 2015; Paradise et al., 2021). It is expected that this diversity also extends to their obliquity and atmospheric mass and composition. Hence, terrestrial exoplanets could display seasonality that is very different from that of Earth or any other solar system planet. For example, the seasonal signal could be boosted if photochemical lifetimes were shorter and\or saturated bands were not saturated. Regarding the latter, there is a trade off between the abundance of a gas and its variability which is really key for potentially detecting seasonal changes. Eccentric planets may have better characterised seasonality as the competing effects of admixed hemispheres will not exist. With increasing orbital obliquity, the seasonal contrast increases as the ice and vegetation cover would vary. A moderately high obliquity promotes increased photosynthetic activity and associated oxygen flux to the atmosphere. In general, the biological activity will be increased in such a scenario leading to heightened variations in biosignature gases over more intense seasonal cycles, making life perhaps easier to detect (Barnett and Olson, 2022). Yet, as the detectability of seasonality depends on both the magnitude of the biogenic signal and the extent to which observation conditions mute that signal, the detectability of seasonality as a biosignature is likely optimized at intermediate obliquity that is sufficient to produce a large-magnitude signal but not so large as to preclude viewing of the winter hemisphere (Olson et al., 2018b).

3.4.4 Anthropogenic Contribution in the Data

Using data from Earth-orbiting satellites to study its thermal emission and, especially, the seasonality of its bio-indicators in order to apply it to exoplanets has some limitations due to the anthropogenic contribution. Specifically, the abundance of biosignatures like CH_4 or N_2O, which are both more powerful greenhouse gases than CO_2 with their high radiative forcing capabilities, are strongly

affected by human activities. For example, according to Canadell et al. (2021) the human contribution and perturbation of the natural nitrogen cycle through the use of synthetic fertilizers and manure, as well as nitrogen deposition resulting from land-based agriculture and fossil fuel burning has been the largest driver of the increase in atmospheric N_2O of 31.0 ± 0.5 ppb (10%) between 1980 and 2019. The average annual tropospheric growth rate in the most recent decade of 2010-2019, in which our consecutive year sample of 2016-2019 lies, was 0.85 ± 0.03 ppb yr^{-1}. The growth rate of methane and carbon dioxide was even larger in the same decade. Hence, the anthropogenic factor needs to be accounted for, for longer time baseline studies. In the case of our four year sample, a slightly increasing trend is visible for N_2O and CH_4 in the equivalent width plots, specifically, for NP, SP and EqP (see appendix figures 3.12a, 3.12b and 3.12d).

3.5 Summary and Conclusions

In this work, we presented our exclusive dataset comprising 2690 disk-integrated mid-infrared thermal emission spectra derived from remote sensing observations for four different viewing geometries at a high temporal resolution over a time baseline of four years. Using this dataset, we have investigated how Earth's MIR spectral appearance changes as a function of viewing geometry, seasons, and phase angles and quantified the atmospheric seasonality of different bio-indicators. We found a representative, disk-integrated thermal emission spectrum of Earth does not exist. Instead, both the thermal emission spectrum and the strength of biosignature absorption features show seasonal variability and depend strongly on viewing geometry.

Earth's appearance from afar is dominated on large scales by oceans, deserts, ice as well as vegetation and clouds. The contribution of these different surface types (and climate zones) to the latitudinally disk-integrated signal and the annual variability depends on their abundance fraction and distribution as well as on their thermal properties. Thus, landmass dominated Earth views did not only show higher flux readings but larger annual variabilities over one full orbit than ocean dominated views. Specifically, the northern hemisphere pole-on view (NP) and the Africa-centered equatorial view (EqA) showed annual variabilities of 33% and 22% at Earth's peak wavelength at ≈ 10.2 µm, respectively. On the other hand, viewing geometries with a high sea fraction such as the southern hemisphere pole-on (SP) and the Pacific-centered, equatorial view (EqP) show

smaller annual variabilities due to the large thermal inertia of oceans. In this specific case, both viewing geometries displayed a similar variability of ~11% at 10.2 microns, therefore, varying by a factor of three and two less compared to NP and EqA, respectively. Furthermore, concerning near pole-on observations which will probe only one hemisphere, we found that for Earth the annual variability of the two hemispheres differ by a factor of three across all the spectral windows evaluated in this study. Out of the four viewing geometries, the ocean dominated view EqP showed the least variability in terms of annual, seasonal and diurnal variations.

Due to the disk-integrated data and the annual variability of the thermal emission spectrum, the data shows a strong degeneracy. Differentiating between the two hemispheres is especially challenging during vernal equinox since the spectra of NP and SP overlap in all three spectral windows. Furthermore, the large annual variability of NP covers the flux ranges of EqP and SP, indicating the difficulties of uniquely interpreting and characterizing planetary characteristics from disk-integrated data. In the case of Earth, the only viewing geometry that remained separated flux wise from other Earth-views at Earth's peaking wavelength in the MIR, is the Africa-centered equatorial view EqA, despite, showing the second largest annual variability. Thus, without sufficient knowledge about a planet's orbital parameters and obliquity, even for Earth, interpreting the space and time averaged data based on single-epoch measurements is quite challenging. Hence, multi-epoch measurements and the resulting time-dependent signals may be required to help break the degeneracy in the thermal emission spectra in order to fully characterize a planetary environment.

We quantified the amplitudes and seasonal variation in absorption strength by calculating the equivalent widths of absorption features of biosignatures imprinted in the disk-integrated spectra. The detected variability is reduced for certain viewing geometries, i.e., from pole-on toward equatorial views. In general, the northern hemisphere pole-on observation geometry showed larger amplitudes of atmospheric seasonality for the investigated bio-indicators followed by SP and the two equatorial views. Except for carbon dioxide, whose seasonal variation was found to be the largest among all targets, where seasonal variations of 15.76% and 8.65% for SP and NP were derived, respectively. In Earth's modern biosphere, gas oscillations vary typically in the order of 1-3% for CO_2 and CH_4, thus, the seasonal variation in equivalent width is affected by varying cloud covers that induce additional variation plus potentially non-LTE effects for CO_2. This is further

supported by the fact that the layer of emission lies in the middle to upper troposphere. However, differences in the H_2O continuum are also impacting CH_4 and non-LTE effects are impacting CO_2. Future work is required to investigate how cloud fraction, cloud seasonality and their thermodynamical phase properties affect the detection and result of atmospheric seasonality.

Using Earth as our test bed, we learned that a planet and its characteristics cannot be described by a single thermal emission spectrum but multi-epoch measurements, preferably in both reflected light and thermal emission, are required. Its spectral appearance in terms of flux levels and strength of spectral features change continuously along the orbit due to processes driven by obliquity and eccentricity which impact nearly every constituent in the atmosphere and, if present, biosphere. Moreover, we found a strong spectral degeneracy with respect to viewing geometry due to variable blending of time-variable thermal emission from hemispheres with opposing seasonal signals in the disk-integrated views.

This complexity makes remote characterization of planetary environments very challenging. Yet, the degeneracy is in favour of MIR thermal emission observations since irrespective of when a planet would be observed the overall variation (in flux or absorption bands) is typically $\leq 10\%$ for a given viewing angle. Although disentangling these variations from the noise in future observations is non-trivial, we find that our result is relatively insensitive to diurnal or seasonal effects, unlike in the case for reflected light measurements. We therefore conclude that observing exoplanets with thermal emission could provide unique and complementary information that is necessary for the characterization of terrestrial planets around other stars.

Contribution

I was the main author and contributor of Chapter 3. I carried out the analyses, created the figures, and wrote the bulk part of the manuscript. Ravit Helled and Sascha P. Quanz guided the project. Stephanie L. Olson, Edward W. Schwieterman and an anonymous referee provided valuable comments. All co-authors discussed the results and commented on the manuscript.

Appendix

3.A Disk-Integrated Thermal Emission Spectra for NP, SP and EqC

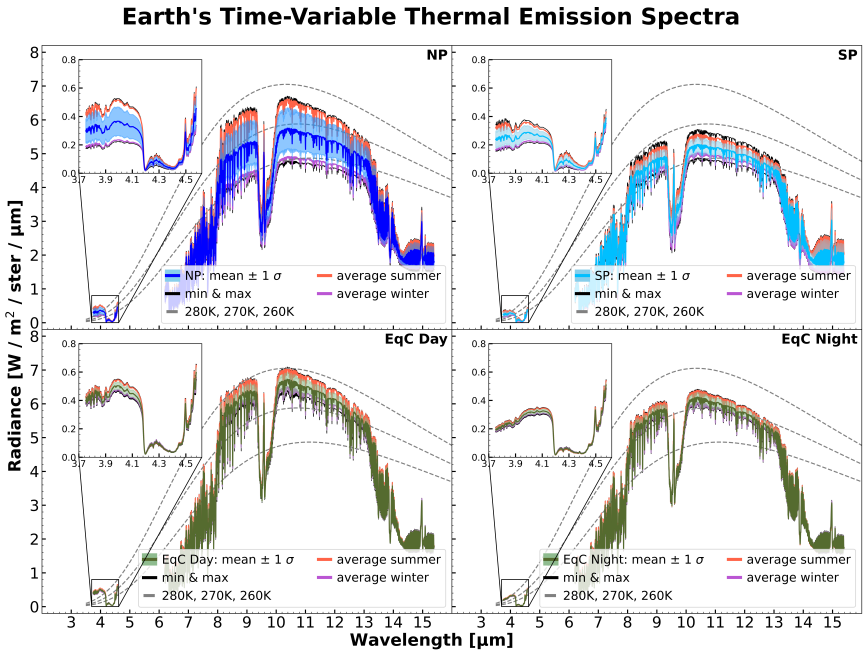

Figure 3.11: A comparison of the disk-integrated thermal emission spectrum for three different observing geometries (NP, SP, EqC). The mean represents the annual spectrum averaged over 4 years. The shaded area corresponds to the standard deviation of all measurements for that particular observing geometry. Summer and winter were defined as the months with the highest and lowest flux levels at 10 microns, respectively. For the northern hemisphere this turned out to be July and January and for the south pole vice versa.

3.B Atmospheric Seasonality Figures

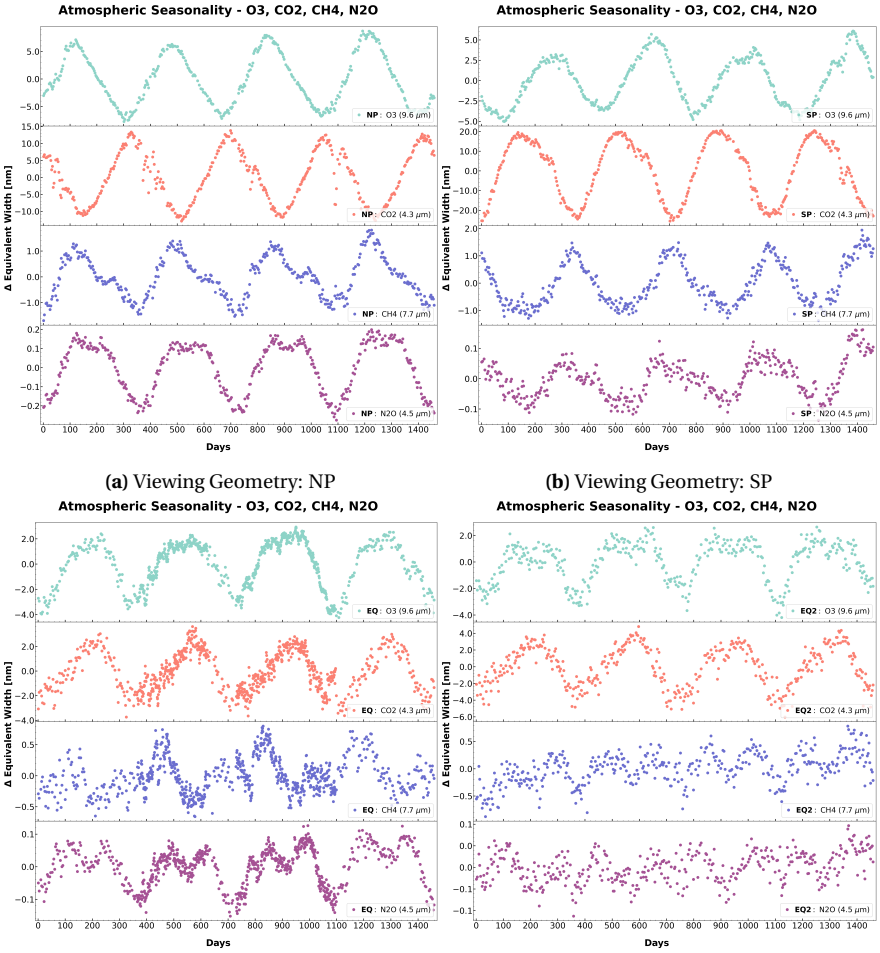

(a) Viewing Geometry: NP

(b) Viewing Geometry: SP

(c) Viewing Geometry: EqA

(d) Viewing Geometry: EqP

Figure 3.12: Figures 3.12a - 3.12d show the full temporal variations in abundance for each viewing geometry over four years.

4 Characterizing Our Home Planet Using the Large Interferometer for Exoplanets (LIFE)

Adapted from:
"Earth as an Exoplanet. III. Using Empirical Thermal Emission Spectra as Input for Atmospheric Retrieval of an Earth-Twin Exoplanet"

J.- N. Mettler, **B. S. Konrad**, S. P. Quanz, R. Helled

Submitted to The Astrophysical Journal

Abstract

In this study, we treat Earth as an exoplanet and investigate our home planet by means of a future mid-infrared (MIR) space mission concept called the Large Interferometer For Exoplanets (LIFE). We combine thermal spectra from a comprehensive empirical dataset of disk-integrated Earth observations with a noise model for LIFE to create mock observations. We then apply a state-of-the-art atmospheric retrieval framework to characterize the planet, assess the potential for detecting the known bioindicators, and investigate the impacts of variables such as viewing geometry, seasonality, and patchy clouds on the characterization. From these analyses we can conclude that: (1) we are observing a temperate habitable planet with significant abundances of CO_2, H_2O, O_3, and CH_4; (2) seasonal

variations in the surface and equilibrium temperature, as well as in the Bond albedo are detectable; (3) the viewing geometry and the spatially and temporally unresolved nature of our observations only have a minor impact on the characterization of an Earth-like planet; (4) Earth's variable H_2O profile and patchy cloud coverage lead to biased retrieval results for the atmospheric structure and trace gas abundances; (5) the limited extent of Earth's seasonal variations in biosignature abundances makes the direct detection of its biosphere through atmospheric seasonality unlikely. Our results suggest that LIFE would be able to correctly identify Earth as a planet where life could thrive, with detectable levels of bioindicators, a temperate climate, and surface conditions that allow for liquid surface water. Even if atmospheric seasonality is not easily observable, which complicates the direct detection of a biosphere and the quantification of biological fluxes, our study gives us confidence that next generation, optimized space missions can assess whether nearby temperate terrestrial exoplanets are habitable or even inhabited.

4.1 Introduction

The atmospheric characterization of terrestrial exoplanets in the habitable zone (HZ; Kasting et al., 1993; Kopparapu et al., 2013) and the search for life are key endeavors in exoplanet science (e.g., Astrobiology Strategy and Astro 2020 Decadal Survey in the United States: Hays et al., 2017; National Academies of Sciences, Engineering, and Medicine, 2021). Constraining the composition, structure, and dynamics of exoplanet atmospheres yields valuable insights into planetary habitability and could lead to the detection of life beyond our solar system.

Terrestrial HZ exoplanets are detectable with current observatories (see, e.g., Hill et al., 2023, for a catalogue). Exoplanet transit surveys such as the Kepler mission (Borucki et al., 2010) and the Transiting Exoplanet Survey Satellite (TESS; Ricker et al., 2015) as well as current long-term radial velocity (RV) surveys have revealed that HZ planets with Earth-like radii and masses are abundant in the galaxy (e.g., Bryson et al., 2021). Such exoplanets have already been detected within 20 pc of the sun with both the transit (e.g., Berta-Thompson et al., 2015; Gillon et al., 2017; Vanderspek et al., 2019) and the RV (e.g., Anglada-Escudé et al., 2016; Ribas et al., 2016; Zechmeister et al., 2019) methods. Ongoing observations with the James Webb Space Telescope (JWST) are revealing whether terrestrial HZ exoplanets transiting nearby M dwarfs have significant atmospheres (e.g., Koll et al., 2019;

Greene et al., 2023; Zieba et al., 2023; Lustig-Yaeger et al., 2023a; Ih et al., 2023; Lincowski et al., 2023; Madhusudhan et al., 2023; Lim et al., 2023). However, performing a detailed atmospheric characterization for such planets with JWST is challenging (e.g., Morley et al., 2017; Krissansen-Totton et al., 2018). Observations with the future 40 m ground-based extremely large telescopes (ELTs) will reach unprecedented spatial resolution and sensitivity. The ELTs will directly detect HZ exoplanets around the nearest stars via their thermal emission (e.g., Quanz et al., 2015; Bowens et al., 2021) and the reflected stellar light (e.g., Kasper et al., 2021). However, none of the current or approved future ground- or space-based instruments is capable of performing an in-depth atmosphere characterization for a statistically meaningful sample (dozens) of such exoplanets.

Therefore, the exoplanet community is working toward more capable observatories. LUVOIR (The LUVOIR Team, 2019) and HabEx (Gaudi et al., 2020) were designed to directly detect the stellar light reflected by terrestrial exoplanets at ultraviolet, optical, and near-infrared (UV/O/NIR) wavelengths. Following the evaluation of both concepts in the Astro 2020 Decadal Survey in the United States (National Academies of Sciences, Engineering, and Medicine, 2021), the space-based UV/O/NIR Habitable Worlds Observatory (HWO) was recommended. However, also the mid-infrared (MIR) thermal emission of exoplanets (and its time variability) contains a wealth of unique information about the planetary atmosphere and surface conditions (e.g., Des Marais et al., 2002; Hearty et al., 2009; Catling et al., 2018; Schwieterman et al., 2018; Mettler et al., 2020, 2023). The Large Interferometer For Exoplanets (LIFE), a space-based MIR nulling interferometer concept, aims to directly measure the MIR spectrum of terrestrial HZ exoplanets (Kammerer and Quanz, 2018a; Quanz et al., 2021b, 2022).

One key challenge in exoplanet characterization is the correct interpretation of their spectra. Measured exoplanet spectra are global averages (due to the large exoplanet-observer separation). Hence, local variations in the atmospheric composition, pressure-temperature (P–T) structure, and clouds are unresolved. Further, since signals from terrestrial exoplanets are faint, the temporal and spectral resolution of observations is limited. Such temporally and spatially unresolved observations can lead to degeneracies, making it hard to interpret the observations. Finally, the inference of planetary characteristics from such spectra is model-dependent (e.g., Paradise et al., 2021; Mettler et al., 2023). Without thorough exploration and validation of our characterization methods, it will not be possible to accurately infer the wide range of climate states expected for

habitable planets. Currently, in-situ data, which are necessary for the validation of our methods, can only be acquired for solar system objects. While the spectral libraries and the knowledge about the formation, composition, and atmospheric properties of solar system planets and their moons is continuously growing, Earth remains the most extensively studied planet and the sole known globally habitable planet harboring life. Therefore, Earth and its unique characteristics remain the key reference point to study the factors required for habitability and (the origin of) life (e.g., Meadows and Barnes, 2018; Robinson and Reinhard, 2018).

4.1.1 Disk-Integrated Earth Spectra Characteristics

From space, Earth's appearance is dominated by oceans, deserts, vegetation, ice, and clouds. Earth's surface is dominated by oceans (≈ 70% of surface), and the land-to-ocean ratio differs between the hemispheres (Northern Hemisphere ≈ 2/3, Southern Hemisphere ≈ 1/4; Pidwirny, 2006). The contribution of different surface types and climate zones to a disk-integrated Earth spectrum (and its seasonal variability) depends on their thermal properties, their fractional contributions, and positions on the observed hemisphere.

In general, in the thermal emission spectrum of Earth, land-dominated views show not only higher flux readings but also larger flux variations over one full orbit than ocean-dominated views (e.g., Hearty et al., 2009; Gómez-Leal et al., 2012; Mettler et al., 2023). Specifically, from Table 2 in Mettler et al. (2023), we see that at Earth's peak emission wavelength (≈ 10.2 µm) the disk-integrated Northern Hemisphere pole-on view (NP) and the Africa-centered equatorial view (EqA) show annual flux variations of 33% and 22%, respectively. In contrast, the ocean dominated Southern Hemisphere pole-on view (SP) and the Pacific-centered equatorial view (EqP), show smaller annual variations (≈ 11%) due to the large thermal inertia of oceans.

Another distinctive characteristic of Earth is its patchy cloud cover (see also Appendix 4.B). Earth's patchy cloud coverage is unique among the three terrestrial planets with significant atmospheres in the Solar System (Venus is completely covered in clouds; Mars has negligible cloud coverage). Using nearly a decade of satellite data, King et al. (2013) show that roughly 67% of Earth's surface is covered by clouds at all times. The cloud fraction over land is approximately 55% and shows a distinct seasonal cycle. Over oceans, cloudiness is significantly higher

(≈ 72%) and shows smaller seasonal variations. In addition, the cloud fraction is nearly identical during day and night, with only modest diurnal variation. Clouds are particularly abundant in the mid-latitudes (latitudes of ≈ ±60°), and infrequent at latitudes from ±15° to ±30° (often characterized by arid desert conditions). Thus, there are three bands with a high cloud fraction in Earth's atmosphere: a narrowband at the equator and two wider mid-latitude bands.

Atmospheric clouds can significantly impact both the reflected light and thermal emission spectrum of a planet and can reduce or eliminate spectral features (particularly in the UV/O/NIR; e.g., Des Marais et al., 2002; Lu, 2023). Parameters such as cloud fraction, composition, particle size, and altitude as well as multi-layered cloud coverage and cloud seasonality all affect the resulting spectrum significantly (e.g., Des Marais et al., 2002; Tinetti et al., 2006a,b; Hearty et al., 2009; Kitzmann et al., 2011; Rugheimer et al., 2013; Vasquez et al., 2013; Komacek et al., 2020). Konrad et al. (2023) ran retrievals on simulated MIR thermal emission spectra of a Venus-twin exoplanet. They showed that the presence of clouds can be inferred and requires a minimal spectral resolution of 50 and a signal-to-noise ratio of 20. Further, clouds inhibit the accurate retrieval of surface conditions. In addition, inadequate cloud treatment in retrievals (i.e., choosing too complex/simple cloud model given the quality of the input spectrum) can bias the estimates for important planetary parameters (e.g., planet radius, equilibrium temperature, and Bond albedo). However, despite recent efforts to understand how patchy clouds could alter the spectra of terrestrial exoplanets (e.g., May et al., 2021; Windsor et al., 2023), it remains unclear how they affect the characterization of terrestrial HZ exoplanets through MIR retrievals.

4.1.2 MIR Observables of Habitable and Inhabited Worlds

Habitability refers to the degree to which a global environment can support life, and depends on a myriad of factors (Meadows and Barnes, 2018). The characteristics of a planet and its atmosphere, the architecture of the planetary system, the host star, and the galactic environment all affect habitability (for an extensive list, see, e.g., Meadows and Barnes, 2018). For exoplanets, which can only be observed via remote sensing, we require observable characteristics to assess their habitability.

Analyzing MIR thermal emission spectra of exoplanets with atmospheric retrievals

(see, e.g., Section 4.3; Madhusudhan, 2018a) and/or climate models yields constraints on the planet's atmospheric structure and composition. Such constraints yield valuable insights into a planet's habitability and could be used to infer the presence of a biosphere. In the following, we list observable signatures of habitability and biospheres in ascending order of difficulty to observe:

- **Planetary energy budget:** A planet's effective temperature and Bond albedo can be calculated from its thermal emission spectrum.
- **Water and other molecules:** Important atmospheric species, such as water (H_2O), carbon dioxide (CO_2), or ozone (O_3), have strong spectral MIR features.
- **Atmospheric P–T structure:** The P–T structure can be constrained in retrievals and provides vital information about the atmospheric state.
- **Surface conditions:** If not fully obscured by clouds, thermal emission spectra contain information about a planet's surface temperature and pressure.
- **Molecular biosignatures:** Important biogenic gases, such as methane (CH_4) or nitrous oxide (N_2O), have MIR features. The presence of a biosphere can be inferred if abiotic sources can be ruled out.
- **Atmospheric seasonality:** Seasonal periodicities in molecular abundances that are attributable to life are small for Earth (Mettler et al., 2023) and thus challenging to detect in the MIR. However, they could be strong indicators for biological activity (Olson et al., 2018b).

For an in-depth review about evaluating planetary habitability and detectable signs of life, we refer to Schwieterman et al. (2018) and references therein.

4.1.3 Context and Goals of this Study

In a previous study (Mettler et al., 2020), we analyzed 15 years of thermal emission Earth observation data for five spatially resolved locations. We investigated flux levels and variations as a function of wavelength range and surface type (i.e., climate zone and surface thermal properties) and looked for periodic signals. From the spatially resolved single-surface-type measurements, we found that typically strong absorption bands from CO_2 (15 µm) and O_3 (9.65 µm) are significantly less pronounced and partially absent in polar regions. This implies that estimating

correct abundance levels for these molecules might not be representative of the bulk abundances in these viewing geometries. Additionally, the time-resolved thermal emission spectrum provided insights into seasons/planetary obliquity, but its significance depended on viewing geometry and spectral band.

In a follow-up study (Mettler et al., 2023), we expanded our analyses from spatially resolved locations to disk-integrated Earth views. We presented an exclusive dataset consisting of 2,690 disk-integrated mid-infrared (MIR) thermal emission spectra ($3.75 - 15.4$ µm, resolution $R \approx 1200$). The spectra were derived from remote sensing observations for four different viewing geometries at a high temporal resolution. Using this dataset, we investigated how Earth's MIR spectral appearance changes as a function of viewing geometry, seasons, and phase angles and quantified the atmospheric seasonality of different bioindicators. We found that a representative, disk-integrated thermal emission spectrum of Earth does not exist. Instead, both the thermal emission spectrum and the strength of biosignature absorption features show seasonal variability and depend strongly on viewing geometry.

In this work, we treat Earth as a directly imaged exoplanet to assess the detectability of its characteristics from MIR observations with LIFE. For the first time, we perform a systematic retrieval analysis of real disk- and time-averaged Earth spectra. We investigate how the retrieval characterization depends on factors such as the viewing geometry and the season. Uniquely, in this study we do not only have access to the real Earth spectra, but also to ground truth data from remote sensing satellites. Hence, for the first time, we can compare retrieval results from real spectra to ground truth values. This allows us to evaluate the accuracy of the retrieved constraints and thereby validate our retrieval approach. Despite providing a unique opportunity to validate retrieval frameworks and their underlying assumptions, comparable retrieval studies on solar system observations are rare (e.g., Tinetti et al., 2006a; Robinson and Salvador, 2023; Lustig-Yaeger et al., 2023b). However, such studies are indispensable to obtain a correct characterization of terrestrial exoplanets in the future.

In Section 4.2, we introduce the disk-integrated MIR thermal emission dataset and the level 3 satellite products used to derive the ground truths. We introduce our atmospheric retrieval routine and the used atmospheric model in Section 4.3. In Section 4.4, we present the retrieval results and put them into context in Section 4.5. Finally, in Section 4.6, we draw conclusions and discuss the implications

for future observations.

4.2 Datasets and Methodology

In order to compile our ground truth and spectral radiance datasets, we make use of Earth remote sensing climate data obtained from NASA's Atmospheric Infrared Sounder (AIRS; Chahine et al., 2006) aboard the Aqua satellite. For comparison and validation, we have also analyzed data from the Infrared Atmospheric Sounding Interferometer (IASI; Blumstein et al., 2004) instrument aboard the MetOp satellite. The details of the datasets and the data reduction is discussed in Sections 4.2.2 and 4.2.3. Although we briefly cover the methodology behind our calculation of disk-averaged spectra and the dataset, we refer to Mettler et al. (2023) for a more comprehensive description.

4.2.1 Using Earth Observation Data to Study Earth as an Exoplanet

While there are several methods to study Earth from afar, such as Earth-shine measurements or spacecraft flybys (for a recent review see, e.g., Robinson and Reinhard, 2018, and references therein), we chose a remote sensing approach. This approach offers the extensive temporal, spatial, and spectral coverage needed to investigate the effect of observing geometries on disk-integrated thermal emission spectra and time-varying signals. However, for Earth-orbiting spacecrafts it is impossible to view the full disk of Earth and the spatially resolved satellite datasets have to be combined into a spatially resolved, global map of Earth, which can then be disk-integrated (e.g., Tinetti et al., 2006a; Hearty et al., 2009; Gómez-Leal et al., 2012). Furthermore, due to the swath geometry of satellites, daily remote sensing data contain gores, which are regions with no data points, between orbit passes near the equator. In the case of Aqua/AIRS these regions are filled within 48 hours as the satellite continues scanning Earth while orbiting it.

For our analysis we defined four specific Earth observing geometries as shown in Figure 4.1: North (NP) and South Pole (SP), as well as Africa- (EqA) and Pacific-centered (EqP) equatorial views. For each viewing geometry, we mapped, calibrated, and geolocated radiances onto the globe and calculated the disk-integrated MIR thermal emission spectra. The spectra cover the 3.75 – 15.4 µm

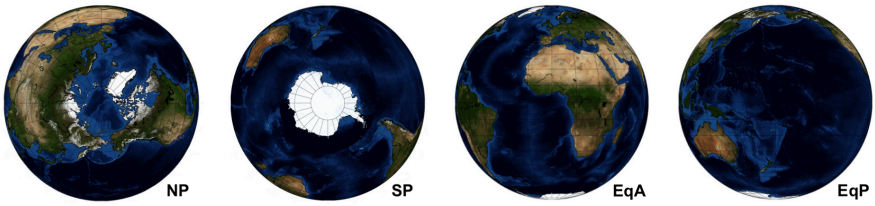

Figure 4.1: The four observing geometries studied (taken from Mettler et al., 2023). From left to right: North Pole (NP), South Pole (SP), Africa-centered equatorial view (EqA), and Pacific-centered equatorial view (EqP). Due to the continuously evolving view of low latitude viewing geometries as the planet rotates, the two equatorial views EqA & EqP were combined to one observing geometry, EqC.

wavelength range (with a gap between 4.6 – 6.2 µm) at a nominal resolution of $R \approx 1200$ and comprise 2378 spectral channels. The radiances originate from an AIRS Infrared (IR) level 1C product (V6.7) called AIRICRAD[1] and are given in physical units of $\mathrm{Wm}^{-2}\mu\mathrm{m}^{-1}\mathrm{sr}^{-1}$ (Manning et al., 2019). The total dataset contains 2690 disk-integrated thermal emission spectra for four consecutive years (2016-2019) at a high temporal resolution for the four full-disk observing geometries (for an overview, see Table 1 in Mettler et al., 2023).

The viewing geometries as portrayed in Figure 4.1 evolve throughout the year for a distant observer due to Earth's nonzero obliquity. Whereas the equatorial view blends seasons and has a diurnal cycle, the polar views show one season but blend day and night. Over the expected integration time of future direct imaging missions, the spectral appearance and characteristics of a planet change as it rotates around its spin axis and as spatial differences from clear and cloudy regions, contributions from different surface types as well as from different hemispheres vary with time. In accordance with the preliminary minimum LIFE requirements motivated in Konrad et al. (2022), we adopt a typical integration time of 30 days, which is significantly longer than Earth's rotation period. Hence, we average over the EqA and EqP views and denote the resulting dataset EqC.

To capture the largest variability between observations, our analyses focus on observing Earth at its extremes in January and July. This choice is motivated by the measured relative flux change for these months at Earth's peaking wavelength in the disk-integrated thermal emission signal (Mettler et al., 2023). Although

[1] https://cmr.earthdata.nasa.gov/search/concepts/C1675477037-GES_DISC.html

Table 4.1: Data and observation details, and spectral information.

Data and Observation Details	Value	Unit
Year of Data Origin	2017	
Months of Observation	January & July	
Integration Time	30	days
Observed Viewing Geometries	NP, SP, EqC	

Spectral Information	Value	Unit
Spectral Coverage	3.75–15.4	μm
Nominal Resolution	1200	
Number of Spectral Channels	2378	

a pacific-dominated view shows comparable variability to the South Pole view, Earth's rotation causes Africa and the Pacific to rotate in and out of the field of view. This rotation impacts the observed seasonal variability due to the different surface characteristics of EqA and EqP. The study details are summarized in Table 4.1.

4.2.2 Compiling and Processing the MIR Spectra

The disk-integrated thermal emission spectra for this study are derived from our previously published dataset. Since Earth's MIR spectrum exhibited negligible differences between consecutive years for a fixed viewing geometry (e.g., Mettler et al., 2020, 2023), we randomly chose the year 2017 and used the data of that year in order to calculate the monthly averages for January and July for the three viewing geometries: NP, SP and EqC. Blending day and night data to simulate the phase of Earth at its orbital position was unnecessary for polar views due to Earth's obliquity, so they naturally include data of both types. However, in the case of the EqC view, we blended day and night data to simulate a rotating Earth at quadrature. This orbital position is preferred for the direct imaging of exoplanets due to the large apparent angular separation between the exoplanet and its host star.

AIRS spectra exhibit a gap between 4.6 – 6.2 μm due to dead instrument channels. This gap lies in a H_2O absorption feature centered at 6.2 μm (e.g., Catling et al., 2018). Due to concerns that the partially missing H_2O feature might deteriorate our retrieval results, we sourced level 1C data[2] for the year 2017 from the IASI

[2]IASI Level 1C - All Spectral Samples - Metop - Global, Collection ID: EO:EUM:DAT:METOP:IASIL1C-

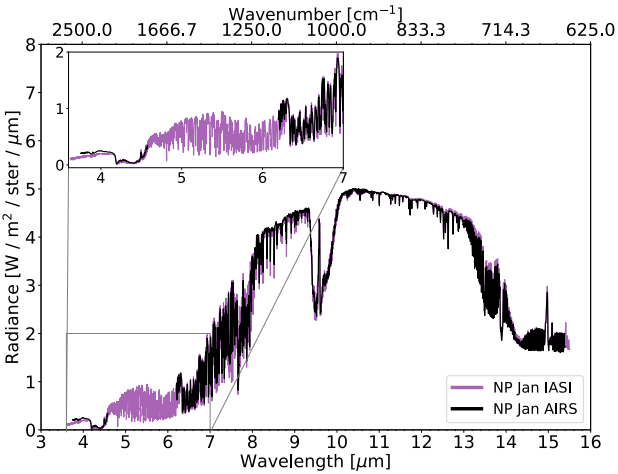

Figure 4.2: Comparison between a single-day disk-integrated AIRS (black) and IASI (purple) spectrum for the NP view. The gap between 4.6 – 6.2 µm is clearly visible in the AIRS spectrum.

instrument aboard the MetOP satellite. We applied the same data reduction steps as for the AIRS dataset described in Section 4.2.1 and Section 2 of Mettler et al. (2023). Covering the 3.62 – 15.50 µm wavelength regime with 8461 channels, IASI delivers a continuous spectrum comparable to that of AIRS, which makes it a suitable alternative instrument (see Figure 4.2). However, test retrievals showed no significant discrepancies between the retrieval results obtained for the gapped AIRS and continuous IASI spectra. The lack of discrepancies can be attributed to LIFE's noise level at these lower MIR wavelengths (e.g., Figure 4.4). Thus, since no significant differences were observed and the fact that our ground truth data introduced in Section 4.2.3 is based on Aqua/AIRS level 3 monthly standard physical retrievals, we opted to use AIRS spectra for this study for consistency.

4.2.3 Compiling and Processing the Ground Truths

In Section 4.4, we compare the retrieval outputs to a level 3 (L3) satellite product comprising the P–T profile and the trace-gas abundances. Specifically, we have used the Aqua/AIRS L3 Monthly Standard Physical Retrieval (AIRS-only) 1 degree

ALL, available at EUMETSAT distribution center

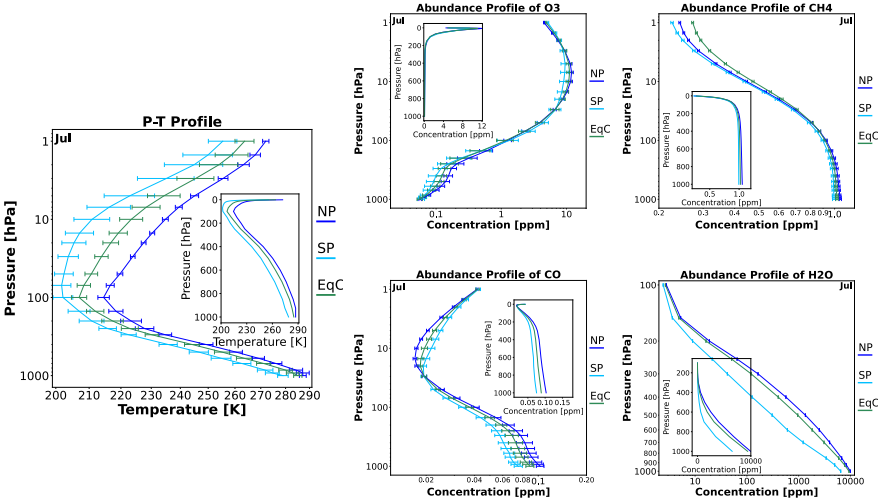

Figure 4.3: Disk-integrated atmospheric profiles for July. From left to right: $P-T$ profile followed by O_3, CH_4, CO, and H_2O atmospheric profiles. The error bars are the error propagated uncertainties of the retrieved parameters from the AIRS L3 standard product. The different colors correspond to the viewing geometries: NP (blue), SP (turquoise), EqC (green). The insets display the profiles on a linear scale instead of a logarithmic one.

x 1 degree V7.0 (AIRS3STM) product (AIRS Project, 2020), from which we extracted the surface temperature (land and sea surface) as well as the $P-T$ profile. From the trace-gas parameters we extracted the total integrated column burdens and vertical profiles (mass mixing ratios) of H_2O, CO, CH_4, and O_3. Both, the $P-T$ profile and trace-gas abundances are reported on 24 standard pressure levels ranging from 1000 to 1.0 hPa, which are roughly matched to the instrument's vertical resolution (Tian et al., 2020a). The H_2O profile is an exception, as it is only provided at twelve layers ranging from 1000 to 100 hPa, spanning from the surface to the tropopause.

Since the AIRS3STM product did not contain any CO_2 abundances, we sourced the corresponding ground truth from a gridded monthly CO_2 assimilated dataset[3] based on observations from the Orbiting Carbon Observatory 2 (OCO-2). The OCO-2 mission provides the highest quality space-based XCO2 retrievals to date,

[3] OCO-2 GEOS Level 3 monthly, 0.5x0.625 assimilated CO_2 V10r (OCO2_ GEOS_L3CO2_MONTH) at GES DISC (NASA/GSFC/GMAO Carbon Group, 2021)

where the level 3 data are produced by ingesting OCO-2 L2 retrievals every 6 hours with GEOS CoDAS, a modeling and data assimilation system maintained by NASA's Global Modeling and Assimilation Office (GMAO; NASA/GSFC/GMAO Carbon Group, 2021). The data assimilation (or 'state estimation') technique is employed in order to estimate missing values based on the scientific understanding of Earth's carbon cycle and atmospheric transport. The missing values are mainly the result of the instrument's narrow 10 km ground track and limited ability to penetrate through clouds and dense aerosols.

Following the data reduction of the radiances in Section 4.2.1, the $P-T$ profile and trace-gas abundances were mapped onto the globe for the different viewing geometries and then disk-integrated at each pressure level. For consistency, we also applied the empirical limb/weighting function to the ground truths. The uncertainties of the retrieved parameters from the AIRS L3 standard product were error propagated, and the resulting error bars are displayed for each data point. The results obtained for July and January are shown in Figure 4.3 and Appendix 4.A, respectively.

4.3 Atmospheric Retrievals

First, we introduce the disk-integrated Earth spectra and the LIFESIM noise model used as input for our retrievals (Section 4.3.1). In Section 4.3.2, we briefly describe our Bayesian atmospheric retrieval routine. Then, in Section 4.3.3, we focus on the 1D plane-parallel atmosphere model used as retrieval forward model. Last, we motivate our choice of prior distributions (Section 4.3.4).

4.3.1 Input Spectra for the Retrievals

As input for our atmospheric retrievals, we use reduced-resolution versions of the disk-integrated ARIS spectra from Section 4.2.1 (NP, SP, and EqC viewing geometries for January and July). All spectra cover the $3.8-15.3$ µm wavelength range, with a gap between 4.6 µm and 6.2 µm.

Based on the preliminary minimal LIFE requirements presented in Konrad et al. (2022, 2023) and Alei et al. (2022) ($R=50$, $S/N=10$), we consider two resolution cases ($R=50,100$) and two signal-to-noise ratios ($S/N=10,20$) for each of the six disk-integrated spectra. We define R as $\lambda/\Delta\lambda$, with the width of a wavelength bin

$\Delta\lambda$ and the wavelength at the bin center λ. Further, the S/N value corresponds to the S/N in the 11.2 µm wavelength bin. We choose the 11.2 µm bin because it does not coincide with any strong spectral features. In Figure 4.4, we show the six $R = 50$ input spectra together with the two different noise levels.

We model the wavelength-dependent S/N expected for LIFE with LIFESIM (Dannert et al., 2022), which accounts for astrophysical noise sources (photon noise of planet emission, stellar leakage, and local- as well as exozodiacal dust emission)[4]. To estimate the LIFESIM noise, we put Earth on a 1 AU orbit around a G2V star located 10 pc from the observer. The exozodiacal dust emission of the system was assumed to reach three times the local zodiacal level[5].

In our retrievals, we interpret the noise as uncertainty to the points of the disk-integrated spectra. Thus, the spectral points correspond to the true flux values and are not randomized according to the LIFESIM S/N. While randomized spectra would provide a more accurate simulated observation, a retrieval study based on a single noise realization will yield biased parameter estimates. Ideally, we would run retrievals for multiple ($\gtrsim 10$) noise realizations of each spectrum. However, the number of retrievals required make such a study computationally unfeasible. Yet, Konrad et al. (2022) motivate that results from retrievals on unrandomized spectra provide reliable estimates for the average expected retrieval performance on randomized spectra.

4.3.2 Bayesian Retrieval Routine

For this study, we utilized the Bayesian retrieval routine introduced in Konrad et al. (2022). The initial routine was improved and modified in Alei et al. (2022) and Konrad et al. (2023). We provide a brief summary of the routine here, and refer to the original publications for an in depth description.

Our retrieval framework uses the radiative transfer code `petitRADTRANS` (Mollière et al., 2019, 2020; Alei et al., 2022) to calculate the theoretical emission spectrum of a 1D plane-parallel atmosphere model. `petitRADTRANS` assumes a black-body spectrum at the surface and models the interaction of each at-

[4]Thus, we implicitly assume that a large LIFE-like future space mission will not be dominated by instrumental noise terms (Dannert et al., in prep.).

[5]This corresponds to the median level of exozodiacal dust emission found by the HOSTS survey for Sun-like stars (Ertel et al., 2020).

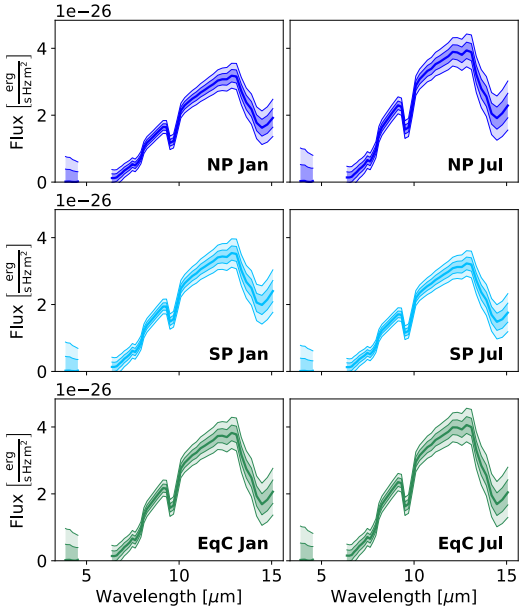

Figure 4.4: Disk-integrated $R = 50$ Earth spectra considered in our retrieval study. We indicate the $S/N = 10$ and $S/N = 20$ LIFESIM noise levels as shaded areas. Spectra from the top left to the bottom right: NP Jan, NP Jul, SP Jan, SP Jul, EqC Jan, EqC Jul.

mospheric layer with the radiation to calculate the spectrum at the top of the atmosphere. The model atmosphere is defined via a set of forward model parameters (see Section 4.3.3 for our forward model). In a retrieval, we search the space spanned by the prior probability distributions (or "priors") of the forward model parameters for the parameter combination that best reproduces the input spectrum. To efficiently search the prior volume, we use the `pyMultiNest` (Buchner et al., 2014) package, which uses the `MultiNest` (Feroz et al., 2009) implementation of the Nested Sampling algorithm (Skilling, 2006). Here, we ran all retrievals using 700 live points and a sampling efficiency of 0.3[6].

The retrieval yields the posterior probability distribution (or "posterior") for the model parameters. The posterior estimates how likely a certain combination of model parameter values is given the observed spectrum. Further, our routine

[6]As suggested for evidence evaluation by the `MultiNest` documentation: https://github.com/farhanferoz/MultiNest

estimates the Bayesian evidence $\mathfrak{Z}$, which is a measure for how well the used forward model fits the input spectrum and can be used for model comparison (see Appendix 4.C).

4.3.3 Atmospheric Model in the Retrievals

As in Konrad et al. (2022, 2023), and Alei et al. (2022), we characterize each layer of the model atmosphere by its temperature, pressure, and the opacity sources present. We provide a list of all model parameters in Table 4.2. A comparison between different forward models to justify our choice is provided in Appendix 4.C.

In our forward model we parameterized the atmospheric $P-T$ profile using a fourth order polynomial:

$$T(P) = \sum_{i=0}^{4} a_i P^i. \tag{4.1}$$

Here, P is the pressure, T the corresponding temperature, and the a_i are the parameters of the $P-T$ model. As shown in Konrad et al. (2022), a polynomial $P-T$ model allows us to minimize the number of $P-T$ parameters and thereby minimize the retrieval's computational complexity. Learning based $P-T$ models require fewer parameters, but their accuracy for terrestrial planets is currently limited by the availability of sufficient training data (e.g., Gebhard et al., 2023).

We consider various opacities in our forward model. First, we account for the MIR absorption and emission by CO_2, H_2O, O_3, and CH_4 (see Table 4.3 for line lists, broadening coefficients, and cutoffs). We assume constant vertical abundance profiles for all molecules and discuss potential effects of this simplification in Section 4.5.1. Second, we model collision-induced absorption (CIA) and Rayleigh scattering features (CIA-pairs and Rayleigh-species are listed in Table 4.3).

We neglect scattering and absorption by clouds. The patchy clouds in Earth's atmosphere partially block contributions from high-pressure atmosphere layers and thereby impede the characterization thereof. Konrad et al. (2023) show that neglecting clouds in retrievals can lead to systematic errors in the retrieved surface temperature, surface pressure, and the planet radius. We provide a detailed discussion on potential effects of this simplification in Section 4.5.1.

4.3.4 Prior Distributions

We list the priors assumed for all retrievals in Table 4.2. The priors on the P–T parameters a_i and the surface pressure P_0 cover a wide range of atmospheric structures (from tenuous Mars-like to thick Venus-like atmospheres). For N_2, O_2, CO_2, H_2O, O_3, and CH_4, we select broad uniform priors that extend significantly below the minimal detectable abundances estimated in Konrad et al. (2022) ($\approx 10^{-7}$ in mass fraction for our R and S/N cases).

As in Konrad et al. (2022, 2023) and Alei et al. (2022), we use Gaussian priors for the planet radius $R_{\rm pl}$ and mass $M_{\rm pl}$. The $R_{\rm pl}$ prior is based on Dannert et al. (2022), who suggest that a planet detection with LIFE yields a constraint on $R_{\rm pl}$[7]. The statistical mass-radius relation `Forecaster`[8] (Chen and Kipping, 2016), is then used to infer the prior on $\log_{10}(M_{\rm pl})$ from the $R_{\rm pl}$ prior.

Table 4.2: Parameters of the retrieval forward model. The third column lists the priors assumed in the retrievals. We denote a boxcar prior with lower threshold x and upper threshold y as $\mathcal{U}(x,y)$; For a Gaussian prior with mean μ and standard deviation σ, we write $\mathcal{G}(\mu,\sigma)$.

Parameter	Description	Prior
a_4	P-T parameter (degree 4)	$\mathcal{U}(0,10)$
a_3	P-T parameter (degree 3)	$\mathcal{U}(0,100)$
a_2	P-T parameter (degree 2)	$\mathcal{U}(0,500)$
a_1	P-T parameter (degree 1)	$\mathcal{U}(0,500)$
a_0	P-T parameter (degree 0)	$\mathcal{U}(0,1000)$
$\log_{10}(P_0)$	$\log_{10}$(Surface pressure [bar])	$\mathcal{U}(-4,2)$
$R_{\rm pl}$	Planet radius [$R_\oplus$]	$\mathcal{G}(1.0,0.2)$
$\log_{10}(M_{\rm pl})$	$\log_{10}$(Planet mass [$M_\oplus$])	$\mathcal{G}(0.0,0.4)$
$\log_{10}(N_2)$	$\log_{10}$(N_2 mass fraction)	$\mathcal{U}(-10,0)$
$\log_{10}(O_2)$	$\log_{10}$(O_2 mass fraction)	$\mathcal{U}(-10,0)$
$\log_{10}(CO_2)$	$\log_{10}$(CO_2 mass fraction)	$\mathcal{U}(-10,0)$
$\log_{10}(H_2O)$	$\log_{10}$(H_2O mass fraction)	$\mathcal{U}(-10,0)$
$\log_{10}(O_3)$	$\log_{10}$(O_3 mass fraction)	$\mathcal{U}(-10,0)$
$\log_{10}(CH_4)$	$\log_{10}$(CH_4 mass fraction)	$\mathcal{U}(-10,0)$

[7] For a HZ terrestrial planet, a radius estimate $R_{\rm est}$ for the true radius $R_{\rm true}$ with $R_{\rm est}/R_{\rm true} = 0.97 \pm 0.18$ is predicted

[8] https://github.com/chenjj2/forecaster

Table 4.3: Line and continuum opacities used in retrievals. P-broadening abbreviates pressure-brodening (HA98) Harvey et al. (1998); (HN20) Gordon et al. (2022); (KA19) Karman et al. (2019); (SU05) Sneep and Ubachs (2005); (TH14) Thalman et al. (2014); (TH17) Thalman et al. (2017).

Molecular Line Opacities				CIA		Rayleigh Scattering	
Molecule	Line List	Pressure-broadening	Wing cutoff	Pair	Reference	Molecule	Reference
CO_2	HN20	γ_{air}	25 cm^{-1}	N_2–N_2	KA19	N_2	TH14, TH17
H_2O	HN20	γ_{air}	25 cm^{-1}	N_2–O_2	KA19	O_2	TH14, TH17
O_3	HN20	γ_{air}	25 cm^{-1}	O_2–O_2	KA19	CO_2	SU05
CH_4	HN20	γ_{air}	25 cm^{-1}	CO_2–CO_2	KA19	CH_4	SU05
CO	HN20	γ_{air}	25 cm^{-1}	CH_4–CH_4	KA19	H_2O	HA98
N_2O	HN20	γ_{air}	25 cm^{-1}	H_2O–H_2O	KA19		
				H_2O–N_2	KA19		

4.4 Retrieval Results

Here, we present the retrieval results obtained with the forward model from Section 4.3.3. In Figure 4.5, we summarize the results from the retrieval on the $R = 100$, $S/N = 20$ EqC Jul spectrum, which are representative of all retrieval results. We show the retrieved P–T structure, the posteriors of the atmospheric trace gases and radius R_{pl}, and estimates for the equilibrium temperature T_{eq} and the Bond albedo A_B (derived from the posteriors using the method outlined in Appendix 4.D). The N_2 and O_2 posteriors are not shown since we did not constrain either abundance. We further plot the ground truths for all parameters. The true atmospheric abundances of H_2O, O_3, and CH_4 depend on the atmospheric pressure (see Figure 4.3). To indicate the range of these ground truth profiles, we plot the ground truths at four different pressures (1 bar, 10^{-1} bar, 10^{-2} bar, 10^{-3} bar). We provide the P–T profile results from all other retrievals in Appendix 4.F. The posteriors for all retrievals (excluding the P–T parameters a_i) along with T_{eq} and A_B estimates are shown in Figure 4.7a. We list the corresponding numeric values in Appendix 4.F.

From the results shown in Figure 4.5, we would rightly conclude that we are observing a potentially habitable planet. We find temperate surface conditions that would allow for liquid water to exist and easily detect the highly relevant atmospheric gases CO_2, H_2O, and O_3. Importantly, we also detect the potential biosignature CH_4. These findings hold for all considered viewing geometries, seasons, R, and S/N.

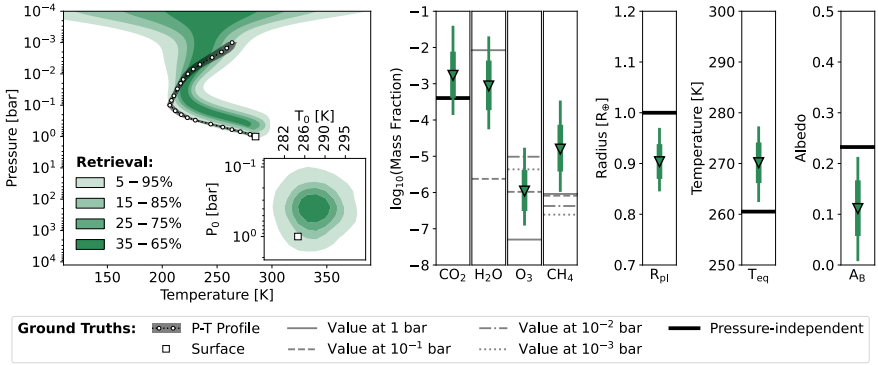

Figure 4.5: Retrieval results for the $R = 100$, $S/N = 20$ EqC Jul Earth spectrum. The leftmost panel shows the retrieved $P-T$ structure. Green-shaded areas indicate percentiles of the retrieved $P-T$ profiles. The white square marks the true surface conditions (P_0, T_0). The white circles and the gray area show the true $P-T$ structure and the uncertainty thereon. In the bottom right of the $P-T$ panel, we show the retrieved constraints on the surface conditions. The remaining panels show the posteriors of the trace gas abundances and other parameters. Green lines indicate posterior percentiles (thick: 16% – 84%; thin: 2% – 98%). Thick black lines indicate pressure-independent ground truths. Thin gray lines show the true abundance at different atmospheric pressures (solid: 1 bar; dashed: 10^{-1} bar; dashed-dotted: 10^{-2} bar; dotted: 10^{-3} bar).

In the following, we address systematic differences between our retrieval results and the ground truths.

From the retrieved $P-T$ profiles in Figure 4.5 and Appendix 4.F, we see that our retrieved estimates for the surface conditions and the overall atmospheric $P-T$ structure are inaccurate. While T_0 is well retrieved (roughly centered on the ground truth, uncertainty $\leq \pm 20$ K), P_0 is underestimated by up to an order of magnitude (uncertainty $\leq \pm 0.5$ dex). This observation does not only hold for the surface conditions but for the entire $P-T$ profile. The shape of the temperature structure is accurately retrieved, but shifted to lower pressures relative to the ground truth. This effect is observable for all spectra, and becomes smaller for the higher R and S/N cases. Further, constraints on the $P-T$ structure in the upper atmosphere ($\lesssim 10^{-3}$ bar) are weaker, which we expect due to negligible signatures from these layers in MIR emission spectra. The obtained constraints are due to extrapolation of the polynomial $P-T$ model and thus not physical.

Considering the parameter posteriors in Figure 4.7a, we observe that most param-

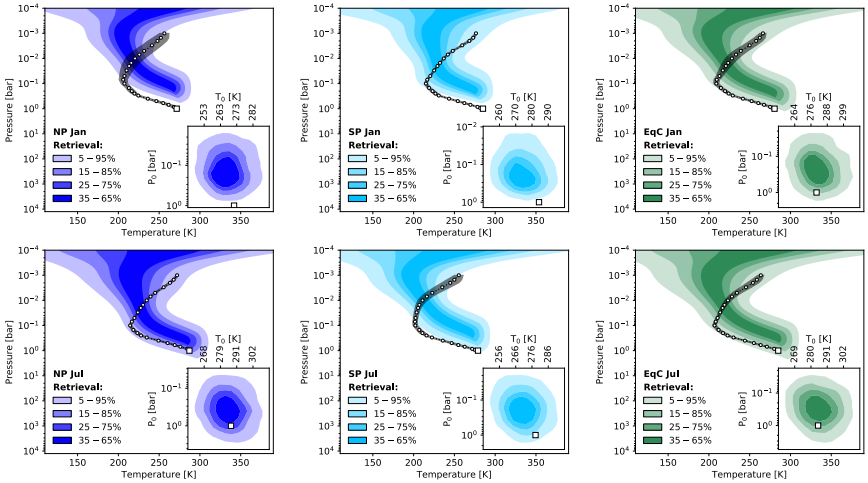

Figure 4.6: $P-T$ profiles retrieved for the six disk-integrated, $R = 50$ and LIFEsim $S/N = 10$ Earth spectra. The color-shaded areas indicate percentiles of the retrieved $P-T$ profiles. The white square marker shows the true surface pressure P_0 and temperature T_0, the white circular markers show the true $P-T$ structure, and the gray shaded area indicates the uncertainty thereon. In the bottom right, we plot the 2D P_0-T_0 posterior, to visualize the constraints on the retrieved surface conditions. Each panel shows the result for one viewing angle. From top-left to bottom-right: NP Jan, SP Jan, EqC Jan, NP Jul, SP Jul, and EqC Jul.

eters are well retrieved (i.e. at least one of the disk-integrated ground truths lies within the 16% – 84% percentile of the posterior). Further, as expected, the constraints on the posteriors get stronger as we consider higher R and S/N spectra, since these spectra contain more information and thus yield stronger constraints.

However, several parameter posteriors are biased relative to the ground truths. We already observed biases on P_0 and the lack thereof on T_0 in the $P-T$ profiles. From the posteriors, we see that the systematic underestimation of P_0 is accompanied by a systematic overestimation of the gas abundances. The effect is most apparent for CO_2 and CH_4, for which the ground truths do not vary strongly with atmospheric pressure. The shifts in the retrieved $P-T$ profiles translate to biased CO_2 and CH_4 abundances due to a degeneracy between the trace-gas abundances and the pressure-induced line-broadening by the bulk atmosphere (see, e.g., Misra et al., 2014; Schwieterman et al., 2015). For CO_2, we clearly observe that an underestimated P_0 is linked to an overestimated CO_2 abundance.

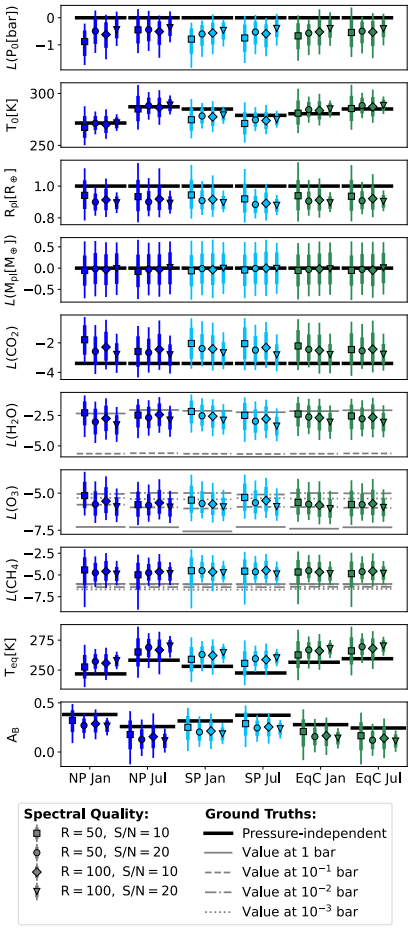

(a) Posteriors combinations of R (50, 100) and S/N (10, 20) for the six disk-integrated Earth spectra. Here, $L(\cdot)$ abbreviates $\log_{10}(\cdot)$. The marker shape represents the spectral R and S/N, the color shows the viewing geometry. Colored lines indicate posterior percentiles (thick: 16% – 84%; thin: 2% – 98%). Thick black lines indicate ground truths which are independent of the atmospheric pressure. Thin gray lines show ground truth abundances at different atmospheric pressures (solid: 1 bar; dashed: 10^{-1} bar; dashed-dotted: 10^{-2} bar; dotted: 10^{-3} bar). Columns (left to right) show the results for: NP Jan, NP Jul, SP Jan, Sp Jul, EqC Jan, and EqC Jul.

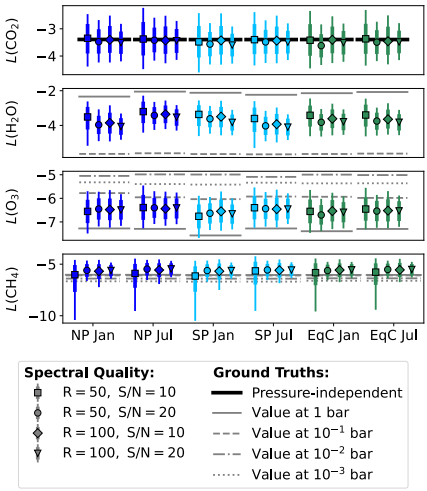

(b) Abundance posteriors reduced to the true P_0 value of 1 bar (following the method in Appendix 4.E). The figure structure is equivalent to Figure 4.7a.

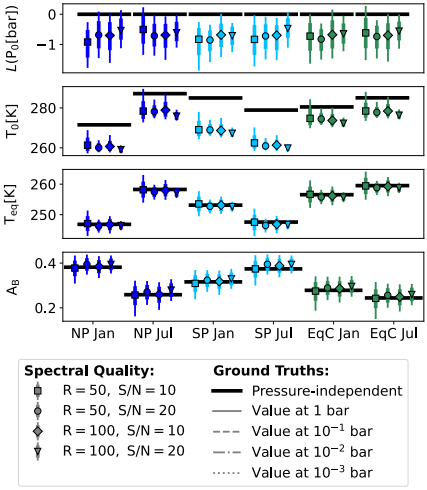

(c) Selected posteriors reduced to the true R_{pl} value of 1 $R_\oplus$ (following the method in Appendix 4.E). The figure structure is equivalent to Figure 4.7a.

Figure 4.7: Reduced posterior results.

For CH_4, this effect is less clearly visible due to the larger uncertainty on the posteriors. The degeneracy also affects the H_2O and O_3 posteriors. However, due to the strong dependence of the ground truth on the atmospheric pressure, biases are not directly observable since the posteriors lie within the ground truth range. Yet, lower retrieved P_0 lead to higher H_2O and O_3 estimates, implying a degeneracy.

Further, R_{pl} is significant underestimated, especially by the $S/N = 20$ retrievals. Unlike the $P-T$ and abundance biases, the R_{pl} biases do not decrease for higher R and S/N spectra. The underestimated R_{pl} leads to too low T_{eq} and A_B estimates, since both parameters are derived from the R_{pl} posterior (see Appendix 4.D). A possible cause of these biases are the effects of patchy H_2O clouds on the disk-integrated spectra (see Appendix 4.B). Clouds block the thermal emission from the surface and lower atmospheric layers, reducing the planet's thermal emission. For patchy clouds, contributions from the lowest atmospheric layers are still present in the MIR spectrum, which enables the accurate retrieval of T_0. However, to account for the reduction in the planet's total emission by patchy clouds, R_{pl} is underestimated (see Section 4.5.1 for a detailed discussion).

4.4.1 Reduced Posteriors

To demonstrate the links between the underestimation of P_0 and R_{pl} and the biases on the remaining parameters, we reduce the posteriors to Earth's true P_0 and R_{pl} values. For the reduction, we assume linear correlations between P_0 or R_{pl} and the other parameters, which is a good approximation of the true posterior correlations. Further details on the posterior reduction can be found in Appendix 4.E.

To demonstrate the effects of underestimating P_0, we reduce the abundance posteriors to Earth's true P_0 of 1 bar. The resulting reduced posteriors are shown in Figure 4.7b (numerical values in Tables 4.6 to 4.8). The posterior reduction to the true P_0, leads to significantly better estimates for CO_2 and CH_4. For CO_2, the reduced posteriors are perfectly centered on the true value, while the CH_4 abundances are significantly less overestimated. This demonstrates, that the shifts in the CO_2 and CH_4 posteriors in Figure 4.7a are directly linked to the inaccurately retrieved P_0. For O_3 and H_2O, the reduced posteriors are shifted to lower abundances and show a smaller variance between the individual retrievals.

These findings suggest that the P_0 reduction improves estimates for atmospheric O_3 and H_2O abundances.

In order to investigate how $R_{\rm pl}$ affects the other posteriors, we reduce the $R_{\rm pl}$ posterior to 1 $R_\oplus$. We plot the reduced posteriors of P_0, T_0, $T_{\rm eq}$, and $A_{\rm B}$ in Figure 4.7c (numerical values in Tables 4.6 to 4.8). First, we observe no significant differences between the reduced and the true P_0 posteriors from Figure 4.7a. This indicates that no direct correlation between the $R_{\rm pl}$ and the P_0 posterior exists. For T_0, which is accurately estimated by the retrieval, the reduced posteriors underestimate the truth by ≥ 5 K, which indicates that Earth's disk-integrated flux is smaller than what is expected for a 1 $R_\oplus$ planet with surface temperature T_0. This suggests that patchy clouds, which partially block the emission from the high pressure atmospheric layers and thereby reduce the total planet flux, are the likely cause of the $R_{\rm pl}$ biases. Finally, the reduced $T_{\rm eq}$ and $A_{\rm B}$ posteriors are unbiased and provide accurate truth estimates (uncertainties: $\leq \pm 2$ K for $T_{\rm eq}$; $\leq \pm 0.1$ for $A_{\rm B}$), which demonstrates the correlations with $R_{\rm pl}$.

4.4.2 Relative Abundance Posteriors

Degeneracies between model parameters can lead to biased posteriors. Reducing posteriors, as done in Section 4.4.1, can eliminate such biases. However, posterior reduction requires us to fix one parameter value (e.g., P_0 or $R_{\rm pl}$ in Section 4.4.1). For Earth, this is possible because the ground truths are known. For exoplanets however, where the ground truths are unknown, such a reduction would be arbitrary.

Instead, one can consider the point-wise ratio of two posteriors (i.e., divide one posterior by another). This is useful for parameters affected by the same degeneracies. As seen above, a degeneracy with P_0 strongly affects the trace-gas abundance posteriors. Also, we expect the trace-gas posteriors to be impacted by a physical degeneracy with the planet's surface gravity g_{pl} and thus $M_{\rm pl}$ (see, e.g., Mollière et al., 2015; Feng et al., 2018; Madhusudhan, 2018a; Konrad et al., 2022; Alei et al., 2022; Konrad et al., 2023)[9]. Such degeneracies could be largely eliminated by considering abundance ratios. Importantly, in contrast to reduced posteriors (Section 4.4.1), no assumptions about the true atmosphere are made. Despite

[9]The degeneracy with g_{pl} (and $M_{\rm pl}$) is caused by the dependence of the hydrostatic equilibrium on g_{pl}. In the hydrostatic equilibrium, g_{pl} is degenerate with the mean molecular weight of the atmosphere, which is directly linked to the trace-gas abundances.

lacking information on absolute abundances, relative abundances are of interest since they can help identify states of atmospheric chemical disequilibrium, which can indicate biological activity (Lovelock, 1965; Lovelock et al., 1975).

We present the relative abundance posteriors for all trace-gas combinations in Figure 4.8 (numerical values in Tables 4.6 to 4.8). The uncertainties on the relative trace-gas abundances are significantly smaller than on the absolute abundances due to the elimination of mutual degeneracies. Further, in contrast to the absolute abundance posteriors (Figure 4.7a), all abundance ratios lie within the range of the relative ground truth values, indicating that biases can be largely eliminated.

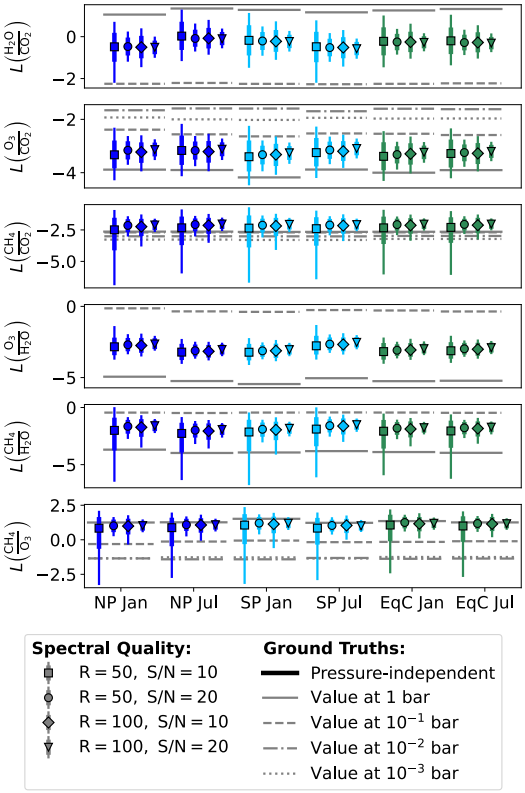

Figure 4.8: Posteriors of atmospheric trace-gas abundances relative to each other. The figure structure is equivalent to Figure 4.7a.

4.5 Discussion

4.5.1 Comparison to Previous LIFE Retrieval Studies

Previous studies have evaluated how well LIFE could characterize terrestrial HZ exoplanets. Konrad et al. (2022) find preliminary estimates for LIFE's minimal R and S/N requirements by running retrievals on simulated Earth spectra (generated assuming a 1D cloud-free atmosphere with vertically constant trace-gas abundances). Next, Alei et al. (2022) run retrievals on cloudy and cloud-free spectra from Rugheimer and Kaltenegger (2018), which represent Earth at different stages in its temporal evolution. The 1D atmosphere models used to generate the Earth spectra are more complex and assume vertically variable trace-gas abundances. Last, Konrad et al. (2023) study how well LIFE can characterize cloudy atmospheres by studying a Venus-twin exoplanet. Alei et al. (2022) and Konrad et al. (2023) use the same retrieval routine to reevaluate the LIFE requirements from Konrad et al. (2022) by analyzing more complex emission spectra.

However, all these previous studies considered theoretical spectra based on simplified, temporally constant, 1D atmosphere models. The present study is the first that systematically ran retrievals on real disk- and time-averaged MIR Earth spectra. This yields more robust estimates for the characterization capabilities of LIFE and is a crucial step toward the characterization of terrestrial exoplanets.

Generally, the constraint strength is comparable for all studies (the $16-84$ percentile range corresponds to < 1.0 dex for pressures, $< 0.2 R_\oplus$ for radii, < 40 K for temperatures, and < 2.0 dex for trace-gas abundances). Especially CH_4, which is the main driver for the minimum LIFE requirements from Konrad et al. (2022) ($R = 50$, $S/N = 10$), remains detectable in this study despite considering real Earth input spectra and not models.

Yet, as discussed in Section 4.4.1, our posteriors for P_0, and the trace-gas abundances are biased with respect to the ground truths. Specifically, the biases on the P_0 posteriors are directly linked to the offsets in the trace-gas abundance posteriors. In contrast, Konrad et al. (2022), who used the same 1D atmosphere model that generated the Earth-twin spectrum as forward model in their retrievals, manage to retrieve accurate estimates for all parameters. Here, the disk-integrated Earth-spectra used as retrieval inputs stem from a 3D temporally variable atmosphere. The observed biases are likely evoked by our strongly simplified 1D Earth

forward model, which cannot fully describe the true atmospheric state of Earth and the resulting MIR thermal emission.

Importantly, our 1D forward model assumes vertically constant trace-gas abundances. Especially for the strong MIR absorber H_2O, the abundance strongly decreases by more than three orders of magnitude between 1 bar and 0.1 bar (see, e.g., Figure 4.3). Roughly 25 layers of our atmospheric forward model fall within the specified pressure range. Since the H_2O features in Earth's spectrum probe a large range of atmospheric pressure regimes, a vertically constant H_2O profile is a strong simplification that can bias the retrieved $P-T$ structure and trace-gas abundances. In Alei et al. (2022), where spectra from Rugheimer and Kaltenegger (2018) with vertically variable H_2O abundances were used as input for the retrievals, the same tendency to underestimate pressures and overestimate abundances was observed. To investigate this further, first test retrievals that assume fixed non-constant H_2O profiles reduce biases on P_0, the $P-T$ profile, and the abundances. Yet, all attempts to retrieve the H_2O profile did not yield constraints. Future studies that investigate the impact of non-constant abundance profiles on retrievals are clearly needed.

An additional important simplification of this study is our disregarding of clouds in the forward model. For Earth, patchy clouds reduce the total MIR flux by partially blocking the emission from the warm, high-pressure atmosphere layers. This can impact retrieval results significantly, especially if clouds are ignored in the forward model. Alei et al. (2022) run cloud-free retrievals on simulated patchy-cloud and cloud-free Earth spectra. Similar to this work, they retrieve biased $R_{\rm pl}$ and P_0 estimates in retrievals on cloudy spectra, which are significantly more biased than for the cloud-free spectra. Konrad et al. (2023) considered a Venus-twin to study the effects of a full planet cloud coverage on retrievals. It was found that cloud-free retrievals on cloudy emission spectra can lead to biased $R_{\rm pl}$ posteriors. However, for the R and S/N cases considered here, they find that cloudy forward models are not preferred in Bayesian model selection. In first patchy-cloud test retrievals (with fixed cloud fraction and position in the atmosphere) we find reduced $R_{\rm pl}$ biases. However, both cloud fraction and position can not be constrained in free retrievals.

In addition, further factors, which were not considered in the previous LIFE retrieval studies, could contribute to the observed biases. First, recent intercomparison efforts show that both retrievals (e.g., Barstow et al., 2020) and atmospheric

modelling (e.g., Sergeev et al., 2022) can strongly depend on the used framework. Specificities such as the used line-lists, pressure broadening coefficients, and line-cutoffs can affect results. Thus, community efforts (e.g., the CUISINES Working Group[10]) that benchmark, compare, and validate different models are indispensable. Second, systematic measurement or post-processing errors in either the disk-integrated MIR Earth spectra or the ground truths could contribute to the observed biases. However, these effects are likely to be smaller than the aforementioned shortcomings of our 1D atmospheric forward model.

In conclusion, our retrieval results for disk-integrated Earth spectra are consistent with the results presented in previous LIFE retrieval studies. This suggests that retrievals on real exoplanet spectra are expected to yield biased parameter estimates. While care needs to be taken when considering the absolute posteriors, reduced posteriors or posterior ratios can yield less biased relative parameter estimates (see Sections 4.4.1 and 4.4.2).

4.5.2 Effects of Viewing Geometries and Seasons

As described in Section 4.1.1, Earth exhibits an uneven distribution of land and ocean regions. It is dominated by different surface types with different spectral and thermal characteristics (e.g., Hearty et al., 2009; Gómez-Leal et al., 2012; Madden and Kaltenegger, 2020). Also, the distribution of life on Earth is non-uniform with a measurable gradient in the abundance and diversity of life, both spatially (e.g., from deserts to rain forests) and temporally (e.g., from seasonal to geological timescales) (Méndez et al., 2021). In Mettler et al. (2023), we find that a representative, disk-integrated thermal emission spectrum of Earth does not exist. Instead, the MIR spectrum and the strength of absorption features show seasonal variations and depend on the viewing geometry. For future observations of HZ terrestrial exoplanets, the viewing geometry will be unknown. Thus, we must understand how the viewing geometry impacts exoplanet characterization, observable habitability markers, and signatures of life.

From Figure 4.7a, we see that there are no significant differences between the viewing geometries for most parameter posteriors. Thus, we expect the viewing angle to have only a minor impact on most parameters.

[10] https://nexss.info/cuisines/

Yet, T_{eq} and T_0 posteriors do depend on the viewing angle and the season. Especially for the NP view, the differences in T_0 and T_{eq} between January and July are detectable for a LIFE-like observatory for all R and S/N cases. We observe similar, but smaller, seasonality differences for the SP and EqC views, which are likely not observable with LIFE. This is in agreement with Mettler et al. (2023), who find the seasonal disk-integrated thermal emission flux differences for the ocean dominated SP and EqP (Pacific-centered equatorial view) views to be 11%, and 33% for the landmass dominated NP view. Thus, the T_0 variance observed for the NP view could be assigned to a large landmass fraction. Further, our results indicate that the SP and EqC views cannot be differentiated despite different characteristics like climate zones and landmass fractions, highlighting the strong spectral degeneracy with respect to seasons and viewing geometries. This agrees with other studies (e.g., Gómez-Leal et al., 2012; Mettler et al., 2023).

For the retrieved A_B in Figure 4.7a (numerical values in Tables 4.6 to 4.8), we also observe seasonal variations between January and July, with the NP, SP, and EqC views exhibiting variations of 46%, 17%, and 16%, respectively. The retrieved A_B tends to be higher during winter for the NP and SP views, which is in agreement with the observed decrease in T_0 and T_{eq}. However, the large uncertainties (± 0.5 to ± 1.0) and biases (see Section 4.4) on A_B prohibit a confident inference of the presence and extent of seasonal variations.

However, as shown in Section 4.4.1 and Figure 4.7c, better constraints on R_{pl} (e.g., due to followup observations or assuming an otherwise motivated R_{pl} value as in Figure 4.7c), help reveal seasonal T_0, T_{eq}, and A_B variations. For example, an accurate and strong R_{pl} constraint would yield correct A_B estimates with uncertainties below ± 0.03. Given such constraints, Earth's seasonal T_0, T_{eq}, and A_B variations are easily detectable for the NP view with a future LIFE-like observatory for all R and S/N cases. For the SP view, detections of seasonal variations are also possible (except for the $R = 50$, $S/N = 10$ case). For the EqC view, which blends the two hemispheres, the seasonal variations are too small to yield significant detections.

4.5.3 Bioindicators and Their Atmospheric Seasonality

Earth's MIR spectrum contains features from numerous bioindicator gases. Examples are O_3 (photochemical product of bioindicator O_2), CH_4, and N_2O (see,

e.g., Schwieterman et al., 2018, for an extensive list). While N_2O is not detectable at the R and S/N considered, O_3 and CH_4 are (see Appendix 4.C). Yet, the sole detection of bioindicator gases is insufficient to infer life, since gases can be produced abiotically (see, e.g., Catling et al., 2018; Schwieterman et al., 2018; Harman and Domagal-Goldman, 2018). However, it remains unknown how accurately the absolute abundances of such gases need to be measured for a robust life inference. Thus, more work is required to conclude if the constraints on the absolute abundances presented in Section 4.4 (biases $\leq +1.0$ dex, uncertainties $\leq \pm 1.0$ dex) are sufficiently strong.

In contrast to detecting individual bioindicator gases, the simultaneous detection of multiple bioindicators is a more robust marker for biological activity. Further, as demonstrated in Section 4.4.2 and Figure 4.8, the constraints on relative gas abundances are better (uncertainty mostly $\leq \pm 0.5$ dex) and less biased than for absolute gas abundances. One multiple bioindicator we detect is the 'triple fingerprint', which is the simultaneous detection of atmospheric CO_2, H_2O, and O_3 (see, e.g., Selsis et al., 2002). Depending on the viewing angle, the retrieved $\log_{10}(H_2O/CO_2)$ ranges from -0.2 dex to -0.5 dex and the $\log_{10}(O_3/H_2O)$ from -2.6 dex to -3.2 dex (uncertainties $\leq \pm 0.6$ dex). These values lie between the average 1 bar and 0.1 bar ground truths ($\log_{10}(H_2O/CO_2)$: 1.2 dex at 1 bar, -2.3 dex at 0.1 bar; $\log_{10}(O_3/H_2O)$: -0.3 dex at 1 bar, -5.2 dex at 0.1 bar).

Another promising multiple bioindicator is the simultaneous detection of reducing and oxidizing species in an atmosphere (i.e. a strong chemical disequilibrium). An example hereof is the simultaneous presence of O_2 (or its photochemical product O_3) and CH_4 (Lovelock, 1965; Lippincott et al., 1967). Since the two species will react rapidly with each other, simultaneous presence over large timescales is only possible if both are continually replenished at a high rate by life (Lederberg, 1965). We find both O_3 and CH_4 to be present in Earth's atmosphere. For all but the $R = 50$, $S/N = 10$ retrievals, we constrain the relative abundance to $\log_{10}(CH_4/O_3) = 1.1$ dex (uncertainty $\leq \pm 0.5$ dex), which agrees with the 1 bar ground truth ratio of 1.2 dex.

While this constraint by itself is not a biosignature, it suggests that the atmosphere is in chemical disequilibrium. To determine the extent of the chemical disequilibrium, we require estimates of the atmospheric O_2 abundance, which is not directly constrainable via MIR observations. However, as suggested by Kozakis et al. (2022), the retrieved O_3 abundance can be used to estimate atmospheric

O_2 levels. This would allow us to quantify the strength of the disequilibrium and could provide a first indication for biological activity. Especially, in the context of an Earth-like planet orbiting a Sun-like star, the detection of such an O_2/O_3-CH_4 disequilibrium would represent a strong potential biosignature.

Research on the detectability of exoplanet biosignatures has predominantly focused on static evidence for life (e.g., the coexistence of O_2 and CH_4). However, the anticipated range of terrestrial planet atmospheres and the potential for both "false positives" and "false negatives" in conventional biosignatures (e.g., Selsis, 2002; Meadows, 2006; Reinhard et al., 2017; Catling et al., 2018; Krissansen-Totton et al., 2022) underscore the necessity to explore additional life detection strategies. A time-varying signal, like the seasonal variation in atmospheric composition, has been proposed to be a strong biosignature (e.g., Olson et al., 2018b), because it is a biologically modulated phenomenon that arises naturally on Earth and is highly likely to occur on other non-zero obliquity and eccentricity planets. Olson et al. (2018b) suggest, that atmospheric seasonality as a biosignature avoids many assumptions about specificities of metabolisms. Further, it offers a direct means to quantify biological fluxes, which would allow us to characterize, rather than simply identify, exoplanet biospheres. Yet, if we hope to leverage such time-dependent modulations to infer biological activity, they must be inferrable from disk-averaged exoplanet spectra.

In Mettler et al. (2023), we quantified the amplitudes of the seasonal variations in absorption strength by measuring the equivalent widths of the biosignature related absorption features in disk-integrated Earth spectra. Although we detected an atmospheric seasonality for O_3, CO_2, CH_4, and N_2O, the amplitude for Earth is small. Given the seasonal abundance variations of CO_2 and CH_4 on modern Earth (1% to 3%), disentangling such variations from the observational in future exoplanet observations seems unfeasible.

Since the retrieved absolute trace-gas abundances in Figure 4.7a are biased by degeneracies, we consider abundance ratios (Figure 4.8) to search for temporal variations. Generally, the uncertainties on the relative abundances for the $R = 50$, $S/N = 20$ and the $R = 100$ retrievals are small ($\leq \pm 0.4$ dex), and no significant differences between the viewing geometries are observable. Since these months represent Earth's two extremes, we expect the relative abundances for any other month to lie between these two extremes. In the ground truths, H_2O shows the

largest variability with 0.2 dex and 0.1 dex for the NP and SP views, respectively[11] (see Tables 4.6 and 4.8). Given these variances, a high confidence detection of seasonal variations in H_2O on Earth with LIFE is not possible for the considered R and S/N cases. Consequentially, detecting the atmospheric seasonality of other trace gases as a biosignature is not feasible either. Higher R and S/N LIFE observations of Earth would be required to be sensitive to such small variations in the trace gas abundances.

However, terrestrial exoplanets could display seasonality patterns that are very different from that of Earth or other Solar System planets. Given the extensive diversity among exoplanets (e.g., in terms of mass, size, host star type, and orbit), it is very well possible that some exhibit larger seasonal variations than Earth. Such seasonal signals could be amplified by several factors (see, e.g., Section 4.3 in Mettler et al., 2023): (1) shorter photochemical lifetimes and/or if saturated spectral bands were not saturated, (2) increasing orbital obliquity, which leads to greater seasonal contrast due to varying ice and vegetation cover, (3) moderately high obliquity promotes biological activity (e.g. photosynthetic activity) consequently leading to heightened variations in biosignature gases, (4) absence of competing effects from admixed hemispheres, which is particularly relevant for eccentric planets. The detectability of seasonality depends on both the magnitude of the biogenic signal and the degree to which the observation conditions mute that signal, and is likely optimized at intermediate obliquities, which are sufficient to produce a large-magnitude signal, yet not so extreme as to preclude viewing of the winter hemisphere.

For an Earth-like planet, the detectability of seasonality depends on the integration time required to reach the desired R and S/N. In this study, we assumed an integration time of 30 days for all spectra (see Section 4.2.1). For shorter integration times (e.g., 10 days), we do not expect our findings to change. Local daily and weekly changes in, for example, the surface temperature or the cloud coverage will not affect our characterization significantly, since they average out on a planetary scale. Further, seasonal changes on Earth occur on much larger timescales of several months. In contrast, seasonal changes will occur for longer observations (e.g., 90 days). The resulting spectrum will be averaged over the integration time, which results in smaller seasonal differences between two observations. Thus, the

[11] For the EqC view, the ground truth H_2O profile shows no significant differences between January and July. The reduced seasonality for equatorial views is expected, since the seasonal contrast increases with obliquity, and the effect of obliquity is the strongest near the poles.

detectability of seasonal variations will decrease for extended integration times.

4.6 Summary and Conclusion

In this study, we treated Earth as an exoplanet to examine how well it can be characterized from its MIR thermal emission spectrum. This is the first study that systematically ran atmospheric retrievals on simulated LIFE observations of real disk-integrated MIR Earth spectra for different viewing angles and seasons. By comparing the results to ground truths, we assessed the accuracy and robustness of the retrieved constraints and explored the applicability of simple 1D atmosphere models for characterizing the atmosphere of a real habitable planet with a global biosphere. Further, we investigated whether the viewing geometry has a measurable impact on the characterization of an Earth-like exoplanet and searched for signs of atmospheric seasonality, indicative of a biosphere.

Despite the biases evoked by parameter degeneracies, our results at the minimal LIFE requirements ($R = 50$, $S/N = 10$) find Earth to be a temperate habitable planet with detectable levels of CO_2, H_2O, O_3, CH_4. Moreover, we find that viewing geometry and the spatially and temporally integrated spectra only have a minor impact on the detectability of molecules, the retrieved relative abundances, and thus the characterization of Earth. The seasonal flux difference of 33% for the North Pole view leads to variations in the surface temperature T_0, the equilibrium temperature $T_{\rm eq}$, and the Bond albedo $A_{\rm B}$, which are detectable with LIFE for all tested R and S/N cases. If the planet radius $R_{\rm pl}$ is well constrained, temporal variations in $T_{\rm eq}$ and $A_{\rm B}$ are also observable for both the South Pole and mixed equatorial view (for $R = 50$, $S/N = 20$ and $R = 100$ retrievals). Finally, we find that Earth-like seasonal variations in biosignature gas abundances are not detectable with LIFE for the R and S/N cases considered.

Hence, from the six MIR observables of habitable and inhabited worlds listed in Section 4.1.2, we are able to constrain four (planetary energy budget, the presence of water and other molecules, the P–T-structure, and the molecular biosignatures). Regarding the surface conditions, we are able to accurately constrain T_0 despite Earth's patchy cloud nature. In contrast, all retrieved P_0 estimates are biased. In order to obtain a set of possible planetary surface condition solutions, climate models are required, which is beyond the scope of this work. Further, we looked for atmospheric seasonality in biosignature gases, which are

not detectable for all considered cases.

By running atmospheric retrievals on real disk-integrated Earth spectra and comparing the results to ground truths, we demonstrate retrievals on real exoplanet spectra will likely yield biased parameter estimates. Thus, care needs to be taken when considering the absolute posteriors. Instead, reduced posteriors or posterior ratios should be considered. These provide significantly less biased parameter estimates while retaining valuable information about the atmospheric state. This could help identify seasonal variations or bioindicators. Furthermore, we find that the commonly used simplifying assumptions of vertically constant abundance profiles and a cloud-free atmosphere will likely significantly bias retrieval results. Future work is required to investigate such effects in detail and search for potential remedies.

Nevertheless, from investigating Earth from afar, we learn that LIFE would correctly identify Earth as a planet where life could thrive, with detectable levels of bioindicators, a temperate climate, and surface conditions that allow for liquid surface water. The journey to characterize Earth-like planets and detect potentially habitable worlds has only started. Our work demonstrates that next generation, optimized space missions can assess whether nearby temperate terrestrial exoplanets are habitable or even inhabited. This provides a promising step forward in our quest to understand distant worlds.

Appendix

4.A Disk-Integrated Atmospheric Profiles Ground Truths for January

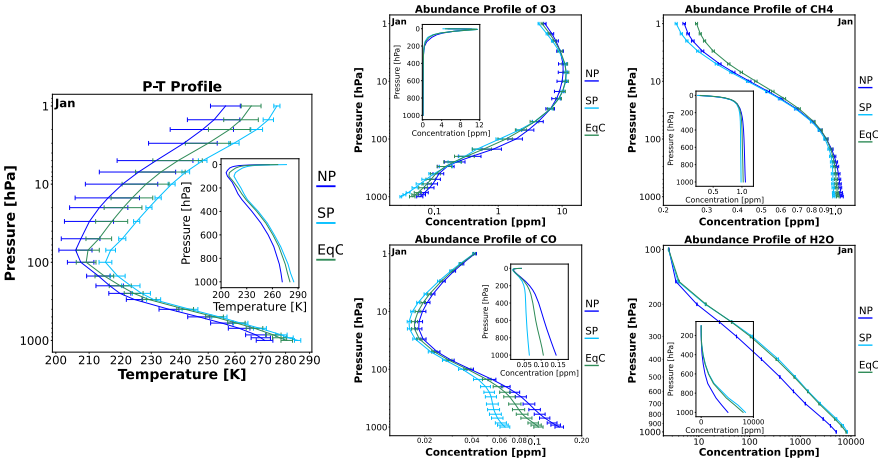

Figure 4.9: Disk-integrated atmospheric profiles for January: From left to right: P–T profile followed by O_3, CH_4, CO, and H_2O atmospheric profiles. The different colors correspond to the viewing geometries: NP (blue), SP (turquoise), EqC (green)

4.B Cloud Fractions for 2017

In order to compile Figure 4.10, we have sourced daily level 3 satellite data for the year 2017 from the CERES-Flight Model 3 (FM3) and FM4 instruments on the Aqua platform. Specifically, we have used the CERES Time-Interpolated TOA Fluxes, Clouds and Aerosols Daily Aqua Edition4A `CER_SSF1deg-Day_Aqua-MODIS_Edition4A` data product (NASA/LARC/SD/ASDC, 2015). The provided cloud properties are averaged for both day and night (24-hour) and day-only time periods. Furthermore, they are stratified into 4 atmospheric layers (surface-700 hPa, 700 hPa - 500 hPa, 500 hPa - 300 hPa, 300 hPa - 100 hPa) and a total of all layers. For our analysis we have used the latter, mapped the total cloud fractions onto the globe and calculated the disk-averaged value for each viewing geometry per day.

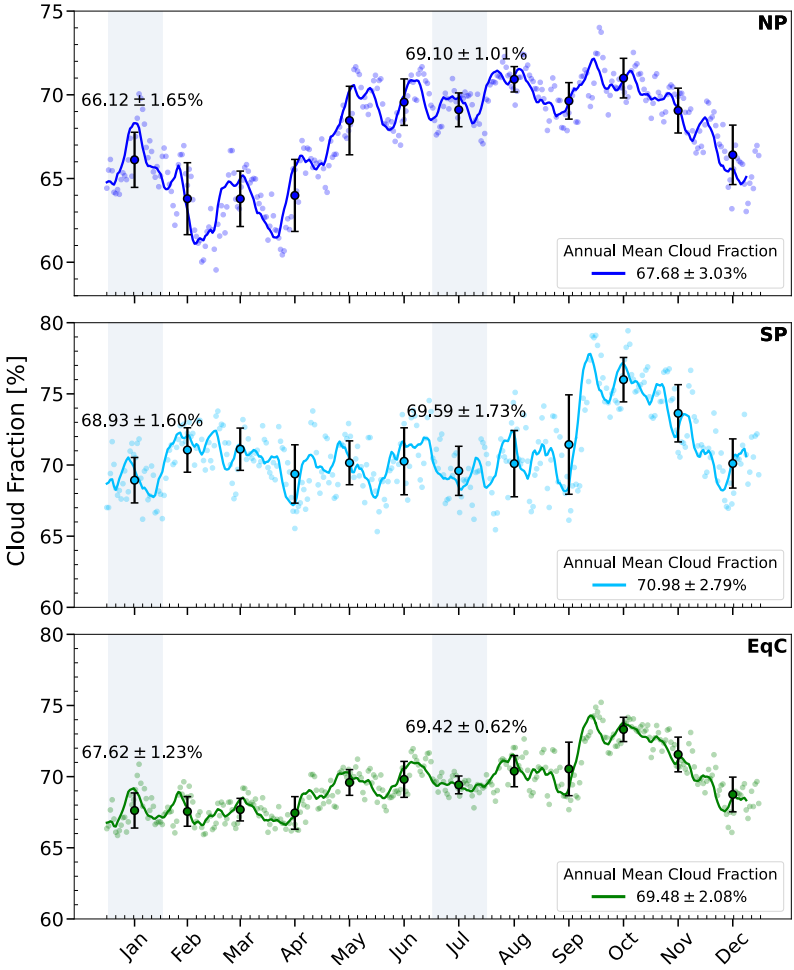

Figure 4.10: Total Cloud Fractions: This figure illustrates the total cloud fractions for the year 2017 across the investigated viewing geometries in this study. The data are derived from a level 3 satellite product (NASA/LARC/SD/ASDC, 2015). The scattered points represent daily measurements, while the solid line depicts their rolling average with a window size of 8 days. The central points in the error bar scatter plot represent the monthly mean cloud coverage, while the accompanying error bars indicate the corresponding standard deviation. The shaded areas highlight the months January and July which were investigated in this study. The annotated cloud coverage values signify the monthly cloud fractions for these specific months.

4.C Retrieval Model Selection

We performed a Bayesian model comparison to justify our choice of atmospheric forward model used for the retrieval analysis in this work (see Section 4.3.3 and Table 4.2). In our analysis, we ran atmospheric retrievals (using the routine introduced in Section 4.3) assuming the following six atmospheric forward models $\mathscr{M}_\mathrm{i}$ of increasing complexity (see Table 4.4 for the full parameter configuration of each model and the assumed priors):

- $\mathscr{M}_1$: (11 parameters) – In addition to the five polynomial P–T parameters a_i (see Eq. 4.1 in Section 4.3.3), we retrieve for the planet's radius R_pl, mass M_pl, and surface pressure P_0. The model atmosphere only contains N_2, O_2, and CO_2.
- $\mathscr{M}_2$: (12 parameters) – In addition to the $\mathscr{M}_1$ parameters, we add H_2O to the species present in the model atmosphere.
- $\mathscr{M}_3$: (13 parameters) – In addition to the $\mathscr{M}_2$ parameters, we add O_3 to the species present in the model atmosphere.
- $\mathscr{M}_4$: (14 parameters) – In addition to the $\mathscr{M}_3$ parameters, we add CH_4 to the species present in the model atmosphere.
- $\mathscr{M}_5$: (15 parameters) – In addition to the $\mathscr{M}_4$ parameters, we add CO to the species present in the model atmosphere.
- $\mathscr{M}_6$: (15 parameters) – In addition to the $\mathscr{M}_4$ parameters, we add N_2O to the species present in the model atmosphere.

Let us consider two retrievals assuming different atmospheric forward models $\mathscr{A}$ and $\mathscr{B}$ on the same disk-integrated Earth spectrum. Both results are characterized by their respective log-evidences $\ln(\mathscr{Z}_\mathscr{A})$ and $\ln(\mathscr{Z}_\mathscr{B})$. The Bayes' factor K can be calculated from the evidences as follows:

$$\log_{10}(K) = \frac{\ln(\mathscr{Z}_\mathscr{A}) - \ln(\mathscr{Z}_\mathscr{B})}{\ln(10)}. \tag{4.2}$$

The Bayes' factor K provides a metric that quantifies which out of the two models $\mathscr{A}$ and $\mathscr{B}$ performs better for a given spectrum. The Jeffreys scale (Jeffreys, 1998, Table 4.5) provides a possible interpretation for the value of the Bayes factor K. A

$\log_{10}(K)$ value above zero marks a preference for model $\mathcal{A}$, whereas values below zero indicate preference for $\mathcal{B}$.

Figure 4.11 summarizes the results from our model comparison efforts for all considered disk-integrated Earth spectra (viewing geometries, R, and S/N). The $\mathcal{M}_i$ correspond to the models listed above, while the $\mathcal{S}_i$ represent different combinations of R and S/N of the input spectra ($\mathcal{S}_1$: $R = 50$, $S/N = 10$; $\mathcal{S}_2$: $R = 50$, $S/N = 20$; $\mathcal{S}_3$: $R = 100$, $S/N = 10$; $\mathcal{S}_4$: $R = 100$, $S/N = 20$). Green squares indicate positive $\log_{10}(K)$ values and preference of the $\mathcal{M}_i$ with the high i, while red squares represent negative $\log_{10}(K)$ values and preference of the low i $\mathcal{M}_i$. The color shading indicates the strength of the preference.

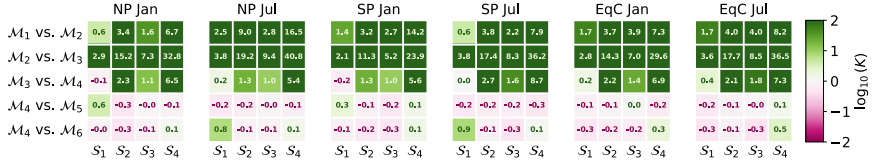

Figure 4.11: Bayes' factor $\log_{10}(K)$ for the comparison of the different models in Appendix 4.C. Positive values of $\log_{10}(K)$ (green) indicate preference of the model $\mathcal{M}_i$ with the higher i value, while negative values (red) indicate the opposite. The color shading indicates the strength of the preference. The $\mathcal{S}_i$ represent different combinations of R and S/N of the input spectra ($\mathcal{S}_1$: $R = 50$, $S/N = 10$; $\mathcal{S}_2$: $R = 50$, $S/N = 20$; $\mathcal{S}_3$: $R = 100$, $S/N = 10$; $\mathcal{S}_4$: $R = 100$, $S/N = 20$). Columns summarize the results obtained for the viewing geometries. From left to right: NP Jan, NP Jul, SP Jan, Sp Jul, EqC Jan, and EqC Jul.

We observe that $\mathcal{M}_3$ is generally preferred over $\mathcal{M}_2$ and $\mathcal{M}_1$ for all considered spectra. Thus, H_2O and O_3 are confidently detectable with LIFE. Further, $\mathcal{M}_4$ is preferred over $\mathcal{M}_3$ for all but the $R = 50$, $S/N = 10$ cases, suggesting that also CH_4 is detectable. In contrast, the $\log_{10}(K)$ value of roughly 0 indicates that models $\mathcal{M}_5$ and $\mathcal{M}_6$ perform similarly well as model $\mathcal{M}_4$. However, since $\mathcal{M}_5$ and $\mathcal{M}_6$ each require one additional parameter (abundance of CO or N_2O, respectively), we prefer model $\mathcal{M}_4$. This indicates that neither CO nor N_2O are detectable in Earth's atmosphere at the R and S/N considered here, which is in agreement with the findings in Konrad et al. (2022). In conclusion, $\mathcal{M}_4$ shows the best performance of all models considered. Therefore, we used $\mathcal{M}_4$ as forward model in the retrieval analyses presented in main part of this manuscript.

Table 4.4: Parameter configurations of the nine tested retrieval forward models. In the third column we specify the priors assumed in the retrievals. We denote a boxcar prior with lower threshold x and upper threshold y as $\mathcal{U}(x, y)$; For a Gaussian prior with mean μ and standard deviation σ, we write $\mathcal{G}(\mu, \sigma)$. The last nine columns summarize the model parameters used by each of the different forward models tested in the retrievals (✓ = used, × = unused).

Parameter	Description	Prior	Parameter Configuration					
			$\mathcal{M}_1$	$\mathcal{M}_2$	$\mathcal{M}_3$	$\mathcal{M}_4$	$\mathcal{M}_5$	$\mathcal{M}_6$
a_4	P–T parameter (degree 4)	$\mathcal{U}(0, 10)$	✓	✓	✓	✓	✓	✓
a_3	P–T parameter (degree 3)	$\mathcal{U}(0, 100)$	✓	✓	✓	✓	✓	✓
a_2	P–T parameter (degree 2)	$\mathcal{U}(0, 500)$	✓	✓	✓	✓	✓	✓
a_1	P–T parameter (degree 1)	$\mathcal{U}(0, 500)$	✓	✓	✓	✓	✓	✓
a_0	P–T parameter (degree 0)	$\mathcal{U}(0, 1000)$	✓	✓	✓	✓	✓	✓
$\log_{10}(P_0)$	$\log_{10}$(Surface pressure [bar])	$\mathcal{U}(-4, 2)$	✓	✓	✓	✓	✓	✓
$R_{\rm pl}$	Planet radius [$R_\oplus$]	$\mathcal{G}(1.0, 0.2)$	✓	✓	✓	✓	✓	✓
$\log_{10}(M_{\rm pl})$	$\log_{10}$(Planet mass [$M_\oplus$])	$\mathcal{G}(0.0, 0.4)$	✓	✓	✓	✓	✓	✓
$\log_{10}(N_2)$	$\log_{10}$(N_2 mass fraction)	$\mathcal{U}(-10, 0)$	✓	✓	✓	✓	✓	✓
$\log_{10}(O_2)$	$\log_{10}$(O_2 mass fraction)	$\mathcal{U}(-10, 0)$	✓	✓	✓	✓	✓	✓
$\log_{10}(CO_2)$	$\log_{10}$(CO_2 mass fraction)	$\mathcal{U}(-10, 0)$	✓	✓	✓	✓	✓	✓
$\log_{10}(H_2O)$	$\log_{10}$(H_2O mass fraction)	$\mathcal{U}(-10, 0)$	×	✓	✓	✓	✓	✓
$\log_{10}(O_3)$	$\log_{10}$(O_3 mass fraction)	$\mathcal{U}(-10, 0)$	×	×	✓	✓	✓	✓
$\log_{10}(CH_4)$	$\log_{10}$(CH_4 mass fraction)	$\mathcal{U}(-10, 0)$	×	×	×	✓	✓	✓
$\log_{10}(CO)$	$\log_{10}$(CO mass fraction)	$\mathcal{U}(-10, 0)$	×	×	×	×	✓	×
$\log_{10}(N_2O)$	$\log_{10}$(N_2O mass fraction)	$\mathcal{U}(-10, 0)$	×	×	×	×	×	✓

Table 4.5: Jeffreys scale (Jeffreys, 1998). Scale for interpretation of the Bayes' factor K for two models $\mathcal{A}$ and $\mathcal{B}$. The scale is symmetrical, i.e., negative values of $\log_{10}(K)$ correspond to very weak, substantial, strong, or decisive support for model $\mathcal{B}$.

$\log_{10}(K)$	Probability	Strength of Evidence
< 0	< 0.5	Support for $\mathcal{B}$
$0 - 0.5$	$0.5 - 0.75$	Very weak support for $\mathcal{A}$
$0.5 - 1$	$0.75 - 0.91$	Substantial support for $\mathcal{A}$
$1 - 2$	$0.91 - 0.99$	Strong support for $\mathcal{A}$
> 2	> 0.99	Decisive support for $\mathcal{A}$

4.D Calculation of the Equilibrium Temperature and Bond albedo

The equilibrium temperature $T_{\rm eq}$ and the Bond albedo $A_{\rm B}$ are not directly determined in our atmospheric retrievals. However, both parameters provide important information about the energy budget of Earth. In the following, we summarize how we derive estimates for $T_{\rm eq}$ and $A_{\rm B}$ from the retrieved parameter posteriors.

To determine $T_{\rm eq}$, we first calculate the MIR spectra corresponding to the retrieved parameter posteriors over a wide wavelength range. For each spectrum, we then integrate the flux to estimate the total emitted flux and use the Stefan-Boltzmann law to compute the effective temperature $T_{\rm eff}$ of a black-body with the same flux, which corresponds to the $T_{\rm eq}$ of the planet. From the resulting $T_{\rm eq}$ distribution, we can deduce the planetary $A_{\rm B}$ distribution using:

$$A_{\rm B} = 1 - 16\pi\sigma \frac{a_P^2 T_{\rm eq}^4}{L_*}. \tag{4.3}$$

Here, σ is the Stefan–Boltzmann constant, a_P is the semi-major axis of the planet orbit around its star, and L_* is the luminosity of the star. To calculate $A_{\rm B}$, we assume that a_P and L_* to be known with an accuracy of ±1% (i.e., for an exo-Earth, $a_P = 1.00 \pm 0.01$ AU, $L_* = 1.00 \pm 0.01\ L_\odot$ with the solar luminosity $L_\odot$). For each value in the $T_{\rm eq}$ distribution, we randomly draw an a_P and L_* value from two uncorrelated normal distributions and calculate the corresponding $A_{\rm B}$ value. This yields the distribution for the planetary Bond albedo $A_{\rm B}$.

4.E Reduction of Retrieved Posteriors

In Section 4.4.1, we reduced the retrieved posterior distributions to fixed values of $P_0 = 1$ bar and $R_{\rm pl} = 1 R_\oplus$ by assuming a linear correlation between P_0 or $R_{\rm pl}$ and the remaining posteriors. Here, we outline the method used to reduce the posterior distributions. A schematic illustration showing both the true and the reduced posteriors can be found in Figure 4.12.

For $\beta_{\rm H_2O}$ (slope of H_2O abundance profile), we choose a broad prior that allows for both vertically increasing and decreasing H_2O profiles.

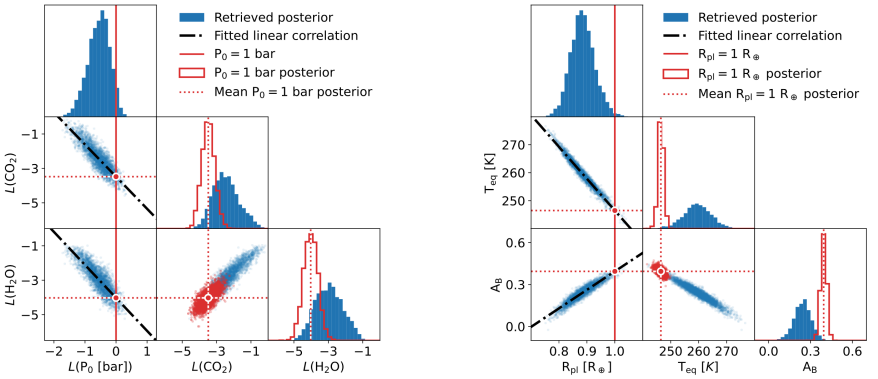

Figure 4.12: Reduction of selected retrieved posterior distributions with respect to P_0 (left plot) and R_{pl} (right plot). The blue-filled histograms on the diagonal of the corner plots show the true retrieved parameter posteriors. Red-outlined histograms indicate the reduced posteriors. Below the diagonal, we show the 2D parameter posteriors in blue (true posteriors) and red (reduced posteriors) scatter plots. Black dashed-dotted lines represent the fitted linear correlation between parameters. Solid red lines mark the $P_0 = 1$ bar and $R_{\mathrm{pl}} = 1 R_{\oplus}$ position corresponding to the reduced posteriors, red-dotted lines indicate the median of the reduced posteriors.

In the following, let us consider one point in the true posterior distribution. We denote the value of P_0 or R_{pl} parameter (i.e., the parameter we want to reduce over) as $\theta_{\mathrm{reduce,true}}$ and the remaining parameter values as $\theta_{\mathrm{param,true}}$. We assume a linear correlation between $\theta_{\mathrm{red,true}}$ and $\theta_{\mathrm{param,true}}$. This means that we can predict a value $\theta_{\mathrm{param,pred}}$ for a given value $\theta_{\mathrm{red,true}}$ as follows:

$$\theta_{\mathrm{param,pred}} = m \cdot \theta_{\mathrm{red,true}} + q. \tag{4.4}$$

Here, m is the slope and q the offset with respect to the origin of the linear model. $\theta_{\mathrm{param,pred}}$ is the parameter value predicted by the linear model. We search for the best fit linear model by minimizing the square difference Δ between $\theta_{\mathrm{param,pred}}$ and $\theta_{\mathrm{param,true}}$:

$$\Delta = \sum_{\mathrm{Posterior}} \left(\theta_{\mathrm{param,pred}} - \theta_{\mathrm{param,true}}\right)^2 = \sum_{\mathrm{Posterior}} \left(m \cdot \theta_{\mathrm{red,true}} + q - \theta_{\mathrm{param,true}}\right)^2. \tag{4.5}$$

The best fit linear models are indicated in Figure 4.12 as black dash-dotted lines. From the figure, we see that the correlations between the parameters considered here are well described by our linear model. In the next step, we fix the value of $\theta_{\text{red,true}}$ to $\theta_{\text{red,fix}}$ and calculate the reduced posterior values $\theta_{\text{param,red}}$ of the other parameters as follows:

$$\theta_{\text{param,red}} = \theta_{\text{param,true}} + m \cdot \left(\theta_{\text{red,fix}} - \theta_{\text{red,true}}\right). \tag{4.6}$$

This yields the reduced posterior distribution of a parameter, which we plot in Figure 4.12. This reduction method allows us to remove the effect of one parameter on the posterior distribution, and identify the origin of biases in the retrieval results.

4.F Supplementary Data from the Retrievals

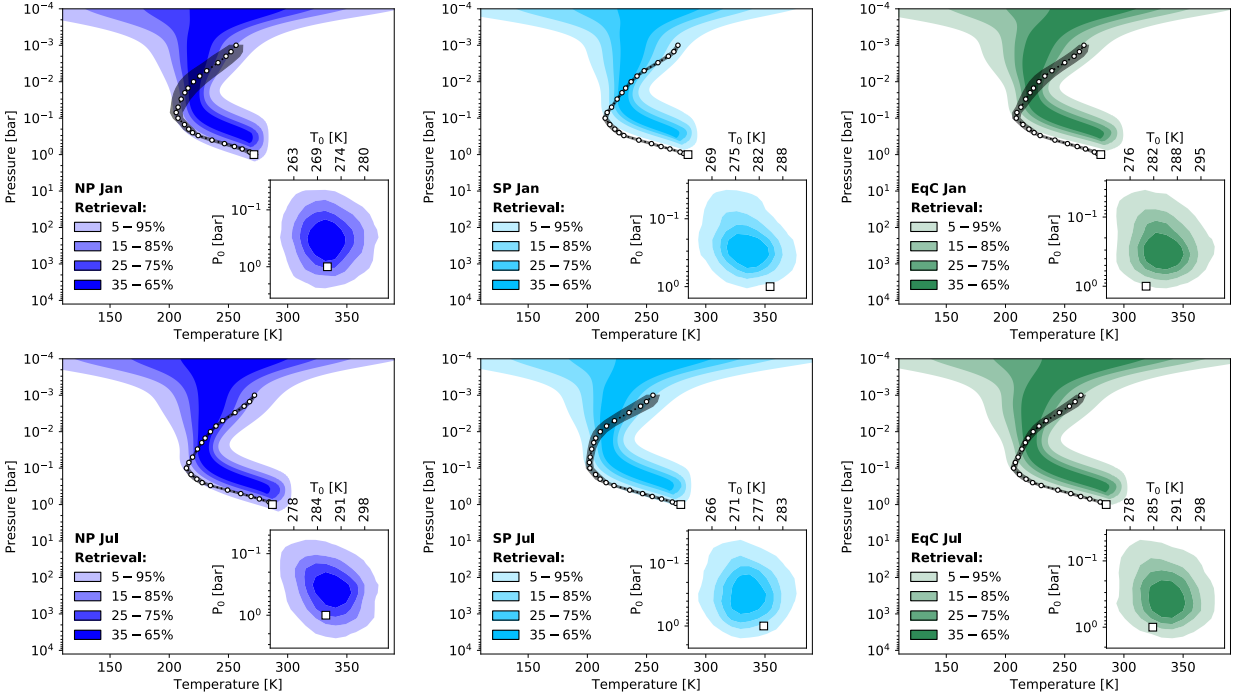

Figure 4.13: P–T profiles retrieved for the six disk-integrated, $R = 50$ and LIFEsim $S/N = 20$ Earth spectra. The color-shaded areas indicate percentiles of the retrieved P–T profiles. The white square marker shows the true surface pressure P_0 and temperature T_0, the white circular markers show the true P–T structure, and the gray shaded area indicates the uncertainty thereon. In the bottom right of each panel, we plot the 2D P_0-T_0 posterior, to visualize the constraints on the retrieved surface conditions. Each panel shows the result for one viewing angle. From top-left to bottom-right: NP Jan, SP Jan, EqC Jan, NP Jul, SP Jul, and EqC Jul.

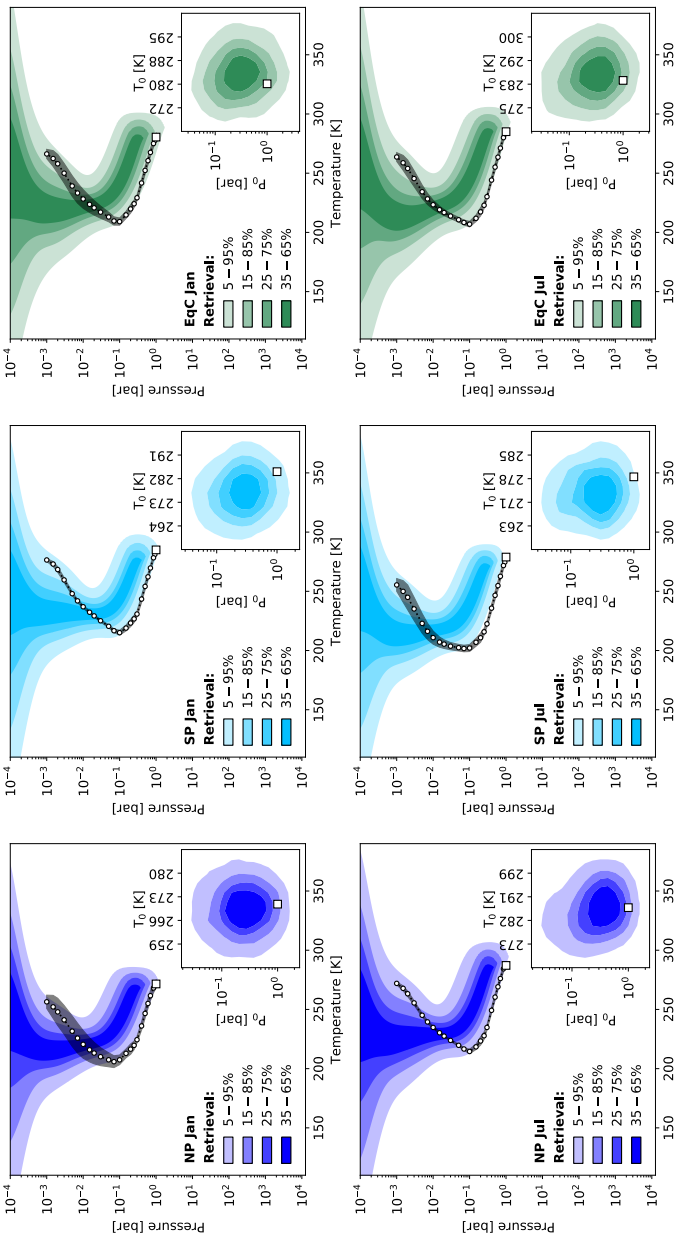

Figure 4.14: As for Figure 4.13, but for the $R = 100$ and LIFESIM $S/N = 10$ Earth spectra.

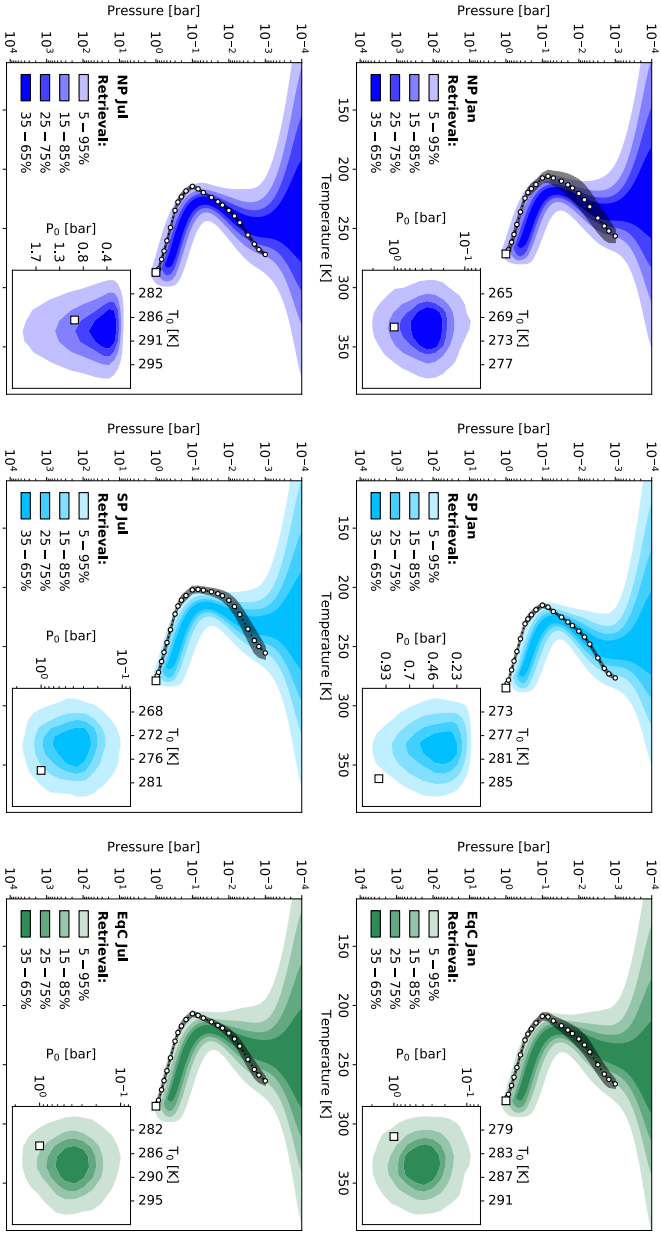

Figure 4.15: As for Figure 4.13, but for the $R = 100$ and LIFESIM $S/N = 20$ Earth spectra.

Table 4.6: Numeric values corresponding to the retrieved parameter posteriors in Figures 4.7a, 4.7b, 4.7c, and 4.8 for the NP viewing angle. Here, $L(\cdot)$ abbreviates $\log_{10}(\cdot)$. We provide the median of the retrieved posterior and indicate the 16% − 84% range via +/− indices. We further provide the ground truth values. If independent of the atmospheric pressure, we provide a single value. Otherwise, we provide the ground truths at pressures 1 bar, 10^{-1} bar, 10^{-2} bar, and 10^{-3} bar if available.

		NP Jan − Ground Truths				NP Jan − Posteriors				NP Jul − Ground Truths				NP Jul − Posteriors			
		Pressure Levels [bar]				$R = 50$		$R = 100$		Pressure Levels [bar]				$R = 50$		$R = 100$	
	Posterior	1	10^{-1}	10^{-2}	10^{-3}	$S/N = 10$	$S/N = 20$	$S/N = 10$	$S/N = 20$	1	10^{-1}	10^{-2}	10^{-3}	$S/N = 10$	$S/N = 20$	$S/N = 10$	$S/N = 20$
Figure 6	$L(P_0[\text{bar}])$	0.0				$-0.9^{+0.3}_{-0.5}$	$-0.5^{+0.4}_{-0.4}$	$-0.6^{+0.4}_{-0.4}$	$-0.4^{+0.3}_{-0.3}$	0.0				$-0.4^{+0.4}_{-0.4}$	$-0.4^{+0.4}_{-0.4}$	$-0.5^{+0.3}_{-0.4}$	$-0.4^{+0.3}_{-0.2}$
	T_0[K]	271.5				$267.3^{+9.2}_{-8.4}$	$271.3^{+5.2}_{-4.8}$	$270.0^{+6.6}_{-6.4}$	$271.6^{+3.5}_{-3.5}$	287.2				$285.1^{+10.9}_{-10.2}$	$288.3^{+6.0}_{-6.3}$	$286.5^{+7.8}_{-7.6}$	$288.9^{+4.0}_{-4.3}$
	$R_{pl}[R_\oplus]$	1.0				$0.9^{+0.1}_{-0.1}$	$0.9^{+0.0}_{-0.0}$	$0.9^{+0.1}_{-0.1}$	$0.9^{+0.0}_{-0.0}$	1.0				$0.9^{+0.1}_{-0.1}$	$0.9^{+0.1}_{-0.0}$	$0.9^{+0.1}_{-0.1}$	$0.9^{+0.0}_{-0.0}$
	$L(M_{pl}[M_\oplus])$	0.0				$-0.1^{+0.3}_{-0.3}$	$-0.0^{+0.3}_{-0.3}$	$-0.0^{+0.3}_{-0.3}$	$-0.0^{+0.3}_{-0.3}$	0.0				$-0.1^{+0.4}_{-0.3}$	$-0.0^{+0.3}_{-0.3}$	$-0.0^{+0.3}_{-0.3}$	$0.0^{+0.3}_{-0.4}$
	$L(CO_2)$	−3.4				$-1.8^{+0.9}_{-0.9}$	$-2.6^{+0.9}_{-0.8}$	$-2.3^{+0.9}_{-0.8}$	$-2.8^{+0.6}_{-0.6}$	−3.4				$-2.6^{+0.9}_{-0.9}$	$-2.7^{+0.8}_{-0.7}$	$-2.4^{+0.9}_{-0.7}$	$-2.8^{+0.6}_{-0.6}$
	$L(H_2O)$	−2.3	−5.6	–	–	$-2.3^{+0.8}_{-0.9}$	$-3.0^{+0.9}_{-0.9}$	$-2.7^{+0.9}_{-0.9}$	$-3.3^{+0.6}_{-0.6}$	−2.1	−5.6	–	–	$-2.5^{+0.7}_{-0.9}$	$-2.7^{+0.7}_{-0.7}$	$-2.4^{+0.8}_{-0.8}$	$-2.9^{+0.6}_{-0.6}$
	$L(O_3)$	−7.3	−5.8	−5.0	−5.3	$-5.2^{+0.8}_{-0.7}$	$-5.8^{+0.8}_{-0.6}$	$-5.5^{+0.8}_{-0.7}$	$-5.9^{+0.5}_{-0.5}$	−7.3	−6.0	−5.0	−5.4	$-5.8^{+0.8}_{-0.7}$	$-5.8^{+0.7}_{-0.6}$	$-5.6^{+0.8}_{-0.6}$	$-5.9^{+0.5}_{-0.5}$
	$L(CH_4)$	−6.0	−6.1	−6.4	−6.7	$-4.4^{+1.2}_{-1.6}$	$-4.7^{+0.9}_{-0.8}$	$-4.6^{+1.0}_{-0.9}$	$-4.9^{+0.6}_{-0.6}$	−6.0	−6.1	−6.4	−6.7	$-5.0^{+1.2}_{-1.5}$	$-4.7^{+0.8}_{-0.7}$	$-4.6^{+1.0}_{-0.8}$	$-4.8^{+0.6}_{-0.6}$
	T_{eq}[K]	246.8				$252.6^{+8.5}_{-8.2}$	$257.2^{+4.7}_{-4.6}$	$255.8^{+6.1}_{-6.5}$	$257.9^{+3.2}_{-3.2}$	258.3				$265.1^{+10.0}_{-10.7}$	$269.0^{+5.5}_{-6.8}$	$266.8^{+7.4}_{-8.3}$	$270.1^{+3.6}_{-4.1}$
	A_B	0.38				$0.32^{+0.09}_{-0.10}$	$0.27^{+0.05}_{-0.06}$	$0.29^{+0.07}_{-0.07}$	$0.26^{+0.04}_{-0.04}$	0.26				$0.18^{+0.13}_{-0.13}$	$0.13^{+0.09}_{-0.08}$	$0.16^{+0.10}_{-0.10}$	$0.11^{+0.05}_{-0.05}$
Figure 7	$L(CO_2)$	−3.4				$-3.3^{+0.5}_{-0.5}$	$-3.5^{+0.4}_{-0.4}$	$-3.4^{+0.4}_{-0.4}$	$-3.5^{+0.3}_{-0.3}$	−3.4				$-3.4^{+0.6}_{-0.5}$	$-3.4^{+0.4}_{-0.4}$	$-3.4^{+0.4}_{-0.4}$	$-3.4^{+0.4}_{-0.4}$
	$L(H_2O)$	−2.3	−5.6	–	–	$-3.5^{+0.5}_{-0.6}$	$-4.0^{+0.4}_{-0.4}$	$-3.9^{+0.5}_{-0.5}$	$-4.1^{+0.4}_{-0.4}$	−2.1	−5.6	–	–	$-3.2^{+0.5}_{-0.6}$	$-3.4^{+0.4}_{-0.4}$	$-3.4^{+0.4}_{-0.4}$	$-3.5^{+0.3}_{-0.4}$
	$L(O_3)$	−7.3	−5.8	−5.0	−5.3	$-6.6^{+0.4}_{-0.4}$	$-6.5^{+0.4}_{-0.4}$	$-6.5^{+0.4}_{-0.4}$	$-6.5^{+0.3}_{-0.3}$	−7.3	−6.0	−5.0	−5.4	$-6.4^{+0.5}_{-0.4}$	$-6.4^{+0.3}_{-0.3}$	$-6.4^{+0.4}_{-0.4}$	$-6.4^{+0.3}_{-0.4}$
	$L(CH_4)$	−6.0	−6.1	−6.4	−6.7	$-6.0^{+0.8}_{-1.5}$	$-5.6^{+0.4}_{-0.5}$	$-5.7^{+0.5}_{-0.6}$	$-5.6^{+0.4}_{-0.4}$	−6.0	−6.1	−6.4	−6.7	$-5.9^{+0.7}_{-1.2}$	$-5.5^{+0.4}_{-0.4}$	$-5.6^{+0.5}_{-0.5}$	$-5.5^{+0.4}_{-0.4}$
Figure 8	$L(P_0[\text{bar}])$	0.0				$-0.9^{+0.3}_{-0.5}$	$-0.7^{+0.4}_{-0.4}$	$-0.7^{+0.4}_{-0.4}$	$-0.5^{+0.3}_{-0.2}$	0.0				$-0.5^{+0.4}_{-0.4}$	$-0.7^{+0.3}_{-0.3}$	$-0.7^{+0.3}_{-0.4}$	$-0.6^{+0.3}_{-0.2}$
	T_0[K]	271.5				$261.3^{+2.9}_{-2.0}$	$260.1^{+1.3}_{-1.0}$	$260.7^{+1.9}_{-1.3}$	$259.1^{+0.7}_{-0.6}$	287.2				$278.4^{+4.1}_{-3.0}$	$278.2^{+2.2}_{-1.6}$	$278.9^{+3.3}_{-2.3}$	$275.8^{+1.1}_{-0.9}$
	T_{eq}[K]	246.8				$247.1^{+1.9}_{-1.8}$	$246.3^{+0.9}_{-0.9}$	$246.8^{+1.2}_{-1.3}$	$246.4^{+0.6}_{-0.6}$	258.3				$258.2^{+2.1}_{-2.0}$	$257.4^{+1.0}_{-1.0}$	$258.0^{+1.5}_{-1.4}$	$257.2^{+0.7}_{-0.7}$
	A_B	0.38				$0.38^{+0.03}_{-0.03}$	$0.39^{+0.02}_{-0.02}$	$0.38^{+0.02}_{-0.02}$	$0.39^{+0.02}_{-0.02}$	0.26				$0.26^{+0.03}_{-0.04}$	$0.27^{+0.02}_{-0.03}$	$0.26^{+0.03}_{-0.03}$	$0.28^{+0.02}_{-0.02}$
Figure 9	$L\left(\frac{H_2O}{CO_2}\right)$	1.1	−2.2	–	–	$-0.5^{+0.6}_{-0.6}$	$-0.5^{+0.3}_{-0.3}$	$-0.5^{+0.4}_{-0.4}$	$-0.5^{+0.2}_{-0.2}$	1.3	−2.2	–	–	$0.0^{+0.6}_{-0.6}$	$-0.1^{+0.3}_{-0.3}$	$-0.1^{+0.4}_{-0.4}$	$-0.1^{+0.2}_{-0.2}$
	$L\left(\frac{O_3}{CO_2}\right)$	−3.9	−2.4	−1.7	−1.9	$-3.3^{+0.5}_{-0.4}$	$-3.2^{+0.3}_{-0.3}$	$-3.2^{+0.3}_{-0.3}$	$-3.1^{+0.2}_{-0.2}$	−3.9	−2.6	−1.6	−2.0	$-3.2^{+0.5}_{-0.5}$	$-3.2^{+0.3}_{-0.3}$	$-3.2^{+0.3}_{-0.3}$	$-3.1^{+0.2}_{-0.2}$
	$L\left(\frac{CH_4}{CO_2}\right)$	−2.6	−2.7	−3.0	−3.3	$-2.5^{+0.8}_{-1.5}$	$-2.1^{+0.3}_{-0.4}$	$-2.2^{+0.4}_{-0.6}$	$-2.1^{+0.2}_{-0.2}$	−2.6	−2.7	−3.0	−3.3	$-2.3^{+0.7}_{-1.2}$	$-2.1^{+0.3}_{-0.4}$	$-2.1^{+0.4}_{-0.5}$	$-2.0^{+0.2}_{-0.2}$
	$L\left(\frac{O_3}{H_2O}\right)$	−4.9	−0.1	–	–	$-2.8^{+0.5}_{-0.4}$	$-2.7^{+0.3}_{-0.3}$	$-2.7^{+0.4}_{-0.4}$	$-2.6^{+0.2}_{-0.2}$	−5.2	−0.4	–	–	$-3.2^{+0.4}_{-0.4}$	$-3.1^{+0.3}_{-0.2}$	$-3.2^{+0.3}_{-0.3}$	$-3.0^{+0.2}_{-0.2}$
	$L\left(\frac{CH_4}{H_2O}\right)$	−3.7	−0.4	–	–	$-2.0^{+0.9}_{-1.6}$	$-1.7^{+0.4}_{-0.4}$	$-1.7^{+0.5}_{-0.6}$	$-1.6^{+0.3}_{-0.3}$	−4.0	−0.5	–	–	$-2.3^{+0.7}_{-1.5}$	$-2.0^{+0.4}_{-0.4}$	$-2.1^{+0.5}_{-0.6}$	$-1.9^{+0.2}_{-0.3}$
	$L\left(\frac{CH_4}{O_3}\right)$	1.3	−0.3	−1.3	−1.3	$0.8^{+0.6}_{-1.3}$	$1.0^{+0.3}_{-0.3}$	$1.0^{+0.4}_{-0.4}$	$1.0^{+0.2}_{-0.2}$	1.3	−0.1	−1.4	−1.3	$0.9^{+0.6}_{-1.2}$	$1.1^{+0.3}_{-0.3}$	$1.1^{+0.3}_{-0.4}$	$1.1^{+0.2}_{-0.2}$

		SP Jan – Ground Truths				SP Jan – Posteriors				SP Jul – Ground Truths				SP Jul – Posteriors			
		Pressure Levels [bar]				$R = 50$		$R = 100$		Pressure Levels [bar]				$R = 50$		$R = 100$	
	Posterior	1	10^{-1}	10^{-2}	10^{-3}	$S/N = 10$	$S/N = 20$	$S/N = 10$	$S/N = 20$	1	10^{-1}	10^{-2}	10^{-3}	$S/N = 10$	$S/N = 20$	$S/N = 10$	$S/N = 20$
Figure 6	$L(P_0[\text{bar}])$	0.0				$-0.8^{+0.3}_{-0.5}$	$-0.6^{+0.3}_{-0.4}$	$-0.6^{+0.3}_{-0.4}$	$-0.5^{+0.2}_{-0.3}$	0.0				$-0.7^{+0.4}_{-0.5}$	$-0.5^{+0.3}_{-0.4}$	$-0.6^{+0.3}_{-0.4}$	$-0.4^{+0.3}_{-0.3}$
	T_0[K]	285.0				$274.7^{+9.6}_{-8.9}$	$278.3^{+5.6}_{-5.6}$	$277.5^{+7.0}_{-6.9}$	$279.3^{+3.6}_{-3.7}$	278.9				$271.1^{+9.4}_{-8.9}$	$274.6^{+5.4}_{-5.0}$	$273.8^{+6.7}_{-6.4}$	$274.8^{+3.8}_{-3.5}$
	$R_{pl}[R_\oplus]$	1.0				$0.9^{+0.1}_{-0.1}$	$0.9^{+0.1}_{-0.0}$	$0.9^{+0.1}_{-0.1}$	$0.9^{+0.0}_{-0.0}$	1.0				$0.9^{+0.1}_{-0.1}$	$0.9^{+0.0}_{-0.0}$	$0.9^{+0.1}_{-0.1}$	$0.9^{+0.0}_{-0.0}$
	$L(M_{pl}[M_\oplus])$	0.0				$-0.1^{+0.3}_{-0.3}$	$-0.0^{+0.3}_{-0.3}$	$-0.0^{+0.3}_{-0.3}$	$-0.0^{+0.3}_{-0.3}$	0.0				$-0.0^{+0.3}_{-0.3}$	$-0.0^{+0.3}_{-0.3}$	$-0.0^{+0.3}_{-0.3}$	$-0.0^{+0.3}_{-0.3}$
	$L(CO_2)$	−3.4				$-2.0^{+0.9}_{-0.9}$	$-2.4^{+0.9}_{-0.6}$	$-2.4^{+0.8}_{-0.8}$	$-2.7^{+0.6}_{-0.6}$	−3.4				$-2.1^{+1.0}_{-0.9}$	$-2.5^{+0.8}_{-0.7}$	$-2.3^{+0.9}_{-0.7}$	$-2.8^{+0.6}_{-0.6}$
	$L(H_2O)$	−2.1	−5.7	–	–	$-2.2^{+0.7}_{-0.8}$	$-2.5^{+0.8}_{-0.7}$	$-2.6^{+0.7}_{-0.8}$	$-2.9^{+0.6}_{-0.6}$	−2.2	−5.7	–	–	$-2.5^{+0.9}_{-1.1}$	$-3.0^{+0.8}_{-0.8}$	$-2.8^{+0.9}_{-0.8}$	$-3.4^{+0.6}_{-0.6}$
	$L(O_3)$	−7.6	−6.0	−5.0	−5.4	$-5.5^{+0.9}_{-0.7}$	$-5.7^{+0.7}_{-0.5}$	$-5.7^{+0.7}_{-0.6}$	$-5.9^{+0.5}_{-0.5}$	−7.3	−5.9	−5.1	−5.3	$-5.3^{+0.8}_{-0.8}$	$-5.6^{+0.7}_{-0.6}$	$-5.5^{+0.8}_{-0.6}$	$-5.9^{+0.5}_{-0.5}$
	$L(CH_4)$	−6.1	−6.1	−6.4	−6.7	$-4.5^{+1.3}_{-1.5}$	$-4.5^{+0.8}_{-0.7}$	$-4.7^{+0.9}_{-0.9}$	$-4.7^{+0.6}_{-0.6}$	−6.1	−6.1	−6.4	−6.7	$-4.6^{+1.1}_{-1.4}$	$-4.6^{+0.9}_{-0.7}$	$-4.5^{+0.9}_{-0.8}$	$-4.9^{+0.6}_{-0.6}$
	T_{eq}[K]	253.1				$259.0^{+8.7}_{-8.9}$	$263.0^{+5.3}_{-6.1}$	$262.1^{+6.6}_{-6.8}$	$264.5^{+3.5}_{-3.6}$	247.6				$255.6^{+8.7}_{-8.9}$	$259.5^{+4.9}_{-4.8}$	$258.7^{+6.2}_{-6.1}$	$260.2^{+3.4}_{-3.2}$
	A_B	0.32				$0.25^{+0.10}_{-0.11}$	$0.2^{+0.07}_{-0.07}$	$0.21^{+0.08}_{-0.08}$	$0.18^{+0.05}_{-0.05}$	0.37				$0.29^{+0.10}_{-0.10}$	$0.24^{+0.06}_{-0.06}$	$0.25^{+0.07}_{-0.08}$	$0.24^{+0.04}_{-0.04}$
Figure 7	$L(CO_2)$	−3.4				$-3.5^{+0.5}_{-0.5}$	$-3.6^{+0.4}_{-0.4}$	$-3.4^{+0.5}_{-0.4}$	$-3.6^{+0.3}_{-0.3}$	−3.4				$-3.4^{+0.5}_{-0.5}$	$-3.5^{+0.4}_{-0.4}$	$-3.4^{+0.5}_{-0.4}$	$-3.5^{+0.3}_{-0.3}$
	$L(H_2O)$	−2.1	−5.7	–	–	$-3.4^{+0.4}_{-0.6}$	$-3.6^{+0.3}_{-0.4}$	$-3.5^{+0.5}_{-0.5}$	$-3.8^{+0.3}_{-0.4}$	−2.2	−5.7	–	–	$-3.6^{+0.5}_{-0.7}$	$-4.0^{+0.4}_{-0.4}$	$-3.9^{+0.5}_{-0.5}$	$-4.1^{+0.4}_{-0.4}$
	$L(O_3)$	−7.6	−6.0	−5.0	−5.4	$-6.8^{+0.4}_{-0.4}$	$-6.6^{+0.3}_{-0.4}$	$-6.6^{+0.4}_{-0.4}$	$-6.7^{+0.3}_{-0.3}$	−7.3	−5.9	−5.1	−5.3	$-6.4^{+0.4}_{-0.4}$	$-6.4^{+0.3}_{-0.4}$	$-6.5^{+0.4}_{-0.4}$	$-6.5^{+0.4}_{-0.3}$
	$L(CH_4)$	−6.1	−6.1	−6.4	−6.7	$-6.2^{+0.8}_{-1.3}$	$-5.6^{+0.4}_{-0.4}$	$-5.7^{+0.6}_{-0.6}$	$-5.6^{+0.4}_{-0.4}$	−6.1	−6.1	−6.4	−6.7	$-5.7^{+0.7}_{-1.1}$	$-5.6^{+0.4}_{-0.4}$	$-5.6^{+0.5}_{-0.5}$	$-5.6^{+0.4}_{-0.4}$
Figure 8	$L(P_0[\text{bar}])$	0.0				$-0.8^{+0.3}_{-0.5}$	$-0.9^{+0.3}_{-0.3}$	$-0.7^{+0.3}_{-0.3}$	$-0.7^{+0.2}_{-0.2}$	0.0				$-0.8^{+0.4}_{-0.5}$	$-0.7^{+0.3}_{-0.4}$	$-0.7^{+0.3}_{-0.4}$	$-0.5^{+0.3}_{-0.2}$
	T_0[K]	285.0				$269.1^{+3.6}_{-2.3}$	$269.0^{+2.0}_{-1.4}$	$268.7^{+2.3}_{-1.6}$	$267.3^{+1.0}_{-0.7}$	278.9				$262.5^{+2.9}_{-1.9}$	$260.9^{+1.4}_{-0.9}$	$261.4^{+1.8}_{-1.3}$	$259.9^{+0.6}_{-0.6}$
	T_{eq}[K]	253.1				$253.5^{+1.8}_{-1.9}$	$252.7^{+0.9}_{-1.0}$	$253.1^{+1.2}_{-1.3}$	$252.6^{+0.6}_{-0.6}$	247.6				$247.5^{+1.8}_{-2.0}$	$246.5^{+0.9}_{-0.9}$	$246.9^{+1.2}_{-1.3}$	$246.7^{+0.6}_{-0.6}$
	A_B	0.32				$0.31^{+0.03}_{-0.03}$	$0.32^{+0.02}_{-0.02}$	$0.32^{+0.02}_{-0.03}$	$0.33^{+0.02}_{-0.02}$	0.37				$0.37^{+0.03}_{-0.03}$	$0.39^{+0.02}_{-0.02}$	$0.39^{+0.02}_{-0.02}$	$0.39^{+0.02}_{-0.02}$
Figure 9	$L\left(\frac{H_2O}{CO_2}\right)$	1.3	−2.3	–	–	$-0.2^{+0.6}_{-0.6}$	$-0.2^{+0.3}_{-0.3}$	$-0.2^{+0.4}_{-0.4}$	$-0.2^{+0.2}_{-0.2}$	1.2	−2.3	–	–	$-0.5^{+0.6}_{-0.6}$	$-0.5^{+0.3}_{-0.3}$	$-0.5^{+0.4}_{-0.4}$	$-0.6^{+0.2}_{-0.2}$
	$L\left(\frac{O_3}{CO_2}\right)$	−4.2	−2.6	−1.6	−2.0	$-3.4^{+0.5}_{-0.5}$	$-3.3^{+0.3}_{-0.3}$	$-3.3^{+0.3}_{-0.3}$	$-3.3^{+0.2}_{-0.2}$	−3.9	−2.5	−1.7	−1.9	$-3.2^{+0.5}_{-0.4}$	$-3.1^{+0.2}_{-0.2}$	$-3.2^{+0.3}_{-0.3}$	$-3.1^{+0.2}_{-0.2}$
	$L\left(\frac{CH_4}{CO_2}\right)$	−2.7	−2.7	−3.0	−3.3	$-2.4^{+0.8}_{-1.4}$	$-2.1^{+0.3}_{-0.4}$	$-2.2^{+0.5}_{-0.6}$	$-2.1^{+0.2}_{-0.2}$	−2.7	−2.7	−3.0	−3.3	$-2.4^{+0.7}_{-1.2}$	$-2.1^{+0.3}_{-0.3}$	$-2.2^{+0.4}_{-0.5}$	$-2.1^{+0.2}_{-0.2}$
	$L\left(\frac{O_3}{H_2O}\right)$	−5.5	−0.4	–	–	$-3.2^{+0.4}_{-0.4}$	$-3.1^{+0.3}_{-0.3}$	$-3.1^{+0.3}_{-0.3}$	$-3.0^{+0.2}_{-0.2}$	−5.0	−0.3	–	–	$-2.8^{+0.5}_{-0.5}$	$-2.7^{+0.3}_{-0.3}$	$-2.7^{+0.3}_{-0.3}$	$-2.5^{+0.2}_{-0.2}$
	$L\left(\frac{CH_4}{H_2O}\right)$	−3.9	−0.4	–	–	$-2.1^{+0.9}_{-1.5}$	$-1.9^{+0.4}_{-0.5}$	$-2.0^{+0.5}_{-0.7}$	$-1.8^{+0.2}_{-0.3}$	−3.8	−0.4	–	–	$-1.9^{+0.8}_{-1.3}$	$-1.6^{+0.4}_{-0.4}$	$-1.6^{+0.5}_{-0.5}$	$-1.5^{+0.2}_{-0.3}$
	$L\left(\frac{CH_4}{O_3}\right)$	1.5	−0.1	−1.4	−1.3	$1.1^{+0.6}_{-1.2}$	$1.2^{+0.3}_{-0.3}$	$1.1^{+0.4}_{-0.5}$	$1.2^{+0.2}_{-0.2}$	1.2	−0.2	−1.3	−1.4	$0.8^{+0.6}_{-1.0}$	$1.0^{+0.3}_{-0.3}$	$1.0^{+0.3}_{-0.4}$	$1.0^{+0.2}_{-0.2}$

Table 4.7: Numeric values corresponding to the retrieved parameter posteriors in Figures 4.7a, 4.7b, 4.7c, and 4.8 for the SP viewing angle. Here, $L(\cdot)$ abbreviates $\log_{10}(\cdot)$. We provide the median of the retrieved posterior and indicate the 16% – 84% range via +/− indices. We Further provide the ground truth values. If independent of the atmospheric pressure, we provide a single value. Otherwise, we provide the ground truths at pressures 1 bar, 10^-1 bar, 10^-2 bar, and 10^-3 bar if available.

Table 4.8: Numeric values corresponding to the retrieved parameter posteriors in Figures 4.7a, 4.7b, 4.7c, and 4.8 for the EqC viewing angle. Here, $L(\cdot)$ abbreviates $\log_{10}(\cdot)$. We provide the median of the retrieved posterior and indicate the 16% – 84% range via +/− indices. We Further provide the ground truth values. If independent of the atmospheric pressure, we provide a single value. Otherwise, we provide the ground truths at pressures 1 bar, $10^{-}1$ bar, $10^{-}2$ bar, and $10^{-}3$ bar if available.

		EqC Jan – Ground Truths				EqC Jan – Posteriors				EqC Jul – Ground Truths				EqC Jul – Posteriors			
		Pressure Levels [bar]				$R = 50$		$R = 100$		Pressure Levels [bar]				$R = 50$		$R = 100$	
	Posterior	1	10^{-1}	10^{-2}	10^{-3}	$S/N = 10$	$S/N = 20$	$S/N = 10$	$S/N = 20$	1	10^{-1}	10^{-2}	10^{-3}	$S/N = 10$	$S/N = 20$	$S/N = 10$	$S/N = 20$
Figure 6	$L(P_0[\text{bar}])$	0.0				$-0.7^{+0.4}_{-0.4}$	$-0.6^{+0.3}_{-0.4}$	$-0.5^{+0.4}_{-0.4}$	$-0.4^{+0.3}_{-0.3}$	0.0				$-0.5^{+0.4}_{-0.5}$	$-0.5^{+0.3}_{-0.4}$	$-0.5^{+0.3}_{-0.4}$	$-0.4^{+0.3}_{-0.2}$
	T_0[K]	280.5				$281.0^{+10.6}_{-9.4}$	$284.4^{+5.7}_{-5.5}$	$283.5^{+7.2}_{-6.9}$	$285.1^{+3.7}_{-3.5}$	285.1				$285.5^{+10.6}_{-10.3}$	$288.3^{+5.8}_{-5.9}$	$287.0^{+7.8}_{-7.4}$	$288.5^{+3.8}_{-3.7}$
	$R_{pl}[R_\oplus]$	1.0				$0.9^{+0.1}_{-0.1}$	$0.9^{+0.0}_{-0.0}$	$0.9^{+0.1}_{-0.1}$	$0.9^{+0.0}_{-0.0}$	1.0				$0.9^{+0.1}_{-0.1}$	$0.9^{+0.0}_{-0.0}$	$0.9^{+0.1}_{-0.1}$	$0.9^{+0.0}_{-0.0}$
	$L(M_{pl}[M_\oplus])$	0.0				$-0.1^{+0.3}_{-0.3}$	$-0.0^{+0.3}_{-0.3}$	$-0.0^{+0.3}_{-0.3}$	$-0.0^{+0.3}_{-0.3}$	0.0				$-0.1^{+0.3}_{-0.3}$	$-0.0^{+0.3}_{-0.3}$	$-0.0^{+0.3}_{-0.3}$	$0.0^{+0.3}_{-0.3}$
	$L(CO_2)$	−3.4				$-2.2^{+1.0}_{-0.9}$	$-2.4^{+0.9}_{-0.7}$	$-2.5^{+0.9}_{-0.8}$	$-2.8^{+0.6}_{-0.6}$	−3.4				$-2.5^{+1.0}_{-0.9}$	$-2.5^{+0.8}_{-0.7}$	$-2.4^{+1.0}_{-0.8}$	$-2.8^{+0.6}_{-0.5}$
	$L(H_2O)$	−2.1	−5.6	–	–	$-2.4^{+0.8}_{-0.9}$	$-2.6^{+0.8}_{-0.7}$	$-2.7^{+0.8}_{-0.9}$	$-3.0^{+0.6}_{-0.6}$	−2.1	−5.6	–	–	$-2.5^{+0.8}_{-0.9}$	$-2.8^{+0.8}_{-0.8}$	$-2.7^{+0.9}_{-0.8}$	$-3.1^{+0.6}_{-0.6}$
	$L(O_3)$	−7.4	−5.9	−5.0	−5.4	$-5.6^{+0.8}_{-0.7}$	$-5.7^{+0.7}_{-0.6}$	$-5.8^{+0.8}_{-0.7}$	$-6.0^{+0.5}_{-0.5}$	−7.3	−6.0	−5.0	−5.4	$-5.8^{+0.8}_{-0.7}$	$-5.8^{+0.6}_{-0.6}$	$-5.7^{+0.8}_{-0.6}$	$-6.0^{+0.5}_{-0.5}$
	$L(CH_4)$	−6.0	−6.1	−6.4	−6.6	$-4.7^{+1.2}_{-1.3}$	$-4.5^{+0.8}_{-0.7}$	$-4.7^{+1.0}_{-0.9}$	$-4.8^{+0.6}_{-0.6}$	−6.0	−6.1	−6.4	−6.6	$-4.9^{+1.2}_{-1.3}$	$-4.6^{+0.8}_{-0.7}$	$-4.6^{+1.0}_{-0.8}$	$-4.8^{+0.6}_{-0.5}$
	T_{eq}[K]	256.5				$262.7^{+10.0}_{-9.6}$	$266.8^{+5.0}_{-5.8}$	$266.0^{+6.6}_{-7.0}$	$268.0^{+3.3}_{-3.4}$	259.5				$266.0^{+9.9}_{-9.9}$	$269.5^{+5.4}_{-5.8}$	$268.1^{+6.9}_{-7.6}$	$270.2^{+3.4}_{-3.5}$
	A_B	0.28				$0.21^{+0.11}_{-0.13}$	$0.16^{+0.07}_{-0.07}$	$0.17^{+0.09}_{-0.09}$	$0.14^{+0.05}_{-0.05}$	0.24				$0.17^{+0.12}_{-0.13}$	$0.12^{+0.08}_{-0.07}$	$0.14^{+0.10}_{-0.09}$	$0.11^{+0.05}_{-0.05}$
Figure 7	$L(CO_2)$	−3.4				$-3.4^{+0.5}_{-0.5}$	$-3.6^{+0.4}_{-0.4}$	$-3.4^{+0.4}_{-0.4}$	$-3.5^{+0.4}_{-0.4}$	−3.4				$-3.4^{+0.5}_{-0.5}$	$-3.5^{+0.4}_{-0.4}$	$-3.5^{+0.5}_{-0.4}$	$-3.5^{+0.3}_{-0.3}$
	$L(H_2O)$	−2.1	−5.6	–	–	$-3.4^{+0.5}_{-0.5}$	$-3.8^{+0.4}_{-0.4}$	$-3.6^{+0.4}_{-0.4}$	$-3.8^{+0.4}_{-0.4}$	−2.1	−5.6	–	–	$-3.4^{+0.5}_{-0.6}$	$-3.7^{+0.4}_{-0.4}$	$-3.6^{+0.5}_{-0.4}$	$-3.8^{+0.4}_{-0.4}$
	$L(O_3)$	−7.4	−5.9	−5.0	−5.4	$-6.6^{+0.4}_{-0.4}$	$-6.7^{+0.3}_{-0.3}$	$-6.5^{+0.4}_{-0.4}$	$-6.6^{+0.4}_{-0.3}$	−7.3	−6.0	−5.0	−5.4	$-6.5^{+0.4}_{-0.4}$	$-6.5^{+0.4}_{-0.3}$	$-6.5^{+0.4}_{-0.4}$	$-6.5^{+0.3}_{-0.3}$
	$L(CH_4)$	−6.0	−6.1	−6.4	−6.6	$-5.8^{+0.7}_{-1.0}$	$-5.6^{+0.4}_{-0.4}$	$-5.6^{+0.5}_{-0.5}$	$-5.6^{+0.4}_{-0.4}$	−6.0	−6.1	−6.4	−6.6	$-5.8^{+0.7}_{-1.1}$	$-5.5^{+0.4}_{-0.4}$	$-5.6^{+0.5}_{-0.5}$	$-5.5^{+0.4}_{-0.4}$
Figure 8	$L(P_0[\text{bar}])$	0.0				$-0.7^{+0.4}_{-0.4}$	$-0.8^{+0.3}_{-0.4}$	$-0.7^{+0.4}_{-0.4}$	$-0.7^{+0.3}_{-0.3}$	0.0				$-0.6^{+0.4}_{-0.4}$	$-0.7^{+0.3}_{-0.3}$	$-0.7^{+0.3}_{-0.4}$	$-0.6^{+0.3}_{-0.2}$
	T_0[K]	280.5				$274.8^{+3.9}_{-2.5}$	$274.5^{+2.0}_{-1.4}$	$273.7^{+2.3}_{-1.6}$	$272.3^{+0.9}_{-0.7}$	285.1				$278.5^{+3.3}_{-2.4}$	$277.8^{+1.8}_{-1.3}$	$278.4^{+2.7}_{-1.8}$	$276.3^{+0.9}_{-0.8}$
	T_{eq}[K]	256.5				$256.7^{+1.9}_{-2.1}$	$255.8^{+1.0}_{-1.0}$	$256.2^{+1.4}_{-1.4}$	$255.8^{+0.6}_{-0.6}$	259.5				$259.4^{+2.1}_{-2.1}$	$258.8^{+1.0}_{-1.0}$	$259.3^{+1.4}_{-1.4}$	$258.8^{+0.7}_{-0.7}$
	A_B	0.28				$0.27^{+0.03}_{-0.04}$	$0.29^{+0.02}_{-0.02}$	$0.29^{+0.03}_{-0.03}$	$0.3^{+0.02}_{-0.02}$	0.24				$0.24^{+0.03}_{-0.04}$	$0.26^{+0.02}_{-0.02}$	$0.25^{+0.03}_{-0.03}$	$0.26^{+0.02}_{-0.02}$
Figure 9	$L\left(\frac{H_2O}{CO_2}\right)$	1.3	−2.3	–	–	$-0.2^{+0.6}_{-0.6}$	$-0.3^{+0.3}_{-0.3}$	$-0.3^{+0.4}_{-0.4}$	$-0.3^{+0.2}_{-0.2}$	1.3	−2.2	–	–	$-0.2^{+0.5}_{-0.5}$	$-0.3^{+0.3}_{-0.3}$	$-0.3^{+0.4}_{-0.4}$	$-0.3^{+0.2}_{-0.2}$
	$L\left(\frac{O_3}{CO_2}\right)$	−4.0	−2.5	−1.6	−2.0	$-3.4^{+0.4}_{-0.4}$	$-3.3^{+0.2}_{-0.2}$	$-3.3^{+0.3}_{-0.3}$	$-3.2^{+0.2}_{-0.2}$	−3.9	−2.6	−1.6	−2.0	$-3.3^{+0.4}_{-0.4}$	$-3.2^{+0.2}_{-0.2}$	$-3.3^{+0.3}_{-0.3}$	$-3.2^{+0.2}_{-0.2}$
	$L\left(\frac{CH_4}{CO_2}\right)$	−2.6	−2.7	−3.0	−3.2	$-2.5^{+0.8}_{-1.5}$	$-2.1^{+0.3}_{-0.4}$	$-2.2^{+0.4}_{-0.6}$	$-2.1^{+0.2}_{-0.2}$	−2.6	−2.7	−3.0	−3.2	$-2.3^{+0.7}_{-1.2}$	$-2.1^{+0.3}_{-0.4}$	$-2.1^{+0.4}_{-0.5}$	$-2.0^{+0.2}_{-0.2}$
	$L\left(\frac{O_3}{H_2O}\right)$	−5.3	−0.3	–	–	$-2.8^{+0.5}_{-0.4}$	$-2.7^{+0.3}_{-0.3}$	$-2.7^{+0.4}_{-0.4}$	$-2.6^{+0.2}_{-0.2}$	−5.2	−0.4	–	–	$-3.2^{+0.4}_{-0.4}$	$-3.1^{+0.3}_{-0.2}$	$-3.2^{+0.3}_{-0.3}$	$-3.0^{+0.2}_{-0.2}$
	$L\left(\frac{CH_4}{H_2O}\right)$	−3.9	−0.4	–	–	$-2.0^{+0.9}_{-1.6}$	$-1.7^{+0.4}_{-0.4}$	$-1.7^{+0.5}_{-0.6}$	$-1.6^{+0.3}_{-0.3}$	−4.0	−0.5	–	–	$-2.3^{+0.7}_{-1.5}$	$-2.0^{+0.4}_{-0.4}$	$-2.1^{+0.5}_{-0.6}$	$-1.9^{+0.2}_{-0.3}$
	$L\left(\frac{CH_4}{O_3}\right)$	1.4	−0.2	−1.4	−1.2	$0.8^{+0.6}_{-1.3}$	$1.0^{+0.3}_{-0.3}$	$1.0^{+0.4}_{-0.4}$	$1.0^{+0.2}_{-0.2}$	1.3	−0.1	−1.4	−1.2	$0.9^{+0.6}_{-1.2}$	$1.1^{+0.3}_{-0.3}$	$1.1^{+0.3}_{-0.4}$	$1.1^{+0.2}_{-0.2}$

Contribution

Chapter 4 benefits from the underlying work of Chapter 3 and the dataset that was compiled, reduced and analysed in that chapter. Björn Konrad performed the retrievals and helped in the interpretation of the results. Björn Konrad and I, have equally contributed to this work. Both carried out analyses, created figures, and have written essential parts of the manuscript.

5 Conclusion and Outlook

5.1 Summary and Conclusion

In this thesis, I have leveraged the wealth of Earth observation data to investigate the spectral characteristics and time-variability of Earth as an exoplanet in the MIR. With future attempts to characterize distant HZ planets in mind, studying Earth from afar offers a unique opportunity to explore a truly habitable and inhabited world by means of remote characterization. While this is not a novel approach and has been done before by some studies in both reflected light and thermal emission, this work is the first to employ a data-driven and systematic approach based on real MIR Earth observation data. I initially investigated Earth's time-resolved and spectrally-limited thermal emission spectrum for five specific target locations. Then I expanded the analyses from time-resolved to spatially- and time-unresolved MIR spectra for different full-disk observing geometries. Lastly, I used these disk-integrated MIR spectra as input for atmospheric retrievals. Hence, my research yielded two comprehensive datasets. The first is a spectrally-limited dataset (16 channels, 3.66−14.40 µm) derived from MODIS observations spanning 15 years and comprising a total of 1800 SEDs for five distinct single-surface-type target locations. The second dataset is based on AIRS data and includes 2690 disk-integrated MIR thermal emission spectra (3.75 − 15.40 µm, $R = 1200$) for four different full-disk observing geometries over a four-year timeframe. Additionally, I have derived ground truth data matching the AIRS dataset, encompassing cloud coverage, $P-T$ profiles, and trace-gas abundances of H_2O, CO, CO_2, CH_4, and O_3.

In Chapter 2, using the MODIS dataset I explored the effect of spectrally-limited observations on the characteristics of the MIR spectra of five single-surface-type target locations representing different climate zones and thermal properties. In the first part, I analyzed whether differences between these target locations in flux levels and variability are detectable. In the second part, I applied a Fourier analysis to the measured spectral radiance variations for each spectral band and target location to look for evidence of planetary obliquity (Earth's tilted axis) therein. I was able to show that despite the coarse spectral resolution, the inferred SEDs show a strong viewing geometry dependency in the strength of flux levels and absorption features. The different underlying surface types cannot be inferred from single observations alone; multiple observations over different epochs to perform time-variability analyses are required. However, even with these approaches, the challenge of spectral degeneracy persists. Furthermore, regions close to the equator and toward the North Pole show more dominant O_3 (9.65 μm) and CO_2 (15 μm) absorption features than the South Pole. These typically strong absorption bands are significantly less pronounced and partially absent in data from the polar regions implying that estimating correct abundance levels for these molecules might be challenging in these cases. The Fourier analysis of the spectral radiance variations showed that the time-resolved thermal emission spectrum encodes information about planetary obliquity, but the significance depends on the number of observations, viewing geometry, and spectral band considered.

In Chapter 3, I expanded the analyses to disk-integrated Earth views. Using the AIRS dataset, I first studied how Earth's disk-integrated MIR spectral appearance changes as a function of viewing geometry, seasons, and phase angles. In the second part, I isolated four spectral features of bioindicators and habitability markers (CO_2, O_3, CH_4, N_2O) found imprinted in the MIR spectrum and investigated their seasonality and detectability in the context of atmospheric seasonality being a biosignature. The results show that a representative, disk-integrated thermal emission spectrum of Earth does not exist. Instead, both the thermal emission spectrum and the strength of biosignature absorption features show seasonal variability and depend strongly on viewing geometry. In addition, a strong spectral degeneracy with respect to viewing geometry and season is found. This indicates that multi-epoch measurements and time-dependent signals may be required in order to fully characterize planetary environments. Irrespective of when Earth was observed the overall variation (in flux or absorption bands) is typically ≤10% for a given viewing angle. Although disentangling these varia-

tions from the noise in future observations is nontrivial, the result is relatively insensitive to diurnal or seasonal effects, unlike in the case of reflected light measurements. Therefore, observing an exoplanet's thermal emission could provide unique and complementary information that is necessary for the characterization of terrestrial planets around other stars.

In Chapter 4, the AIRS and ground truth datasets are used to study Earth as a directly imaged exoplanet by means of the future MIR space mission concept LIFE. For the first time, we performed a systematic retrieval analysis of real disk- and time-averaged Earth spectra and compared the retrieval results to ground truths. This allowed us to evaluate the accuracy of the retrieved constraints and thereby validate our retrieval approach. Despite the biases evoked by parameter degeneracies, our results at the minimal LIFE requirements ($R = 50$, $S/N = 10$) find Earth to be a temperate habitable planet with detectable levels of CO_2, H_2O, O_3, CH_4. Moreover, we find that viewing geometry and the spatially and temporally integrated spectra only have a minor impact on the detectability of molecules, the retrieved relative abundances, and thus the characterization of Earth. Seasonal variations in the surface and equilibrium temperature, as well as in the Bond albedo are detectable. However, the limited extent of Earth's seasonal variations in biosignature abundances makes the direct detection of its biosphere through atmospheric seasonality unlikely. Furthermore, Earth's variable H_2O profile and patchy cloud coverage led to biased retrieval results for the atmospheric structure and trace gas abundance which requires future work to investigate the effects and search for potential remedies. In general, we demonstrated that next generation, optimized space missions can assess whether nearby temperate terrestrial exoplanets are habitable or even inhabited.

5.2 Concluding Remarks and Outlook

The analyses and results presented in this thesis, demonstrate the power of thermal emission data for the characterization of habitable terrestrial exoplanets, but they also caution us to be careful in the analysis and interpretation. Depending on the observing geometry, underlying surface types, atmospheric composition and conditions, as well as when along the orbit it is observed, the same planet may appear significantly different in the disk- and time-averaged signal. Furthermore, we learned that a planet and its characteristics cannot be described by a single observation due to spectral degeneracy. This complexity makes remote character-

ization of planetary environments very challenging. Multi-epoch measurements, preferably in both reflected light and thermal emission, and the resulting time-dependent signals could assist in characterizing the planetary environment by resolving certain ambiguities or uncertainties. In addition, seasonal periodicities in molecular abundances that are attributable to life are strong indicators for biological activity. Yet, even for Earth, these variances are small. As show in this work, a high confidence detection of seasonal variations in H_2O or other trace gases as a biosignature is not feasible for LIFE, given the preliminary minimal instrument requirements. Although disentangling these variations from the noise in future observations is nontrivial, higher R and S/N observations of Earth could lead to increased sensitivity to such small variations.

A promising step forward in our quest to understand distant worlds was achieved through the systematic atmospheric retrieval study performed on real disk-averaged MIR Earth spectra. The comparison of the retrieved parameters to ground truths indicated that LIFE would correctly identify Earth as a planet where life could thrive, with detectable levels of bioindicators, a temperate climate, and surface conditions that allow for liquid surface water. The viewing geometry and the spatially and temporally averaged nature of the data only had minor impact on the detectability of molecules, the retrieved relative abundances, and thus the characterization of Earth. This result is particularly compelling as the retrieval approach was validated against Earth observation ground truths.

The validation of atmospheric retrieval routines against solar system observations is an inevitable step toward characterizing the unknown environments of terrestrial exoplanets in the future. To understand their diagnostic power as well as potential limitations, *in situ* data from other Solar System bodies is necessary. The data we collected so far about our neighboring planets and their moons has been acquired through a limited number of spacecraft flybys, probes, and orbiters. While all the planets have been visited, some of the moons, such as Titan and Enceladus, along with others like Europa, Ganymede, Io, and Charon, have also been visited by these missions. However, these celestial bodies were not explored to the same degree of detail, and their observations exhibit significant variations in terms of temporal and spatial coverage. Of course, these observations fall short of the comprehensive level of study that Earth has received. Nevertheless, with the upcoming JUpiter ICy moons Explorer (JUICE) mission more observations will be added to the (spectral) library around 2030. JUICE is a European Space Agency (ESA) spacecraft mission designed to investigate the properties of Jupiter's

magnetosphere, study the atmosphere and magnetosphere of Ganymede, and assess the potential habitability of Jupiter's icy moons, particularly Ganymede, Europa, and Callisto. Furthermore, JWST is currently observing some Solar System planets and their moons with its Near-Infrared Spectrograph (NIRSpec) Integral Field Unit (IFU)[1], which will also provide more spectral observations of Solar System bodies. Future data-driven analyses and systematic approaches, similar to this thesis, based on current and future observations of Solar System bodies should be strongly encouraged as the result will yield valuable insights for the exoplanet community.

The integration of exoplanetary science, planetary science, and remote sensing of Solar System bodies offers a promising framework for the interpretation of future observations of potentially habitable worlds. The interdisciplinary approach combines statistical insights into planetary architectures and formation scenarios from exoplanetary science, detailed planetary models for comprehensive characterization from planetary science, and the remote sensing (analysis) techniques necessary to pave the way for the detection of life beyond our solar system.

Contribution

I was the main author and contributor of Chapter 5.

[1] (e.g., Trumbo and Brown, 2023)

Bibliography

AIRS Project. Aqua/AIRS L3 monthly standard physical retrieval (AIRS-only) 1 degree x 1 degree v7.0, 2020.

AIRS Science Team/Joao Teixeira . Airs/aqua l3 daily standard physical retrieval (airs-only) 1 degree x 1 degree v006, 2013. doi: 10.5067/Aqua/AIRS/DATA303.

E. Alei, R. Claudi, A. Bignamini, & M. Molinaro. Exo-MerCat: a merged exoplanet catalog with Virtual Observatory connection. *arXiv e-prints*, art. arXiv:2002.01834, Feb 2020.

E. Alei, B. S. Konrad, D. Angerhausen, et al. Large Interferometer For Exoplanets (LIFE). V. Diagnostic potential of a mid-infrared space interferometer for studying Earth analogs. *A&A*, 665:A106, Sept. 2022. doi: 10.1051/0004-6361/202243760.

G. Anglada-Escudé, P. J. Amado, J. Barnes, et al. A terrestrial planet candidate in a temperate orbit around Proxima Centauri. *Nature*, 536:437–440, Aug. 2016. doi: 10.1038/nature19106.

aqua.nasa.gov. Earth science reference handbook: Mission - aqua, 2006. URL https://atrain.nasa.gov/publications/Aqua.pdf.

G. Arney, S. D. Domagal-Goldman, V. S. Meadows, et al. The pale orange dot: The spectrum and habitability of hazy archean earth. *Astrobiology*, 16(11):873–899, Nov 2016. ISSN 1557-8070. doi: 10.1089/ast.2015.1422. URL http://dx.doi.org/10.1089/ast.2015.1422.

H. Aumann, M. Chahine, C. Gautier, et al. Airs/amsu/hsb on the aqua mission: design, science objectives, data products, and processing systems. *IEEE Transactions on Geoscience and Remote Sensing*, 41(2):253–264, 2003. doi: 10.1109/TGRS.2002.808356.

A. L. Baker, L. R. Baker, E. Beshore, et al. The imaging photopolarimeter experiment on pioneer 11. *Science*, 188(4187):468–472, 1975. doi: 10.1126/science.188.4187.468. URL https://www.science.org/doi/abs/10.1126/science.188.4187.468.

M. N. Barnett, & S. L. Olson. Moderately high obliquity promotes biospheric oxygenation. *The Planetary Science Journal*, 3(6):132, jun 2022. doi: 10.3847/psj/ac6dce. URL https://doi.org/10.3847/psj/ac6dce.

J. G. Barrientos, R. J. MacDonald, N. K. Lewis, & L. Kaltenegger. In search of the edge: A bayesian exploration of the detectability of red edges in exoplanet reflection spectra. *The Astrophysical Journal*, 946(2):96, apr 2023. doi: 10.3847/1538-4357/acaf59. URL https://doi.org/10.3847%2F1538-4357%2Facaf59.

J. K. Barstow, Q. Changeat, R. Garland, et al. A comparison of exoplanet spectroscopic retrieval tools. *MNRAS*, 493(4):4884–4909, Apr. 2020. doi: 10.1093/mnras/staa548.

N. M. Batalha. Exploring exoplanet populations with nasa's kepler mission. *Proceedings of the National Academy of Sciences*, 111(35):12647–12654, 2014. ISSN 0027-8424. doi: 10.1073/pnas.1304196111. URL https://www.pnas.org/content/111/35/12647.

M. L. Bender, P. W. Callaway, S. C. Chase, G. F. Moore, & R. D. Ruiz. Infrared radiometer for the pioneer 10 and 11 missions to jupiter. *Appl. Opt.*, 13(11):2623–2628, Nov 1974. doi: 10.1364/AO.13.002623. URL http://opg.optica.org/ao/abstract.cfm?URI=ao-13-11-2623.

Z. K. Berta-Thompson, J. Irwin, D. Charbonneau, et al. A rocky planet transiting a nearby low-mass star. *Nature*, 527(7577):204–207, Nov. 2015. doi: 10.1038/nature15762.

D. Blumstein, G. Chalon, T. Carlier, et al. Iasi instrument: Technical overview and measured performances. *Proceedings of SPIE - The International Society for Optical Engineering*, 5543, 11 2004. doi: 10.1117/12.560907.

W. J. Borucki, D. Koch, G. Basri, et al. Kepler planet-detection mission: Introduction and first results. *Science*, 327(5968):977–980, 2010. ISSN 0036-8075. doi: 10.1126/science.1185402. URL http://science.sciencemag.org/content/327/5968/977.

R. Bowens, M. R. Meyer, C. Delacroix, et al. Exoplanets with ELT-METIS. I. Estimating the direct imaging exoplanet yield around stars within 6.5 parsecs. *A&A*, 653:A8, Sept. 2021. doi: 10.1051/0004-6361/202141109.

S. Bryson, M. Kunimoto, R. K. Kopparapu, et al. The Occurrence of Rocky Habitable-zone Planets around Solar-like Stars from Kepler Data. *AJ*, 161(1):36, Jan. 2021. doi: 10.3847/1538-3881/abc418.

J. Buchner, A. Georgakakis, K. Nandra, et al. X-ray spectral modelling of the agn obscuring region in the cdfs: Bayesian model selection and catalogue. *A&A*, 564:A125, Apr. 2014. ISSN 1432-0746. doi: 10.1051/0004-6361/201322971. URL http://dx.doi.org/10.1051/0004-6361/201322971.

C. Burke, J. Christiansen, F. Mullally, et al. Terrestrial planet occurrence rates for the kepler gk dwarf sample. *Astrophysical Journal*, 809(1), 8 2015. ISSN 0004-637X. doi: 10.1088/0004-637X/809/1/8.

N. Butchart. The brewer-dobson circulation. *Reviews of Geophysics*, 52(2):157–184, 2014. doi: 10.1002/2013RG000448. URL https://agupubs.onlinelibrary.wiley.com/doi/abs/10.1002/2013RG000448.

J. Canadell, P. Monteiro, M. Costa, et al. Climate change 2021: The physical science basis. Technical report, 2021. pp. 673–816.

A. Cassan, D. Kubas, J. P. Beaulieu, et al. One or more bound planets per milky way star from microlensing observations. *Nature*, 481:167 EP –, 01 2012. URL https://doi.org/10.1038/nature10684.

D. C. Catling, & J. F. Kasting. *Atmospheric Evolution on Inhabited and Lifeless Worlds*. Cambridge University Press, 2017. doi: 10.1017/9781139020558.

D. C. Catling, J. Krissansen-Totton, N. Y. Kiang, et al. Exoplanet biosignatures: A framework for their assessment. *Astrobiology*, 18(6):709–738, 2018. doi: 10.1089/ast.2017.1737. URL https://doi.org/10.1089/ast.2017.1737. PMID: 29676932.

M. T. Chahine, T. S. PAGANO, H. H. AUMANN, et al. Airs: Improving weather forecasting and providing new data on greenhouse gases. *Bulletin of the American Meteorological Society*, 87(7):911 – 926, 2006. doi: 10.1175/BAMS-87-7-911. URL https://journals.ametsoc.org/view/journals/bams/87/7/bams-87-7-911.xml.

J. Chen, & D. Kipping. Probabilistic forecasting of the masses and radii of other worlds. *ApJ*, 834(1):17, Dec. 2016. ISSN 1538-4357. doi: 10.3847/1538-4357/834/1/17. URL http://dx.doi.org/10.3847/1538-4357/834/1/17.

P. R. Christensen, & J. C. Pearl. Initial data from the mars global surveyor thermal emission spectrometer experiment: Observations of the earth. *Journal of Geophysical Research: Planets*, 102(E5): 10875–10880, 1997. doi: 10.1029/97JE00637. URL https://agupubs.onlinelibrary.wiley.com/doi/abs/10.1029/97JE00637.

N. B. Cowan, E. Agol, V. S. Meadows, et al. Alien maps of an ocean-bearing world. *The Astrophysical Journal*, 700(2):915, 2009. URL http://stacks.iop.org/0004-637X/700/i=2/a=915.

N. B. Cowan, A. Voigt, & D. S. Abbot. Thermal Phases of Earth-like Planets: Estimating Thermal Inertia from Eccentricity, Obliquity, and Diurnal Forcing. *ApJ*, 757(1):80, Sept. 2012. doi: 10.1088/0004-637X/757/1/80.

F. A. Dannert, M. Ottiger, S. P. Quanz, et al. Large Interferometer For Exoplanets (LIFE). II. Signal simulation, signal extraction, and fundamental exoplanet parameters from single-epoch observations. *A&A*, 664:A22, Aug. 2022. doi: 10.1051/0004-6361/202141958.

D. J. Des Marais, M. O. Harwit, K. W. Jucks, et al. Remote sensing of planetary properties and biosignatures on extrasolar terrestrial planets. *Astrobiology*, 2(2):153–181, 2002. doi: 10.1089/15311070260192246. URL https://doi.org/10.1089/15311070260192246. PMID: 12469366.

D. J. Des Marais, J. A. Nuth, L. J. Allamandola, et al. The nasa astrobiology roadmap. *Astrobiology*, 8 (4):715–730, 2008. doi: 10.1089/ast.2008.0819. URL https://doi.org/10.1089/ast.2008.0819. PMID: 18793098.

S. G. DeSouza-Machado, L. L. Strow, S. E. Hannon, et al. Fast forward radiative transfer modeling of 4.3 μm nonlocal thermodynamic equilibrium effects for infrared temperature sounders. *Geophysical Research Letters*, 34(1), 2007. doi: https://doi.org/10.1029/2006GL026684. URL https://agupubs.onlinelibrary.wiley.com/doi/abs/10.1029/2006GL026684.

T. DeVries, C. L. Quéré, O. Andrews, et al. Decadal trends in the ocean carbon sink. *Proceedings of the National Academy of Sciences*, 116(24):11646–11651, 2019. doi: 10.1073/pnas.1900371116. URL https://www.pnas.org/doi/abs/10.1073/pnas.1900371116.

J. A. Dittmann, J. M. Irwin, D. Charbonneau, et al. A temperate rocky super-earth transiting a nearby cool star. *Nature*, 544:333 EP –, 04 2017. URL https://doi.org/10.1038/nature22055.

P. Drossart, J. Rosenqvist, T. Encrenaz, et al. Earth global mosaic observations with nims-galileo. *Planetary and space science*, 41(7):551–561, 1993.

S. Ertel, D. Defrère, P. Hinz, et al. The HOSTS Survey for Exozodiacal Dust: Observational Results from the Complete Survey. *AJ*, 159(4):177, Apr. 2020. doi: 10.3847/1538-3881/ab7817.

B. Farr, W. M. Farr, N. B. Cowan, H. M. Haggard, & T. Robinson. exocartographer: A bayesian framework for mapping exoplanets in reflected light. *The Astronomical Journal*, 156(4):146, sep 2018. doi: 10.3847/1538-3881/aad775.

T. J. Fauchez, M. Turbet, G. L. Villanueva, et al. Impact of clouds and hazes on the simulated JWST transmission spectra of habitable zone planets in the TRAPPIST-1 system. *The Astrophysical Journal*, 887(2):194, dec 2019. doi: 10.3847/1538-4357/ab5862. URL https://doi.org/10.3847/1538-4357/ab5862.

Y. K. Feng, T. D. Robinson, J. J. Fortney, et al. Characterizing Earth Analogs in Reflected Light: Atmospheric Retrieval Studies for Future Space Telescopes. *AJ*, 155(5):200, May 2018. doi: 10.3847/1538-3881/aab95c.

F. Feroz, M. P. Hobson, & M. Bridges. Multinest: an efficient and robust bayesian inference tool for cosmology and particle physics. *MNRAS*, 398(4):1601–1614, Oct. 2009. ISSN 1365-2966. doi: 10.1111/j.1365-2966.2009.14548.x. URL http://dx.doi.org/10.1111/j.1365-2966.2009.14548.x.

L. N. Fletcher. The Atmosphere of Uranus. *arXiv e-prints*, art. arXiv:2105.06377, May 2021.

L. N. Fletcher, T. K. Greathouse, J. I. Moses, S. Guerlet, & R. A. West. Saturn's Seasonally Changing Atmosphere: Thermal Structure, Composition and Aerosols. *arXiv e-prints*, art. arXiv:1510.05690, Oct. 2015.

E. B. Ford, S. Seager, & E. L. Turner. Characterization of extrasolar terrestrial planets from diurnal photometric variability. *Nature*, 412(6850):885–887, Aug. 2001. doi: 10.1038/35091009.

F. Fressin, G. Torres, D. Charbonneau, et al. The False Positive Rate of Kepler and the Occurrence of Planets. *ApJ*, 766(2):81, Apr. 2013. doi: 10.1088/0004-637X/766/2/81.

Y. Fujii, H. Kawahara, Y. Suto, et al. COLORS OF a SECOND EARTH: ESTIMATING THE FRACTIONAL AREAS OF OCEAN, LAND, AND VEGETATION OF EARTH-LIKE EXOPLANETS. *The Astrophysical Journal*, 715(2):866–880, may 2010. doi: 10.1088/0004-637x/715/2/866. URL https://doi.org/10.1088%2F0004-637x%2F715%2F2%2F866.

Y. Fujii, H. Kawahara, Y. Suto, et al. COLORS OF a SECOND EARTH. II. EFFECTS OF CLOUDS ON PHOTOMETRIC CHARACTERIZATION OF EARTH-LIKE EXOPLANETS. *The Astrophysical Journal*, 738(2):184, aug 2011. doi: 10.1088/0004-637x/738/2/184. URL https://doi.org/10.1088/0004-637x/738/2/184.

J. P. Gardner, J. C. Mather, M. Clampin, et al. The james webb space telescope. *Space Science Reviews*, 123(4):485–606, Nov 2006. ISSN 1572-9672. doi: 10.1007/s11214-006-8315-7. URL http://dx.doi.org/10.1007/s11214-006-8315-7.

D. M. Gates, H. J. Keegan, J. C. Schleter, & V. R. Weidner. Spectral properties of plants. *Appl. Opt.*, 4 (1):11–20, Jan 1965. doi: 10.1364/AO.4.000011. URL https://opg.optica.org/ao/abstract.cfm?URI=ao-4-1-11.

B. S. Gaudi, S. Seager, B. Mennesson, et al. The habitable exoplanet observatory (habex) mission concept study final report, 2020.

T. D. Gebhard, D. Angerhausen, B. S. Konrad, et al. Parameterizing pressure-temperature profiles of exoplanet atmospheres with neural networks. *arXiv e-prints*, art. arXiv:2309.03075, Sept. 2023. doi: 10.48550/arXiv.2309.03075.

T. Gehrels. The results of the imaging photopolarimeter on Pioneers 10 and 11. In T. Gehrels, & S. Matthews, editors, *IAU Colloq. 30: Jupiter: Studies of the Interior, Atmosp here, Magnetosphere and Satellites*, pages 531–563, Jan. 1976.

E. A. Gilbert, T. Barclay, J. E. Schlieder, et al. The first habitable zone earth-sized planet from tess. i: Validation of the toi-700 system, 2020.

M. Gillon, A. H. M. J. Triaud, B.-O. Demory, et al. Seven temperate terrestrial planets around the nearby ultracool dwarf star trappist-1. *Nature*, 542, February 2017. doi: 10.1038/nature21360;. URL http://dx.doi.org/10.1038/nature21360.

I. Gómez-Leal, E. Pallé, & F. Selsis. Photometric Variability of the Disk-integrated Thermal Emission of the Earth. *ApJ*, 752:28, June 2012. doi: 10.1088/0004-637X/752/1/28.

I. Gómez-Leal, F. Codron, & F. Selsis. Thermal light curves of Earth-like planets: 1. Varying surface and rotation on planets in a terrestrial orbit. *Icarus*, 269:98–110, May 2016. doi: 10.1016/j.icarus.2015.12.050.

R. Goody, & H. Hu. Radiative transfer | absorption and thermal emission. In J. R. Holton, editor, *Encyclopedia of Atmospheric Sciences*, pages 1863–1871. Academic Press, Oxford, 2003. ISBN 978-0-12-227090-1. doi: https://doi.org/10.1016/B0-12-227090-8/00337-7. URL https://www.sciencedirect.com/science/article/pii/B0122270908003377.

I. E. Gordon, L. S. Rothman, R. J. Hargreaves, et al. The HITRAN2020 molecular spectroscopic database. *JQSRT*, 277:107949, Jan. 2022. doi: 10.1016/j.jqsrt.2021.107949.

K. M. Gorski, E. Hivon, A. J. Banday, et al. HEALPix - A Framework for high resolution discretization, and fast analysis of data distributed on the sphere. *Astrophys. J.*, 622:759–771, 2005. doi: 10.1086/427976.

T. P. Greene, T. J. Bell, E. Ducrot, et al. Thermal emission from the Earth-sized exoplanet TRAPPIST-1 b using JWST. *Nature*, 618(7963):39–42, June 2023. doi: 10.1038/s41586-023-05951-7.

J. L. Grenfell. *Atmospheric Biosignatures*, pages 3159–3172. Springer International Publishing, Cham, 2018. ISBN 978-3-319-55333-7. doi: 10.1007/978-3-319-55333-7_68. URL https://doi.org/10.1007/978-3-319-55333-7_68.

J. L. Grenfell, B. Stracke, P. von Paris, et al. The response of atmospheric chemistry on earthlike planets around f, g and k stars to small variations in orbital distance. *Planetary and Space Science*, 55 (5):661–671, 2007. ISSN 0032-0633. doi: https://doi.org/10.1016/j.pss.2006.09.002. URL https://www.sciencedirect.com/science/article/pii/S0032063306002613. Extrasolar Planets and Planetary Formation.

J. L. Grenfell, S. Gebauer, P. v. Paris, M. Godolt, & H. Rauer. Sensitivity of biosignatures on Earth-like planets orbiting in the habitable zone of cool M-dwarf Stars to varying stellar UV radiation and surface biomass emissions. *Planet. Space Sci.*, 98:66–76, Aug. 2014. doi: 10.1016/j.pss.2013.10.006.

I. Guendelman, & Y. Kaspi. Atmospheric dynamics on terrestrial planets: The seasonal response to changes in orbital, rotational, and radiative timescales. *The Astrophysical Journal*, 881(1):67, aug 2019. doi: 10.3847/1538-4357/ab2a06. URL https://doi.org/10.3847/1538-4357/ab2a06.

R. Hanel, B. Conrath, D. Gautier, et al. The Voyager Infrared Spectroscopy and Radiometry Investigation. *SSRv*, 21(2):129–157, Nov. 1977. doi: 10.1007/BF00200848.

R. A. Hanel, B. J. Conrath, V. G. Kunde, et al. The nimbus 4 infrared spectroscopy experiment: 1. calibrated thermal emission spectra. *Journal of Geophysical Research*, 77(15):2629–2641, 1972. doi: 10.1029/JC077i015p02629. URL https://agupubs.onlinelibrary.wiley.com/doi/abs/10.1029/JC077i015p02629.

C. E. Harman, & S. Domagal-Goldman. *Biosignature False Positives*, page 71. Springer Cham, 2018. doi: 10.1007/978-3-319-55333-7_71.

A. H. Harvey, J. S. Gallagher, & J. M. H. L. Sengers. Revised formulation for the refractive index of water and steam as a function of wavelength, temperature and density. *Journal of Physical and Chemical Reference Data*, 27(4):761–774, 1998. doi: 10.1063/1.556029. URL https://doi.org/10.1063/1.556029.

L. E. Hays, M. H. New, & M. A. Voytek. 2015 NASA Astrobiology Strategy Document and the Vision for Solar System Exploration. In LPI Editorial Board, editor, *Planetary Science Vision 2050 Workshop*, volume 1989 of *LPI Contributions*, page 8141, Feb. 2017.

T. Hearty, I. Song, S. Kim, & G. Tinetti. Mid-infrared properties of disk averaged observations of earth with airs. *The Astrophysical Journal*, 693(2):1763, 2009. URL http://stacks.iop.org/0004-637X/693/i=2/a=1763.

C. Hedges, & N. Madhusudhan. Effect of pressure broadening on molecular absorption cross sections in exoplanetary atmospheres. *Monthly Notices of the Royal Astronomical Society*, 458(2):1427–1449, 03 2016. ISSN 0035-8711. doi: 10.1093/mnras/stw278. URL https://doi.org/10.1093/mnras/stw278.

T. Heidar, E. J. Thrastarson, & S. R. Fetzer. Overview of the AIRS Mission: Instruments, Processing Algorithms, Products, and Documentation, 2nd Edition, 5 2021. URL https://docserver.gesdisc.eosdis.nasa.gov/public/project/AIRS/Overview_of_the_AIRS_Mission.pdf.

M. L. Hill, K. Bott, P. A. Dalba, et al. A catalog of habitable zone exoplanets. *The Astronomical Journal*, 165(2):34, jan 2023. doi: 10.3847/1538-3881/aca1c0. URL https://dx.doi.org/10.3847/1538-3881/aca1c0.

K. I. Hodges, D. W. Chappell, G. J. Robinson, & G. Yang. An improved algorithm for generating global window brightness temperatures from multiple satellite infrared imagery. *Journal of Atmospheric and Oceanic Technology*, 17(10):1296 – 1312, 2000. doi: 10.1175/1520-0426(2000)017<1296:AIAFGG>2.0.CO;2. URL https://journals.ametsoc.org/view/journals/atot/17/10/1520-0426_2000_017_1296_aiafgg_2_0_co_2.xml.

S. R. Hudson, & R. E. Brandt. A look at the surface-based temperature inversion on the antarctic plateau. *Journal of Climate*, 18(11):1673–1696, 2005. doi: 10.1175/JCLI3360.1. URL https://doi.org/10.1175/JCLI3360.1.

J. Hurley, P. Irwin, A. Adriani, et al. Analysis of rosetta/virtis spectra of earth using observations from envisat/aatsr, terra/modis and envisat/sciamachy, and radiative-transfer simulations. *Planetary and Space Science*, 90:37 – 59, 2014. ISSN 0032-0633. doi: https://doi.org/10.1016/j.pss.2013.06.012. URL http://www.sciencedirect.com/science/article/pii/S0032063313001530.

J. Ih, E. M. R. Kempton, E. A. Whittaker, & M. Lessard. Constraining the Thickness of TRAPPIST-1 b's Atmosphere from Its JWST Secondary Eclipse Observation at 15 μm. *ApJL*, 952(1):L4, July 2023. doi: 10.3847/2041-8213/ace03b.

A. Ingersoll, G. Münch, G. Neugebauer, & G. Orton. Results of the infrared radiometer experiment on pioneers 10 and 11. In *IAU Colloq. 30: Jupiter: Studies of the Interior, Atmosp here, Magnetosphere and Satellites*, pages 197–205, 1976.

A. P. Ingersoll. The Runaway Greenhouse: A History of Water on Venus. *Journal of Atmospheric Sciences*, 26(6):1191–1198, Nov. 1969. doi: 10.1175/1520-0469(1969)026<1191:TRGAHO>2.0.CO;2.

International Earth rotation and Reference systems Service. International earth rotation and reference systems, 2014. URL https://www.iers.org/IERS/EN/. [Online; accessed 21-December-2018].

H. Jeffreys. *The Theory of Probability*. Oxford Classic Texts in the Physical Sciences. OUP Oxford, 1998. ISBN 9780191589676.

J. H. Jiang, A. J. Zhai, J. Herman, et al. Using deep space climate observatory measurements to study the earth as an exoplanet. *The Astronomical Journal*, 156(1):26, jun 2018. doi: 10.3847/1538-3881/aac6e2. URL https://bit.ly/3fMUgu4.

T. V. Johnson, C. M. Yeates, & R. Young. *Space Science Reviews Volume on Galileo Mission Overview*, pages 3–21. Springer Netherlands, Dordrecht, 1992. ISBN 978-94-011-2512-3. doi: 10.1007/978-94-011-2512-3_1. URL https://bit.ly/3ElVJld.

C. Jurgenson, D. Fischer, T. McCracken, et al. EXPRES: a next generation RV spectrograph in the search for earth-like worlds. In C. J. Evans, L. Simard, & H. Takami, editors, *Ground-based and Airborne Instrumentation for Astronomy VI*, volume 9908, pages 2051 – 2070. International Society for Optics and Photonics, SPIE, 2016. doi: 10.1117/12.2233002. URL https://doi.org/10.1117/12.2233002.

L. Kaltenegger. How to characterize habitable worlds and signs of life. *Annual Review of Astronomy and Astrophysics*, 55(1):433–485, 2017. doi: 10.1146/annurev-astro-082214-122238. URL https://doi.org/10.1146/annurev-astro-082214-122238.

L. Kaltenegger, W. A. Traub, & K. W. Jucks. Spectral evolution of an earth-like planet. *The Astrophysical Journal*, 658(1):598–616, Mar 2007. ISSN 1538-4357. doi: 10.1086/510996. URL http://dx.doi.org/10.1086/510996.

J. Kammerer, & S. P. Quanz. Simulating the exoplanet yield of a space-based mid-infrared interferometer based on kepler statistics. *A&A*, 609:A4, 2018a. doi: 10.1051/0004-6361/201731254. URL https://doi.org/10.1051/0004-6361/201731254.

J. Kammerer, & S. P. Quanz. Simulating the exoplanet yield of a space-based mid-infrared interferometer based on kepler statistics. *A&A*, 609:A4, 2018b. doi: 10.1051/0004-6361/201731254. URL https://doi.org/10.1051/0004-6361/201731254.

S. R. Kane, M. L. Hill, J. F. Kasting, et al. A Catalog of Kepler Habitable Zone Exoplanet Candidates. *ApJ*, 830(1):1, Oct. 2016. doi: 10.3847/0004-637X/830/1/1.

T. Karman, I. E. Gordon, A. van der Avoird, et al. Update of the hitran collision-induced absorption section. *Icarus*, 328:160–175, 2019. ISSN 0019-1035. doi: https://doi.org/10.1016/j.icarus.2019.02.034. URL https://www.sciencedirect.com/science/article/pii/S0019103518306997.

M. Kasper, N. Cerpa Urra, P. Pathak, et al. PCS — A Roadmap for Exoearth Imaging with the ELT. *The Messenger*, 182:38–43, Mar. 2021. doi: 10.18727/0722-6691/5221.

J. F. Kasting, & D. Catling. Evolution of a habitable planet. *Annual Review of Astronomy and Astrophysics*, 41(1):429–463, 2003. doi: 10.1146/annurev.astro.41.071601.170049. URL https://doi.org/10.1146/annurev.astro.41.071601.170049.

J. F. Kasting, D. P. Whitmire, & R. T. Reynolds. Habitable zones around main sequence stars. *Icarus*, 101(1):108–128, 1993. ISSN 0019-1035. doi: https://doi.org/10.1006/icar.1993.1010. URL https://www.sciencedirect.com/science/article/pii/S0019103583710109.

J. F. Kasting, D. P. Whitmire, & R. T. Reynolds. Habitable Zones around Main Sequence Stars. *Icarus*, 101(1):108–128, Jan. 1993. doi: 10.1006/icar.1993.1010.

H. Kawahara. Frequency modulation of directly imaged exoplanets: Geometric effect as a probe of planetary obliquity. *The Astrophysical Journal*, 822(2):112, May 2016. ISSN 1538-4357. doi: 10.3847/0004-637x/822/2/112. URL http://dx.doi.org/10.3847/0004-637X/822/2/112.

C. D. Keeling. The concentration and isotopic abundances of carbon dioxide in the atmosphere. *Tellus*, 12(2):200–203, 5 1960. ISSN 2153-3490. doi: 10.1111/j.2153-3490.1960.tb01300.x. URL https://doi.org/10.1111/j.2153-3490.1960.tb01300.x.

C. D. Keeling, R. B. Bacastow, A. E. Bain-Bridge, et al. Atmospheric carbon dioxide variations at Mauna Loa Observatory, Hawaii. *Tellus*, 28:538, Jan. 1976. doi: 10.3402/tellusa.v28i6.11322.

C. D. Keeling, J. F. S. Chin, & T. P. Whorf. Increased activity of northern vegetation inferred from atmospheric co2 measurements. *Nature*, 382(6587):146–149, 1996. doi: 10.1038/382146a0. URL https://doi.org/10.1038/382146a0.

M. A. K. Khalil, & R. A. Rasmussen. Sources, sinks, and seasonal cycles of atmospheric methane. *Journal of Geophysical Research: Oceans*, 88(C9):5131–5144, 1983. doi: https://doi.org/10.1029/JC088iC09p05131. URL https://agupubs.onlinelibrary.wiley.com/doi/abs/10.1029/JC088iC09p05131.

M. D. King, S. Platnick, W. P. Menzel, S. A. Ackerman, & P. A. Hubanks. Spatial and temporal distribution of clouds observed by modis onboard the terra and aqua satellites. *IEEE Transactions on Geoscience and Remote Sensing*, 51(7):3826–3852, 2013. doi: 10.1109/TGRS.2012.2227333.

D. Kitzmann, A. B. C. Patzer, P. von Paris, M. Godolt, & H. Rauer. Clouds in the atmospheres of extrasolar planets. II. Thermal emission spectra of Earth-like planets influenced by low and high-level clouds. *A&A*, 531:A62, July 2011. doi: 10.1051/0004-6361/201014343.

L. Klein, D. Ilg, D. Wynne, & R. Gejjagaraguppe. Hdf-eos library user's guide volume 1: Overview and examples, 1999. URL https://edhs1.gsfc.nasa.gov/waisdata/sdp/pdf/tp17050001.pdf.

A. J. Kliore, & P. M. Woiceshyn. Structure of the atmosphere of Jupiter from Pioneer 10 and 11 radio occultation measurements. In T. Gehrels, & S. Matthews, editors, *IAU Colloq. 30: Jupiter: Studies of the Interior, Atmosp here, Magnetosphere and Satellites*, pages 216–237, Jan. 1976.

C. E. Kohlhase, & P. A. Penzo. Voyager Mission Description. *SSRv*, 21(2):77–101, Nov. 1977. doi: 10.1007/BF00200846.

D. D. B. Koll, M. Malik, M. Mansfield, et al. Identifying Candidate Atmospheres on Rocky M Dwarf Planets via Eclipse Photometry. *ApJ*, 886(2):140, Dec. 2019. doi: 10.3847/1538-4357/ab4c91.

T. D. Komacek, T. J. Fauchez, E. T. Wolf, & D. S. Abbot. Clouds will likely prevent the detection of water vapor in jwst transmission spectra of terrestrial exoplanets. *The Astrophysical Journal*, 888(2):L20, Jan. 2020. doi: 10.3847/2041-8213/ab6200. URL https://doi.org/10.3847/2041-8213/ab6200.

K. Y. Kondratyev. *Climatic Effects of Aerosols and Clouds*. Heidelberg: Springer, 1999.

B. S. Konrad, E. Alei, S. P. Quanz, et al. Large interferometer for exoplanets (life) - iii. spectral resolution, wavelength range, and sensitivity requirements based on atmospheric retrieval analyses of an exo-earth. *A&A*, 664:A23, 2022. doi: 10.1051/0004-6361/202141964. URL https://doi.org/10.1051/0004-6361/202141964.

B. S. Konrad, E. Alei, S. P. Quanz, et al. Large Interferometer For Exoplanets (LIFE). IX. Assessing the impact of clouds on atmospheric retrievals at mid-infrared wavelengths with a Venus-twin exoplanet. *A&A*, 673:A94, May 2023. doi: 10.1051/0004-6361/202245655.

R. K. Kopparapu, R. Ramirez, J. F. Kasting, et al. Habitable Zones around Main-sequence Stars: New Estimates. *ApJ*, 765(2):131, Mar. 2013. doi: 10.1088/0004-637X/765/2/131.

R. K. Kopparapu, R. Ramirez, J. F. Kasting, et al. HABITABLE ZONES AROUND MAIN-SEQUENCE STARS: NEW ESTIMATES. *The Astrophysical Journal*, 765(2):131, feb 2013. doi: 10.1088/0004-637x/765/2/131. URL https://doi.org/10.1088/0004-637x/765/2/131.

T. Kozakis, J. M. Mendonça, & L. A. Buchhave. Is ozone a reliable proxy for molecular oxygen?. I. The O_2-O_3 relationship for Earth-like atmospheres. *A&A*, 665:A156, Sept. 2022. doi: 10.1051/0004-6361/202244164.

J. Krissansen-Totton, D. S. Bergsman, & D. C. Catling. On detecting biospheres from chemical thermodynamic disequilibrium in planetary atmospheres. *Astrobiology*, 16(1):39–67, 2016. doi: 10.1089/ast.2015.1327. URL https://doi.org/10.1089/ast.2015.1327. PMID: 26789355.

J. Krissansen-Totton, R. Garland, P. Irwin, & D. C. Catling. Detectability of Biosignatures in Anoxic Atmospheres with the James Webb Space Telescope: A TRAPPIST-1e Case Study. *AJ*, 156(3):114, Sep 2018. doi: 10.3847/1538-3881/aad564.

J. Krissansen-Totton, S. Olson, & D. C. Catling. Disequilibrium biosignatures over earth history and implications for detecting exoplanet life. *Science Advances*, 4(1):eaao5747, 2018. doi: 10.1126/sciadv.aao5747. URL https://www.science.org/doi/abs/10.1126/sciadv.aao5747.

J. Krissansen-Totton, M. Thompson, M. L. Galloway, & J. J. Fortney. Understanding planetary context to enable life detection on exoplanets and test the Copernican principle. *Nature Astronomy*, 6:189–198, Feb. 2022. doi: 10.1038/s41550-021-01579-7.

M. Langlois, R. Gratton, A. M. Lagrange, et al. The SPHERE infrared survey for exoplanets (SHINE). II. Observations, data reduction and analysis, detection performances, and initial results. *A&A*, 651:A71, July 2021. doi: 10.1051/0004-6361/202039753.

J. Lederberg. Signs of Life: Criterion-System of Exobiology. *Nature*, 207(4992):9–13, July 1965. doi: 10.1038/207009a0.

A. Leffler, N. M. Schneider, Z. Milby, et al. Seasonal Mars Circulation Patterns as seen through Observations and Mars General Circulation Models. In *AGU Fall Meeting Abstracts*, volume 2019, pages P41B–3429, Dec. 2019.

O. R. Lehmer, D. C. Catling, M. N. Parenteau, N. Y. Kiang, & T. M. Hoehler. The peak absorbance wavelength of photosynthetic pigments around other stars from spectral optimization. *Frontiers in Astronomy and Space Sciences*, 8, 2021. ISSN 2296-987X. doi: 10.3389/fspas.2021.689441. URL https://www.frontiersin.org/article/10.3389/fspas.2021.689441.

G. Lessin, L. Polimene, Y. Artioli, et al. Modeling the seasonality and controls of nitrous oxide emissions on the northwest european continental shelf. *Journal of Geophysical Research: Biogeosciences*, 125(6):e2019JG005613, 2020. doi: https://doi.org/10.1029/2019JG005613. URL https://agupubs.onlinelibrary.wiley.com/doi/abs/10.1029/2019JG005613. e2019JG005613 2019JG005613.

O. Lim, B. Benneke, R. Doyon, et al. Atmospheric Reconnaissance of TRAPPIST-1 b with JWST/NIRISS: Evidence for Strong Stellar Contamination in the Transmission Spectra. *arXiv e-prints*, art. arXiv:2309.07047, Sept. 2023. doi: 10.48550/arXiv.2309.07047.

G. G. Lin, R. E. Wolfe, P. Zhang, et al. Thirty-six combined years of MODIS geolocation trending. In J. J. Butler, X. J. Xiong, & X. Gu, editors, *Earth Observing Systems XXIV*, volume 11127, pages 219 – 230. International Society for Optics and Photonics, SPIE, 2019. doi: 10.1117/12.2529447. URL https://doi.org/10.1117/12.2529447.

A. P. Lincowski, V. S. Meadows, S. Zieba, et al. Potential atmospheric compositions of trappist-1 c constrained by jwst/miri observations at 15 μm, 2023.

M. Line, S. P. Quanz, E. W. Schwieterman, et al. The Importance of Thermal Emission Spectroscopy for Understanding Terrestrial Exoplanets. *BAAS*, 51(3):271, May 2019.

E. R. Lippincott, R. V. Eck, M. O. Dayhoff, & C. Sagan. Thermodynamic Equilibria in Planetary Atmospheres. *The Astrophysical Journal*, 147:753, Feb. 1967. doi: 10.1086/149051.

T. A. Livengood, L. D. Deming, M. F. A'Hearn, et al. Properties of an earth-like planet orbiting a sun-like star: Earth observed by the epoxi mission. *Astrobiology*, 11(9):907–930, 2011. doi: 10.1089/ast.2011.0614. URL https://doi.org/10.1089/ast.2011.0614.

M. C. Long, B. B. Stephens, K. McKain, et al. Strong southern ocean carbon uptake evident in airborne observations. *Science*, 374(6572):1275–1280, 2021. doi: 10.1126/science.abi4355. URL https://www.science.org/doi/abs/10.1126/science.abi4355.

J. E. Lovelock. A Physical Basis for Life Detection Experiments. *Nature*, 207(4997):568–570, Aug. 1965. doi: 10.1038/207568a0.

J. E. Lovelock, I. R. Kaplan, & N. W. Pirie. Thermodynamics and the recognition of alien biospheres. *Proceedings of the Royal Society of London. Series B. Biological Sciences*, 189(1095):167–181, 1975. doi: 10.1098/rspb.1975.0051. URL https://royalsocietypublishing.org/doi/abs/10.1098/rspb.1975.0051.

L. Lu. Observation and feature measurements of cloud and haze in exoplanet atmosphere based on transmission spectra. *HSET*, 38:90–96, 2023. doi: 10.54097/hset.v38i.5738.

J. Lustig-Yaeger, V. S. Meadows, & A. P. Lincowski. The detectability and characterization of the TRAPPIST-1 exoplanet atmospheres with JWST. *The Astronomical Journal*, 158(1):27, jun 2019. doi: 10.3847/1538-3881/ab21e0. URL https://doi.org/10.3847/1538-3881/ab21e0.

J. Lustig-Yaeger, G. Fu, E. M. May, et al. A JWST transmission spectrum of the nearby Earth-sized exoplanet LHS 475 b. *Nature Astronomy*, Aug. 2023a. doi: 10.1038/s41550-023-02064-z.

J. Lustig-Yaeger, V. S. Meadows, D. Crisp, M. R. Line, & T. D. Robinson. Earth as a Transiting Exoplanet: A Validation of Transmission Spectroscopy and Atmospheric Retrieval Methodologies for Terrestrial Exoplanets. *arXiv e-prints*, art. arXiv:2308.14804, Aug. 2023b. doi: 10.48550/arXiv.2308.14804.

M. López-Valverde, M. López-Puertas, B. Funke, et al. Modeling the atmospheric limb emission of co2 at 4.3 μm in the terrestrial planets. *Planetary and Space Science*, 59(10):988–998, 2011. ISSN 0032-0633. doi: https://doi.org/10.1016/j.pss.2010.02.001. URL https://www.sciencedirect.com/science/article/pii/S0032063310000425. Comparative Planetology: Venus-Earth-Mars.

J. Madden, & L. Kaltenegger. How surfaces shape the climate of habitable exoplanets. *Monthly Notices of the Royal Astronomical Society*, 495(1):1–11, 02 2020. ISSN 0035-8711. doi: 10.1093/mnras/staa387. URL https://doi.org/10.1093/mnras/staa387.

N. Madhusudhan. Atmospheric retrieval of exoplanets. *Handbook of Exoplanets*, page 2153–2182, 2018a. doi: 10.1007/978-3-319-55333-7_104. URL http://dx.doi.org/10.1007/978-3-319-55333-7_104.

N. Madhusudhan. Atmospheric retrieval of exoplanets. *Handbook of Exoplanets*, page 2153–2182, 2018b. doi: 10.1007/978-3-319-55333-7_104. URL http://dx.doi.org/10.1007/978-3-319-55333-7_104.

N. Madhusudhan, S. Sarkar, S. Constantinou, et al. Carbon-bearing molecules in a possible hycean atmosphere, 2023.

E. M. Manning, L. L. Strow, & H. H. Aumann. AIRS version 6.6 and version 7 level-1C products. In J. J. Butler, X. J. Xiong, & X. Gu, editors, *Earth Observing Systems XXIV*, volume 11127, pages 247 – 253. International Society for Optics and Photonics, SPIE, 2019. doi: 10.1117/12.2529400. URL https://doi.org/10.1117/12.2529400.

D. J. D. Marais, & M. R. Walter. Astrobiology: Exploring the origins, evolution, and distribution of life in the universe. *Annual Review of Ecology and Systematics*, 30(1):397–420, 1999. doi: 10.1146/annurev.ecolsys.30.1.397. URL https://doi.org/10.1146/annurev.ecolsys.30.1.397.

G. W. Marcy, L. M. Weiss, E. A. Petigura, et al. Occurrence and core-envelope structure of 1-4×earth-size planets around sun-like stars. *Proceedings of the National Academy of Sciences of the United States of America*, 111(35):12655–12660, 09 2014. doi: 10.1073/pnas.1304197111. URL https://www.ncbi.nlm.nih.gov/pubmed/24912169.

L. Margulis, & J. Lovelock. Biological modulation of the earth's atmosphere. *Icarus*, 21(4):471–489, 1974. ISSN 0019-1035. doi: https://doi.org/10.1016/0019-1035(74)90150-X. URL https://www.sciencedirect.com/science/article/pii/001910357490150X.

C. Marois, B. Macintosh, T. Barman, et al. Direct imaging of multiple planets orbiting the star hr 8799. *Science*, 322(5906):1348–1352, 2008. doi: 10.1126/science.1166585. URL https://www.science.org/doi/abs/10.1126/science.1166585.

C. Marois, B. Zuckerman, Q. M. Konopacky, B. Macintosh, & T. Barman. Images of a fourth planet orbiting hr 8799. *Nature*, 468(7327):1080–1083, 2010. doi: 10.1038/nature09684. URL https://doi.org/10.1038/nature09684.

T. May, E., K. J., M. T., Line, & V. Parmentier. Water ice cloud variability and multi-epoch transmission spectra of trappist-1e. *ApJL*, 911:L30, 2021. doi: 10.3847/2041-8213/abeeff.

M. Mayor, & D. Queloz. A jupiter-mass companion to a solar-type star. *Nature*, 378:355 EP –, 11 1995. URL https://doi.org/10.1038/378355a0.

V. Meadows. *Planetary Environmental Signatures for Habitability and Life*. Springer Praxis Books. Springer, Berlin, Heidelberg, 2008.

V. S. Meadows. Modelling the diversity of extrasolar terrestrial planets. *Proceedings of the International Astronomical Union*, 1(C200):25–34, 2006. doi: 10.1017/S1743921306009033.

V. S. Meadows, & R. K. Barnes. *Factors Affecting Exoplanet Habitability*, pages 2771–2794. Springer International Publishing, Cham, 2018. ISBN 978-3-319-55333-7. doi: 10.1007/978-3-319-55333-7_57. URL https://doi.org/10.1007/978-3-319-55333-7_57.

A. Méndez, E. G. Rivera-Valentín, D. Schulze-Makuch, et al. Habitability Models for Astrobiology. *Astrobiology*, 21(8):1017–1027, Aug. 2021. doi: 10.1089/ast.2020.2342.

J.-N. Mettler, S. P. Quanz, & R. Helled. Earth as an Exoplanet. I. Time Variable Thermal Emission Using Spatially Resolved Moderate Imaging Spectroradiometer Data. *The Astrophysical Journal*, 160(6):246, nov 2020. doi: 10.3847/1538-3881/abbc15. URL https://doi.org/10.3847/1538-3881/abbc15.

J.-N. Mettler, S. P. Quanz, R. Helled, S. L. Olson, & E. W. Schwieterman. Earth as an Exoplanet. II. Earth's Time-variable Thermal Emission and Its Atmospheric Seasonality of Bioindicators. *ApJ*, 946(2):82, Apr. 2023. doi: 10.3847/1538-4357/acbe3c. URL https://ui.adsabs.harvard.edu/abs/2023ApJ...946...82M.

A. Misra, V. Meadows, M. Claire, & D. Crisp. Using Dimers to Measure Biosignatures and Atmospheric Pressure for Terrestrial Exoplanets. *Astrobiology*, 14(2):67–86, Feb. 2014. doi: 10.1089/ast.2013.0990.

MODIS User Guide. Modis level 1b product user's guide, 2017. URL https://mcst.gsfc.nasa.gov/sites/default/files/file_attachments/M1054E_PUG_2017_0901_V6.2.2_Terra_V6.2.1_Aqua.pdf.

modis.gsfc.nasa.gov. Nasa - modis webpage, 2023. URL https://modis.gsfc.nasa.gov/about/design.php. [Online; accessed 31-July-2023].

M. J. Molina, & F. S. Rowland. Stratospheric sink for chlorofluoromethanes: chlorine atom-catalysed destruction of ozone. *Nature*, 249:810 EP –, 06 1974. URL https://doi.org/10.1038/249810a0.

P. Mollière, J. P. Wardenier, R. van Boekel, et al. petitRADTRANS. A Python radiative transfer package for exoplanet characterization and retrieval. *A&A*, 627:A67, July 2019. doi: 10.1051/0004-6361/201935470.

P. Mollière, T. Stolker, S. Lacour, et al. Retrieving scattering clouds and disequilibrium chemistry in the atmosphere of hr 8799e. *A&A*, 640:A131, 2020. doi: 10.1051/0004-6361/202038325. URL https://doi.org/10.1051/0004-6361/202038325.

P. Mollière, R. v. Boekel, C. Dullemond, T. Henning, & C. Mordasini. Model atmospheres of irradiated exoplanets: The influence of stellar parameters, metallicity, and the c/o ratio. *ApJ*, 813(1):47, Oct. 2015. ISSN 1538-4357. doi: 10.1088/0004-637x/813/1/47. URL http://dx.doi.org/10.1088/0004-637X/813/1/47.

B. T. Montet, T. D. Morton, D. Foreman-Mackey, et al. Stellar and Planetary Properties of K2 Campaign 1 Candidates and Validation of 17 Planets, Including a Planet Receiving Earth-like Insolation. *ApJ*, 809(1):25, Aug 2015. doi: 10.1088/0004-637X/809/1/25.

C. V. Morley, L. Kreidberg, Z. Rustamkulov, T. Robinson, & J. J. Fortney. Observing the Atmospheres of Known Temperate Earth-sized Planets with JWST. *ApJ*, 850(2):121, Dec 2017. doi: 10.3847/1538-4357/aa927b.

NASA/GSFC/GMAO Carbon Group. OCO-2 GEOS level 3 monthly, 0.5x0.625 assimilated CO2 v10r (OCO2_GEOS_L3CO2_MONTH) at GES DISC, 2021.

NASA/LARC/SD/ASDC. Ceres time-interpolated toa fluxes, clouds and aerosols daily aqua edition4a, 8 2015. URL https://doi.org/10.5067/AQUA/CERES/SSF1DEGDAY_L3.004A.

National Academies of Sciences, Engineering, and Medicine. *Pathways to Discovery in Astronomy and Astrophysics for the 2020s*. The National Academies Press, Washington, DC, 2021. ISBN 978-0-309-46734-6. doi: 10.17226/26141. URL https://nap.nationalacademies.org/catalog/26141/pathways-to-discovery-in-astronomy-and-astrophysics-for-the-2020s.

E. L. Nielsen, R. J. De Rosa, B. Macintosh, et al. The Gemini Planet Imager Exoplanet Survey: Giant Planet and Brown Dwarf Demographics from 10 to 100 au. *AJ*, 158(1):13, July 2019. doi: 10.3847/1538-3881/ab16e9.

C. Nixon, R. Achterberg, P. Romani, et al. Abundances of jupiter's trace hydrocarbons from voyager and cassini. *Planetary and Space Science*, 58:1667 – 1680, 2010. ISSN 0032-0633. doi: 10.1016/j.pss.2010.05.008.

S. L. Olson, E. W. Schwieterman, C. T. Reinhard, & T. W. Lyons. *Earth: Atmospheric Evolution of a Habitable Planet*, pages 1–37. Springer International Publishing, Cham, 2018a. ISBN 978-3-319-30648-3. doi: 10.1007/978-3-319-30648-3_189-1. URL https://bit.ly/3ebtyem.

S. L. Olson, E. W. Schwieterman, C. T. Reinhard, et al. Atmospheric seasonality as an exoplanet biosignature. *The Astrophysical Journal*, 858(2):L14, may 2018b. doi: 10.3847/2041-8213/aac171. URL https://doi.org/10.3847%2F2041-8213%2Faac171.

E. Pallé, P. R. Goode, V. Yurchyshyn, et al. Earthshine and the Earth's albedo: 2. Observations and simulations over 3 years. *Journal of Geophysical Research (Atmospheres)*, 108(D22):4710, Nov. 2003. doi: 10.1029/2003JD003611.

E. Pallé, M. R. Z. Osorio, R. Barrena, P. Montañés-Rodríguez, & E. L. Martín. Earth's transmission spectrum from lunar eclipse observations. *Nature*, 459(7248):814–816, 2009. doi: 10.1038/nature08050. URL https://doi.org/10.1038/nature08050.

A. Paradise, K. Menou, C. Lee, & B. L. Fan. Fundamental Challenges to Remote Sensing of Exo-Earths. *arXiv e-prints*, art. arXiv:2106.00079, May 2021.

C. L. Parkinson. Aqua - brochure, 2003a. URL https://www.nasa.gov/pdf/151986main_Aqua_brochure.pdf.

C. L. Parkinson. Aqua: an earth-observing satellite mission to examine water and other climate variables. *IEEE Transactions on Geoscience and Remote Sensing*, 41(2):173–183, Feb 2003b. ISSN 0196-2892. doi: 10.1109/TGRS.2002.808319.

J. Peixoto, & A. Oort. *Physics of Climate*. American Institute of Physics, 1992. ISBN 9780883187128. URL https://books.google.ch/books?id=3tjKa0YzFRMC.

F. Pepe, P. Molaro, S. Cristiani, et al. ESPRESSO: The next European exoplanet hunter. *Astronomische Nachrichten*, 335(1):8, Jan. 2014. doi: 12.1002/asna.201312004.

E. A. Petigura, A. W. Howard, & G. W. Marcy. Prevalence of earth-size planets orbiting sun-like stars. *Proceedings of the National Academy of Sciences*, 110(48):19273–19278, 2013. doi: 10.1073/pnas.1319909110. URL https://www.pnas.org/doi/abs/10.1073/pnas.1319909110.

F. Petitcolin, & E. Vermote. Land surface reflectance, emissivity and temperature from modis middle and thermal infrared data. *Remote Sensing of Environment*, 83(1):112 – 134, 2002. ISSN 0034-4257. doi: https://doi.org/10.1016/S0034-4257(02)00094-9. URL http://www.sciencedirect.com/science/article/pii/S0034425702000949. The Moderate Resolution Imaging Spectroradiometer (MODIS): a new generation of Land Surface Monitoring.

M. Pidwirny. *Introduction to the Oceans*. Fundamentals of Physical Geography, 2006. URL http://www.physicalgeography.net/fundamentals/8o.html.

S. P. Quanz, I. Crossfield, M. R. Meyer, E. Schmalzl, & J. Held. Direct detection of exoplanets in the 3-10 μm range with E-ELT/METIS. *International Journal of Astrobiology*, 14(2):279–289, Apr 2015. doi: 10.1017/S1473550414000135.

S. P. Quanz, J. Kammerer, D. Defrère, et al. Exoplanet science with a space-based mid-infrared nulling interferometer. In *Proc. SPIE*, volume 10701 of *Society of Photo-Optical Instrumentation Engineers (SPIE) Conference Series*, page 107011I, Jul 2018. doi: 10.1117/12.2312051.

S. P. Quanz, O. Absil, D. Angerhausen, et al. Atmospheric characterization of terrestrial exoplanets in the mid-infrared: biosignatures, habitability & diversity. *Experimental Astronomy*, 09 2021a. doi: 10.1007/s10686-021-09791-z.

S. P. Quanz, O. Absil, D. Angerhausen, et al. Atmospheric characterization of terrestrial exoplanets in the mid-infrared: biosignatures, habitability & diversity. *Experimental Astronomy*, 09 2021b. doi: 10.1007/s10686-021-09791-z.

S. P. Quanz, M. Ottiger, E. Fontanet, et al. Large Interferometer For Exoplanets (LIFE). I. Improved exoplanet detection yield estimates for a large mid-infrared space-interferometer mission. *A&A*, 664:A21, Aug. 2022. doi: 10.1051/0004-6361/202140366.

E. V. Quintana, T. Barclay, S. N. Raymond, et al. An earth-sized planet in the habitable zone of a cool star. *Science*, 344(6181):277–280, 2014. doi: 10.1126/science.1249403. URL https://www.science.org/doi/abs/10.1126/science.1249403.

A. Quirrenbach, P. J. Amado, J. A. Caballero, et al. *CARMENES instrument overview*, volume 9147 of *Society of Photo-Optical Instrumentation Engineers (SPIE) Conference Series*, page 91471F. 2014. doi: 10.1117/12.2056453.

H. Rauer, C. Catala, C. Aerts, et al. The plato 2.0 mission. *Experimental Astronomy*, 38(1-2):249–330, Sep 2014. ISSN 1572-9508. doi: 10.1007/s10686-014-9383-4. URL http://dx.doi.org/10.1007/s10686-014-9383-4.

C. T. Reinhard, S. L. Olson, E. W. Schwieterman, & T. W. Lyons. False negatives for remote life detection on ocean-bearing planets: Lessons from the early earth. *Astrobiology*, 17(4):287–297, 2017. doi: 10.1089/ast.2016.1598. URL https://doi.org/10.1089/ast.2016.1598. PMID: 28418704.

L. A. Remer, Y. J. Kaufman, D. Tanré, et al. The modis aerosol algorithm, products, and validation. *Journal of the Atmospheric Sciences*, 62(4):947 – 973, 2005. doi: https://doi.org/10.1175/JAS3385.1. URL https://journals.ametsoc.org/view/journals/atsc/62/4/jas3385.1.xml.

I. Ribas, E. Bolmont, F. Selsis, et al. The habitability of Proxima Centauri b. I. Irradiation, rotation and volatile inventory from formation to the present. *A&A*, 596:A111, Dec. 2016. doi: 10.1051/0004-6361/201629576.

G. R. Ricker, J. N. Winn, R. Vanderspek, et al. Transiting Exoplanet Survey Satellite (TESS). *Journal of Astronomical Telescopes, Instruments, and Systems*, 1:014003, Jan 2015. doi: 10.1117/1.JATIS.1.1.014003.

T. Robinson, & A. Salvador. Exploring and validating exoplanet atmospheric retrievals with solar system analog observations. *The Planetary Science Journal*, 4:10, 01 2023. doi: 10.3847/PSJ/acac9a.

T. D. Robinson. MODELING THE INFRARED SPECTRUM OF THE EARTH-MOON SYSTEM: IMPLICATIONS FOR THE DETECTION AND CHARACTERIZATION OF EARTHLIKE EXTRASOLAR PLANETS AND THEIR MOONLIKE COMPANIONS. *The Astrophysical Journal*, 741(1):51, oct 2011. doi: 10.1088/0004-637x/741/1/51. URL https://doi.org/10.1088%2F0004-637x%2F741%2F1%2F51.

T. D. Robinson, & C. T. Reinhard. Earth as an Exoplanet. *arXiv e-prints*, art. arXiv:1804.04138, Apr. 2018.

T. D. Robinson, V. S. Meadows, & D. Crisp. Detecting Oceans on Extrasolar Planets Using the Glint Effect. *ApJL*, 721(1):L67–L71, Sept. 2010. doi: 10.1088/2041-8205/721/1/L67.

T. D. Robinson, K. Ennico, V. S. Meadows, et al. Detection of ocean glint and ozone absorption using lcross earth observations. *The Astrophysical Journal*, 787(2):171, 2014. URL http://stacks.iop.org/0004-637X/787/i=2/a=171.

W. B. Rossow, & R. A. Schiffer. Advances in understanding clouds from isccp. *Bull. Amer. Meteorol. Soc.*, 80:2261–2288, 1999. doi: 10.1175/1520-0477(1999)080\%3C2261\%3AAIUCFI\%3E2.0.CO\;2.

W. B. Rossow, & Y.-C. Zhang. Calculation of surface and top-of-atmosphere radiative fluxes from physical quantities based on isccp datasets: 2. validation and first results. *J. Geophys. Res.*, 100:1167–1197, 1995. doi: 10.1029/94JD02746.

S. Rugheimer, & L. Kaltenegger. Spectra of Earth-like Planets through Geological Evolution around FGKM Stars. *ApJ*, 854(1):19, Feb. 2018. doi: 10.3847/1538-4357/aaa47a.

S. Rugheimer, & L. Kaltenegger. Spectra of earth-like planets through geological evolution around FGKM stars. *The Astrophysical Journal*, 854(1):19, feb 2018. doi: 10.3847/1538-4357/aaa47a. URL https://doi.org/10.3847%2F1538-4357%2Faaa47a.

S. Rugheimer, L. Kaltenegger, A. Zsom, A. Segura, & D. Sasselov. Spectral Fingerprints of Earth-like Planets Around FGK Stars. *Astrobiology*, 13(3):251–269, Mar. 2013. doi: 10.1089/ast.2012.0888.

S. Rugheimer, L. Kaltenegger, A. Segura, J. Linsky, & S. Mohanty. Effect of UV Radiation on the Spectral Fingerprints of Earth-like Planets Orbiting M Stars. *ApJ*, 809(1):57, Aug. 2015. doi: 10.1088/0004-637X/809/1/57.

C. Sagan, W. R. Thompson, R. Carlson, D. Gurnett, & C. Hord. A search for life on earth from the galileo spacecraft. *Nature*, 365:715 EP –, 10 1993. URL https://doi.org/10.1038/365715a0.

N. Schneider, F. Selsis, J. Urban, et al. Seasonal and diurnal ozone variations. *Journal of Atmospheric Chemistry*, 50(1):25–47, 2005. doi: 10.1007/s10874-005-1172-z. URL https://hal.archives-ouvertes.fr/hal-00256287.

J. C. Schwartz, C. Sekowski, H. M. Haggard, E. Pallé, & N. B. Cowan. Inferring planetary obliquity using rotational and orbital photometry. *Monthly Notices of the Royal Astronomical Society*, 457(1):926–938, Jan 2016. ISSN 1365-2966. doi: 10.1093/mnras/stw068. URL http://dx.doi.org/10.1093/mnras/stw068.

E. W. Schwieterman. *Exploring Habitability Markers, Biosignatures, and Their False Positives Using Spectral Models of Terrestrial Exoplanets*. Phd thesis, University of Washington, Seattle, WA, Aug 2016.

E. W. Schwieterman. *Surface and Temporal Biosignatures*, pages 3173–3201. Springer International Publishing, Cham, 2018. ISBN 978-3-319-55333-7. doi: https://doi.org/10.1007/978-3-319-55333-7_69. URL https://bit.ly/3SMbyGc.

E. W. Schwieterman, T. D. Robinson, V. S. Meadows, A. Misra, & S. Domagal-Goldman. Detecting and Constraining N_2 Abundances in Planetary Atmospheres Using Collisional Pairs. *ApJ*, 810(1):57, Sept. 2015. doi: 10.1088/0004-637X/810/1/57.

E. W. Schwieterman, T. D. Robinson, V. S. Meadows, A. Misra, & S. Domagal-Goldman. DETECTING AND CONSTRAINING n2 ABUNDANCES IN PLANETARY ATMOSPHERES USING COLLISIONAL PAIRS. *The Astrophysical Journal*, 810(1):57, aug 2015. doi: 10.1088/0004-637x/810/1/57. URL https://doi.org/10.1088/0004-637x/810/1/57.

E. W. Schwieterman, N. Y. Kiang, M. N. Parenteau, et al. Exoplanet biosignatures: A review of remotely detectable signs of life. *Astrobiology*, 18(6):663–708, Jun 2018. ISSN 1557-8070. doi: 10.1089/ast.2017.1729. URL http://dx.doi.org/10.1089/ast.2017.1729.

S. Seager, E. Turner, J. Schafer, & E. Ford. Vegetation's red edge: A possible spectroscopic biosignature of extraterrestrial plants. *Astrobiology*, 5(3):372–390, jun 2005. doi: 10.1089/ast.2005.5.372. URL https://doi.org/10.1089%2Fast.2005.5.372.

A. Segura, J. F. Kasting, V. Meadows, et al. Biosignatures from earth-like planets around m dwarfs. *Astrobiology*, 5(6):706–725, 2005.

Segura, A., Meadows, V. S., Kasting, J. F., Crisp, D., & Cohen, M. Abiotic formation of o2 and o3 in high-co2 terrestrial atmospheres. *A&A*, 472(2):665–679, 2007. doi: 10.1051/0004-6361:20066663. URL https://doi.org/10.1051/0004-6361:20066663.

F. Selsis. Search for signatures of life on exoplanets. In B. H. Foing, & B. Battrick, editors, *Earth-like Planets and Moons*, volume 514 of *ESA Special Publication*, pages 251–258, Oct. 2002.

F. Selsis, D. Despois, & J. P. Parisot. Signature of life on exoplanets: Can Darwin produce false positive detections? *A&A*, 388:985–1003, June 2002. doi: 10.1051/0004-6361:20020527.

F. Selsis, L. Kaltenegger, & J. Paillet. Terrestrial exoplanets: Diversity, habitability and characterization. *Physica Scripta*, 2008:014032, 07 2008. doi: 10.1088/0031-8949/2008/T130/014032.

D. E. Sergeev, N. T. Lewis, F. H. Lambert, et al. Bistability of the Atmospheric Circulation on TRAPPIST-1e. *PSJ*, 3(9):214, Sept. 2022. doi: 10.3847/PSJ/ac83be.

Y. Shliakhetska, & A. P. Vidmachenko. Seasonal changes in Jupiter's atmosphere restored their periodicity. In *New Trends in Astrophysics, Cosmology and HEP after Gamow*, pages 55–56, Aug. 2019.

J. Skilling. Nested sampling for general bayesian computation. *Bayesian Anal.*, 1(4):833–859, 12 2006. doi: 10.1214/06-BA127. URL https://doi.org/10.1214/06-BA127.

M. Sneep, & W. Ubachs. Direct measurement of the Rayleigh scattering cross section in various gases. *JQSRT*, 92(3):293–310, May 2005. doi: 10.1016/j.jqsrt.2004.07.025.

I. Snellen, R. de Kok, J. L. Birkby, et al. Combining high-dispersion spectroscopy with high contrast imaging: Probing rocky planets around our nearest neighbors. *A&A*, 576:A59, Apr 2015. doi: 10.1051/0004-6361/201425018.

L. L. Strow, S. E. Hannon, S. De-Souza Machado, H. E. Motteler, & D. C. Tobin. Validation of the atmospheric infrared sounder radiative transfer algorithm. *Journal of Geophysical Research: Atmospheres*, 111(D9), 2006. doi: https://doi.org/10.1029/2005JD006146. URL https://agupubs.onlinelibrary.wiley.com/doi/abs/10.1029/2005JD006146.

Y. Tan, R. V. Kochanov, L. S. Rothman, & I. E. Gordon. Introduction of water-vapor broadening parameters and their temperature-dependent exponents into the hitran database: Part i—co2, n2o, co, ch4, o2, nh3, and h2s. *Journal of Geophysical Research: Atmospheres*, 124(21):11580–11594, 2019. doi: https://doi.org/10.1029/2019JD030929. URL https://agupubs.onlinelibrary.wiley.com/doi/abs/10.1029/2019JD030929.

R. Thalman, K. J. Zarzana, M. A. Tolbert, & R. Volkamer. Rayleigh scattering cross-section measurements of nitrogen, argon, oxygen and air. *JQSRT*, 147:171–177, Nov. 2014. doi: 10.1016/j.jqsrt.2014.05.030.

R. Thalman, K. J. Zarzana, M. A. Tolbert, & R. Volkamer. Erratum to "Rayleigh scattering cross-section measurements of nitrogen, argon, oxygen and air" J Quant Spectrosc Radiat Transf 147 (2014) 171-177. *JQSRT*, 189:281–282, Mar. 2017. doi: 10.1016/j.jqsrt.2016.12.014.

The LUVOIR Team. The LUVOIR Mission Concept Study Final Report. *arXiv e-prints*, art. arXiv:1912.06219, Dec 2019.

B. Tian, E. Manning, J. Roman, et al. Airs version 7 level 3 product user guide, 2020a. URL https://docserver.gesdisc.eosdis.nasa.gov/public/project/AIRS/V7_L3_User_Guide.pdf.

H. Tian, R. Xu, J. Canadell, et al. A comprehensive quantification of global nitrous oxide sources and sinks. *Nature*, 586(7828):248–256, Oct. 2020b. ISSN 0028-0836. doi: 10.1038/s41586-020-2780-0.

G. Tinetti, V. S. Meadows, D. Crisp, et al. Detectability of planetary characteristics in disk-averaged spectra. i: The earth model. *Astrobiology*, 6(1):34–47, 2006a. doi: 10.1089/ast.2006.6.34. URL https://doi.org/10.1089/ast.2006.6.34.

G. Tinetti, V. S. Meadows, D. Crisp, et al. Detectability of planetary characteristics in disk-averaged spectra ii: Synthetic spectra and light-curves of earth. *Astrobiology*, 6(6):881–900, 2006b. doi: 10.1089/ast.2006.6.881. URL https://doi.org/10.1089/ast.2006.6.881. PMID: 17155887.

M. G. Trainer, M. H. Wong, T. H. McConnochie, et al. Seasonal Variations in Atmospheric Composition as Measured in Gale Crater, Mars. *Journal of Geophysical Research (Planets)*, 124(11):3000–3024, Nov. 2019. doi: 10.1029/2019JE006175.

W. A. Traub. The Colors of Extrasolar Planets. In D. Deming, & S. Seager, editors, *Scientific Frontiers in Research on Extrasolar Planets*, volume 294 of *Astronomical Society of the Pacific Conference Series*, pages 595–602, Jan. 2003.

L. Tremblay, M. R. Line, K. Stevenson, et al. The detectability and constraints of biosignature gases in the near- and mid-infrared from transit transmission spectroscopy. *The Astronomical Journal*, 159(3):117, feb 2020. doi: 10.3847/1538-3881/ab64dd. URL https://iopscience.iop.org/article/10.3847/1538-3881/ab64dd.

S. K. Trumbo, & M. E. Brown. The distribution of co2 on europa indicates an internal source of carbon. *Science*, 381(6664):1308–1311, 2023. doi: 10.1126/science.adg4155. URL https://www.science.org/doi/abs/10.1126/science.adg4155.

C. Tschudi, & H. M. Schmid. Quantitative polarimetry of the disk around HD 169142. *A&A*, 655:A37, Nov. 2021. doi: 10.1051/0004-6361/202141028.

C. Tschudi, H. M. Schmid, M. Nowak, et al. Sphere refplanets: Search for ϵ eridani b and warm dust. in prep.

M. C. Turnbull, W. A. Traub, K. W. Jucks, et al. Spectrum of a habitable world: Earthshine in the near-infrared. *The Astrophysical Journal*, 644(1):551, 2006. URL http://stacks.iop.org/0004-637X/644/i=1/a=551.

R. Vanderspek, C. X. Huang, A. Vanderburg, et al. TESS Discovery of an Ultra-short-period Planet around the Nearby M Dwarf LHS 3844. *ApJL*, 871(2):L24, Feb. 2019. doi: 10.3847/2041-8213/aafb7a.

M. Vasquez, F. Schreier, S. Gimeno García, et al. Infrared radiative transfer in atmospheres of Earth-like planets around F, G, K, and M stars. II. Thermal emission spectra influenced by clouds. *A&A*, 557:A46, Sept. 2013. doi: 10.1051/0004-6361/201220566.

A. Vigan, M. Bonavita, B. Biller, et al. The VLT/NaCo large program to probe the occurrence of exoplanets and brown dwarfs at wide orbits. IV. Gravitational instability rarely forms wide, giant planets. *A&A*, 603:A3, July 2017. doi: 10.1051/0004-6361/201630133.

K. Wagner, A. Boehle, P. Pathak, et al. Imaging low-mass planets within the habitable zone of αcentauri. *Nature Communications*, 12(1):922, 2021. doi: 10.1038/s41467-021-21176-6. URL https://doi.org/10.1038/s41467-021-21176-6.

J. J. Wang, J. R. Graham, R. Dawson, et al. Dynamical constraints on the hr 8799 planets with gpi. *The Astronomical Journal*, 156(5):192, oct 2018. doi: 10.3847/1538-3881/aae150. URL https://dx.doi.org/10.3847/1538-3881/aae150.

S. G. Warren, R. M. Eastman, & C. J. Hahn. A survey of changes in cloud cover and cloud types over land from surface observations, 1971–96. *Journal of Climate*, 20(4):717–738, 2007. doi: 10.1175/JCLI4031.1. URL https://doi.org/10.1175/JCLI4031.1.

J. Windsor, T. Robinson, R. Kopparapu, et al. A radiative-convective model for terrestrial planets with self-consistent patchy clouds. *Planet. Sci. J.*, 4:94, 2023. doi: 10.3847/psj/acbf2d.

D. M. Winker, J. Pelon, & M. P. McCormick. The calipso mission: Spaceborne lidar for observation of aerosols and clouds. *SPIE Proceedings*, 2003. doi: 10.1117/12.466539.

R. Wolstencroft, & J. Raven. Photosynthesis: Likelihood of occurrence and possibility of detection on earth-like planets. *Icarus*, 157(2):535–548, 2002. ISSN 0019-1035. doi: https://doi.org/10.1006/icar.2002.6854. URL https://www.sciencedirect.com/science/article/pii/S0019103502968545.

F. Wunderlich, M. Godolt, J. L. Grenfell, et al. Detectability of atmospheric features of earth-like planets in the habitable zone around m dwarfs. *A&A*, 624:A49, 2019. doi: 10.1051/0004-6361/201834504. URL https://doi.org/10.1051/0004-6361/201834504.

W. Yang, A. Marshak, T. Várnai, & Y. Knyazikhin. Epic spectral observations of variability in earth's global reflectance. In *Remote Sensing*, 2018.

J. Young, T. Naylor, M. Brake, et al. Design and integration of the HARPS3 software system. In J. C. Guzman, & J. Ibsen, editors, *Software and Cyberinfrastructure for Astronomy V*, volume 10707, pages 732 – 741. International Society for Optics and Photonics, SPIE, 2018. doi: 10.1117/12.2312830. URL https://doi.org/10.1117/12.2312830.

M. Zechmeister, S. Dreizler, I. Ribas, et al. The CARMENES search for exoplanets around M dwarfs. Two temperate Earth-mass planet candidates around Teegarden's Star. *A&A*, 627:A49, July 2019. doi: 10.1051/0004-6361/201935460.

S. Zieba, L. Kreidberg, E. Ducrot, et al. No thick carbon dioxide atmosphere on the rocky exoplanet TRAPPIST-1 c. *Nature*, 620(7975):746–749, Aug. 2023. doi: 10.1038/s41586-023-06232-z.

List of Abbreviations

AIRS	Atmospheric Infrared Sounder
DAACs	Distributed Active Archive Centers
DB	Direct Broadcast
ELT	Extremely Large Telescopes
EOS	Earth Observing System
EOSDIS	EOS Data and Information Service
ESA	European Space Agency
EUMETSAT	European Organisation for the Exploitation of Meteorological Satellites
EW	Equivalent Width
IASI	Infrared Atmospheric Sounding Interferometer
IFU	Integral Field Unit
JUICE	JUpiter ICy moons Explorer
JWST	James Webb Space Telescope
LIFE	the Large Interferometer For Exoplanets
MIR	mid-Infrared
MODIS	Moderate Imaging Spectroradiometer
NIRSpec	Near-Infrared Spectrograph
NSIDC	National Snow and Ice Data Center
SED	spectral energy distribution
VLT	Very Large Telescope

Acknowledgement

What a journey it was, facing all the challenges and overcoming them step by step until I reached the pinnacle of earning a PhD. This achievement is a testament to the collective efforts of many, and I am sincerely grateful for the contributions of each individual who played a role in my academic journey. Your support, guidance, and encouragement has made this accomplishment possible, and for that, I am deeply thankful.

My heartfelt gratitude goes to my supervisors Ravit Helled and Sascha Quanz, whose exceptional dedication and enthusiasm for the field of astrophysics and exoplanet science was a tremendous inspiration throughout my studies and PhD. Thank you for your support and mentorship as well as for offering me this captivating PhD project that kept me exploring and traveling Earth (via satellites) although being in lockdown during the challenging times of Covid-19.

It has been an invaluable experience working at two research groups across different departments and universities. Thanks to everyone from ETH's Exoplanets and Habitability group and UZH's ICS group. Special thanks to Christian, Björn, Gabo, and Benno for the wonderful times we shared and the many engaging conversations that marked memorable moments. I could not have gone through this PhD without the incredible support of you, the gym bros and the triangle of sadness. This journey would not have been nearly as fun without all the good laughs and the great sarcastic humour!

An immense thank you to my PhD office buddy Christian! Although I lost track of who is leading in our countless nerf gun, dart, and mini-golf battles (... pretty sure I am...), I am sure we will keep this up before we agree on a tie. Without you the whole journey would not have been the same. Thanks for the good laughs, the 11 o'clock lunches and all the great memories. I wish you all the best for your future and always safe rides!

To my family, friends, and loved ones, your encouragement, patience, and belief in me sustained my motivation during challenging times. I am always thankful for the support I have received, especially from my mother, who has always believed in me and supported my pursuit of education.